COLLECTIVITY OF NEUTRON-RICH 30,31 Na STUDIED BY HEAVY-ION INELASTIC SCATTERING AT INTERMEDIATE ENERGIES

By

Roy Salinas

A DISSERTATION

Submitted to
Michigan State University
in partial fulfillment of the requirements
for the degree of

Physics – Doctor of Philosophy

October 13, 2025

ABSTRACT

COLLECTIVITY OF NEUTRON-RICH ^{30,31}Na STUDIED BY HEAVY-ION INELASTIC SCATTERING AT INTERMEDIATE ENERGIES

By

Roy Salinas

Within the framework of the nuclear shell model, the properties of a nucleus with a given number of protons and neutrons are governed by the occupation of the lowest energy single-particle levels allowed by the Pauli exclusion principle. The validity of this model was primarily evidenced through deviations in experimental observables, such as enhanced stability at certain proton and neutron numbers, leading to what is now known as the magic numbers. Understanding how nuclear structure evolves as a function of proton-to-neutron ratio underpins one of the primary goals of modern nuclear structure studies. In particular, the N=20 island of inversion is a neutronrich region of the nuclear landscape where the expected shell gap between the sd and fp shells is reduced, leading to the emergence of collective phenomena. In this region, neutron-rich nuclei such as ^{30,31}Na display ground states dominated by intruder configurations characterized by particle-hole excitations across the shell gap. Despite the evidence for dominant intruder configurations in the ground states of ^{30,31}Na, it remains an open question as to whether the associated deformation is sufficiently robust enough to persist into their low-lying excited states. Addressing this issue is further complicated by the scarcity of data on rotational bands near the neutron drip line, where experimental challenges limit available measurements. In light of this, quantifying the reduced electric quadrupole transition strengths (B(E2)) to the low-lying excited states provides a sensitive probe of collective behavior, offering insight into the extent of the ground-state deformation. Particularly, procuring the E2 transition strengths in 30,31 Na within the N=20 island of inversion can reveal whether static deformation develops into the first and second excited states. Thus, it becomes paramount to accurately determine the B(E2) values stemming from Coulomb excitations.

This dissertation reports on the heavy-ion inelastic scattering measurement performed to investigate the reduced electric quadrupole transition strengths for low-lying excited states in ³⁰Na

and 31 Na. The measurements were performed with the Coupled-Cyclotron Facility and A1900 fragment separator, with an experimental setup composed of the Gamma-ray Energy Tracking Inbeam Nuclear Array (GRETINA), the TRIPLEX device, and the S800 Spectrograph. To extract the $B(E2\uparrow)$ values, simultaneous measurements were carried out with 9 Be and 181 Ta foils separated by 25 mm, where the Be foil was utilized to constrain the nuclear contributions to the excitation cross section measured on the Ta foil. The present work details the excitation cross sections for the (3^+) and (4^+) states in 30 Na, and the $(5/2^+)$ and $(7/2^+)$ in 31 Na. These cross sections were utilized in conjunction with a coupled-channel calculation software (FRESCO) to extract the $B(E2\uparrow)$ values for each excited state.

The $B(E2\uparrow)$ values determined from this analysis were compared to shell-model calculations utilizing three effective interactions to describe each nucleus: FSU, which assumes the promotion of two nucleons across the N=20 shell gap (i.e. pure 2p-2h configuration), SDPF-M, which incorporates a mixture of particle-hole configurations between the sd and fp shells, and USDB, which serves as a reference for sd-shell calculations adopting a pure 0p-0h configuration. The comparison between the experimental results and theoretical calculations suggests a persistence of ground-state deformation in the low-lying excited states of 30 Na and 31 Na.

ACKNOWLEDGEMENTS

I would first like to acknowledge my family, for whom I am (and always will be) grateful towards. I am thankful that we have stayed close despite my time away during undergraduate and graduate studies. To my sisters, Angelica, Mercedes, Victoria, and Isabella, y'all are a funny bunch; each uniquely wonderful. To my brother Kevin, just as I have grown, so have you. We have both made some dumb (and often times fun) decisions together. To my late step-father, Rafael, you taught me enough about cars to begin working on them on my own, while also providing anecdotes along the way. Working on my car (out of necessity most of the time) in graduate school was always a reward after a long day. A mi mamá, Norma, siempre me distes tu apoyo inquebrantable aunque no estaba haciendo lo que debía hacer. Gracias por los sacrificios que hiciste por mí.

To my research advisor and chair of my committee, Dr. Hiro Iwasaki, you have taught me valuable lessons in all aspects of my personal and professional life. I am grateful for your continual commitment to my research progress and development as a scientist, as I am a better person for it now. To my research committee, Drs. Aldric Revel, Remco Zegers, Dean Lee, and Michael Murillo, each one of you contributed positively to my experience in graduate school. I would like to thank the current graduate student members of the Lifetime group: Andrew Douglas and Ian Luebbers, our discussions were always scintillating. To the former and current post-docs I have had the pleasure to work with, Jin Wu and George Zimba, respectively, thank you for fostering my growth in the discussions I have had with you.

To my undergraduate mentors and teachers, Drs. Jim Drachenberg and Larry Isenhower, who always advised me and guided me in a Christ-like manner, thank you for your help in channeling my interest in science and public outreach. I gained so much from interacting with each one of you in and out of the classroom as an undergraduate student. To the Women and Minorities in the Physical Sciences (WaMPS) graduate student organization and the people therein, thank you for the joyful and pleasant experiences I had leading and working with you.

It would be remiss of me to not acknowledge my office mates, Andrew (Andy) Sanchez and

Peter Farris, who have made sharing an office a unique and phenomenal experience. Andy, thank you for always being someone I could talk to and relate to, for sharing good stories, for helping me understand physics concepts, and helping me proofread a lot of things. I am grateful to Peter, for you also listened to my woes and dumb jokes, for engaging in meaningful conversations across a wide range of topics, and for all the technical support you provided to me over the years. You both made coming into the office an enriching experience for me. I am also grateful for Joseph (Joe) Chung-Jung, who even though you recently became an office mate, you have always been a friend.

I must also thank the members of the "MSU Physics Running Club" and the "Basketball group" that I am part of. Staying active was always important to me, but y'all made my time in graduate school memorable in a very unique manner, beyond just physical fitness. To all of my friends here at MSU, I couldn't have asked for a better friend group. All of our celebrations (shoutout to Stobers) and hangouts (shoutout again to Stobers) made all the difference.

To my girlfriend Karina Martirosova, who I am immensely grateful for. You were (and still are) there for me, and continue to show your support through the grace, kindness, and love you extend towards me; a long day wanes away when we are together. Thank you for listening to my burdens, making me laugh, and giving me a different perspective on things in my life. Lastly, to the Lord of my life, thank you for redeeming me and being a light in all that I do in this journey.

So long, and thanks for all the fish.

TABLE OF CONTENTS

| LIST OF | F TABLES | X |
|---------|--|----|
| LIST OF | FFIGURES | хi |
| CHAPT | ER 1 INTRODUCTION | 1 |
| 1.1 | The Nuclear Landscape | 1 |
| 1.2 | The Nuclear Shell Model | 4 |
| | | 8 |
| | | 8 |
| 1.3 | | 11 |
| | | 11 |
| | <u> •</u> | 13 |
| | | 16 |
| 1.4 | | 17 |
| 1.5 | | 19 |
| 1.6 | | 21 |
| 1.0 | Thiomands Thong the 2 Trisotopic Chain Tristriction of the Chain Trist | |
| CHAPT | ER 2 EXPERIMENTAL TECHNIQUES | 23 |
| 2.1 | In-Beam Gamma-Ray Spectroscopy | 23 |
| | | 24 |
| 2.2 | | 27 |
| 2.3 | | 29 |
| | | 30 |
| | | 34 |
| 2.4 | <i>C;</i> | 35 |
| | • | |
| CHAPT | | |
| 3.1 | | 39 |
| 3.2 | The Coupled Cyclotron Facility | 40 |
| 3.3 | Fragment Production and Separation | 43 |
| | 3.3.1 A1900 Fragment Separator | 43 |
| 3.4 | S800 Spectrograph | 45 |
| | 3.4.1 Magnets and Mode of Operation | 47 |
| | 3.4.2 Timing Scintillators | 47 |
| | 3.4.2.1 Timing Corrections | 48 |
| | | 52 |
| | 3.4.3.1 Calibration and Corrections | 52 |
| | | 55 |
| | | 58 |
| 3.5 | | 59 |
| | | 60 |

| | 3.5.2 GRETINA Principle of Operation | |
|--------|---|-------|
| | 3.5.3 Calibration Procedures | 62 |
| 3.6 | ΓRIple PLunger for EXotic beams (TRIPLEX) | 64 |
| 3.7 | Experimental Setup | . 66 |
| | 20.21 | |
| CHAPT | | |
| 4.1 | Data Analysis Tools | |
| | 4.1.1 GrROOT Analysis Software | |
| | 4.1.2 G4Lifetime Simulation Software | |
| | 4.1.2.1 G4Lifetime Calibration | 71 |
| 4.2 | Coupled-Channel Calculations | . 77 |
| | 4.2.1 FRESCO | . 78 |
| | 4.2.1.1 Optical Model Potentials | . 80 |
| | 4.2.2 Determining Angle-Integrated Cross Section | 83 |
| 4.3 | Angular Acceptance Analysis | |
| | 4.3.1 Incorporating Angular Spread to FRESCO Results | |
| | 4.3.1.1 Incoming Beam | |
| | 4.3.1.2 Reaction Products | |
| 4.4 | Benchmark of Analysis Procedure with ³² Mg | |
| 4.5 | Quantifying Background Contamination | |
| 4.6 | ³⁰ Na Analysis | |
| | 4.6.1 Particle Identification of ³⁰ Na | |
| | 4.6.2 Gamma-Ray Spectrum | |
| | 4.6.3 $2_{g,s}^+ \rightarrow (4^+)$ Excitation | |
| | 4.6.4 $2_{g,s}^+ \rightarrow (3^+)$ Excitation | |
| | 4.6.4.1 Gamma-Ray Yield Feeding Corrections | |
| 4.7 | ⁸¹ Na Analysis | |
| , | 4.7.1 Particle Identification of ³¹ Na | |
| | 4.7.2 Gamma-Ray Spectrum | |
| | 4.7.3 $3/2_{g,s}^+ \rightarrow (7/2^+)$ Excitation | |
| | 4.7.4 $3/2_{g,s}^{g,s} \rightarrow (5/2^+)$ Excitation | |
| | 4.7.4.1 Gamma-ray Yield Feeding Corrections | |
| | 4.7.5 Lifetime Determination via Lineshape Analysis for the (7/2+) State | |
| | 7.7.5 Electric Determination via Elifeshape Marysis for the (772) State | 12/ |
| СНАРТ | R 5 DISCUSSION OF RESULTS | . 130 |
| 5.1 | Comparison of B(E2 \uparrow) to Shell-Model Calculations | |
| | 5.1.1 ³⁰ Na Comparison | |
| | 5.1.2 ³¹ Na Comparison | |
| | 5.1.3 Trends of $B(E2)$ and Excitation Energies Along the Na Isotopic Chain | |
| 5.2 | Comparison of $B(E2)$ to Triaxial Particle-Rotor Model Calculations | |
| 5.2 | | |
| CHAPT | R 6 CONCLUSION | 145 |
| | | |
| RIBLIU | PADHV | 1/15 |

| APPENDIX | | | | | _ | | _ | _ | _ | _ | _ | _ | _ | _ | _ | _ | _ | | _ | _ | _ | | _ | _ | _ | _ | _ | _ | | _ | _ | 16 | 51 |
|----------|------|---|-----|-------|---|------|---|---|---|---|---|---|---|---|-------|---|---|---|---|---|---|------|---|---|---|---|---|---|---|---|---|----|----|
| | | • | • • | • | • | | • | • | • | • | • | • | • | • | | • | • | • | • | • | • | | | • | • | • | • | • | • | • | • | 11 | JI |

LIST OF TABLES

| Table 4.1: | Angular acceptances as a function of angular regions spanning 0° –3.5° from the data points in Fig. 4.19 | 94 |
|-------------|---|-----|
| Table 4.2: | Comparison of the excitation cross sections to the 2_1^+ state in 32 Mg using a scattering angle gate of $\theta_{Lab}^{scatt.} \leq 2^{\circ}$ for each target foil obtained from the present benchmark analysis and those reported in Ref. [76] | 102 |
| Table 4.3: | Inelastic scattering cross sections for the $2^+_{g.s.} \to (4^+)$ excitation in 30 Na from the present work. Cross sections for each foil were obtained from the $(4^+) \to (3^+)$ and $(4^+) \to 2^+_{g.s.}$ decays. Results for both Be and Ta targets are shown | 113 |
| Table 4.4: | Extracted nuclear matter deformation lengths (δ_A) from inelastic scattering on the 9 Be target for the $2^+_{g.s.} \rightarrow (4^+)$ excitation. Results from the $^{17}\text{O} + ^{208}\text{Pb}$ [81] and $^{32}\text{Mg} + ^{181}\text{Ta}$ [109] optical model potentials are listed | 115 |
| Table 4.5: | Extracted reduced transition probabilities to the (4^+) state, $B(E2, 2_{g.s.}^+ \rightarrow (4^+))$, from inelastic scattering on the 181 Ta target and δ_A from Table 4.4. Results from the 17 O + 208 Pb [81] and 32 Mg + 181 Ta [109] optical model potentials are listed. Averages are also shown | 115 |
| Table 4.6: | Inelastic scattering cross sections for the $2^+_{g.s.} \to (3^+)$ transition in 30 Na from the present work. Results for both Be and Ta targets are shown | 117 |
| Table 4.7: | Extracted nuclear matter deformation lengths (δ_A) from inelastic scattering on the 9 Be target for the $2^+_{\rm g.s.} \rightarrow (3^+)$ excitation. Results from the $^{17}{\rm O}$ + $^{208}{\rm Pb}$ [81] and $^{32}{\rm Mg}$ + $^{181}{\rm Ta}$ [109] optical model potentials are listed | 117 |
| Table 4.8: | Extracted reduced transition probabilities to the (3^+) state, $B(E2, 2_{g.s.}^+ \rightarrow (3^+))$, from inelastic scattering on the ¹⁸¹ Ta target and δ_A from Table 4.7. Results from the ¹⁷ O + ²⁰⁸ Pb [81] and ³² Mg + ¹⁸¹ Ta [109] optical model potentials are listed. Averages are also shown | 117 |
| Table 4.9: | Inelastic scattering cross sections for the $2^+_{g.s.} \to (7/2^+)$ excitation in 31 Na from the present work. Results for both Be and Ta targets are shown | 123 |
| Table 4.10: | Extracted nuclear matter deformation lengths (δ_A) from inelastic scattering on the ^9Be target for the $3/2^+_{\text{g.s.}} \rightarrow (7/2^+)$ excitation. Results from the ^{17}O + ^{208}Pb [81] and ^{32}Mg + ^{181}Ta [109] optical model potentials are listed | 125 |

| Table 4.11: | Extracted reduced transition probabilities to the $(7/2^+)$ state, $B(E2, 3/2^+_{g.s.} \rightarrow (7/2^+))$, from inelastic scattering on the ¹⁸¹ Ta target and δ_A from Table 4.10. Results from the ¹⁷ O + ²⁰⁸ Pb [81] and ³² Mg + ¹⁸¹ Ta [109] optical model potentials are listed. Averages are also shown | 125 |
|-------------|--|-----|
| Table 4.12: | Inelastic scattering cross sections for the $3/2^+_{g.s.} \rightarrow (5/2^+)$ transition in 31 Na from the present work. Results for both Be and Ta targets are shown | 127 |
| Table 4.13: | Extracted nuclear matter deformation lengths (δ_A) from inelastic scattering on the 9 Be target for the $3/2^+_{\rm g.s.} \rightarrow (5/2^+)$ excitation. Results from the $^{17}{\rm O}$ + $^{208}{\rm Pb}$ [81] and $^{32}{\rm Mg}$ + $^{181}{\rm Ta}$ [109] optical model potentials are listed | 127 |
| Table 4.14: | Extracted reduced transition probabilities to the $(5/2^+)$ state, $B(E2, 3/2_{\rm g.s.}^+ \rightarrow (5/2^+))$, from inelastic scattering on the ¹⁸¹ Ta target and δ_A from Table 4.13. Results from the ¹⁷ O + ²⁰⁸ Pb [81] and ³² Mg + ¹⁸¹ Ta [109] optical model potentials are listed. Averages are also shown | 127 |
| Table 5.1: | Adopted $B(E2 \uparrow)$, β_C , and Q_0 values for 30 Na and 31 Na are compared to previous experimental results [54–56]. β_C and Q_0 values are averaged from the different optical model potential results from the 17 O + 208 Pb [81] and 32 Mg + 181 Ta [109] | 131 |
| Table 5.2: | Present $B(E2 \uparrow)$ for 30 Na results comparing the adopted values from this work with FSU,SDPF-M, and USDB calculations | 137 |
| Table 5.3: | Present $B(E2 \uparrow)$ for ³¹ Na results comparing the adopted values from this work with FSU, SDPF-M, and USDB calculations | 139 |
| | LIST OF FIGURES | |
| Figure 1.1: | The nuclear landscape depicting nuclides as a function of proton (Z) and neutron (N) number. The proton number increases vertically along the y axis whereas the neutron number increases along the x axis. The prominent decay modes of each nuclide are illustrated by color. Black squares denote the valley of stability, a region where nuclei are stable against beta decay. Squares indicate nuclei that have been measured whereas circles are extrapolated from data systematics. The horizontal and vertical solid black lines mark the isotopic and isotonic chains at the magic numbers, respectively. Isotopic chains for each proton magic number have been labeled (e.g. He, O, etc.). The dashed green line denotes the $N=Z$ trend line, highlighting the increasing influence of Coulomb repulsion in heavier nuclei. Data was extracted from Refs. $[1, 2]$ | 2 |

| Figure 1.2: | The one neutron separation energy (S_{1n}) for isotopic chains as a function of neutron numbers N . Isotopic chains at magic numbers are highlighted in red and labeled. The neutron magic numbers are marked by dashed blue lies. The sudden drop in S_{1n} after each magic number denotes a filled shell, marking the subsequent nucleon being less tightly bound due to occupying an open shell. Data was extracted from Refs. $[1, 2]$ | . 4 |
|-------------|--|------|
| Figure 1.3: | Comparison of a Woods-Saxon (red) and harmonic oscillator (blue) potentials. The harmonic oscillator extends to infinity whereas the Woods-Saxon potential diminishes after a finite distance. The flat bottom of the Woods-Saxon potential reflects the saturation of nuclear density, while the harmonic oscillator implies an increasing nuclear density as $r \to 0$ | . 6 |
| Figure 1.4: | Neutron single-particle orbit in 208 Pb calculated using the harmonic oscillator, Woods-Saxon, and Woods-Saxon with spin-orbit potentials. Bracketed numbers denote orbital occupancy, followed by the cumulative occupancy of all prior orbitals. Orbits are labeled by major quantum number N , orbital angular momentum l (using spectroscopic symbols), and the total angular momentum $j = l + s$ where the $2j$ convention is being utilized. Figure is adapted from Ref. [8] | . 7 |
| Figure 1.5: | Schematic illustration of the monopole interaction arising from the tensor force between proton $(j_>, j_<)$ and neutron $(j'_>, j'_<)$ orbits, where the tensor-force is depicted by the black wavy line. Occupation of a neutron $j'_>$ orbit induces an attractive interaction with the proton $j_<$ orbit, making it more bound. In contrast, the similar angular-momentum alignments between the proton $j_>$ and the neutron $j'_>$ orbits invokes a repulsive tensor force interaction, reducing how bound the proton orbit is. Figure was modified from Ref. [18]. | . 9 |
| Figure 1.6: | Evolution of the effective single-particle energies (ESPEs) for the $N=20$ isotones, from $^{40}_{20}$ Ca to $^{28}_{8}$ O, calculated with the SDPF-M interaction. Shaded regions indicate the occupancy of the $d_{3/2}$ (blue), $s_{1/2}$ (orange), and $d_{5/2}$ (green) orbitals. The reduction of the conventional $N=20$ shell gap between the $d_{3/2}$ and $f_{7/2}$ orbitals, together with the emergence of the new $N=16$ gap, arises from the removal of protons from the $d_{5/2}$ orbital. Figure was adapted from Ref. [6] | . 10 |
| Figure 1.7: | Polar diagram illustrating the deformation plane as a function of β , γ . Owing to the symmetry of Eqs. 1.6, 1.7, and 1.8, the plane is partitioned into 6 equivalent segments at increments of $\pi/3$. Shapes along the dashed arrows are identical to those along the solid arrow. Due to the symmetry, the first segment $(0 \le \gamma \le \pi/3)$ is conventionally utilized to describe the shape of the nucleus. Figure was adapted from Ref. [8] | . 13 |

| Figure 1.8: | A super-deformed rotational band in 152 Dy, where the relevant γ -ray transitions between band members have been marked. The constant spacing of the γ -ray energies is characteristic of a system exhibiting the symmetry of an ideal quantum rotor. The observed decreasing intensity pattern for the gamma rays reflects the angular momentum distribution in populating the rotational band in the reaction. The unmarked lower energy peaks correspond to states populated after the decay of the super-deformed band. Figure is adapted from Ref. [32] | 14 |
|-------------|---|----|
| Figure 1.9: | A portion of the nuclear chart emphasizing the $N=20$ island of inversion. The valley of stability is indicated by the black squares, along with the first few proton/neutron magic numbers. The original island of inversion, proposed by Warburton <i>et al.</i> [15], is displayed within the pink squares in the inset. Related to this work are the 30,31 Na isotopes, both of which have been identified as belonging to the $N=20$ island of inversion [44, 45]. Furthermore, the southern shore is now suggested to extend to 28 F [46] | 20 |
| Figure 2.1: | Schematic illustration of an ion emitting a gamma ray in and after passing through a production target. In this figure, the ion's velocity vector is aligned with the laboratory frame's z axis indicated by z_{Lab} . As the ion traverses the target material, it loses velocity (top graph), which impacts the Doppler reconstruction: gamma rays emitted inside the target are reconstructed with different velocities than those emitted outside. Furthermore, due to the decay characteristics of the excited state, gamma rays emitted further downstream are detected at larger emission angles, which also impacts the Doppler reconstruction. | 25 |
| Figure 2.2: | Figure displaying the different contributions to the in-beam gamma-ray resolution as described by Eq. 2.4. The intrinsic resolution ($\delta_{intr.}$) is given by the blue line and the orange line represents contributions due to the uncertainty in the ion's velocity (δ_{β}). The green line denotes the uncertainty contributions stemming from the uncertainty in the emission angle (δ_{θ}), with the sum of all terms given by the red line ($\delta_{tot.}$). For the present figure, values of $\beta = 0.365$, $\Delta\beta = 0.0053$, $\Delta\theta = 0.02$ rad were used together with GRETINA's intrinsic energy resolution of 2.4 keV at 1332 keV [37, 38]. | 27 |
| Figure 2.3: | Schematic illustration of a projectile a undergoing inelastic scattering from a target nucleus A . Part of the system's kinetic energy is transferred to the projectile, leaving it in an excited state a^* . After a characteristic time governed by the lifetime τ of the excited state, the projectile de-excites, emitting radiation as it continues along its trajectory | 28 |

| Figure 2.4: | Schematic illustration of a projectile following a Rutherford trajectory as it approaches the target nucleus. The projectile, with velocity \vec{v} and impact parameter b , undergoes inelastic scattering from the target. During the interaction, collective states in the projectile are excited by the time-dependent Coulomb field generated between the two nuclei. The subsequent emission of a gamma ray from the projectile provides an experimental probe of its internal nuclear structure. | 32 |
|-------------|---|----|
| Figure 2.5: | Graph showcasing the relative importance between the Coulomb and nuclear contributions to the $E2$ excitation cross-section for the 31 Na + Z system. The curves were calculated with FRESCO [78–80] where 31 Na had an incoming beam energy of ~ 102 MeV/u, and representative values of $18~e fm^2$ and $\delta_A = 1.2$ fm for the $E2$ matrix element and nuclear deformation length, respectively. The y axis corresponds to the angle-integrated cross section for events with laboratory-frame scattering angle up to 3° ($\theta_{Lab}^{scatt.} \leq 3^{\circ}$). The angle-integrated cross section was determined from a monte carlo simulation incorporating the incoming beam's angular spread and beam spot size. The x axis corresponds to the proton number z of the target material. The optical potential derived from the elastic scattering of z 0 + z 0 Pb [81] was utilized to produce the curves. | 36 |
| Figure 3.1: | Sectional picture of the Superconduction Source for Ions (SuSI). The image is from Ref. [94] | 40 |
| Figure 3.2: | Schematic view of a portion of the NSCL, highlighting the K500 and K1200 cyclotrons (red), the A1900 fragment separator (orange), the beam switchyard (green), and the analysis line leading to the S800 Spectrograph (blue). The inset at the top left displays an overhead schematic of the NSCL, with blue lines connecting components from the expanded beamline view to their respective experimental vaults. The image is adapted from Ref. [92] | 41 |
| Figure 3.3: | A schematic of the K500 cyclotron. The <i>dees</i> are shown in red, the <i>hills</i> in blue. An accelerating voltage is applied between the <i>dee</i> and the <i>hill</i> , so each time the ionized beam crosses the gap it is accelerated. This image was generated by modifying Fig. 1 of Ref. [89] | 42 |
| Figure 3.4: | A schematic of the NSCL facility, showing the coupled K500 and K1200 cyclotrons and the A1900 fragment separator in the shaded blue region. This image was generated by modifying Fig. 1 of Ref. [89] | 44 |

| - | The S800 Spectrograph. As the beam is injected to the analysis line, it passes through the object station, intermediate image station, and target station. The target station has additional target material to invoke the reaction of interest, with also having an auxiliary detector coupled with the S800. The two giant dipole magnets guide the recoil nuclei produced at the target station up to the focal plane station. The figure was adapted from Ref. [100] | 46 |
|--------------|--|----|
| J | Uncorrected (a) and corrected (b) histograms are shown for dispersive angle in the focal plane (y axis) vs the time-of-flight (TOF) measurement difference between the S800 Object and E1 scintillators (x axis). The corrected histogram show that the TOF and angle are independent of one another, compared to the uncorrected histogram showing a correlation between angle and TOF | 50 |
| | Uncorrected (a) and corrected (b) histograms are shown for dispersive position in the focal plane (y axis) vs the time-of-flight (TOF) measurement difference between the S800 Object and E1 scintillators (x axis). The corrected histogram show that the TOF and position are independent of one another, compared to the uncorrected histogram showing a correlation between position and TOF | 51 |
| _ | Schematic of the S800 spectrograph focal plane showing detectors used in this work. The figure was adapted from Ref. [101] | 53 |
| _ | Ion chamber energy loss signal for ³¹ Na from the fifth ion chamber fit with a Gaussian to determine the mean energy loss | 54 |
| Figure 3.10: | Fitted exponential model (red) to average energy loss per x -bin (blue) for 31 Na | 55 |
| _ | Uncorrected (a) and corrected (b) energy loss 2D histograms for ³¹ Na. The energy loss is displayed along the y-axis and position along the dispersive plane is shown along the x-axis | 56 |
| - | Illustration of an event crossing the Cathode Readout Drift Chambers (CRDCs). The two interaction points (X1,Y1) and (X2,Y2) determine the ion trajectory in the focal plane. In this image, the red line corresponds to the vector of an ion reconstructed from (X1,Y1) and (X2,Y2). The integrated image charge is produced by the accumulation of electrons on the anode wire, parallel to the 224 cathode pads. This figure is adapted from Ref. [102] | 57 |
| _ | Before gain matching (a) and after gain matching (b) a single CRDC. The beam distribution shown corresponds the 31 Na secondary beam. The <i>x</i> -axis corresponds to the 224 pads in the CRDC. The gain matching illustrates the importance in assuring that all pads in a single CRDC are weighted equally | 59 |

| Figure 3.14: | The Gamma-Ray Energy Tracking In-Beam Nuclear Array (GRETINA) [38]. Panel a) shows a photo of an open GRETINA from a prior experiment, illustrating the mounting of the detector modules on one of the hemispheres. The front faces of the detector modules are visible in this picture. The four <i>n</i> -type HPGe crystals within a detector module are shown in panel b) [38], with the A-type and B-type tapered hexagonal shapes labeled. The 36-fold segmentation of an individual crystal is shown in panel c) [38] | 61 |
|--------------|---|----|
| Figure 3.15: | The efficiency of GRETINA measured in the laboratory frame placing a ¹⁵² Eu source on the downstream face of the Be foil (a) and on the downstream face of the Ta foil (b). In both curves the experimental data is in blue and the simulated data is in orange | 63 |
| Figure 3.16: | A picture of the TRIPLEX device. This figure is adapted from Ref. [90] | 65 |
| Figure 3.17: | Illustration of the TRIple PLunger for EXotic beams (TRIPLEX) [90] device. The device can accommodate up to three foils, with adjustable separation distances ranging from 0 mm to 25 mm between the target and first degrader, as well as between the first and second degraders. In this illustration, the incoming beam enters from the left and interacts with the target material before interacting with the first and second degraders. For this experiment, the TRIPLEX device held a 2-mm-thick ⁹ Be foil on the target cone and a 1.3-mm-thick ¹⁸¹ Ta foil on the first degrader cone. This figure was adapted from Ref. [90] | 66 |
| Figure 4.1: | A flow chart displaying the analysis process with the GrROOT software package [104]. The red boxes are programs (e.g. Calculate) from GrROOT, blue boxes represent output (input) files generated (required) by the current (subsequent) program, and green boxes are auxiliary information files for the programs. This figure has been adapted from Ref. [105] | 70 |
| Figure 4.2: | Comparison between experimental (blue) and simulated (red) beam properties for 30 Na. The dispersive angle in the xz plane a_{ta} (top left), non-dispersive angle in the yz plane b_{ta} (top right), kinetic energy distribution d_{ta} (bottom left), and position in the non-dispersive plane y_{ta} (bottom right) are shown. The simulated and experimental beam distributions have been scaled to unity. | 73 |
| Figure 4.3: | Comparison between experimental (blue) and simulated (red) beam properties for 31 Na. The dispersive angle in the xz plane a_{ta} (top left), non-dispersive angle in the yz plane b_{ta} (top right), kinetic energy distribution d_{ta} (bottom left), and position in the non-dispersive plane y_{ta} (bottom right) are shown. The simulated and experimental beam distributions have been scaled to unity. | 74 |

| Figure 4.4: | Comparison between experimental (blue) and simulated (red) beam properties for 32 Mg. The dispersive angle in the xz plane a_{ta} (top left), non-dispersive angle in the yz plane b_{ta} (top right), kinetic energy distribution d_{ta} (bottom left), and position in the non-dispersive plane y_{ta} (bottom right) are shown. The simulated and experimental beam distributions have been scaled to unity. | | 75 |
|-------------|--|---|----|
| Figure 4.5: | GEANT4 rendering of the GRETINA configuration used in this experiment. Liquid cryo-modules are shown in grey, while individual GRETINA crystals are depicted in white and green. The beryllium and tantalum targets are represented by green and red squares, respectively. Two views are provided: a downstream view (left) and an angled downstream view (right). The TRIPLEX device is omitted from the rendering | | 76 |
| Figure 4.6: | G4Lifetime simulation of the GRETINA detector response for a 152 Eu source placed on the downstream face of the tantalum target. Due to the TRIPLEX device being positioned 13 cm upstream from the center of GRETINA, the uppermost edges of the detector modules in the 90° ring exhibit an enhanced response to the incoming radiation. The red hexagon indicates the location of the disabled crystal. The laboratory-frame angles θ_{Lab} and ϕ_{Lab} are the polar and azimuthal angles, respectively | • | 77 |
| Figure 4.7: | FRESCO input file for the 30 Na + 181 Ta reaction. This input file contains an optical potential with the Coulomb term, along with real and imaginary nuclear volume terms. The Coulomb term is associated with an $E2$ matrix element of $18.5 \ efm^2$. The nuclear volume term is deformed with a nuclear deformation length $\delta_A = 1.872$ fm. The real and imaginary values (i.e. type=1, p_1 , , p_6) are from the 17 O + 208 Pb reaction [81]. The $^{3+}$ excited state at 426 keV is designated to belong to the $K=2$ rotational band built upon the $^{2+}_{g.s.}$ via the kkp=2 parameter | | 78 |
| Figure 4.8: | FRESCO input file for the 30 Na + 181 Ta reaction. This input file contains an optical potential with the Coulomb term, along with theoretically derived real and imaginary nuclear volume terms. The Coulomb term is associated with an $E2$ matrix element of $18.5 \ e \text{fm}^2$. The nuclear volume term is deformed with a nuclear deformation length $\delta_A = 1.291$ fm. The real and imaginary values for the nuclear volume term (type=1 in the &POT namelist) were determined from theoretically derived optical model potential [109] constructed with a complex G-matrix interaction. The optical potential for the 32 Mg + 181 Ta system was derived and used for the 30 Na + 181 Ta system. The $^{3+}$ excited state at 426 keV is designated to belong to the $K=2$ rotational band built upon the $^{2+}_{g,s}$ via the kkp=2 parameter | | 79 |

| Figure 4.9: | Integrated excitation cross section to the $5/2^+$ state in ³¹ Na as a function of jtmax. Three different $E2$ matrix elements with $M(E2)$ values of 19.4935, 14.2828, 25 $e \text{fm}^2$ were employed, while the nuclear deformation length was fixed to $\delta_A = 1.204$ fm. As jtmax is increased, the integrated cross-section approaches an asymptotic limit. | • | 80 |
|--------------|---|---|-----|
| Figure 4.10: | Left: Woods-Saxon functions with diffuseness parameters $a=0.3,0.5,$ and 0.8 fm. Right: Derivatives of the Wood-Saxon function (surface term). In both, the radius is given by $R=r_0A^{1/3}$ with $r_0=1.2$ fm and $A=30.\ldots$. | | 82 |
| Figure 4.11: | Illustrative example of the real components of the optical model potential. The Woods-Saxon potential (blue) is parameterized with $V_0 = 50$ MeV, $a = 0.8$ fm, and $R = r_0 A^{1/3}$ with $r_0 = 1.067$ fm and $A = 30$. The Coulomb term (red) assumed $Z = 11$ and $R_C = 1.2A^{1/3}$, with $A = 30$. The spin-orbit term (green) is parameterized identically to the Woods-Saxon term | | 84 |
| Figure 4.12: | Differential cross sections in the laboratory (blue) and center-of-mass (red) frames for the 30 Na + 9 Be FRESCO calculation utilizing the 17 O + 208 Pb optical model potential parameters. The oscillatory pattern seen is due to the incoming wave (i.e. projectile) diffracting from the target nucleus which behaves as a diffracting object | | 87 |
| Figure 4.13: | Differential cross sections in the laboratory (blue) and center-of-mass (red) frames for the 30 Na + 181 Ta FRESCO calculation utilizing the 17 O + 208 Pb optical model potential parameters. The oscillatory pattern seen is due to the incoming wave (i.e. projectile) diffracting from the target nucleus which behaves as a diffracting object | • | 87 |
| Figure 4.14: | Differential cross-section histograms in the laboratory frame with (violet) and without (blue) the angular spread of the incoming beam, along with the corresponding center-of-mass frame distribution (red), all obtained from the monte carlo simulation. These histograms were generated using the FRESCO calculation for the 30 Na + 181 Ta system, utilizing optical model parameters from the 17 O + 208 Pb reaction. The red and blue histograms are identical to the respective curves in Fig. 4.13 up to approximately 5° – 6° , beyond which the low yield is not reproduced by the monte carlo simulation. Incorporating the angular spread into the laboratory-frame via monte carlo greatly diminishes the oscillatory features characteristic of diffraction caused by the interaction of the beam with the target nucleus, and extend the differential cross section | | 0.0 |
| | to larger θ values | | 88 |

| Figure 4.15: | Histograms of $\sigma(\theta)$ versus θ produced with Eq. 4.19 in the laboratory frame with (violet) and without (blue) the angular spread of the incoming beam, along with the corresponding center-of-mass frame distribution (red), all obtained from the monte carlo simulation. These histograms were generated using the FRESCO calculation for the 30 Na + 181 Ta system, utilizing optical model parameters from the 17 O + 208 Pb reaction. Due to incorporating the angular spread, the oscillatory pattern caused by diffraction disappears and the yield extends to larger θ values. | 89 |
|--------------|--|----|
| Figure 4.16: | Two-dimensional b_{ta} vs a_{ta} annular distributions for 31 Na. Each region covered 0.5° ranging from 0° to 3.5° . In this figure, only 0° to 3.0° is shown. For each annular region, an averaged acceptance was determined by fitting various x_{fp} slices from the corresponding two-dimensional a_{fp} vs x_{fp} histograms. | 91 |
| Figure 4.17: | Two-dimensional histogram of the dispersive angle $(a_{\rm fp})$ vs the dispersive position $(x_{\rm fp})$ for 31 Na in the S800 focal plane with an angular coverage of $1.0^{\circ}-1.5^{\circ}$. The two horizontal lines spanning $x_{\rm fp}$ result from the annular shape of the distribution at the target location. A portion of the 31 Na ions are lost toward positive $x_{\rm fp}$, evidenced by the diagonal cutoff | 92 |
| Figure 4.18: | One-dimensional histograms of selected $x_{\rm fp}$ slices from the $a_{\rm fp}$ vs $x_{\rm fp}$ distribution for 31 Na in the angular range $1.0^{\circ}-1.5^{\circ}$. The red curve in (a) shows the piecewise function from Eq. 4.21, fit to the central region (-25 mm to 25 mm) in Fig. 4.17. The red and blue curves in (b) – (d) show the reference and region-specific fits, respectively. Increasing $x_{\rm fp}$ (e.g., $150-160$ mm to $190-200$ mm) reveals the growing loss of 31 Na ions due to the limited $a_{\rm fp}$ acceptance of the S800 | 92 |
| Figure 4.19: | Angular acceptance of the S800 as a function of the polar angle θ , measured from the laboratory-frame z-axis. The red dots represent the acceptance obtained for each angular region, where the weighted average was taken for each region using the different x_{fp} slices. The solid red curve shows a fit to these points | 93 |
| Figure 4.20: | Secondary beam components separated by the time-of-flight (TOF) technique. The time-of-flight technique relies on timing differences between a reference timing signal produced from a scintillator located within the S800 focal plane (E1), and two timing signals produced by scintillators located at the A1900 focal plane (XFP) and Object station (OBJ). Both axes are defined relative to the E1 reference signal: the <i>y</i> -axis represents the timing difference between E1 and XFP, whereas the <i>x</i> -axis shows the difference between E1 and OBJ. The red line represents a software gate applied to select the ³² Mg incoming beam. | 96 |

| Figure 4.21: | Particle identification plot (PID) produced from applying a software gate selecting the ³² Mg secondary beam. The y-axis corresponds to energy loss in the S800 focal plane ion chamber with the x-axis representing the time-of-flight difference between the E1 and OBJ signals. The most prominent cluster corresponds to ³² Mg ions that reached the S800 focal plane. A software gate, shown as a red circle, was applied to select the scattered ³² Mg ions after passing through the TRIPLEX device holding the Beryllium and Tantalum target foils. This ensured that the resulting gamma-ray spectrum contained inelastically scattered ³² Mg ions | 97 |
|--------------|---|-----|
| Figure 4.22: | Two-dimensional Doppler-corrected gamma-ray spectrum for 32 Mg optimized for reactions originating on the Tantalum foil. The y -axis represents the gamma-ray's emission angle defined by the main interaction point in GRETINA. The x -axis is the Doppler-corrected energies of the gamma rays detected by GRETINA. Two distinct lines are observed near 900 keV belonging to the $2_1^+ \rightarrow 0_{g.s.}^+$ transition. The lower-energy gamma-ray line is associated with the de-excitation of the 2_1^+ state following reactions on the Tantalum target, whereas the higher-energy line results from reactions involving the Beryllium target foil | 98 |
| Figure 4.23: | Two-dimensional histogram displaying the selection of prompt gamma rays, visualized as a red rectangle, from de-excitations associated with 32 Mg. The y -axis corresponds to the timestamp difference between events in GRETINA and correlated 32 Mg event in the E1 scintillator. The x -axis is the Doppler-corrected gamma-ray energy | 99 |
| Figure 4.24: | One-dimensional Doppler-corrected gamma-ray spectrum for 32 Mg optimized for reactions originating from the Tantalum target foil. The spectrum was produced from applying gates seen in Figs. 4.20, 4.21, 4.23, with an additional 2° scattering angle gate defined from the laboratory's <i>z</i> -axis. The Tantalum (Ta) and Beryllium (Be) peaks for the $2_1^+ \rightarrow 0_{g.s.}^+$ transition are marked accordingly | 101 |
| Figure 4.25: | First iteration in the process of quantifying background gamma-ray peak contributions for 31 Na. The Doppler-corrected spectrum, shown in the left panel, was fit without any background contributions to determine the initial set of parameters associated with peaks of interest, $P_0 = \{p_1, p_2,\}$. A corresponding fit to the laboratory-frame spectrum, shown on the right, was used to extract the initial background scaling parameter $b_{bkg,0}$. Both spectra were fit with simulations from G4Lifetime | 103 |

| Figure 4.26: | Second iteration in the process of quantifying background gamma-ray peak contributions for 31 Na. The Doppler-corrected spectrum, shown in the left panel, was fit with the background contributions determined from the first iteration ($b_{bkg,0}$) resulting in the second set of scaling parameters for the peaks of interest, $P_1 = \{p_1, p_2,\}$. Subsequently, the laboratory-frame spectrum was fit with the constraint of P_1 , as shown in the right panel, producing an updated background scaling parameter, $b_{bkg,1}$. Both spectra were fit with simulations from G4Lifetime | 103 |
|--------------|--|-----|
| Figure 4.27: | Secondary beam components separated by the time-of-flight (TOF) technique. The time-of-flight technique relies on timing differences between a reference timing signal produced from a scintillator located within the S800 focal plane (E1), and two timing signals produced by scintillators located at the A1900 focal plane (XFP) and Object station (OBJ). Both axes are defined relative to the E1 reference signal: the <i>y</i> -axis represents the timing difference between E1 and XFP, whereas the <i>x</i> -axis shows the difference between E1 and OBJ. The red line represents a software gate applied to select the ³⁰ Na incoming beam. | 105 |
| Figure 4.28: | Particle identification plot (PID) produced from applying a software gate selecting the ³⁰ Na secondary beam. The <i>y</i> -axis corresponds to energy loss in the S800 focal plane ion chamber with the <i>x</i> -axis representing the time-of-flight difference between the E1 and OBJ signals. The most prominent cluster corresponds to ³⁰ Na ions that reached the S800 focal plane. A software gate, shown as a red circle, was applied to select the scattered ³⁰ Na ions after passing through the TRIPLEX device holding the Beryllium and Tantalum target foils. This ensured that the resulting gamma-ray spectrum contained inelastically scattered ³⁰ Na ions. | 106 |
| Figure 4.29: | One-dimensional Doppler-corrected gamma-ray spectra per 50 mm of the S800 spectrograph's $x_{\rm fp}$ for $^{30}{\rm Na}$. The spectra have been optimized for reactions originating from the Ta foil. The dashed vertical red lines in each spectrum display the locations of the Ta components of the 426-keV and 499-keV transitions corresponding to the $(3^+) \rightarrow 2^+_{\rm g.s.}$ and $(4^+) \rightarrow (3^+)$ decays, respectively. The Ta component generally appears more prominent for negative $x_{\rm fp}$ values whereas the Be component becomes further pronounced towards positive values | 107 |

| Figure 4.30: | Two-dimensional histogram showing the relationship between the angular $(a_{\rm fp})$ and spatial $(x_{\rm fp})$ distributions of 30 Na ions at the focal plane of the S800 spectrograph. The spectrograph's acceptance is evidenced by the diagonal boundaries extending into both the positive and negative $x_{\rm fp}$ regions. The incoming 30 Na beam exhibits a non-uniform profile across $x_{\rm fp}$, skewing toward more negative $a_{\rm fp}$ values in the negative spatial region. A sharp cutoff in the beam is observed at large negative $x_{\rm fp}$ values, reflecting the acceptance limits of the S800 spectrograph | . 108 |
|--------------|--|-------|
| Figure 4.31: | Kinematic curves for 30 Na + 9 Be (left) and 30 Na + 181 Ta (right) scattering calculated with LISE++ [123–125]. The dashed horizontal red line corresponds to the energy the ion had before any reaction took place | . 109 |
| Figure 4.32: | Two-dimensional Doppler-corrected gamma-ray spectrum for 30 Na, optimized for reactions on the Tantalum (Ta) foil. The y-axis shows the gamma-ray emission angle, defined by the main interaction point in GRETINA, while the x-axis corresponds to the Doppler-corrected gamma-ray energy. Due to limited statistics, only the $(3^+) \rightarrow 2^+_{\rm g.s.}$ transition components originating from reactions on the Be and Ta foils are distinctly visible. The lower-energy line is associated with the de-excitation of the (3^+) state following reactions on the Ta foil, while the higher-energy line corresponds reactions on the Be foil. The horizontal dashed red line corresponds to the angle cut $\theta_{\rm GRETINA} \leq 55^\circ$ that was imposed | . 110 |
| Figure 4.33: | One-dimensional Doppler-corrected gamma-ray spectrum for ³⁰ Na, optimized for reactions originating on the Tantalum (Ta) foil, gated for the laboratory-frame gamma-ray GRETIINA detection angle up to 55°. A separate gate was applied to restrict the laboratory scattering angle up to 3°. The data are represented with black dots and error bars, with laboratory-frame background contributions shown in gray. Simulated decay of the (3 ⁺) state populated directly in the reaction is shown by the orange histograms, while gamma-ray decays associated with the (4 ⁺) direct population are represented by the blue histograms. The sum of all components is shown by the red histogram. The Tantalum (Ta) and Beryllium (Be) peaks for each transition are marked accordingly | . 111 |
| Figure 4.34: | Effect of the 25 mm target separation on emitted gamma rays. Panel (a) illustrates gamma-ray emission following reactions on the Be (blue) and Ta (red) foils. Panel (b) shows the corresponding two-dimensional histogram, with GRETINA detector angle on the <i>y</i> -axis and Doppler-corrected energy on the <i>x</i> -axis. The energy correction in panel (b) has been optimized for gamma rays originating from the Ta foil | . 112 |
| Figure 4.35: | Diagram outlining the general procedure used in obtaining the nuclear deformation length δ_A and the reduced transition strength $B(E2 \uparrow)$ | . 114 |

| Figure 4.36: | Comparison of branching ratios obtained in the present work with those reported in Refs. [55, 126]. The gamma-ray spectrum was generated using the full $x_{\rm fp}$ range (-300 to 300) to determine the branching ratios. The red histogram represents a simulation based on the branching ratios obtained from this work, while the green histogram corresponds to the literature values. The individual components de-exciting the (3 ⁺) and (4 ⁺) states were constrained in the same manner as in Fig. 4.33, but are not shown here. For reference, the red histogram based on the branching ratios determined in this work is overlaid with the prediction using the values reported in Ref. [126] for the (4 ⁺) \rightarrow (3 ⁺) transition near 500 keV. The disagreement between the green histogram and the experimental data highlights the inconsistency of the literature values. | 118 |
|--------------|--|-----|
| Figure 4.37: | Secondary beam components separated by the time-of-flight (TOF) technique. The time-of-flight technique relies on timing differences between a reference timing signal produced from a scintillator located within the S800 focal plane (E1), and two timing signals produced by scintillators located at the A1900 focal plane (XFP) and Object station (OBJ). Both axes are defined relative to the E1 reference signal: the <i>y</i> -axis represents the timing difference between E1 and XFP, whereas the <i>x</i> -axis shows the difference between E1 and OBJ. The red line represents a software gate applied to select the ³¹ Na incoming beam. | 120 |
| Figure 4.38: | Particle identification plot (PID) produced from applying a software gate selecting the ³¹ Na secondary beam. The <i>y</i> -axis corresponds to energy loss in the S800 focal plane ion chamber with the <i>x</i> -axis representing the time-of-flight difference between the E1 and OBJ signals. The most prominent cluster corresponds to ³¹ Na ions that reached the S800 focal plane. A software gate, shown as a red circle, was applied to select the scattered ³¹ Na ions after passing through the TRIPLEX device holding the Beryllium and Tantalum target foils. This ensured that the resulting gamma-ray spectrum contained inelastically scattered ³¹ Na ions. | 121 |
| Figure 4.39: | Two-dimensional Doppler-corrected gamma-ray spectrum for 31 Na, optimized for reactions on the Tantalum (Ta) foil. The <i>y</i> -axis shows the gamma-ray emission angle, defined by the main interaction point in GRETINA, while the <i>x</i> -axis corresponds to the Doppler-corrected gamma-ray energy. Due to limited statistics, only the $(5/2^+) \rightarrow 3/2^+_{g.s.}$ transition components originating from reactions on the Be and Ta foils are distinctly visible, whereas only a hint of the two-peak structure for the $(7/2^+) \rightarrow (5/2^+)$ decay is apparent at 800 keV. The lower-energy line is associated with the de-excitation of the $(5/2^+)$ state following reactions on the Ta foil, while the higher-energy line corresponds reactions on the Be foil. The horizontal dashed red line corresponds to the angle cut $\theta_{GRETINA} \leq 55^{\circ}$ that was imposed | 122 |

| Figure 4.40: | One-dimensional Doppler-corrected gamma-ray spectrum for 31 Na, optimized for reactions originating on the Tantalum (Ta) foil, gated for the laboratory-frame gamma-ray GRETIINA detection angle up to 55° . A separate gate was applied to restrict the laboratory scattering angle up to 3° . The data are represented with black dots and error bars, with laboratory-frame background contributions shown in gray. Simulated decay of the $(5/2^{+})$ state populated directly in the reaction is shown by the orange histograms, while gamma-ray decays associated with the $(7/2^{+})$ direct population are represented by the blue histograms. The sum of all components is shown by the red histogram. The Tantalum (Ta) and Beryllium (Be) peaks for each transition are marked accordingly |
|--------------|--|
| Figure 4.41: | χ^2 curves as a function of the mean lifetime (τ) for the (7/2+) state in 31 Na. The blue curve shows the χ^2 values obtained from fits that include the bins corresponding to the excess counts observed near 830 keV in Fig. 4.40. The red curve represents fits performed while excluding those bins. Open circles denote the χ^2 values obtained from fitting simulated spectra to the gamma-ray data shown in Fig. 4.40 within the 750–900 keV energy range while varying τ . The red and blue diamonds are where the minimum χ^2 is found for each curve. 128 |
| Figure 5.1: | Comparison of $B(E2\uparrow)$ strengths for 30 Na from this work and those previously reported [54–56] (top) along with available $B(E2,2^+_{\rm g.s.}\to(4^+))/B(E2,2^+_{\rm g.s.}\to(3^+))$ ratios (bottom). In the top panel, triangles denote $B(E2,2^+_{\rm g.s.}\to(3^+))$ values and squares correspond to $B(E2,2^+_{\rm g.s.}\to(4^+))$. Weighted averages of all available measurements, including those from this work, are shown as shaded bands in blue and green for the (3^+) and (4^+) states, respectively 132 |
| Figure 5.2: | Comparison of $B(E2\uparrow)$ strengths for ³¹ Na from this work and those previously reported [54] (top) along with available $B(E2,3/2^+_{g.s.}\to (7/2^+))/B(E2,3/2^+_{g.s.}\to (5/2^+))$ ratios (bottom). In the top panel, triangles denote $B(E2,3/2^+_{g.s.}\to (5/2^+))$ values and squares correspond to $B(E2,3/2^+_{g.s.}\to (7/2^+))$. Weighted averages of all available measurements, including those from this work, are shown as shaded bands in blue and green for the $(5/2^+)$ and $(7/2^+)$ states, respectively |
| Figure 5.3: | Comparison of $B(E2, 2^+_{g.s.} \to (3^+))$ and $B(E2, 2^+_{g.s.} \to (4^+))$ strengths calculated with the FSU and SDPF-M interactions. The sensitivity of calculated $B(E2)$ strengths results to the choice of effective charges [137, 139, 149–152] is highlighted using the FSU interaction |
| Figure 5.4: | Comparison of $B(E2, 3/2_{\rm g.s.}^+ \to (5/2^+))$ and $B(E2, 3/2_{\rm g.s.}^+ \to (7/2^+))$ strengths calculated with the FSU and SDPF-M interactions. The sensitivity of calculated $B(E2)$ strengths results to the choice of effective charges [137, 139, 149–152] is highlighted using the FSU interaction |

| Figure 5.5: | Systematic trends for selected odd- A Na isotopes are presented for (a) reduced transition strengths, (b) $B(E2,3/2^+g.s. \rightarrow 7/2^+)/B(E2,3/2^+g.s. \rightarrow 5/2^+)$ ratios, (c) excitation energies, and (d) excitation-energy ratios of the yrast $7/2^+$ and $5/2^+$ states. The present results are shown in red, while prior data are taken from evaluated data sets [134, 153]. Shell-model predictions using the FSU and SDPF-M interactions are included, with SDPF-M values for 33,35 Na taken from Ref. [36]. USDB energy results for 29,31 Na are omitted from the figure since the ground states are predicted as $5/2^+$, with the $3/2^+$ and $7/2^+$ states at 71 and 2742 keV for 29 Na, and 372 and 4947 keV for 31 Na, respectively. In panel (a), blue symbols denote $5/2^+$ states and green symbols denote $7/2^+$ states |
|-------------|---|
| Figure 5.6: | Comparison of reduced transition strengths between experimental and the triaxial particle-rotor model calculations for 31 Na. Panels (a) and (b) compare the reduced transition strengths for $B(E2, 3/2^+ g.s. \rightarrow 5/2^+)$ and $B(E2, 3/2^+ g.s. \rightarrow 7/2^+)$ with varying ϵ_2 and γ values, respectively, while panel (c) shows the ratio between these values |
| Figure 5.7: | Comparison of state-level energies between experimental and the triaxial particle-rotor model calculations for 31 Na. Panels (a) and (b) compare the state-level energies of $E(5/2^+)$ and $E(7/2^+)$ with varying ϵ_2 and γ values, respectively, while panel (c) shows the ratio between these values |
| Figure B.1: | Coordinate systems in the projectile frame (P) and laboratory frame (G) shown at different stages of incorporating the finite beam spot size and angular spread. Panel (a) overlays coordinate systems P and G , and introduces vectors \vec{z} , \vec{q} , and \vec{s} , which describe the scattering process. The vector \vec{z} corresponds to the ion's initial direction along its trajectory. \vec{q} represents the transverse displacement of the ion at a downstream focal plane located a distance Δz from the origin point A . \vec{s} denotes the scattered trajectory at an angle θ_{MC} relative to the projectile's z -axis. The angle θ_{MC} is sampled from a yield distribution, while the azimuthal angle ϕ is measured from the projectile's y -axis and sampled uniformly from 0 to 2π . Panel (b) illustrates the effect of the ion's angular spread on vectors \vec{z} , \vec{q} , and \vec{s} by rotating coordinate system P . Panel (c) shows the translation of coordinate system P due to the beam spot size, relative to G |

CHAPTER 1

INTRODUCTION

All of the observable matter in the universe is composed of atoms, which are themselves comprised of protons, neutrons, and electrons. Over a century, constituents of the nuclear physics community have striven to illuminate the enigmatic inner workings of the atomic nucleus. The nucleus has an approximate radius 10^{-15} m, yet it possesses a tremendous amount of information on the origin of all observable matter. At its core, the nucleus is a many-body Fermionic quantum system, where protons and neutrons – collectively called nucleons – interact through the interplay of the strong nuclear force, Coulomb repulsion, and quantum effects. It is this eclectic environment of the nucleus that allows it to serve as an indispensable platform to study nature. This serves as the foremost motivation for the work presented in this dissertation, with a specific focus on the internal structure of the neutron-rich isotopes of 30,31 Na. Hence, this chapter will provide a brief overview on the nuclear landscape as it is known presently, the models used to describe nuclear structure and excitation properties, and features of the Z=11 isotopic chain in the context of the N=20 Island of Inversion.

1.1 The Nuclear Landscape

As presented in Fig. 1.1, the nuclear landscape is the result of the scientific enterprise to understand observable matter. The chart of nuclides is organized by the number of protons and neutrons, together called nucleons, which serve to describe the identity of a particular nucleus. The proton number (Z) is given along the y axis and the neutron number (N) is along the x axis in Fig. 1.1. The sum of the proton and neutron numbers is denoted by A = Z + N, and is known as the mass number. Together, all of these symbol describe a nucleus, $\frac{A}{Z}X_N$, where X represents an element from the periodic table of elements. Nuclei that share the same proton number Z but vary in neutron number N are known as isotopes, whereas nuclei with the same neutron numbers are denoted as isotones. In Fig. 1.1, isotopes are arranged horizontally, whereas isotones appear vertically. Nucleons are

not point particles, rather, they themselves harbor a complex internal structure composed of quarks bound together by the strong force mediated through gluons. Protons are comprised of two up quarks and one down quark, whereas the neutron has one up quark and two down quarks. The sum of these quarks, +2/3e for one up quark and -1/3e for one down quark, grants the nucleons their charges; +1e for protons and no charge for neutrons. Beyond the inner structure of a nucleon, the strong force between nucleons (nuclear force) binds these composite Fermionic particles to create a nucleus.

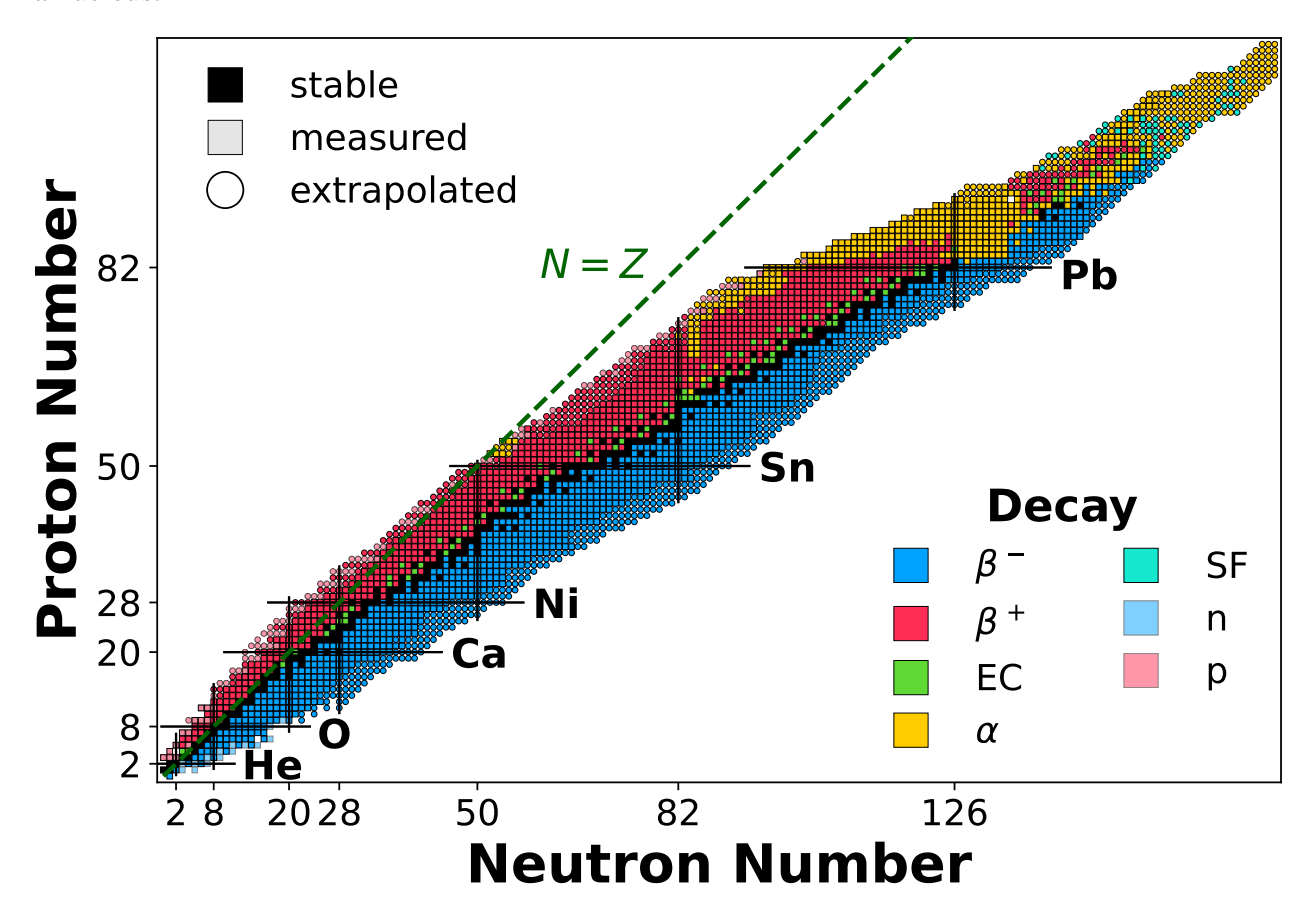


Figure 1.1: The nuclear landscape depicting nuclides as a function of proton (Z) and neutron (N) number. The proton number increases vertically along the y axis whereas the neutron number increases along the x axis. The prominent decay modes of each nuclide are illustrated by color. Black squares denote the valley of stability, a region where nuclei are stable against beta decay. Squares indicate nuclei that have been measured whereas circles are extrapolated from data systematics. The horizontal and vertical solid black lines mark the isotopic and isotonic chains at the magic numbers, respectively. Isotopic chains for each proton magic number have been labeled (e.g. He, O, etc.). The dashed green line denotes the N = Z trend line, highlighting the increasing influence of Coulomb repulsion in heavier nuclei. Data was extracted from Refs. [1, 2].

The nuclear force involved in atomic nuclei is a complex combination of the fundamental strong and weak interactions, where its exact analytical form is still unknown. However, it is possible to phenomenologically characterize the interaction, being repulsive at short distances ($\leq 10^{-15}$ m), attractive on the order of magnitude of $\approx 10^{-15}$ m, and rapidly diminishing at larger distances.

In addition to organizing the several thousand nuclei by proton and neutron numbers, the prominent decay mode of a nucleus may also be utilized to illustrate systematic characteristic of the nuclear terrain, as visualized by the different colors in Fig. 1.1. Through the center of the nuclear chart lies the so-called valley of stability, a narrow region of nuclei that are stable to beta decay. On either side of the valley of beta stability reside nuclei that are susceptible to various forms of decay. Neutron-rich nuclei, on the right-hand side of the valley of stability, show a propensity to beta-minus (β^-) decay, which entails converting a neutron to a proton with the emission of an electron and electron antineutrino. Similarly, the proton-rich nuclei residing on the left-hand side of the valley of stability, undergo beta-plus (β^+) decay, converting a proton to a neutron with the emission of a positron and electron neutrino. Notably, the Coulomb force stemming from the protons veers the nuclear landscape towards more neutron-rich environments, as seen by the deviation from the green N = Z line in Fig 1.1. This is a result of the growing Coulomb repulsion as additional protons are incorporated into the nucleus, necessitating the presence of more neutrons to sufficiently bind all the nucleons.

Among the various trends spanning the nuclear chart, the pronounced stability of nuclei with a particular set of proton and neutron numbers stands out as pivotal [3–5]. These regions of enhanced stability possess nucleon numbers 2, 8, 20, 28, 50, 82, and 126, and are known as the magic numbers. Experimentally, several observables were used to define the magic numbers, with the one neutron separation energy (S_{1n}) – the energy required to remove a single neutron from a nucleus – being one of them. The S_{1n} observable is presented in Fig. 1.2, where it is plotted for various isotopic chains as a function of neutron number. The staggering effect for each isotopic chain is a result of the pairing effect of nucleons. Nucleons that are not paired (e.g. a lone neutron) are less bound than two neutrons that are paired to a J=0 configuration. The steep drop in the one

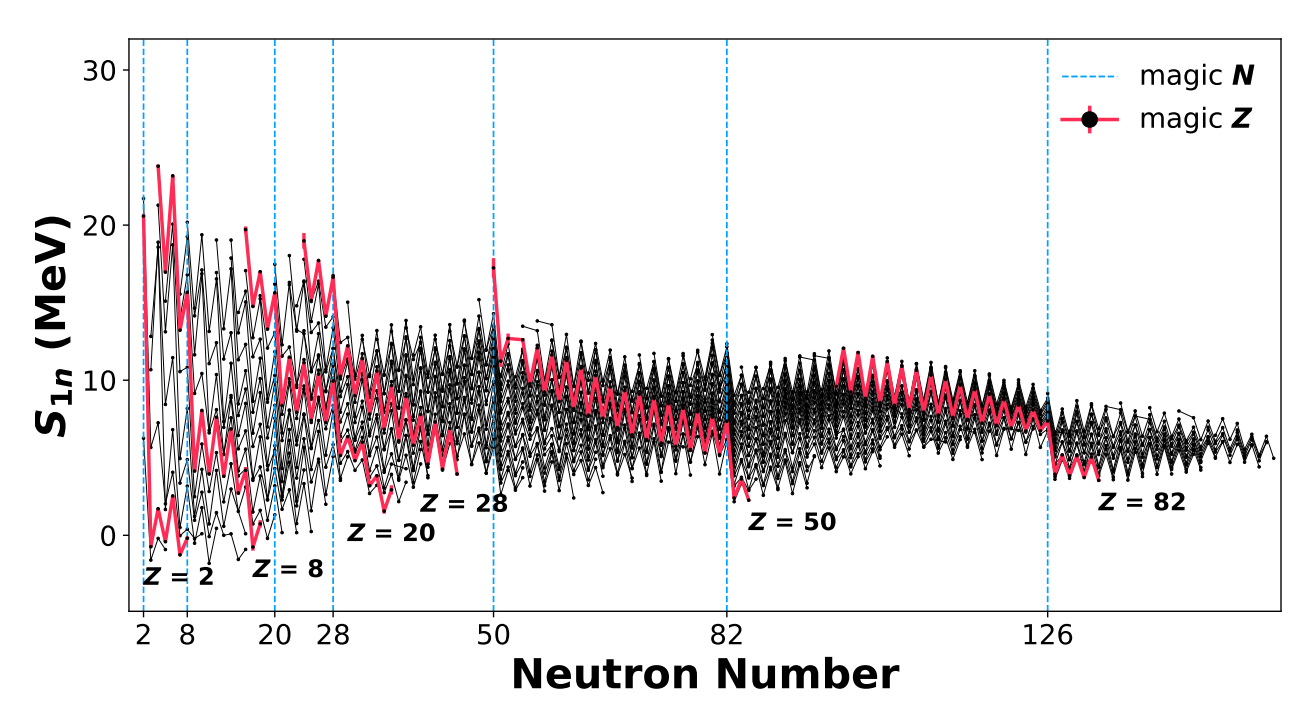


Figure 1.2: The one neutron separation energy (S_{1n}) for isotopic chains as a function of neutron numbers N. Isotopic chains at magic numbers are highlighted in red and labeled. The neutron magic numbers are marked by dashed blue lies. The sudden drop in S_{1n} after each magic number denotes a filled shell, marking the subsequent nucleon being less tightly bound due to occupying an open shell. Data was extracted from Refs. [1, 2].

neutron separation energy after a neutron magic number is indicative of extra stability. Analogous to atomic theory, the drop in S_{1n} after a neutron magic number arises due to additional neutrons occupying the next available shell, which are less bound. The identification of these magic numbers led to the development of the nuclear shell model, which treats the nucleons as independent particles in a central potential, creating discrete energy levels.

1.2 The Nuclear Shell Model

The shell model stands as the first successful framework in describing the phenomenological trends of the nuclear chart microscopically. Its development was driven by extensive experimental evidence revealing systematic features that suggested the nucleus possesses an underlying, predictable structure. The shell model description ascribes the nucleons within the nucleus as independent particles, interacting with a self-generated central potential rather than the individual neutron-neutron (NN) interactions. This assumption of a central potential arises from having a saturated density [6]

in the nucleus's interior, and the nuclear force being attractive at a short range. Each nucleon within the nucleus experiences the collective influence of surrounding nucleons, though the strength of the NN interaction diminishes with distance. Hence, the net effect of all of the individual NN interactions generates a phenomenological potential which flattens out near the central region of the nucleus, becomes shallow near the surface, and vanishes at $r \to \infty$ [7]. It then becomes paramount to select an appropriate central potential capable of emulating these properties. Historically, the harmonic oscillator potential was first utilized but failed due to creating an infinite-range potential and implying that the density is not constant throughout the nucleus. A more suitable candidate was the Woods-Saxon potential, $V_{WS}(r)$, which was able to mimic the expected phenomenological properties of the nucleus,

$$V_{\text{WS}}(r) = \frac{-V_0}{1 + e^{(r-R)/a}} = -V_0 f_{\text{WS}}(r)$$
(1.1)

where a comparison of Eq. 1.1 is made with a harmonic oscillator potential in Fig. 1.3. In Eq 1.1, the depth of the potential is denoted by V_0 and the radius is given by $R = r_0 A^{1/3}$ where a value of $r_0 = 1.2$ fm is typically used. The diffuseness parameter, which is representative of the surface thickness, is given by a. The development of the shell model single-particle energies, starting with the harmonic oscillator potential, is presented in Fig. 1.4. The use of the three-dimensional harmonic oscillator (leftmost column of Fig. 1.4) was a good starting point in endeavoring to reproduce the magic numbers, as it reproduced the 2, 8, and 20 magic numbers. However, it failed to reproduce the phenomenological numbers past that.

The introduction of the Woods–Saxon potential (Eq. 1.1) incorporated key features such as the nuclear radius, surface diffuseness, and potential strength, leading to the splitting of degenerate single-particle energy levels according to their orbital angular momentum l. This degeneracy splitting is seen in the second column of Fig. 1.4. Ultimately, it was the inclusion of the spin-orbit coupling term by Mayer and Jensen [3–5], which conventionally is given as [8]

$$(l \cdot s)V_{ls}(r) = (l \cdot s)V_{ls} \frac{1}{r} \frac{d}{dr} f_{ls}(r)$$
(1.2)

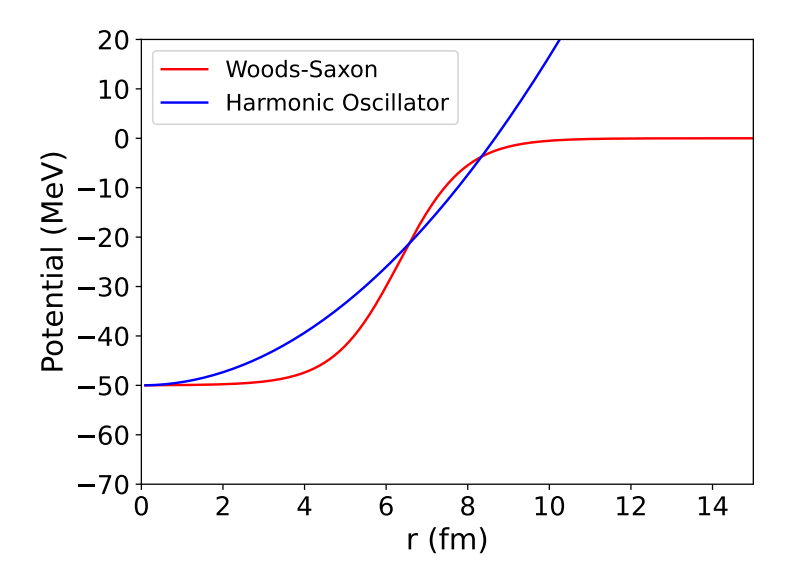


Figure 1.3: Comparison of a Woods-Saxon (red) and harmonic oscillator (blue) potentials. The harmonic oscillator extends to infinity whereas the Woods-Saxon potential diminishes after a finite distance. The flat bottom of the Woods-Saxon potential reflects the saturation of nuclear density, while the harmonic oscillator implies an increasing nuclear density as $r \to 0$.

that successfully reproduced the magic numbers (rightmost column of Fig. 1.4). The strength of the spin-orbit term is give by V_{ls} , and often times parameterized by $f_{ls}(r) = f_{WS}(r)$. Within the shell model, the magic numbers arise from large energy gaps between shells, such that promoting a nucleon to a higher shell requires additional energy and is therefore unfavorable. Because protons and neutrons are distinct particles, each occupies its own set of shells.

Coupling the intrinsic spin s of a nucleon with its orbital angular momentum l further splits the energy levels into j = l + s and j = l - s, where $\pm s$ accounts for the possible spin up or spin down configurations a nucleon may take. The discrete energy levels a nucleon occupies are denoted by principal quantum number n, orbital angular momentum number l, and total angular momentum of an individual nucleon j. Together, an individual energy level is commonly specified using the nl_j notation, where spectroscopic symbols (s, p, d, f, ...) denote orbital angular momentum number l = 0, 1, 2, 3, ... As given in Fig. 1.4, n represents the radial quantum number corresponding to the number of times the radial wave function changes its sign. Furthermore, the parity of a nucleon in a given nl_j orbital is determined by $\pi = (-1)^l$.

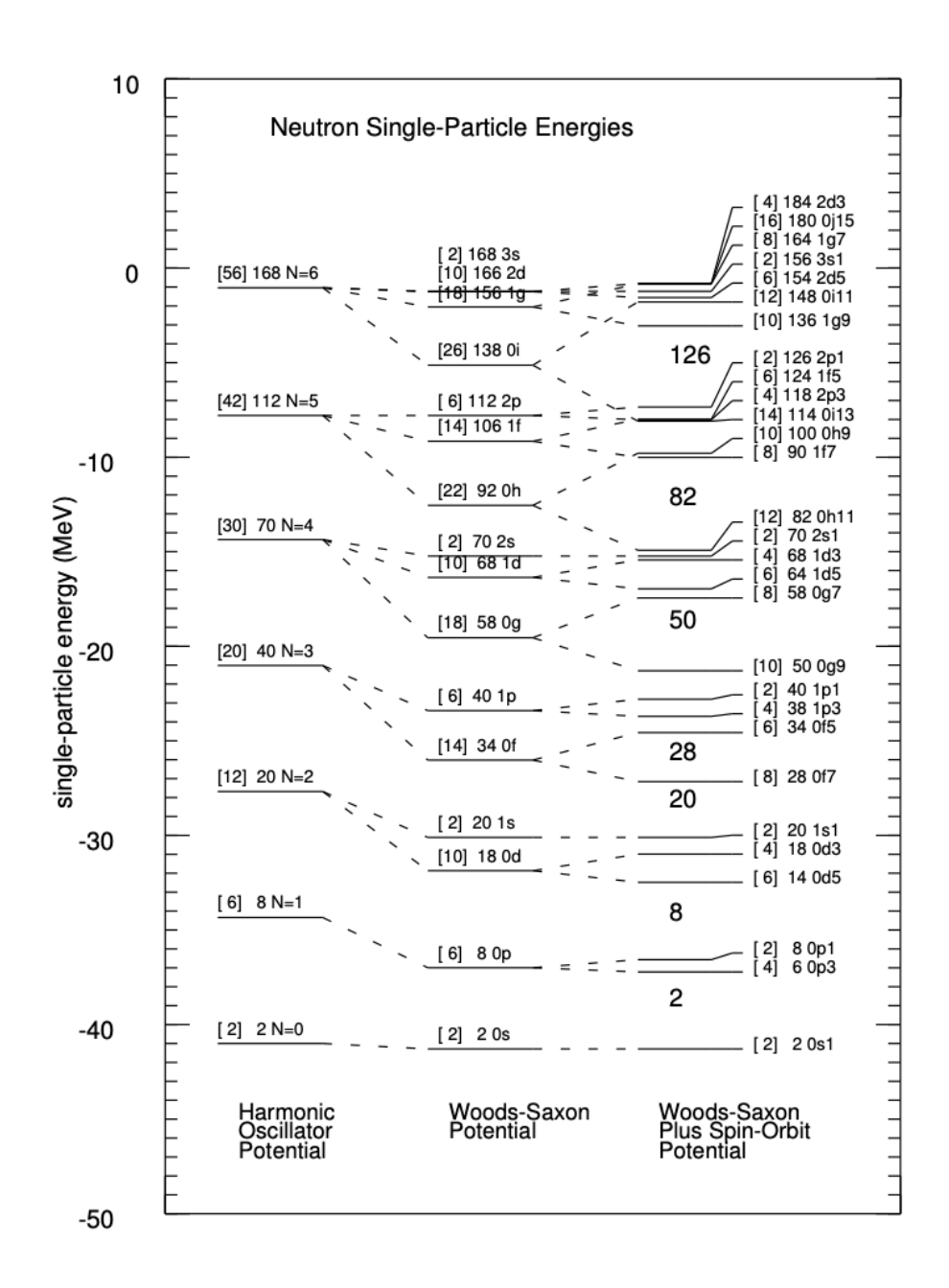


Figure 1.4: Neutron single-particle orbit in 208 Pb calculated using the harmonic oscillator, Woods-Saxon, and Woods-Saxon with spin-orbit potentials. Bracketed numbers denote orbital occupancy, followed by the cumulative occupancy of all prior orbitals. Orbits are labeled by major quantum number N, orbital angular momentum l (using spectroscopic symbols), and the total angular momentum j = l + s where the 2j convention is being utilized. Figure is adapted from Ref. [8]

1.2.1 Single-Particle Excitations

As stated before, nucleons within the shell model may be treated as independent particles under the influence of a central potential. A single-particle excitation corresponds to the promotion of a nucleon in the ground-state, $(nl_j)_{g.s.}$, to a higher-lying single-particle state $(nl_j)_{Ex.}$. This can occur for either proton or neutron shells, where the promotion of the individual nucleon leaves a vacancy in the shell it originated from (called a hole). These type of excitations typically occur near closed shells, where a valence nucleon resides nearest to the subsequent shell. Albeit energetically expensive, it is feasible to promote an already paired nucleon by providing the required energy to break the J=0 pair and promote it to the following shell. The promotion of a nucleon to another orbital, whether it be within the same shell or across to the next shell, dictates the excited-state energy spectrum. When a nucleon is promoted within the same shell, the parity of the resulting excited state remains the same as that of the ground state. In contrast, promoting a nucleon to the next unoccupied shell generally changes the parity of the excited state configuration from that of the ground state.

It is possible to promote two nucleons into the same subsequent shell, where such an excitation would not change the parity of the ground state. An example would be the promotion of two neutrons from the sd shell to the fp shell. The net parity is given by $\pi = \pi_1\pi_2$, where π_1 and π_2 correspond to the parity of the two individual neutrons. Given that energy levels in the fp shell have odd orbital angular momentum values, the overall parity remains positive. Such a promotion would be called a 2p-2h excitation, where two neutrons have been promoted to the ensuing shell.

1.2.2 Evolution of Single-Particle Energies

The nuclear shell model has made tremendous strides in explaining the nuclear phenomena observed near the valley of stability. However, with the advent of rare-isotope beam facilities capable of accessing increasingly exotic nuclei – those far from the valley of stability in Fig. 1.1 – it became evident that their behavior diverged from the predictions of the shell model [9]. Talmi and Unna [10] noticed that the ordering of single-particle levels may evolve due to effective nuclear interactions.

It was the pioneering work on key observables such as atomic masses, nuclear radii and spectra that first suggested an evolution of single particle states near N = 20 [11–17].

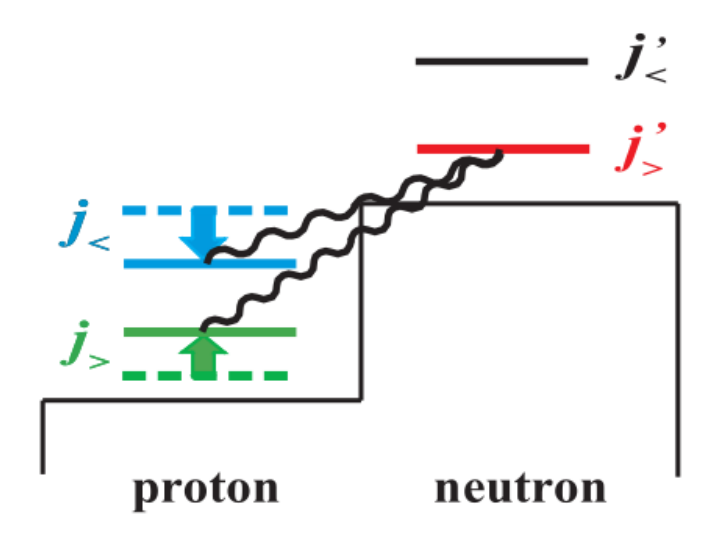


Figure 1.5: Schematic illustration of the monopole interaction arising from the tensor force between proton $(j_>, j_<)$ and neutron $(j_>', j_<')$ orbits, where the tensor-force is depicted by the black wavy line. Occupation of a neutron $j_>'$ orbit induces an attractive interaction with the proton $j_<$ orbit, making it more bound. In contrast, the similar angular-momentum alignments between the proton $j_>$ and the neutron $j_>'$ orbits invokes a repulsive tensor force interaction, reducing how bound the proton orbit is. Figure was modified from Ref. [18].

The evolution of the nuclear shell structure is often attributed to the monopole interaction of the tensor force [6, 18–20]. The interaction arises mainly due to one-pion exchange between nucleons. The tensor force affects the valence single-particle energy levels of closely related protons and neutrons. As illustrated in Fig. 1.5, the monopole interaction of the tensor force is attractive between proton and neutron orbitals with opposite angular-momentum alignments ($j_>$, $j'_>$ or $j_<$, $j'_>$ or $j_>$ in the single-particle energies is largely governed by the monopole component of the tensor force, given by [18]

$$V_{j,j'}^{T} = \frac{\sum_{j} (2J+1) \langle jj' | V | jj' \rangle_{JT}}{\sum_{J} (2J+1)}$$
(1.3)

where V depicts an interaction, and $\langle jj'|V|jj'\rangle_{JT}$ is the diagonal two-body matrix element coupling two nucleons – one with j and the other with j' – to total angular momentum J and isospin T. As the occupation numbers of valence proton and neutron orbitals change, the single-particle energies of these states shift due to the effects of the tensor force. Consequently, it can be stated that the single-particle energies are not static but depend on the number of protons or neutrons. A more intuitive description of this phenomena is offered in Refs. [6, 18–20]

Recent studies of 12 Be [9, 21, 22] and 32 Mg [9, 23–25] provide evidence of structural evolution at the N=8,20 magic numbers, where these conventional shell closures vanish. As a result, this led to the development of new magic numbers, where the occurrence of the N=16 magic number [9, 26, 27] was a result of the evolving single-particle orbitals near N=20, as displayed in Fig. 1.6.

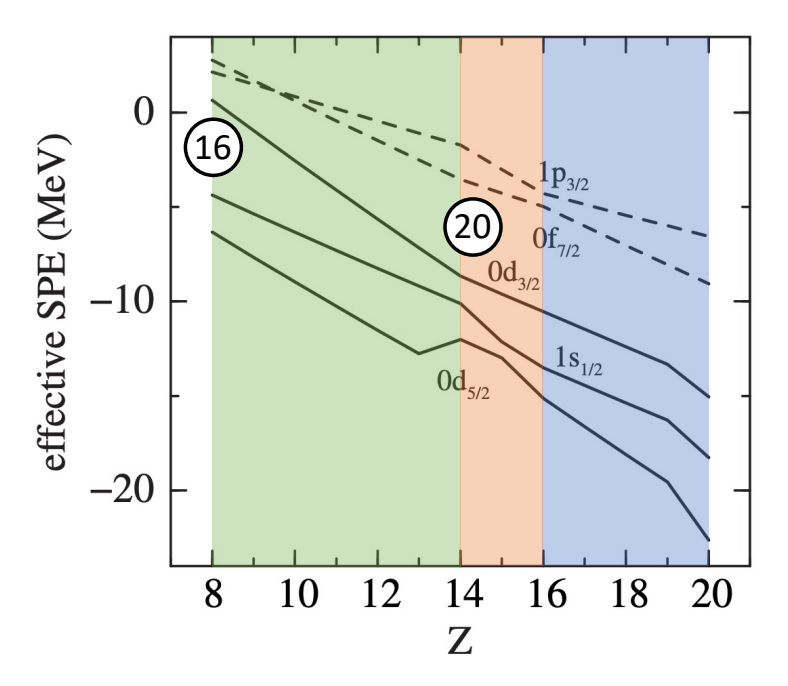


Figure 1.6: Evolution of the effective single-particle energies (ESPEs) for the N=20 isotones, from $^{40}_{20}$ Ca to $^{28}_{8}$ O, calculated with the SDPF-M interaction. Shaded regions indicate the occupancy of the $d_{3/2}$ (blue), $s_{1/2}$ (orange), and $d_{5/2}$ (green) orbitals. The reduction of the conventional N=20 shell gap between the $d_{3/2}$ and $f_{7/2}$ orbitals, together with the emergence of the new N=16 gap, arises from the removal of protons from the $d_{5/2}$ orbital. Figure was adapted from Ref. [6].

This is phenomenon is most apparent for the $Z \le 14$ nuclei along the N = 20 isotonic chain, where the expected spherical shell gap is no longer obtained [9]. The emergence of a new magic number can be qualitatively understood by means of the monopole interaction of the tensor force.

At Z = N = 20 (i.e. 40 Ca), a closed-shell configuration is present which leads to the conventional N = 20 gap. At Z = 14, 6 protons were removed from the $d_{3/2}$ and $s_{1/2}$ shells, leaving an occupied $d_{5/2}$ proton orbital. As protons are then removed from the $d_{5/2}$ orbital, the attractive monopole interaction between the $d_{5/2}$ protons and $d_{3/2}$ neutrons weakens. This reduction raises the neutron $d_{3/2}$ orbital, bringing it in closer proximity to the fp shell, while the $s_{1/2}$ remains relatively unaffected. The resulting energy gap between the neutron $d_{3/2}$ and $s_{1/2}$ orbitals gives rise to the N = 16 magic number.

1.3 Collective Excitations

Collective excitations tend to arise in regions in between the magic numbers, often denoted as transitional nuclei, or in regions in which there is an excess of neutrons. This collective behavior is manifested by vibrations, rotations, or a combination of both, with phenomenological signatures indicating dynamics that extend beyond the predictions of the shell model that relies on a spherical basis. These forms of experimental markers are often explained by macroscopic models that focus on the bulk properties of the nucleus.

1.3.1 Characterization of Nuclear Shapes

The task of describing a nucleus in a time-dependent manner is exceedingly complex, and rapidly becomes an insurmountable with increasing mass number A. The macroscopic description of the nucleus is analogous to treating the bulk properties of the constituent nucleons as a liquid drop [28, 29]. Any closed three-dimensional figure may be parameterized through the use of spherical harmonics [7, 30]. By assuming the nucleus exhibits a homogenous density throughout, its surface may be described by

$$R(\theta, \phi) = R_0 \left(\sum_{\lambda} \sum_{\mu = -\lambda} \alpha_{\lambda, \mu} Y_{\lambda, \mu}(\theta, \phi) \right)$$
 (1.4)

where $R_0 = r_0 A^{1/3}$ denotes the spherical surface radius with r_0 typically taken to be 1.2 fm. The deformation amplitudes are given by $\alpha_{\lambda,\mu}$ and the spherical harmonics are indicated by $Y_{\lambda,\mu}(\theta,\phi)$.

The angular momentum is given by λ , with its projection along the z-axis denoted by μ . The $\lambda = 1$ terms correspond to a translation of the center of mass. The prominent contributions to deviations from a spherical shape stem from quadrupole deformations ($\lambda = 2$), followed by octupole deformations ($\lambda = 3$).

A more natural prescription of the deformation amplitudes can be given by in the principal axis frame of the nucleus, where the intrinsic coordinate system is typically defined so that its axes align with the principal axes of the system's mass distribution [7]. For quadrupole deformations, these parameters are expressed as

$$a_{20} = \beta_2 \cos(\gamma)$$
 $a_{2\pm 1} = 0$ $a_{2\pm 2} = \frac{1}{\sqrt{2}}\beta_2 \sin(\gamma)$ (1.5)

where β_2 informs on the extent of quadrupole deformation and γ gives the degree of axial asymmetry. The radii along the principal axes can then be expresses as

$$R_x = R_0 \left(1 + \beta_2 \sqrt{\frac{5}{4\pi}} \cos\left(\gamma - \frac{2\pi}{3}\right) \right) \tag{1.6}$$

$$R_y = R_0 \left(1 + \beta_2 \sqrt{\frac{5}{4\pi}} \cos\left(\gamma - \frac{4\pi}{3}\right) \right) \tag{1.7}$$

$$R_z = R_0 \left(1 + \beta_2 \sqrt{\frac{5}{4\pi}} \cos(\gamma) \right) \tag{1.8}$$

A $\beta = \gamma = 0$ parameterization returns the expected spherical shape of the nucleus. For $\beta > 0$, $\gamma = 0$, the radii $R_x = R_y$, and $R_z > R_x$ resulting in an axially symmetric prolate shape. As for the $\beta < 0$, $\gamma = 0$ scenario, a difference arises between the principal z axis such as $R_z < R_x$, giving an axially symmetric oblate shape. Note, prolate deformations are elongated along the symmetric axis whereas oblate is compressed. Moreover, the radii defined in Eqs. 1.6, 1.7, and 1.8 display a symmetry corresponding to angular increments of $\pi/3$, partitioning the (β, γ) plane into six regions as displayed in Fig. 1.7. When $\beta > 0$ and $\gamma \neq 0$, the nucleus does not possess axial symmetry, and the associated quadrupole shape is referred to as being triaxial. For such a system, the rigid-rotor moment of inertia is defined as [31]

$$I_{\kappa}^{\text{rigid}} = \frac{2}{5} m A R_0^2 \left(1 - \sqrt{\frac{5}{4\pi}} \beta \cos\left(\gamma - \frac{2\pi}{3}\kappa\right) \right)$$
 (1.9)

where the body-fixed κ -axis for x, y, and z are given by $\kappa = 1, 2, 3$, respectively.

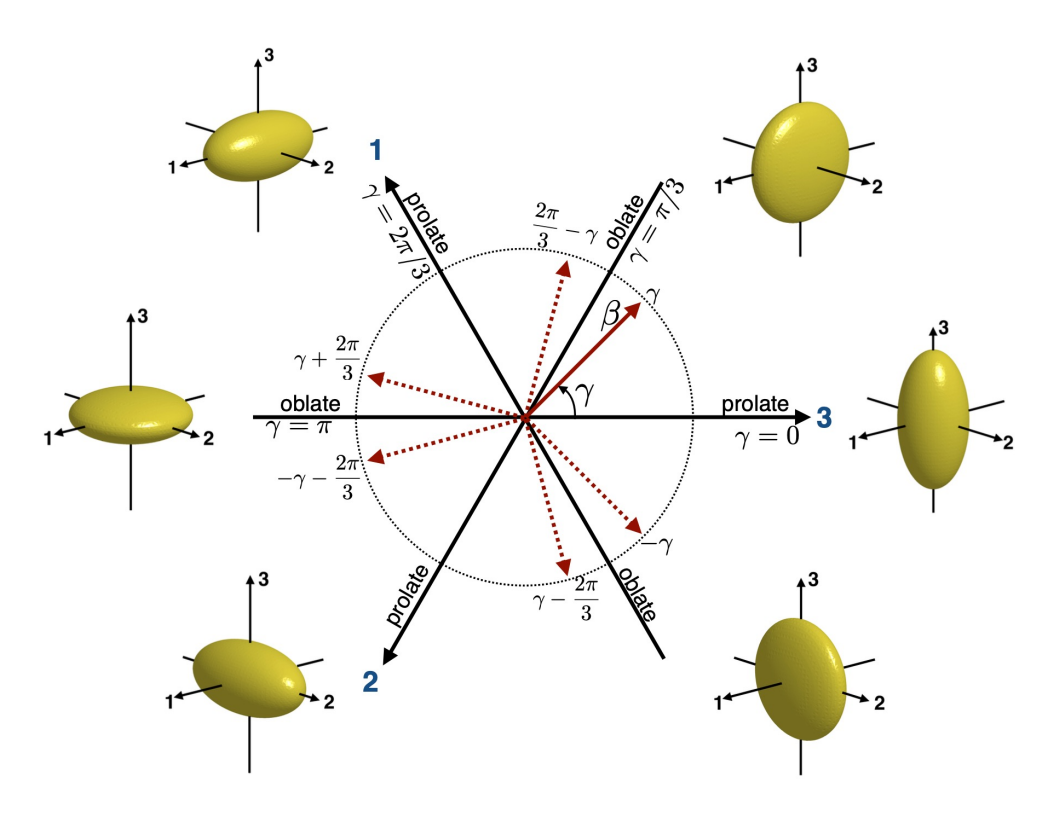


Figure 1.7: Polar diagram illustrating the deformation plane as a function of β , γ . Owing to the symmetry of Eqs. 1.6, 1.7, and 1.8, the plane is partitioned into 6 equivalent segments at increments of $\pi/3$. Shapes along the dashed arrows are identical to those along the solid arrow. Due to the symmetry, the first segment $(0 \le \gamma \le \pi/3)$ is conventionally utilized to describe the shape of the nucleus. Figure was adapted from Ref. [8].

1.3.2 Rotational Excitations

For an axially symmetric deformed nucleus, rotation about an axis perpendicular to that of the symmetry axis induce excitations. This leads to the projection of the angular momentum J onto the symmetry axis – denoted by K – as a constant of the motion [28]. For an even-even nucleus with $J_{g.s.} = 0$, the projection takes on the value of K = 0 and the rotational energy at leading order can be expressed as

$$E_{\text{rot}}(J) = \frac{\hbar^2}{2I}J(J+1)$$
 (1.10)

where \hbar is the reduced Planck's constant, I is the moment of inertia, and J is the angular momentum. For an even-even nucleus with K=0, the allowed values of J are even integers due to the rotational invariance of the rigid rotor. Several excited-state rotational bands in axially deformed nuclei have been found to follow this trend, where a key indicator is the characteristic energy ratio of the lowest-lying 2^+ and 4^+ excited states,

$$\frac{E(4^+)}{E(2^+)} = 3.33\tag{1.11}$$

From Eq. 1.11, it could be surmised that the gamma-ray energies from in-band transitions would be linear in J. Signatures of the linearity in J are present in the energy spectrum of the super deformed ¹⁵²Dy, presented in Fig. 1.8, where a constant energy spacing of $\Delta E = 47$ keV is found

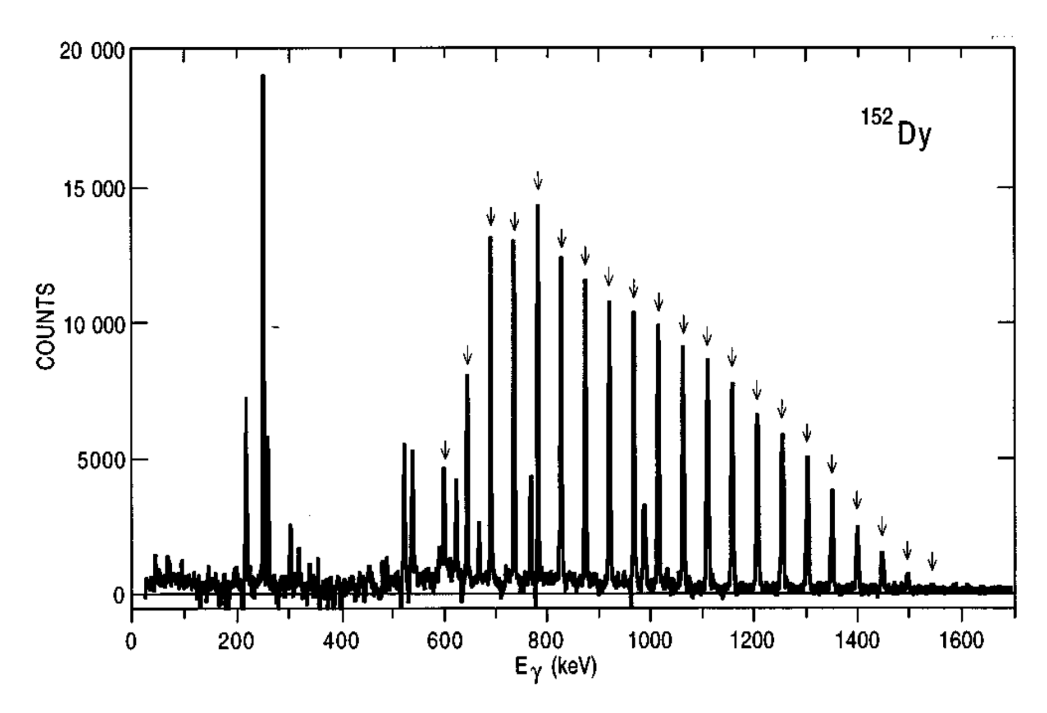


Figure 1.8: A super-deformed rotational band in 152 Dy, where the relevant γ -ray transitions between band members have been marked. The constant spacing of the γ -ray energies is characteristic of a system exhibiting the symmetry of an ideal quantum rotor. The observed decreasing intensity pattern for the gamma rays reflects the angular momentum distribution in populating the rotational band in the reaction. The unmarked lower energy peaks correspond to states populated after the decay of the super-deformed band. Figure is adapted from Ref. [32].

between adjacent gamma rays [32, 33].

When we have $K \neq 0$, the allowed values of J can take J = K, K+1, K+2, ..., and the rotational energy may be expressed as [28, 34]

$$E_{\text{rot}}(J,K) = \frac{\hbar^2}{2J} \left(J(J+1) - K(K+1) \right) \tag{1.12}$$

When considering odd-A systems, the odd-nucleon may be considered as a valence nucleon coupled to an even-even core. This is referred to as the particle-rotor model, in which the odd nucleon is influenced by the rotations of the even-mass core. In such case, the energy of the system can be written as

$$E = E_0 + E_{\text{rot}} + E_{\text{cor}} \tag{1.13}$$

where E_0 is the intrinsic energy the nucleus may already posses, $E_{\rm rot}$ is the rotational energy given by Eq. 1.12, and $E_{\rm cor}$ is the energy from the Coriolis effect due to the rotating even-even core [28, 34]. There are two limits in the particle-rotor model: the strongly coupled (i.e. deformation aligned) and the weakly coupled (i.e. rotation aligned) limits. In the strong-coupling limit, the projection of the angular momentum along the symmetry axis, K, is a good quantum number and becomes large as a result of the valence particle's angular momentum aligning with the symmetry axis. In return, this suppresses Coriolis effects so that changes in single-particle energies due to Coriolis matrix elements are negligible. Within this limit, the intrinsic angular momentum j of the odd particle aligns with the symmetry axis of the deformed core, resulting in a precession of the valence particle that follows the rotation of the even-mass core. That is, Coriolis effects stemming from the rotating core are negligible on the orbit of the valence particle. Hence, one is able to construct an energy ratio – similar to that of Eq. 1.11 – for an odd-mass nucleus using Eq. 1.12. For example, for a $J_{\rm g.s.}^+ = 3/2^+$ nucleus, the energy ratio between the low-lying $5/2^+$ and $7/2^+$ excited states assumes a value of

$$\frac{E(7/2^+) - E(3/2^+)}{E(5/2^+) - E(3/2^+)} = 2.4$$
(1.14)

Recent studies investigating the rotational band structure near the N=20 island of inversion have applied these arguments, finding that nuclei in this region are generally in good agreement with the strong-coupling limit [35, 36]. Conversely, Coriolis effects become significant in the weak-coupling limit, as the motion of the valence nucleon is strongly influenced by the rotation of the even-mass core [31]. In this regime, the valence nucleon's angular momentum aligns with the rotation axis of the core, and the projection K is no longer a good quantum number. The Coriolis interaction dominates over the intrinsic energy-level spacings, mixing states with $\Delta K=\pm 1$, causing a significant change in the rotational spectrum and properties. This effect is strongest for the K=1/2 projection which induces a staggering effect in the observed energy spectrum. Thus, special care ought to be taken into account when determining the energy levels when the Coriolis force may no longer be neglected [28, 31, 34]. Note, the Coriolis force may also have a pronounced effect when the nucleus is weakly deformed due to only small projections K being possible onto the symmetry axis.

1.3.3 Vibrational Excitations

The coherent motion of nucleons may also be explained through vibrational modes. Vibrational phenomena assumes collective oscillations about a spherical equilibrium shape which are interpreted to be as phonons. The excitation energy for n_{λ} phonons in the harmonic approximation is given by [28]

$$E = n_{\lambda} \hbar \omega_{\lambda} \tag{1.15}$$

where the frequency ω_{λ} is determined from the potential, λ denotes the angular momentum carried by the phonon, and n_{λ} corresponds to the number of phonons with angular momentum λ . The different vibrational modes are given by the angular momentum number λ of each phonon. Examples include the $\lambda = 0$ (monopole) mode, corresponding to a uniform inward-outward breathing motion of the spherical nucleus; the $\lambda = 1$ (dipole) mode where protons and neutrons oscillate out of phase with one another; and the $\lambda = 2$ (quadrupole) mode, depicting an alternating compression and expansion of the nucleus. For quadrupole vibrations, each phonon carries 2 units of angular momentum and has positive parity. For a spherical even-even nucleus, coupling a $\lambda = 2$ phonon to the $J^{\pi} = 0^+$ ground state would create the 2^+ excited state. Coupling an additional $\lambda = 2$ phonon would produce the $0^+, 2^+$, and 4^+ states. A key signature of vibrational character is given by the energy ratio of the first 2^+ and 4^+ states,

$$\frac{E(4^+)}{E(2^+)} = 2\tag{1.16}$$

in which the 2^+ state is composed of one $\lambda=2$ phonon, while the 4^+ – originating from coupling two $\lambda=2$ phonons – contains two. When the nucleus possesses deformed characteristics, vibrations may be built upon the deformation. With the most common distortion of spherical nuclei being quadrupole in nature, a $\lambda=2$ vibration is frequently used to describe the low-energy spectra of deformed nuclei. Quadrupole vibrations lead to the development of K=0 and K=2 bands in even-even nuclei, which are characterized as β and γ vibrations, respectively [34]. Vibrations associated with the β deformation parameter (with $\gamma=0$) are oscillations along the symmetry axis of the nucleus, which preserves its axial symmetry. Those known as γ vibrations have a rigid β deformation and oscillate about a specific degree of axial asymmetry γ .

1.4 Electromagnetic Decay

Electromagnetic decay serves as one out of many crucial means in which our understanding of nuclei may be enriched. Markedly, the advent of facilities producing rare-isotope beams and powerful gamma-ray detectors such as GRETINA [37, 38], and to-be commissioned GRETA [39, 40], prove advantageous to probe deeper into the structure of nuclei via gamma-ray transitions. Excited-state gamma rays occur when a nucleus releases a photon as it decays to the ground state. The emission of this photon may be characterize by its mean lifetime (τ) and half-life ($t_{1/2}$) which are related by $\tau = t_{1/2}/\ln(2)$. Phonons are spin-1 bosons that carry energy proportional to their frequency ν . The angular momentum carried by the photon λ depends on the initial J_i and final J_f states, where J_i is designated as the higher-lying state. Angular momentum selection rules dictates that the photon

may carry integer amounts of angular momentum via

$$|J_f - J_i| \le \lambda \le J_f + J_i \tag{1.17}$$

Furthermore, these transitions are either electric (E) or magnetic (M) in nature, with the selection criteria determined by the parity of the J_i and J_f states – a property conserved by the strong interaction [8]. If there is no parity change between the initial and final states, the allowed transitions are $M1, E2, M3, E4, \ldots$ Alternatively, a parity change between the initial and final states results in $E1, M2, E3, M4, \ldots$ The multipolarity of a gamma-ray transition is indicated by its angular momentum λ , specified by Eq. 1.17, and are dipole ($\lambda = 1$), quadrupole ($\lambda = 2$), and octupole ($\lambda = 3$), to name a few.

The decay rate between J_i and J_f may take on more than one multipolarity but it is the lowest λ that usually dominates. The larger the transition rate is between J_i and J_f , the larger overlap between the initial and final state wave functions. This transition rate is formally written as [8]

$$W = \sum_{\pi, \lambda} \left(\frac{8\pi(\lambda + 1)}{\lambda((2\lambda + 1)!!)^2} \right) \left(\frac{k^{2\lambda + 1}}{\hbar} \right) \frac{|\langle J_f || \mathcal{O}(\pi\lambda) || J_i \rangle|^2}{(2J_i + 1)}$$
(1.18)

where $k = E_{\gamma}/\hbar c$ is the wave-number for the electromagnetic transition of energy E_{γ} , and $\mathcal{O}(\pi\lambda)$ is the sum over single-body operators of order λ and parity π denoted by

$$\mathcal{O} = \sum_{k} O(\pi \lambda, k) \tag{1.19}$$

The general reduced transition probability is then obtained from the last factor of Eq. 1.18, and is given as

$$B(\pi\lambda, J_i \to J_f) = \frac{|\langle J_f || \mathcal{O}(\pi\lambda) || J_i \rangle|^2}{2J_i + 1}$$
(1.20)

which for the work presented in this dissertation, the electric quadrupole (E2) reduced matrix element is of importance,

$$B(E2, J_i \to J_f) = \frac{|\langle J_f || \mathcal{O}(E2) || J_i \rangle|^2}{2J_i + 1}$$

$$\tag{1.21}$$

To relate the $B(E2, J_i \to J_f)$ to $B(E2, J_f \to J_i)$, where *i* denotes the higher-lying state and *f* the lower-lying state, the required conversion is

$$B(E2, J_i \to J_f) = \frac{(2J_f + 1)}{(2J_i + 1)} B(E2, J_f \to J_i)$$
(1.22)

The conventional nomenclature for these designate $B(E2,\uparrow) = B(E2,J_f \to J_i)$ and $B(E2,\downarrow) = B(E2,J_i \to J_f)$ which represents the excitation $(J_f \to J_i)$ and decay $(J_i \to J_f)$ between states J_i and J_f , respectively. Relevant to the concept of collective excitations (Sect. 1.3), the Weisskopf estimate is utilized to determine whether a particular transition is weak or strong. The Weisskopf estimate relies on the assumption that a single nucleon is responsible for the transition. The Weisskopf estimates for transitions that are electric in nature are given by

$$B_{W}(E\lambda) = \left(\frac{1}{4\pi}\right) \left(\frac{3}{3+\lambda}\right)^{2} (1.2A^{1/3})^{2\lambda} e^{2} \text{fm}^{2\lambda}$$
 (1.23)

where an E2 Weisskopf estimate results in [8]

$$B_{\rm W}(E2) = 0.0594A^{4/3}e^2 \text{fm}^4 \tag{1.24}$$

By comparing the Weisskopf estimate with the measured reduced transition probability, one can infer that a transition is collective in nature if the measured value significantly exceeds the single-nucleon estimate.

1.5 N = 20 Island of Inversion

The onset of deformation in neutron-rich nuclei near N=20 was first uncovered through pioneering mass measurements, which revealed anomalies in binding energies that could not be reconciled within the conventional shell-model framework [6, 9, 11, 15, 17, 41]. These early findings suggested the presence of unexpected structural phenomena in nuclei far from stability, challenging the

prevailing understanding of shell closures. Theoretical investigations using large-scale shell-model calculations demonstrated that the anomalous binding energy systematics could be attributed to the dominance of the energetically favored intruder-deformed configurations, arising from particle-hole excitations across the sd-fp shell gap [6, 9, 15, 17]. Mean-field theoretical models have also been used to describe the unexpected deformation in the neutron-rich nuclei in the vicinity of N = 20 [42, 43].

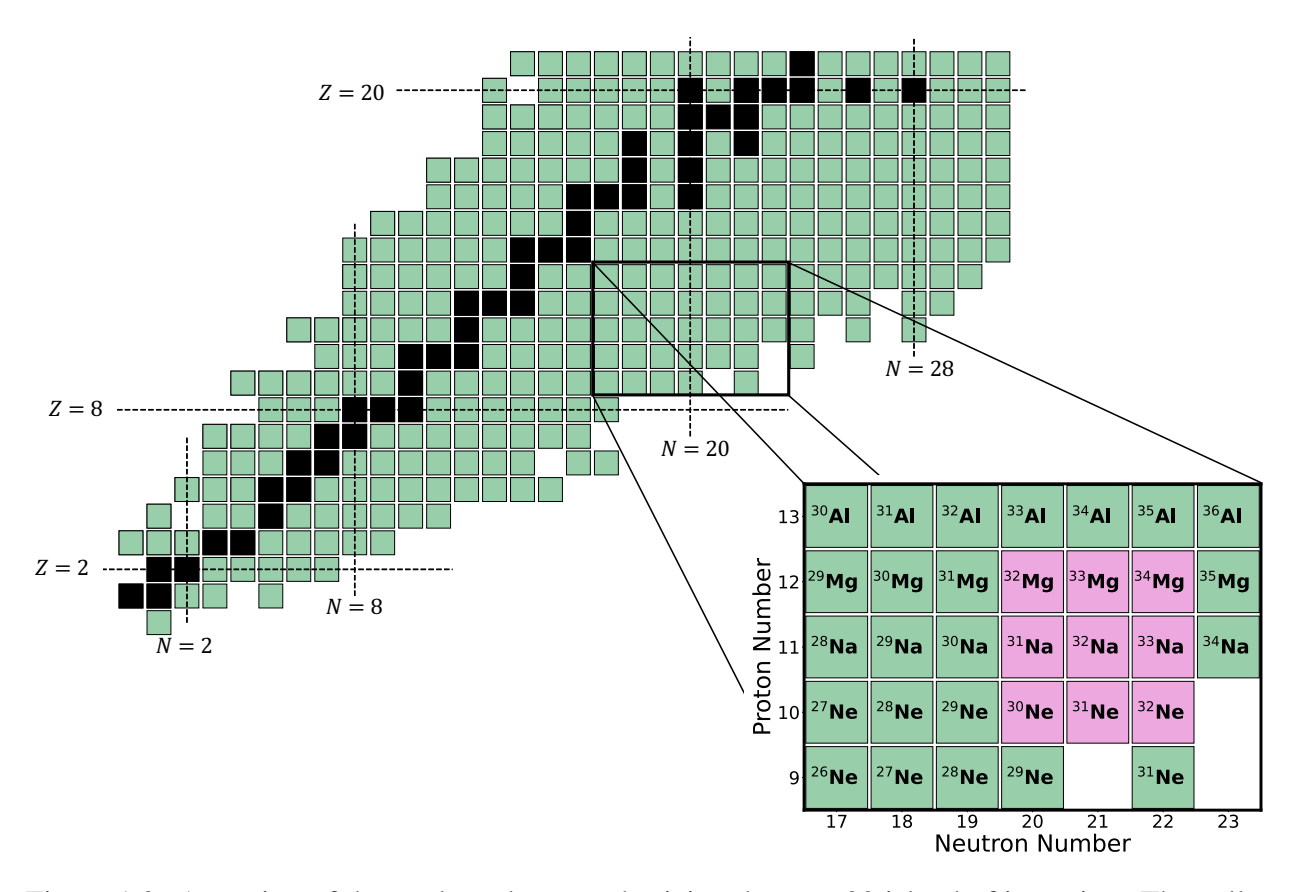


Figure 1.9: A portion of the nuclear chart emphasizing the N=20 island of inversion. The valley of stability is indicated by the black squares, along with the first few proton/neutron magic numbers. The original island of inversion, proposed by Warburton *et al.* [15], is displayed within the pink squares in the inset. Related to this work are the 30,31 Na isotopes, both of which have been identified as belonging to the N=20 island of inversion [44, 45]. Furthermore, the southern shore is now suggested to extend to 28 F [46].

The recognition of this mechanism led to the introduction of the now well-established concept of the island of inversion [15], a region traditionally centered around $Z \simeq 11$ and $N \simeq 20$, as displayed in Fig. 1.9, where nuclei manifest additional correlation energy through $(sd)^{-n}(fp)^n$ configurations.

The significance of this discovery extends well beyond the N=20 region. Similar intruder-driven deformed structures have since been identified in other neutron-rich regions of the nuclear chart [6, 9], demonstrating that shell evolution and configuration mixing play a role in shaping exotic nuclei. Experimental signatures of these effects include anomalously large binding energies, level schemes with lowered excitation energies of yrast states, and enhanced B(E2) transition strengths, all pointing to the emergence of collective behavior in systems once thought to be spherical. In particular, detailed spectroscopic studies of low-lying excited states have proven indispensable for probing the evolution of shell structure as neutrons are added, as well as for distinguishing between static quadrupole deformations and dynamic vibrational correlations. These studies not only illuminate the microscopic origin of deformation in neutron-rich nuclei but also provide critical benchmarks for modern theoretical models that aim to describe the interplay between single-particle motion and collective dynamics far from stability.

1.6 Anomalies Along the Z = 11 Isotopic Chain

The observation of deformation-driven structures within the N=20 island of inversion has prompted significant interest in understanding the extent to which such configurations persist across neighboring isotopic and isotonic chains. In the neutron-rich Z=11 nuclei, the enhancement of spectroscopic quadrupole moments of the ground states has provided compelling evidence for the development of pronounced prolate deformation [47]. This behavior has been interpreted as the result of energetically favored 2p-2h excitations, with minor contributions from 4p-4h components, dominating over the normal 0p-0h configuration. The delicate interplay between spherical and deformed shapes has been further investigated in 32 Na through studies of isomer decay, suggesting the dynamic coexistence of competing nuclear shapes [48].

Theoretical predictions indicate that large quadrupole moments for the $3/2^+$ states may persist across the odd-mass isotopes $^{33-41}$ Na [49], a phenomenon potentially linked to the shell quenching occurring at the N=20 and N=28 magic numbers [36]. For the neutron drip line 39,41 Na isotopes, theoretical studies suggest triaxial deformations may play a more significant role [49, 50].

Moving along the N=20 isotonic line towards 28 O, recent high-precision mass measurements have shown that the empirical shell gap reaches a minimum at 32 Mg but increases markedly for 31 Na [51]. Despite this, the reduced shell gap appears to persist for 28,29 F [46, 52] and 28 O [53], suggesting that the island of inversion extends over a broader region of the nuclear chart than previously anticipated. These findings highlight the intricate balance between spherical and deformed configurations in neutron-rich systems, emphasizing the role of intruder states and cross-shell excitations in shaping nuclear structure far from stability.

With specific regard for 30,31 Na, a question remains as to whether the ground-state deformation induced by intruder configurations persist beyond the first excited states. Currently, reduced E2 transition strengths to the 3^+ and 4^+ excited states – members of a K=2 band – are known for 30 Na, albeit with large uncertainty [54–56]. To further underscore the scarcity of experimental data in this region, only one prior measurement has been reported for the $5/2^+$ excited-state member of the K=3/2 band in 31 Na [54]. Obtaining B(E2) strengths beyond the first low-lying excited states in 30,31 Na offer a means to stringently characterize the Z=11 isotopic chain towards the neutron drip line beyond what is achievable by energy ratios alone.

CHAPTER 2

EXPERIMENTAL TECHNIQUES

The multifaceted nature of experimental nuclear physics is partly reflected through the various means in which observables, such as reduced transition strengths, may be obtained. The progress of experimental nuclear physics is strongly correlated with the development of instrumentation, and therein, the methodologies that emerge from such advancements. This synergy has established nuclear spectroscopy as one of the most indispensable tools in studying atomic nuclei. Pertinent to this thesis are the methods in which gamma rays emitted from rare-isotope beams were studied, alongside the excitation mechanisms for the nuclei being studied. Therefore, this chapter will briefly review in-beam gamma-ray spectroscopy, the inelastic scattering of exotic nuclei, safe and unsafe (intermediate-energy) Coulomb excitation, and heavy-ion inelastic scattering, with the latter being the method employed in the present study.

2.1 In-Beam Gamma-Ray Spectroscopy

In-beam gamma-ray spectroscopy serves as a cornerstone technique in investigating the structure of nuclei. Studying the properties of a nucleus possessing large asymmetries in either proton or neutron numbers necessitates the production of fast rare-isotope beams with energies typically on the order of 100 MeV/u. The produced rare-isotope beams are comprised of a variety of exotic nuclei, which are then utilized in various different reaction mechanisms. These reaction mechanisms may leave a nucleus in an excited state, which prompts the emission of a gamma ray. However, the intensities of the exotic-isotope beams are usually several orders of magnitudes lower than stable beams. In-beam gamma-ray spectroscopy circumvents this shortcoming through the use of thick targets which increases the reaction yield. The large beam velocities (typically exceeding 30% the speed of light) allow for the beam to traverse the reaction target without stopping, minimizing energy and angular straggling, and preserving the kinematic properties of the reaction.

As a result of the relativistic speeds at which the exotic nuclei travel, the gamma rays are

emitted in the forward direction, as opposed to the near isotropic distribution of a particle at rest. Furthermore, the gamma rays are Doppler shifted due to being emitted from nuclei moving at relativistic velocities. Thus, detectors must be sufficiently position sensitive to reconstruct the gamma-ray emission angle of each event. This is achieved by ensuring the detector is granular enough to provide angular information sensitive enough to determine the gamma-ray emission angle. For detectors such as GRETINA (See Sect. 3.5), the signal decomposition procedure, in addition to the segmentation of each crystal, allows for the exploitation of the intrinsic high resolution [37, 38]. In addition to the Doppler broadening of the gamma-ray peak, spectral features such as low- and high-energy tails are a result of lifetime effects from the decay of the excited state. This adds another layer of complexity in disentangling the observed gamma-ray spectrum for a particular nucleus. Relevant to this work, the cross-section values listed in Sects. 4.6 and 4.7 relied on determining the amount of emitted gamma rays in an efficient and accurate manner from in-flight excited ions. The following subsection will detail the relevant equations employed to account for the Doppler broadening effects.

2.1.1 Relativistic Doppler-Shift Corrections

For gamma rays emitted from a nucleus moving at relativistic speeds, the observed gamma-ray energy in the laboratory frame (E_{Lab}) will be subject to Doppler effects. That is, the observed gamma-ray energy E_{Lab} is Doppler shifted relative to the intrinsic excitation energy in the ion's reference frame, E_{ion} . The Doppler-shifted gamma-ray energy in the laboratory frame is given by

$$E_{\text{Lab}} = \frac{E_{\text{ion}}}{\gamma (1 - \beta \cos(\theta_{\gamma}))}$$
 (2.1)

where $\gamma = 1/(\sqrt{1-\beta^2})$ is the associated Lorentz factor, θ_{γ} the laboratory-frame gamma-ray emission angle measured from the ion's velocity vector, and $\beta = v_{\text{ion}}/c$. Given that we are interested in the energy from the ion's reference frame, Eq. 2.1 is rearranged such that

$$E_{\text{ion}} = E_{\text{Lab}} \gamma (1 - \beta \cos(\theta_{\gamma})) \tag{2.2}$$

The effects of the Doppler shift on the intrinsic gamma-ray energy increase with β , and disappear for a stationary nucleus, as is expected. Given the low intensity of exotic beams at rare-isotope facilities, thick targets are necessary to maximize reaction yields. Although beneficial for enhancing the reaction yield, this advantage comes at the expense of reduced resolution in the Doppler-corrected gamma-ray peaks.

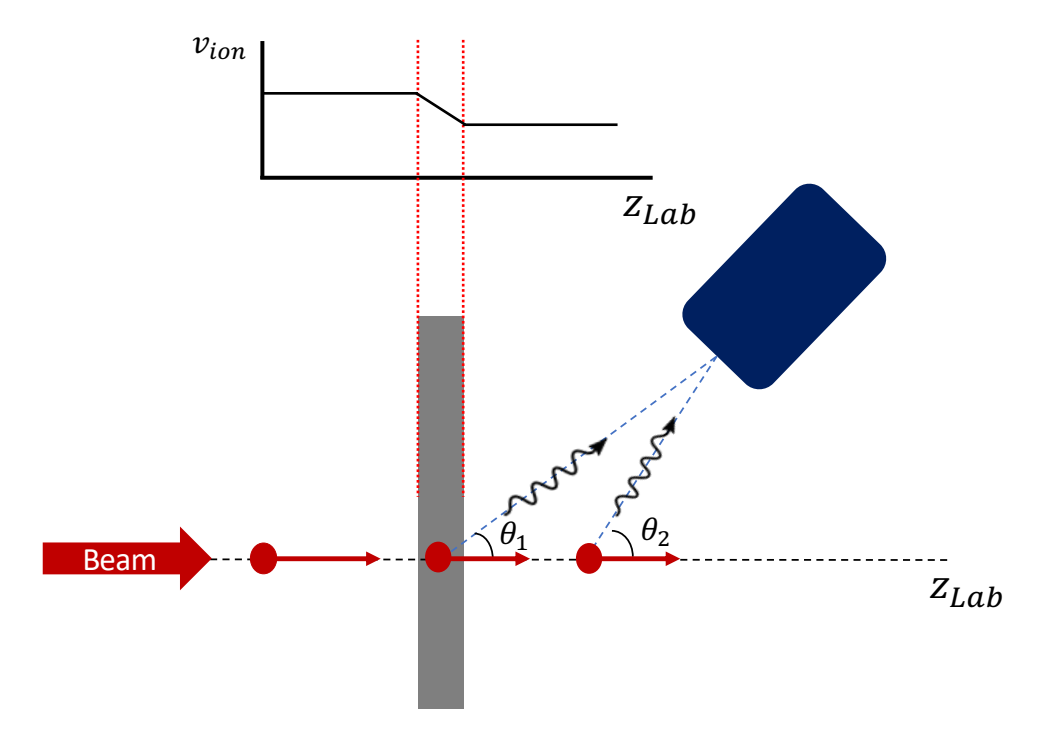


Figure 2.1: Schematic illustration of an ion emitting a gamma ray in and after passing through a production target. In this figure, the ion's velocity vector is aligned with the laboratory frame's z axis indicated by z_{Lab} . As the ion traverses the target material, it loses velocity (top graph), which impacts the Doppler reconstruction: gamma rays emitted inside the target are reconstructed with different velocities than those emitted outside. Furthermore, due to the decay characteristics of the excited state, gamma rays emitted further downstream are detected at larger emission angles, which also impacts the Doppler reconstruction.

The emission angle of the gamma ray relative to the ion's velocity vector governs whether the detected laboratory-frame energy is Doppler upshifted or downshifted. Assuming the velocity vector of the ion is aligned with the z axis of the laboratory frame, gamma-ray energies at forward angles ($\theta_{\gamma} < \pi/2$ in the non-relativistic limit) will experience a positive Doppler shift (i.e. increase in energy). Those detected at backward angles ($\theta_{\gamma} > \pi/2$) experience a negative Doppler shift (i.e. decrease in energy). Furthermore, as the ion traverses through the target, it continuously loses

energy, leading to a varying β . This behavior is illustrated by the graph in Fig. 2.1, which displays the qualitative evolution of the ion's velocity as a function of z_{Lab} . As a result, assuming gamma-ray detectors covering the forward angles, a gamma ray emitted while the ion is still within the target will appear at a higher laboratory-frame energy than one emitted after the ion has exited. This is reflected in the Doppler-corrected gamma-ray spectrum through a high-energy tail for the peak of interest. Conversely, if the decay of an ion occurs further downstream, the laboratory frame energy is typically lower due to the larger emission angle, assuming the velocity vector is aligned with the laboratory-frame z axis. Both high- and low-energy tails are characteristics of lifetime effects manifesting in the observed gamma-ray spectrum, with representative examples given in Refs. [57] and [58], respectively.

The energy resolution of gamma rays emitted in flight have three major contributors which stem from the intrinsic resolution of the detector $\delta_{\text{intr.}}$, uncertainties in the velocity of the ion δ_{β} , and uncertainties in the emission angle of the gamma ray $\delta_{\theta_{\gamma}}$ [7, 59, 60]. Each component that makes up the energy resolution of an in-beam gamma ray is determined by taking derivatives with respect to β and θ_{γ} , and combining it in quadrature with the intrinsic energy resolution. Thus, the total energy resolution of an in-beam gamma ray may be written as [61–63]

$$\delta_{\text{tot.}}^2 = \left(\frac{\Delta E_{\gamma}}{E_{\gamma}}\right)^2 = \delta_{\text{intr.}}^2 + \delta_{\beta}^2 + \delta_{\theta_{\gamma}}^2 \tag{2.3}$$

$$= \left(\frac{\Delta E_{\text{intr.}}}{E_{\gamma,\text{intr}}}\right)^2 + \left(\frac{\beta - \cos(\theta_{\gamma})}{(1 - \beta^2)(1 - \beta\cos(\theta_{\gamma}))}\right)^2 (\Delta \beta)^2 + \left(\frac{\beta\sin(\theta_{\gamma})}{1 - \beta\cos(\theta_{\gamma})}\right)^2 (\Delta \theta_{\gamma})^2 \tag{2.4}$$

The contributions of each term from Eq. 2.4 are plotted in Fig. 2.2 where values of $\beta = 0.365$, $\Delta\beta = 0.0053$, $\Delta\theta = 0.02$ rad were used together with GRETINA's intrinsic energy resolution of 2.4 keV at 1332 keV [37, 38]. For in-beam gamma rays, although there is very good overall balance among the three contributions over the entire angular range, it can be stated that forward-angle detectors tend to have the best energy resolution.

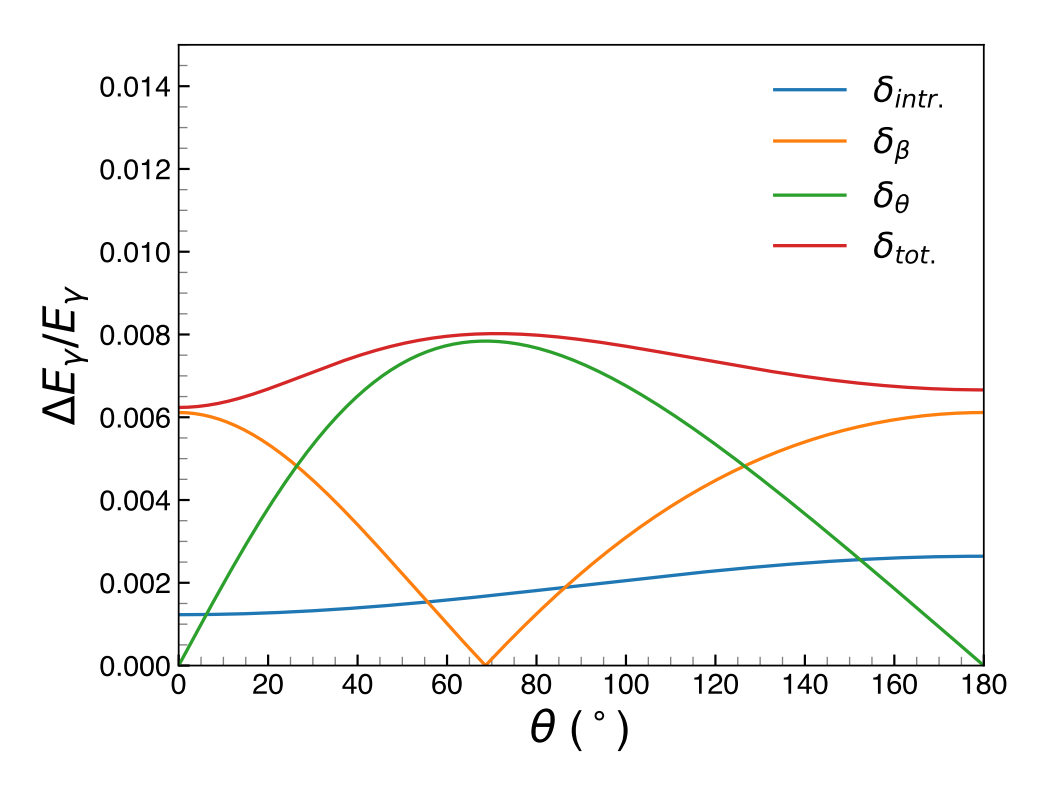


Figure 2.2: Figure displaying the different contributions to the in-beam gamma-ray resolution as described by Eq. 2.4. The intrinsic resolution ($\delta_{intr.}$) is given by the blue line and the orange line represents contributions due to the uncertainty in the ion's velocity (δ_{β}). The green line denotes the uncertainty contributions stemming from the uncertainty in the emission angle (δ_{θ}), with the sum of all terms given by the red line ($\delta_{tot.}$). For the present figure, values of $\beta = 0.365$, $\Delta \beta = 0.0053$, $\Delta \theta = 0.02$ rad were used together with GRETINA's intrinsic energy resolution of 2.4 keV at 1332 keV [37, 38].

2.2 Inelastic Scattering

One approach in quantitatively investigating nuclear structure is through nuclear reactions that selectively probe specific degrees of freedom. For example, the single-particle characteristics may be investigated through direct reactions that involve the addition or removal of one or a few nucleons. Relevant for this dissertation, inelastic scattering has long been employed to study collective modes, which involve the coherent motion of many protons and neutrons. These collective modes are either vibrational (Sect. 1.3.3) or rotational (Sect. 1.3.2) in character, and dominate inelastic spectra. Furthermore, inelastic scattering may be considered as an absorption process due to removing particles flux from the elastic channel and takes the form of [64, 65]

$$a + A \to a' + A^* \tag{2.5}$$

where the incoming projectile is denoted by a, the inelastically scattered projectile by a', and the target by A. This process preserves the identities of both the projectile and target nuclei, while a fraction of the system's kinetic energy is transferred to excite the target nucleus. It is also possible for the projectile, rather than the target, to become excited (or for both to be excited simultaneously). A simple illustration of projectile excitation is shown in Fig. 2.3.

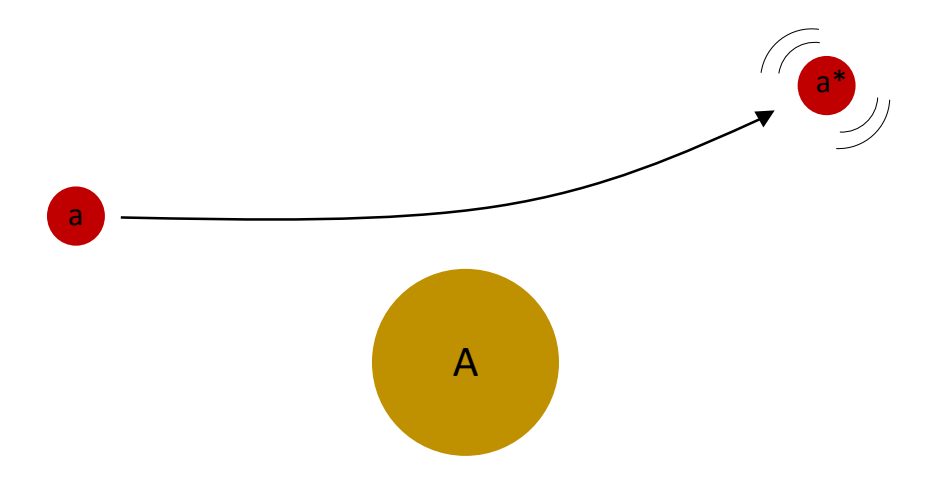


Figure 2.3: Schematic illustration of a projectile a undergoing inelastic scattering from a target nucleus A. Part of the system's kinetic energy is transferred to the projectile, leaving it in an excited state a^* . After a characteristic time governed by the lifetime τ of the excited state, the projectile de-excites, emitting radiation as it continues along its trajectory.

Inelastic scattering involves both Coulomb and nuclear contributions, depending on the projectile energy and the atomic numbers of the projectile and target. These contributions cannot be experimentally separated, as the scattered waves can constructively or destructively interfere with each other. If the nuclear contributions are not negligible, the differential cross section is proportional to the square of the sum of corresponding scattering amplitudes,

$$\frac{d\sigma}{d\Omega} \propto |f_C(\theta) + f_N(\theta)|^2 \tag{2.6}$$

where $f_C(\theta)$ and $f_N(\theta)$ are the Coulomb and nuclear scattering amplitudes, respectively.

In this thesis, the neutron-rich 30,31 Na isotopes were inelastically scattered off low-Z (9 Be) and high-Z (181 Ta) targets using inverse kinematics, where the incoming ion constitutes the object of study and the target functions as the probe [60]. With respect to Eq. 2.5, in inverse kinematics, the nucleus of interest is denoted by A and the probe by a. With these definitions, the inelastic scattering process can be qualitatively represented by $A + a \rightarrow A^* + a'$, with A and A^* depicting the incoming and outgoing ion.

2.3 Coulomb-Excitation Measurements

This chapter focuses on the techniques of Coulomb excitation applied in Refs. [54–56, 66] at safe and intermediate energies. For completeness, this section will briefly outline the Coulomb excitation process at safe and intermediate energies, an essential reaction mechanism for extracting reduced transition probabilities from cross sections measured with rare-isotope beams.

Coulomb excitation is a well-established technique in the field of experimental nuclear physics, having been used to investigate collective modes of excitations of a plethora of nuclei. This form of excitation falls under the category of inelastic scattering, a process in which either the projectile or target is excited by means of a mutually generated time-dependent electromagnetic field. This experimental technique is well-understood, making it an indispensable means in which exotic nuclear structure may be probed. At the advent of this method, stable heavy-ion beams were employed to electromagnetically excite stable-target nuclei [67]. With the development of rare-isotope beam facilities, Coulomb excitation was extended to the projectile itself, thereby enabling studies of short-lived exotic nuclei [68]. The projectile nuclei, having been excited via the Coulomb field of the large-Z target nucleus, are then detected in coincidence with de-excitation gamma rays.

Coulomb excitation may be described as the exchange of virtual photons amongst the projectile and target nuclei, populating states via electromagnetic matrix elements. This entails the absorption of photons virtually created by the electromagnetic field between the projectile-target system. Additionally, from the rest frame of an ion moving relativistically in the laboratory frame, the electromagnetic field of the large-*Z* target nucleus would be denser in the transverse direction of its

motion. Of course, not all inelastic scattering is peripheral, in which its classification is subjected to the incoming beam energy. These regimes are generally categorized by the energy required to surmount Coulomb barrier,

$$E_{\rm B} \approx 1.44 \frac{Z_p Z_t}{1.2(A_p^{1/3} + A_t^{1/3})} {\rm MeV}$$
 (2.7)

where Z_p , Z_t and A_p , A_t are the atomic numbers and mass number of the projectile and target, respectively. Upon surpassing this energy requirement, the inelastic scattering process gains additional contributions from the short-range nuclear force. This leads to what is known as Coulomb-nuclear interference, a phenomenon linked to the wave-like nature of the relativistic moving projectile. This interference may be constructive or destructive, which often times manifest in oscillatory patterns in differential cross-section distributions. The sections below will briefly outline the two regimes of inelastic reactions: safe Coulomb excitation and intermediate-energy Coulomb excitation.

2.3.1 Safe Coulomb Excitation

At collision energies below the Coulomb barrier (Eq. 2.7), the only interaction affecting the projectile nucleus is the electromagnetic field generated by the target. The nomenclature dictates this energy to be a safe energy, where contributions from the short-range nuclear interaction have a negligible influence on the excitation process [68, 69]. In keeping the projectile's bombarding energy below the Coulomb barrier of the target, this ensures the impact parameter b (Eq. 2.8) between the projectile and target nucleus remains large [59]. The scattering angle, and equivalently the impact parameter, are related by [59]

$$b = -\frac{a}{\gamma} \cot(\theta_{\rm CM}/2) \tag{2.8}$$

where a is the half distance of closest approach in a head-on collision,

$$a = \frac{Z_p Z_t e^2}{\mu c^2 \beta^2} \tag{2.9}$$

with $\mu = (A_p A_t/(A_t + A_p))$ being the reduced mass of the projectile-target system, along with the proton numbers of the projectile and target, Z_p and Z_t , respectively. The velocity of the incoming ion in units of the speed of light c is given by $\beta = v_{\text{ion}}/c$, and the Lorentz factor by $\gamma = 1/\sqrt{1-\beta^2}$. The minimum impact parameter b_{min} to enforce a pure Coulomb excitation is typically given by the conservative criteria of [70]

$$b_{\min} = 1.25(A_p^{1/3} + A_t^{1/3} + 5) \text{ fm}$$
 (2.10)

In order to suppress nuclear contributions to the excitation cross-section, forward angles must be selected to restrict the analysis to only peripheral collisions stemming from Coulomb excitation. Low-energy Coulomb excitation selectively populates low-lying states that are collective in nature, where experimental cross-sections deduced in the spectral analysis are direct probes of the *E*2 matrix element [70]. However, other multipolarities, such as the *M*1 transition, remain dominant over the *E*2 in regard to the decay process of the excited state due to its comparatively shorter de-excitation time.

While Coulomb excitation may be completely described quantum mechanically, the semiclassical approach introduced by Alder and Winther [71] is conventionally utilized to circumvent the long-range attribute of the Coulomb force [69]. In this framework, the relative motion between the projectile and target are described by the classical Rutherford trajectory, which is schematically illustrated in Fig. 2.4. It also assumes no overlap of the charge distributions of either projectile or target, guaranteeing the excitation is originating purely from the electromagnetic field. This allows for the reduced transition probability $B(\pi\lambda, J_i \to J_f)$ of the projectile nucleus to be calculated from an angle-integrated cross section. This formalism can be briefly introduced, where the differential cross section to excite the projectile from initial state i to excited state f is give by [71, 72]

$$\left(\frac{d\sigma}{d\Omega}\right)_{i\to f} = \left(\frac{d\sigma}{d\Omega}\right)_{\text{Ruth.}} P_{i\to f} \tag{2.11}$$

where

$$\left(\frac{d\sigma}{d\Omega}\right)_{\text{Ruth.}} = \frac{a^2}{4} \left(\frac{1}{\sin^4(\theta/2)}\right)$$
(2.12)

is the Rutherford differential cross section [73].

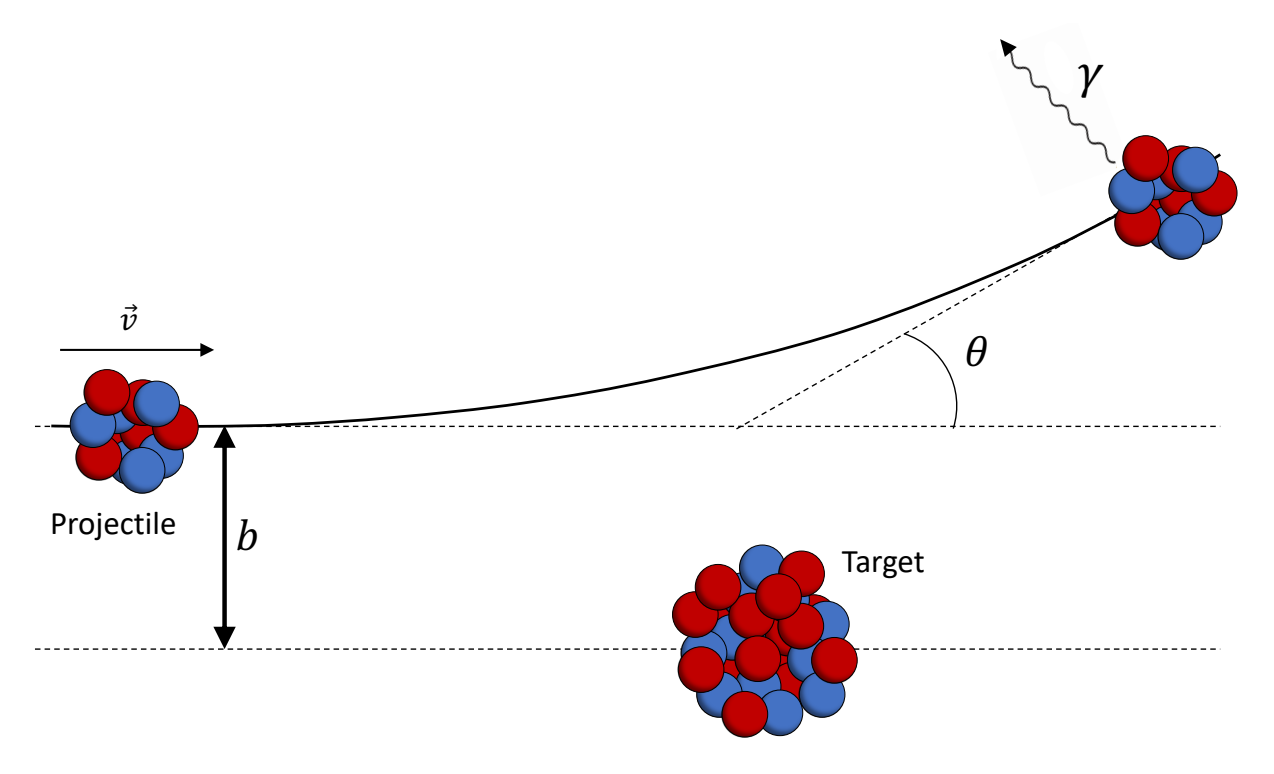


Figure 2.4: Schematic illustration of a projectile following a Rutherford trajectory as it approaches the target nucleus. The projectile, with velocity \vec{v} and impact parameter b, undergoes inelastic scattering from the target. During the interaction, collective states in the projectile are excited by the time-dependent Coulomb field generated between the two nuclei. The subsequent emission of a gamma ray from the projectile provides an experimental probe of its internal nuclear structure.

One can then evaluate the Coulomb excitation probability perturbatively up to first order via

$$P_{i \to f} = |a_{i \to f}|^2 \tag{2.13}$$

$$a_{i\to f} = \frac{1}{i\hbar} \int_{-\infty}^{\infty} e^{i\omega_{fi}t} \langle f|V_C(\vec{r}(t))|i\rangle dt$$
 (2.14)

in which $\omega_{fi} = (E_f - E_i)/\hbar$ is internal transition frequency of the nucleus, with E_f and E_i being the energies of the final and initial states, respectively. Worth mention, the electric field dominates over its magnetic counterpart induced by the moving charged particle as it is reduced by a factor of β^2 comparatively [72]. The cross section stemming from Coulomb excitations, having a multipolarity value of λ , can be related to the reduced matrix element $B(E\lambda)$ as (non-relativistically) [72],

$$\sigma_{E\lambda} = \left(\frac{Z_p e}{\hbar v_i}\right)^2 \left(\frac{Z_p Z_t e^2}{\mu v_i v_f}\right)^{-2\lambda + 2} B(E\lambda) f_{E\lambda}(\xi)$$
(2.15)

with v_i and v_f being the incoming and outgoing velocities of the projectile, respectively, μ the reduced mass, and $f_{E\lambda}(\xi)$ a function that is indicative of the interaction strength. Importantly, the adiabatic parameter ξ informs us of whether the excitation may occur or not. This parameter is defined as [71, 72]

$$\xi = \frac{\tau_{\text{coll}}}{\tau_{\text{nuc.}}} \tag{2.16}$$

$$\tau_{\text{coll}} = \frac{b}{\gamma v_{\text{ion}}} \tag{2.17}$$

$$\tau_{\rm nuc} = \frac{\hbar}{\Delta E} \tag{2.18}$$

where $\tau_{\rm coll}$, in the case of projectile excitation, denotes the amount of time the projectile interacted with the electromagnetic field of the target [74]. The parameter $\tau_{\rm nuc}$ is the characteristic time scale of the nuclear transition corresponding to $\Delta E = E_f - E_i$. In order for the excitation to occur, the perturbation of the electromagnetic field must occur rapidly, that is, $\tau_{\rm coll}$ must be shorter (or roughly on the same order of magnitude) as $\tau_{\rm nuc}$. The impulse from the electric field induces excitations in the nucleus, which are typically collective in nature, such as rotational or vibrational modes. Conversely, if the collision time (Eq. 2.17) greatly exceeds the characteristic nuclear time scale (Eq. 2.18) and the electromagnetic interaction is strong (e.g., for heavy collision partners), multi-step excitations may occur, necessitating a more detailed treatment.

2.3.2 Intermediate-Energy Coulomb Excitation

The technique of intermediate-energy Coulomb excitation utilizes the higher-beam energies to surmount the issue of the low-beam intensity for exotic nuclei. This is done by utilizing thick stable high-Z secondary targets with densities typically a few hundred mg/cm², which increases the experimental yield while relatively not altering the trajectory of the ion [59]. In this energy regime, the possibility of multi-step excitations are greatly suppressed, simplifying the analysis of the resulting gamma-ray spectra [68]. Experimentally, the incoming projectile undergoes inelastic scattering which leaves the traveling ion in an excited state. Under these experimental circumstances, the excitation has the possibility of having Coulomb or nuclear origins. Thus, the experimenter would have to perform particle spectroscopy to identify the inelastically scattered ion, along with determining the scattering angles, followed by utilizing the in-beam gamma-ray technique to quantify the amount of emitted gamma rays. Similar to pure Coulomb excitation, inelastic scattering due to the nuclear interaction shows a pronounced selectivity for collective excited states. Given that contributions from the short-range nuclear force necessitate the nuclei coming close in proximity to each other, it can be qualitatively said that excitations stemming from nuclear inelastic scattering must be a surface phenomenon [64]. In contrast, excitations from Coulomb inelastic scattering involve the coherent motion of the nucleons throughout the nuclear volume by virtue of the infinite range of the Coulomb force [64]. At intermediate energies, one can focus on scattered ions in the forward direction (small scattering angles) to maximize the amount of events associated with Coulomb excitation. For example, recent measurements by Gade et al. (c.f [68, 75]), utilize a reduced radius parameter of $r_0 = 1.2$ fm rather than $r_0 = 1.25$ fm, and set the additional distance to be 2 fm rather than 5 fm in Eq. 2.10 to further restrict the selection of events to Coulomb excitations.

At intermediate energies that are above the Coulomb barrier (Eq. 2.7), the likelihood for the charge distributions of the associated projectile-target system to overlap increases. As a result of this, the short-range nuclear interaction begins to play a role that can't be ignored, as Coulomb-nuclear interference begins to appear. With energies below the Coulomb barrier, the trajectories

could be treated semi-classically in which the relative motion is described by Rutherford trajectories. However, when the energy of the incoming beam is a few hundred MeV/u (on par with the Coulomb barrier), the scattering problem must be treated relativistically, which is underscored by Winther and Alder [71]. The distortion to the Rutherford trajectory of a relativistically moving particle due to the Coulomb force involves rescaling the impact parameter [68, 71],

$$b \to b + \frac{\pi a}{2\gamma} \tag{2.19}$$

which corrects the interaction time $\tau_{coll.}$ (Eq. 2.17) and the adiabaticity parameter (Eq. 2.16). Further details of this correction are found in Refs. [68, 71].

2.4 Heavy-Ion Inelastic Scattering

This dissertation employs the recently developed heavy-ion inelastic-scattering technique [76] at intermediate energies, where the resulting cross sections contain contributions from both Coulomb and nuclear interactions. To this end, cross sections were measured on both low-Z and high-Z targets, with the former providing a constraint on the nuclear contribution to reactions on the latter, under the assumption that the same nuclear process occurs in both cases. With such approach, and the use of coupled-channel calculations, the contributions from nuclear and Coulomb excitation processes were decomposed.

When the projectile's bombarding energy is above the Coulomb barrier, as it is with the work presented here, the nuclear contribution to the excitation mechanism ought to be properly accounted for. This is of particular importance for projectiles with small atomic numbers, where nuclear excitations play a comparatively larger role in the excitation process [77]. To properly estimate the nuclear contribution in the present study, a low-Z target (9 Be) was used simultaneously alongside a high-Z target (181 Ta), which allowed for the nuclear component to be constrained in reactions occurring on the latter. Explicitly, the collective model assumption is taken here, in which identical nuclear deformation lengths are assumed for different targets, expressed as δ_A (9 Be) = δ_A (181 Ta).

Fig. 2.5 illustrates results of coupled-channel calculations used to evaluate the relative impor-

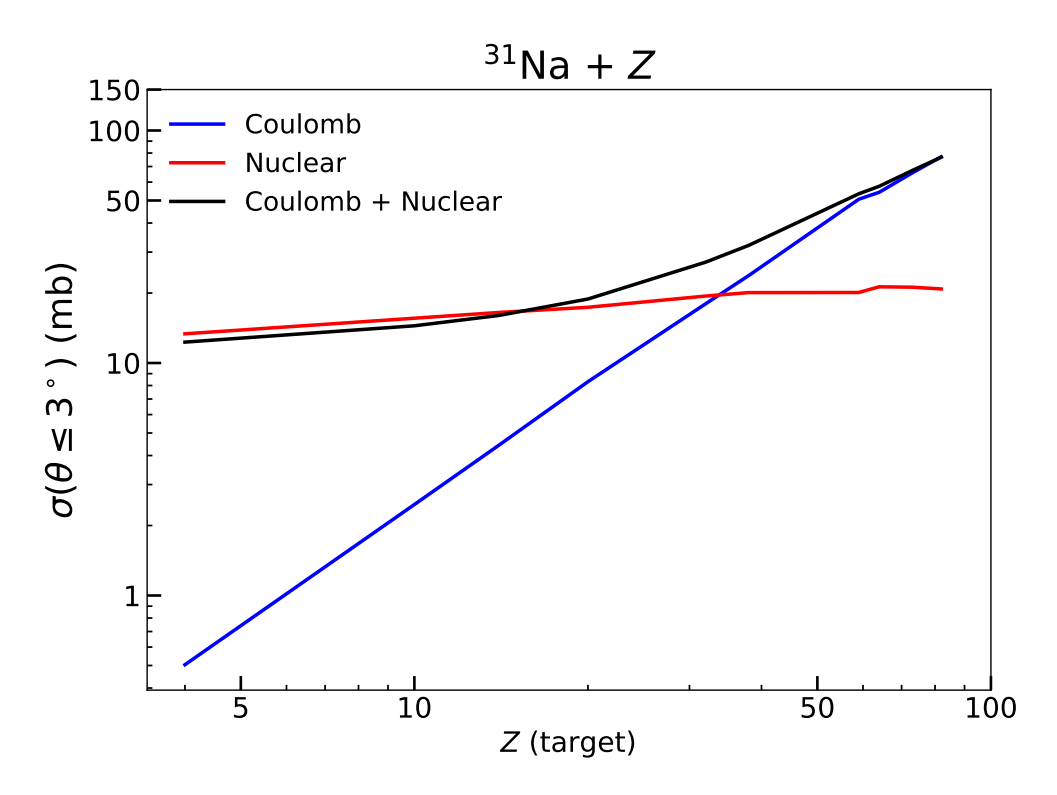


Figure 2.5: Graph showcasing the relative importance between the Coulomb and nuclear contributions to the E2 excitation cross-section for the 31 Na + Z system. The curves were calculated with FRESCO [78–80] where 31 Na had an incoming beam energy of ~ 102 MeV/u, and representative values of 18 efm² and $\delta_A = 1.2$ fm for the E2 matrix element and nuclear deformation length, respectively. The y axis corresponds to the angle-integrated cross section for events with laboratory-frame scattering angle up to 3° ($\theta_{Lab}^{scatt.} \leq 3^{\circ}$). The angle-integrated cross section was determined from a monte carlo simulation incorporating the incoming beam's angular spread and beam spot size. The x axis corresponds to the proton number Z of the target material. The optical potential derived from the elastic scattering of 17 O + 208 Pb [81] was utilized to produce the curves.

tance of each component, in addition to the coherent sum, for the 31 Na + Z system where 31 Na was kept at an incoming beam energy of ~ 102 MeV/u. For the nuclear and Coulomb components, FRESCO [78–80] was employed to calculate the curves utilizing the optical potential derived from the elastic scattering of 17 O + 208 Pb [81]. To understand the behavior of each contribution with respect to 30,31 Na, representative values of 18 efm² and δ_A = 1.2 fm were adopted for the E2 matrix element and nuclear deformation length, respectively. The y axis represents the angle-integrated cross-section for events with laboratory-frame scattering angles up to 3° ($\theta_{\text{Lab}}^{\text{scatt.}} \leq 3^{\circ}$), as determined from a monte carlo simulation that accounts for the incoming beam's angular spread and spot size. Details of this simulation will be discussed later in Chapter 4. The x axis represents the proton

number Z of the target material.

From Fig. 2.5, it can safely be stated that the nuclear contribution dominates over the Coulomb component at a low Z_{target} value, as is the case for the $^{31}_{11}\text{Na} + ^{9}_{4}\text{Be}$ inelastic scattering process. With rising Z_{target} , the Coulomb component rapidly grows, while the nuclear component exhibits a slight increase. This slight increase in the nuclear component is attributed to the approximate $A^{1/3} - A^{2/3}$ dependence of nuclear excitations, and partly due to the selection criterion $\theta_{\rm Lab}^{\rm scatt.} \leq 3^{\circ}$ imposed on the scattered ions, which reduced contributions from the nuclear component [82]. For values of $Z_{target} \sim 30$, the nuclear and Coulomb have an equivalent role in the excitation process. As the proton number further increases, particularly for $Z_{\text{target}} \gg 50$ as in the case for the $^{31}_{11}$ Na + $^{181}_{73}$ Ta, the Coulomb contribution clearly dominates. This clear dominance at larger Z is again due to the selection criteria of $\theta_{\text{Lab}}^{\text{scatt.}} \leq 3^{\circ}$, which shows a preference for Coulomb-based excitations. Nevertheless, the nuclear component still remains non-negligible and must be evaluated to accurately describe the reaction mechanism. The significance of these nuclear contributions is further highlighted by Refs. [77, 83, 84], which demonstrate that the experimentally measured angular distributions could only be reliably reproduced when both Coulomb and nuclear interactions were included. These studies highlight the importance of accounting for both Coulomb and nuclear contributions in intermediate-energy heavy-ion scattering, particularly when extracting excitation cross sections and determining electromagnetic transition probabilities, as performed in the present work.

CHAPTER 3

EXPERIMENTAL DEVICES AND TOOLS

The work discussed within this dissertation is the result of an experiment performed at the National Superconducting Cyclotron Laboratory (NSCL) in 2019. In the present work, features of collective phenomena in the neutron-rich nuclei ^{30,31}Na were investigated by an intermediate-energy heavyion inelastic scattering measurement. In particular, the inquiry was aimed at answering whether the ground-state deformation found in 30 Na (N = 19) and 31 Na (N = 20) [54–56, 66] was robust enough to persist into the low-lying excited states. To answer this question, excitation cross sections were determined from the observed (4⁺) \rightarrow (3⁺), (4⁺) \rightarrow 2⁺_{g.s.}, and (3⁺) \rightarrow 2⁺_{g.s.} transitions in the $^{30}Na~\gamma$ -ray spectrum, and (7/2+) \rightarrow (5/2+), (5/2+) \rightarrow 3/2+, transitions in the $^{31}Na~\gamma$ -ray spectrum. From the excitation cross-sections, reduced electric quadrupole transition strengths, $B(E2 \uparrow)$, were deduced. However, at intermediate energies, the relative importance between nuclear and Coulomb contributions to the excitation cross-section varies with multipolarity [21]. As a result, measurements were taken on both high-Z (¹⁸¹Ta) and low-Z (⁹Be) target materials, allowing for the confirmation of the E2 (l=2) excitation and the estimation of non-negligible nuclear excitation contributions at intermediate energies. For the purpose of deducing a $B(E2 \uparrow)$, the low-Z target material was utilized to determine the amount of nuclear contributions to the excitation cross-section. The high-Z target material was used to determine the amount of Coulomb contributions to the excitation cross-section, assuming a similar amount of nuclear contributions between the low-Z and high-Z target materials.

The success of this experiment necessitated a myriad of devices to work in tandem, in which the relevant devices will be described in this chapter. We will first describe the production of ⁴⁸Ca by the Superconducting Source for Ions (SuSI) [85], which is then accelerated up to 140 MeV/u by the K500 and K1200 cyclotrons [86–88] before impinging on a ⁹Be production target. We will then move downstream and describe devices such as the A1900 fragment separator [89] and elaborate on the use of magnetic rigidities to separate and select our secondary beam of ^{30,31}Na. Following

our secondary beam into the S3 vault, a description of the TRIPLEX device [90] will be given alongside its use in simultaneously holding our ⁹Be and ¹⁸¹Ta target materials to populate excited states in our secondary beam. The released gamma-rays are then detected by GRETINA [37, 38] in which our recoil nuclei enter the S800 Spectrograph [91] for particle identification. The joint use of GRETINA and the S800 allows for coincidence windows to be established between observed gamma rays and detected recoil nuclei.

3.1 Ion Source

The first step in producing our secondary beam of exotic nuclei is to utilize the Superconducting Source for Ions (SuSI) [85] to generate an ionized primary beam of 48 Ca. SuSI, shown in Fig. 3.1, is an electron cyclotron resonance (ECR) [93] ion source capable of operating at 14.5 or 18 GHz. It uses magnetic confinement and cyclotron heating through the use of resonances to produce a plasma comprised of energetic free electrons and ions. This entails injecting a 48 Ca gas into the 100-mm diameter plasma chamber of SuSI along with free electrons. The 48 Ca atoms and free electrons are then confined in the plasma chamber by an external magnetic field generated by superconducting magnets. The atoms and the free electrons oscillate at the cyclotron frequency (ω_c) given by

$$\omega_c = \frac{q}{m} |\vec{B}| \tag{3.1}$$

where $|\vec{B}|$ is the magnitude of the applied transverse magnetic field, and q and m are the charge and mass of the particle, respectively. Due to the charge-to-mass ratio dependence in the cyclotron frequency, the applied magnetic field induces different cyclotron frequencies for the atoms and electrons. Exploiting this feature, a resonance frequency (RF) is applied to match the electron cyclotron frequency ($\omega_{RF} = \omega_{c,e^-}$), thereby accelerating the free electrons in the chamber while minimally heating the atoms. This in turn generates a plasma made up of energetic free electrons and relatively cold atoms. The ⁴⁸Ca atoms in the plasma are then positively ionized through the sequential impact of electrons which generates additional free electrons in the process, increasing the probability of ionization through electron impact. The formed ⁴⁸Ca ions, existing in various

charge states, are guided into the K500 cyclotron through the use of electric fields.

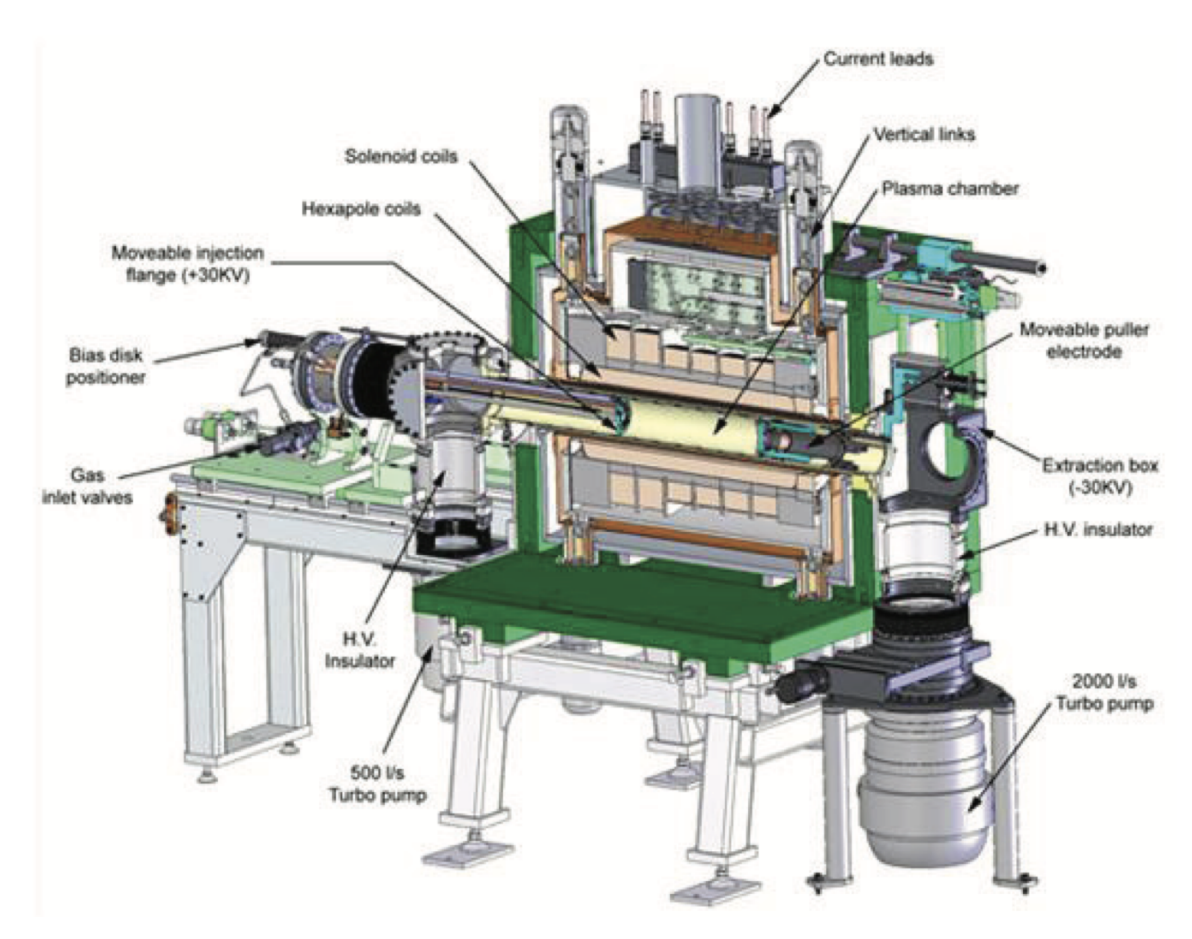


Figure 3.1: Sectional picture of the Superconduction Source for Ions (SuSI). The image is from Ref. [94].

3.2 The Coupled Cyclotron Facility

The Coupled Cyclotron Facility (CCF) consisted of a pair superconducting cyclotrons, the K500 and K1200, working in stages to accelerate and further strip the partially ionized beam from SuSI, as seen in the layout presented Fig. 3.2. The suffix of 500 and 1200 in the name of the cyclotrons represents the maximum kinetic energy (in MeV) that the cyclotron can accelerate a single proton to. To first describe the principle of operation for each cyclotron in the two-stage process, a magnetic field was applied transverse to the velocity of the particle. The motion of a charged particle in a magnetic field \vec{B} with velocity \vec{v} is governed by the Lorentz force, given by

$$\vec{F}^B = q\vec{v} \times \vec{B} \tag{3.2}$$

By setting $|\vec{F}^B|$ equal to the centripetal force, F^C , one can show

$$B\rho = \frac{mv}{q} \tag{3.3}$$

where ρ is the ion's radius of curvature, and m and q are the mass and charge of the particle. This results in a circular motion when \vec{v} and \vec{B} are held constant, and the charge does not change.

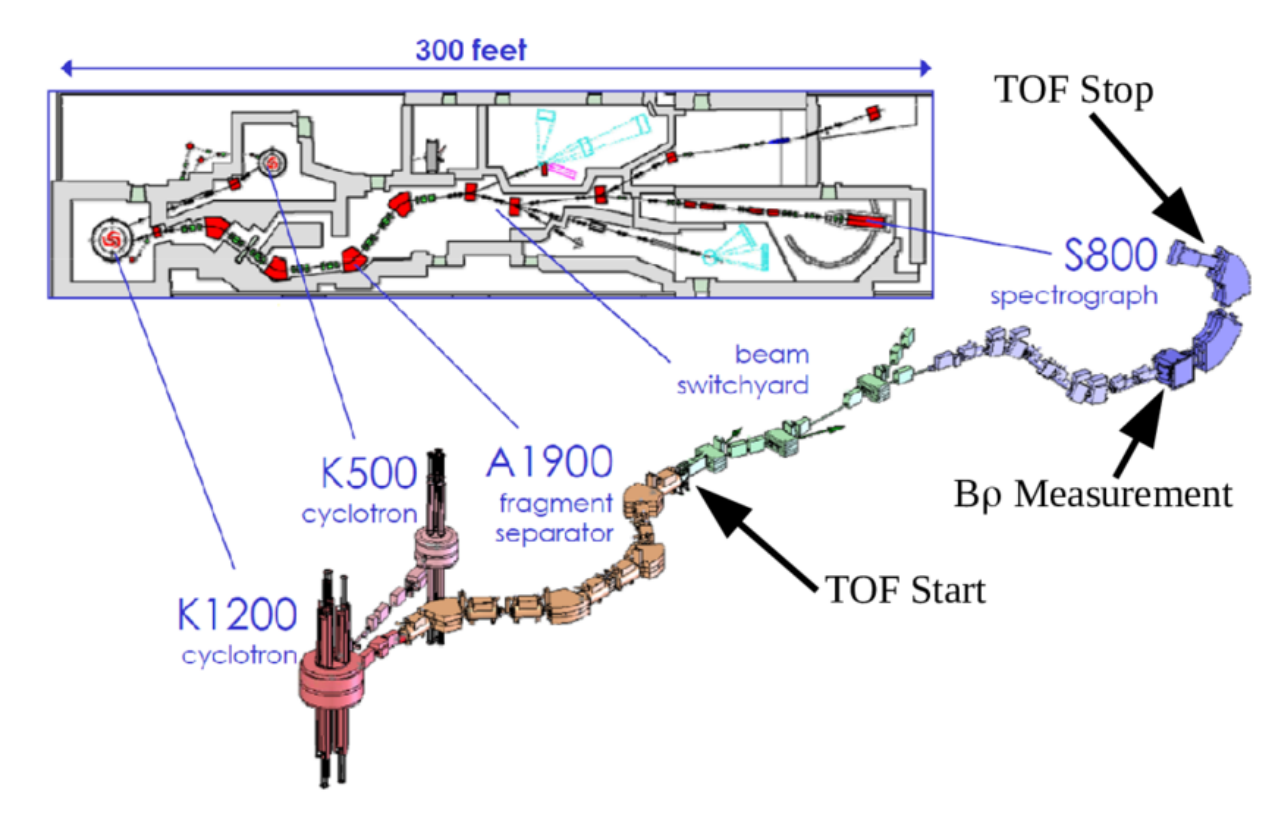


Figure 3.2: Schematic view of a portion of the NSCL, highlighting the K500 and K1200 cyclotrons (red), the A1900 fragment separator (orange), the beam switchyard (green), and the analysis line leading to the S800 Spectrograph (blue). The inset at the top left displays an overhead schematic of the NSCL, with blue lines connecting components from the expanded beamline view to their respective experimental vaults. The image is adapted from Ref. [92].

The quantity $B\rho$ is often referred to as the magnetic rigidity and is measured in Tesla-meters. In order to extract the charged ions from either the K500 or K1200 cyclotrons, a potential is applied between a *dee* and *hill* copper electrode, leading to a strong electric field in the gap between the

dee and hill, as seen in Fig. 3.3. The polarities that are applied to the *dees* and *hills* to produce the electric field in the gap alternate at a frequency that are governed by the cyclotron frequency ω_c of the particular ion of interest. The electric field accelerates the ions, producing an outward spiral trajectory that eventually reaches the extraction point of the cyclotron once the ion has reached its desired energy.

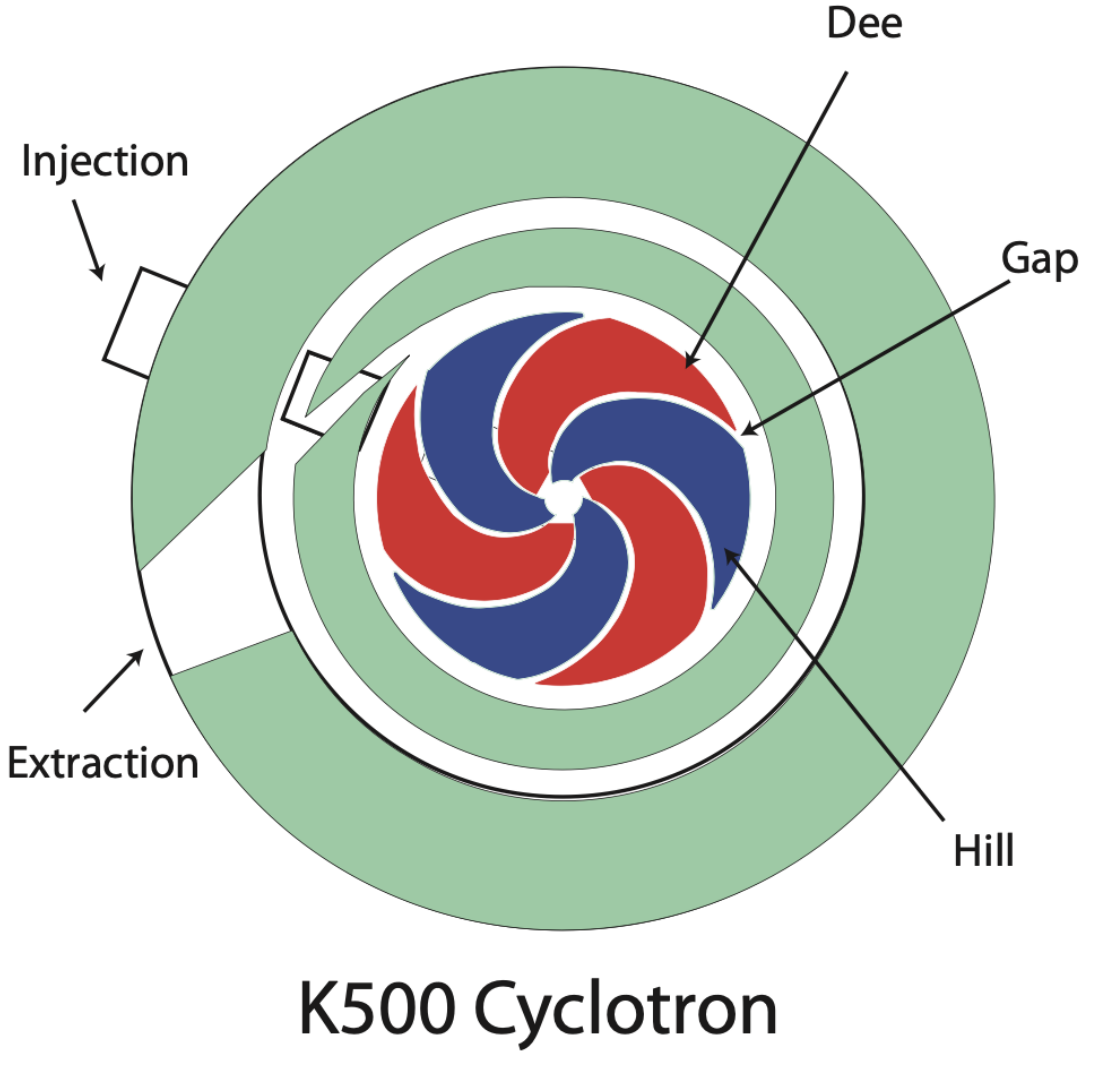


Figure 3.3: A schematic of the K500 cyclotron. The *dees* are shown in red, the *hills* in blue. An accelerating voltage is applied between the *dee* and the *hill*, so each time the ionized beam crosses the gap it is accelerated. This image was generated by modifying Fig. 1 of Ref. [89].

To describe the two-stage process itself, this entails first accelerating the ionized beam from

SuSI in the K500 cyclotron to $\sim 10\%$ of the speed of light. Once the beam has reached its maximum velocity inside the first cyclotron, the partially ionized beam is ejected and transferred to the K1200 cyclotron. Upon entering the K1200 cyclotron, the primary beam is further stripped to its maximum positive charge state by a stripping foil placed in the trajectory of the ion. The use of the stripper foil enhances the K1200's ability to accelerate and bend the ion, increasing the quality of the primary beam. Once the ions have reached their extraction point, they are delivered to the production target. For this experiment, the coupled cyclotrons delivered a primary beam of 48 Ca $^{+20}$ at 140 MeV/u to a 9 Be production target.

3.3 Fragment Production and Separation

Once the primary beam of ⁴⁸Ca⁺²⁰ at 140 MeV/u was produced, it was directed to a ⁹Be production target, where it fragmented to produce variety of reaction products. The material of ⁹Be is employed due to its high number density, increasing the probability of a reaction to occur, its handling properties in atmosphere, and minimal effects from Coulomb interactions due to a low-*Z* number. The fragmentation process predominantly yields nuclei with fewer protons or neutrons, leaving out individual neutrons and protons evaporated during and after fragmentation. In order to select the ions of interest to the experiment, the fragments were separated by the A1900 Fragment Separator [89] through the use of magnetic rigidities and charge. Once the ions of interest were selected, they were transferred to their respective experimental vault.

3.3.1 A1900 Fragment Separator

This section will discuss the operational principles used to guide the secondary beam in the A1900 Fragment Separator [89], shown by the shaded blue region in Fig. 3.4. The A1900 Fragment Separator is composed of four 45° superconducting dipole magnets and 24 superconducting quadrupole magnets. The path of the secondary beam is outlined by the red line in Fig. 3.4, where the journey of our ions began at the ion sources described in Section 3.1. The fragmentation of the ⁴⁸Ca⁺²⁰ primary beam on the ⁹Be production target can be intuitively described by the macroscopic abrasion-ablation

model [95]. This model partitions the production of fragments in two steps: a shearing-off of nucleons from the beam due to peripheral interactions with the target nucleus, followed by an ablation stage where energy gained from the interaction is released through the evaporation of particles. Due to the kinematics of the fragmentation, the resultant products all tend to have minimal energy loss, narrow momentum distributions, and small angular distributions (i.e. forward focused).

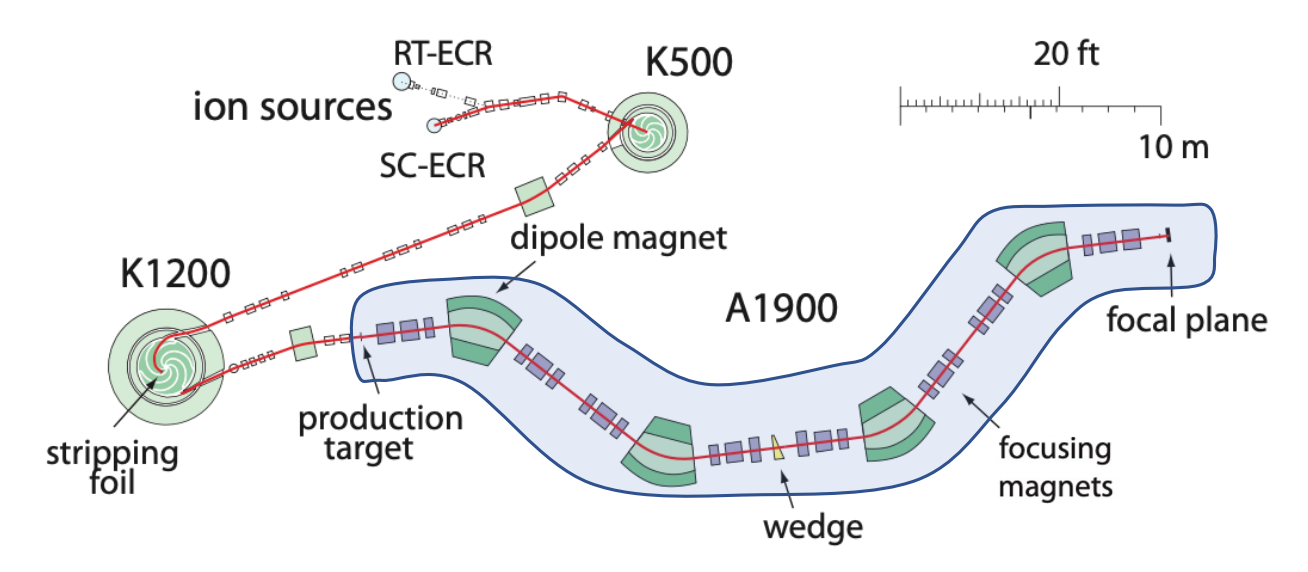


Figure 3.4: A schematic of the NSCL facility, showing the coupled K500 and K1200 cyclotrons and the A1900 fragment separator in the shaded blue region. This image was generated by modifying Fig. 1 of Ref. [89].

Upon entering the first dipole magnet, the secondary beam encounters a magnetic field that bends the trajectory of the ions by 45° based on their magnetic rigidity, $B\rho$, dispersing the ions through the dipole magnet. However, as mentioned previously, the secondary beam constituents all contain similar velocities which reduced the magnetic rigidity of an ion to

$$B\rho \propto \frac{A}{O}$$
 (3.4)

where ρ is the bending radius of an ion in a constant magnetic field B, with A and Q being the mass and the charge, respectively. By controlling the current running through the dipole magnet, the magnetic field can be tuned to allow ions with a certain mass-to-charge ratio (A/Q) to follow a central trajectory through the A1900 and sweep out ions that are not of interest. Once the ions have

passed through the first dipole magnet, sets of quadrupole magnets refocus the beam and transfer it to a secondary dipole magnet. Reaching the second set of dipole magnets, the beam is again bent at 45° and further spatially separated by means of A/Q.

Unambiguous ion identification cannot solely rely on the mass-to-charge ratio, as different ions may share the same value, leading to a degeneracy. To circumvent this problem, an aluminum wedge-shaped degrader is placed after the second dipole magnet but before the third dipole magnet, as seen in Fig. 3.4. The use of the wedge degrader exploits the different identities of the ion as the energy loss of the ion is given by the Bethe-Bloch formula [96, 97] which can be distilled to

$$-\frac{dE}{dx} \propto \frac{Z_p^2}{v_p^2} \tag{3.5}$$

where Z_p is the atomic number and v_p is the velocity of the projectile. The passing of the ions through the wedge produces variable momenta in the constituents of the secondary beam, ridding any degeneracy there may have been in a particular A/Q value. Having been further spatially separated through the use of the wedge, the separation of the ions through the remaining quadrupole and dipole magnets now depends on a mass-to-charge ratio that is approximately proportional to $A^{2.5}/Q^{1.5}$ [98]. After passing through the last set of quadrupole magnets after the fourth (and final) dipole magnet of the A1900, the secondary beam passed through a plastic scintillator located at what is known as the XFP location of the beam line. This plastic scintillator is used to perform Time-of-Flight (TOF) measurements in conjunction with other scintillators located along the beam line. The secondary beam is then sent to a transfer hall where it continues on its journey to its assigned experimental vault, that being the S3 vault for this experiment.

3.4 S800 Spectrograph

The S800 spectrograph [91] is a device at the Facility for Rare Isotope Beams (FRIB) that employs superconducting magnets and various detectors to enable particle identification for experiments. The spectrograph consists of multiple detector stations, divided into two sections: the analysis line and the spectrograph itself, as seen in Fig. 3.5. The analysis line consists of the object,

intermediate image, and target station while the spectrograph consists of two large dipole magnets and the focal plane station. The object station contains a plastic scintillator for Time-of-Flight (TOF) measurements, the intermediate-image station is equipped with two tracking Parallel Plate Avalanche Counters (TPPACs) along with a retractable viewer camera, and the detection system at the target station varies by experiment. The spectrograph section consists of two large dipole magnets below the focal plane station which is comprised of two cathode readout drift chambers (CRDCs), a timing scintillator, and an ionization chamber that measures an ion's energy loss. Through the use of data collected at the focal plane and inverse transfer maps [99], the S800 spectrograph is able to reconstruct an ion's trajectory on an event-by-event basis giving us position and momentum information at the target station.

In this section, the particle identification process through the usage of the various different detectors in the S800 spectrograph will be discussed, followed by an overview of the working principles of the detectors used.

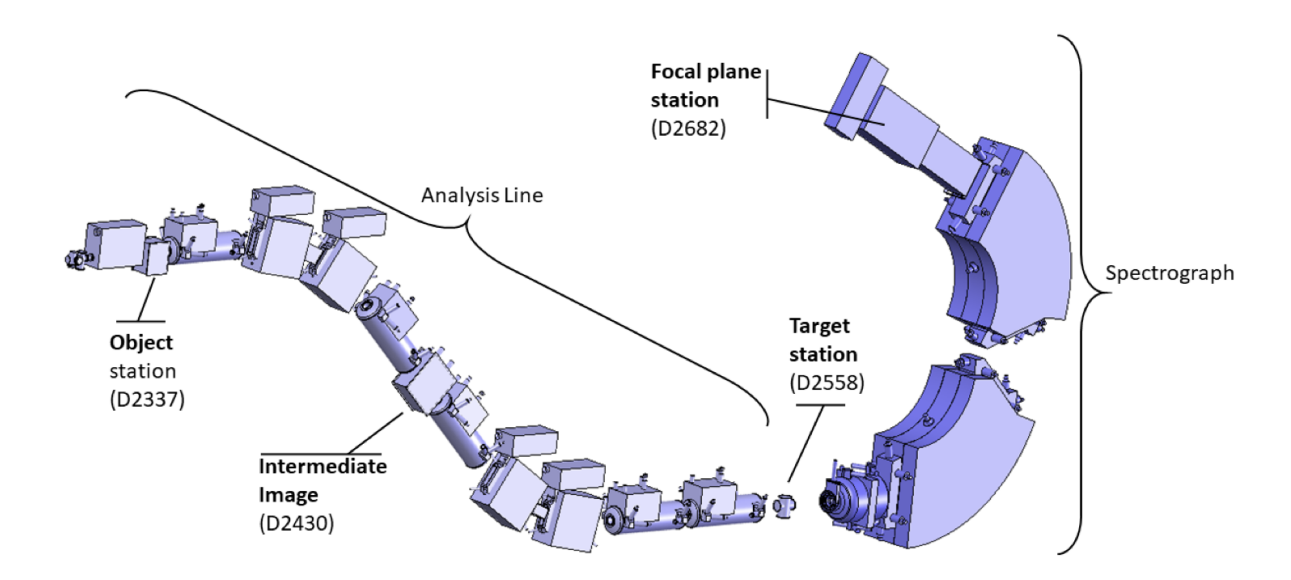


Figure 3.5: The S800 Spectrograph. As the beam is injected to the analysis line, it passes through the object station, intermediate image station, and target station. The target station has additional target material to invoke the reaction of interest, with also having an auxiliary detector coupled with the S800. The two giant dipole magnets guide the recoil nuclei produced at the target station up to the focal plane station. The figure was adapted from Ref. [100].

3.4.1 Magnets and Mode of Operation

The S800 spectrograph is composed of a series of superconducting magnets throughout the analysis line and the spectrograph portion. The principle of operation for the magnets found in the S800 spectrograph are the working principles outlined for the A1900 in Sect. 3.3.1. The trajectory of the ion in the magnets depends on the magnetic rigidity, $B\rho$, the ion had when it was transferred from the A1900 fragment separator to the S800 spectrograph. There are two different modes of operation in the S800: dispersion-matching mode and focus mode. For this experiment, the latter was utilized and therefore our discussion will center around the focus mode of operation. This mode operated the analysis line achromatically and delivered the secondary beam with a small spatial focus (i.e. small beam spot) at the target station with an overall ~5% momentum acceptance $(dp/p = \pm 2.5\%)$ throughout the spectrograph. As the ions leave the target station and enter the spectrograph portion, the two giant dipole magnets separate the ions based on their magnetic rigidity, producing a relationship between the position of the ion and it's momentum. Additionally, the energy resolution in this mode of operation was limited to roughly 1 part in $1000 (dE/E = 10^{-3})$ and a maximum angular dispersion of 50 mrad is reached a the intermediate image plane.

3.4.2 Timing Scintillators

Within the S800 spectrograph, there are several plastic scintillators along the path of the secondary beam that are used for Time-of-Flight (TOF) measurements. The two primary scintillators used for TOF measurements in the S800 are positioned in the Object station and Focal plane station, where the positions of each station is given in Fig. 3.5. As the ionizing radiation (i.e., the ions in the secondary beam) enters the scintillator, it excites the atoms within the material. This excitation consists of providing enough energy to the atomic electrons such that they are promoted from their ground state orbitals to higher-lying orbitals. The excited electrons then release the gained energy by emitting photons which are guided to photomultiplier tubes positioned at each end of the scintillator [101]. The photomultiplier tubes then convert the photons to electrons, which are then amplified to produce a signal to be readout by the electronics. The signal that is produced

is then used for TOF measurements, where the relationship between an ion's mass-to-charge ratio and TOF can be determined by setting the Lorentz force (Eq. 3.2) to the centripetal force F^C ,

$$B\rho = \frac{mv}{q} \tag{3.6}$$

substituting v = d/t for the velocity,

$$TOF \equiv t = \frac{m}{q} \frac{d}{B\rho}$$
 (3.7)

$$TOF \propto \frac{m}{q} \tag{3.8}$$

where m is the mass of the ion, q is the charge of the ion (not necessarily equal to Z due to the possibility of different charge states), and the ratio $d/B\rho$ is roughly constant. The TOF measurements that were used in this analysis consist of taking timing differences between the scintillators at the Object station (known as OBJ) and the S800 Focal Plane station (known as E1), and between the scintillators at the A1900 Focal Plane (known as XFP) and the E1. The TOF measurements are then used to identify the ions at the S800 Focal Plane. Additionally, the E1 serves as a trigger that forms coincidence windows between the S800 and auxiliary detectors (i.e. GRETINA for this experiment)

3.4.2.1 Timing Corrections

To make the unambiguous identification of ions when performing the particle identification, the TOF measurement must be corrected for any dependencies it may have on the momentum (i.e. their position) and the angular distribution of the ion. The TOF of an ion as it traverses the various different magnets should roughly be proportional to the mass-to-charge ratio, as outlined in Eq. 3.8. However, each ion in the secondary beam has a momentum and angular distribution that affects the TOF measurement. For example, two ions of the same kind (same A/q ratio) travel through a constant magnetic field B (which is orthogonal to their path) with different velocities (i.e. different magnitudes of momentum) with ion 1 having velocity v_1 and ion 2 having velocity v_2 such that

 $v_1 > v_2$. This would result in ion 1 having a smaller TOF due to a larger $B\rho$. A similar argument can be made for the relationship between TOF measurement and angular distribution of the ion. The effects of each ion having an angular and momentum distribution can be seen in Figs. 3.6a and 3.7a, respectively. The corrections that are applied take the form of

$$TOF_{corr} = TOF_{uncorr} + C_1 \times a_{fp} + C_2 \times x_{fp}$$
(3.9)

where TOF_{corr} is the corrected time-of-flight measurement, TOF_{uncorr} is the uncorrected time-of-flight measurement, and C_1 and C_2 are the correction factors applied to rid the TOF measurement of its dependence on position (x_{fp}) and angle (a_{fp}) in the dispersive plane (see Sect. 3.4.4 for more information on x_{fp} and a_{fp}). To verify this, the lines in Figs. 3.6a and 3.7a become vertical once the proper corrections have been made, as seen in Figs. 3.6b and 3.7b, indicating that no matter what angle or position the ion may have, the TOF is constant for a particular ion species. The values of $C_1 = 1.66$ and $C_2 = 0.22$ were used in this analysis.

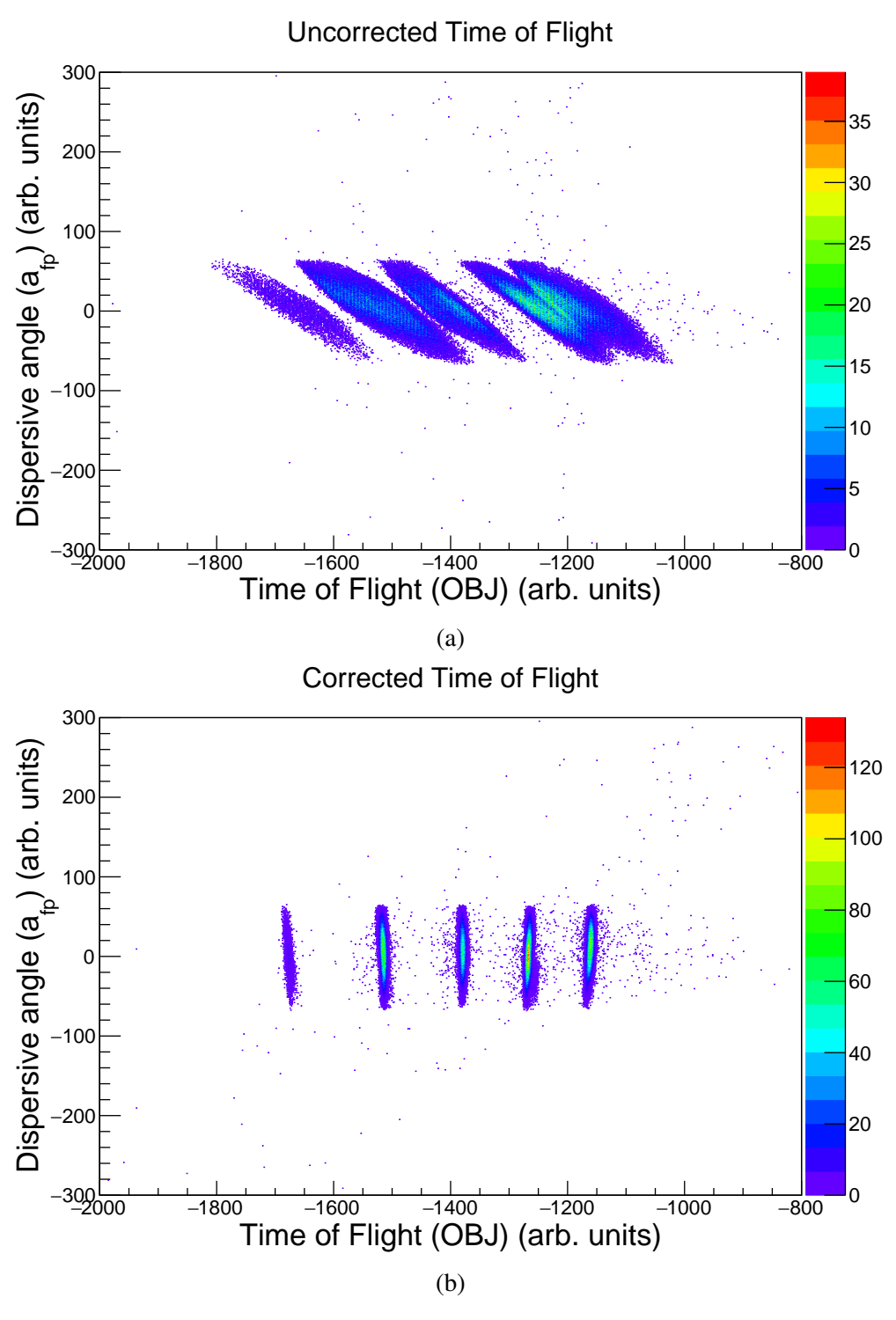


Figure 3.6: Uncorrected (a) and corrected (b) histograms are shown for dispersive angle in the focal plane (y axis) vs the time-of-flight (TOF) measurement difference between the S800 Object and E1 scintillators (x axis). The corrected histogram show that the TOF and angle are independent of one another, compared to the uncorrected histogram showing a correlation between angle and TOF.

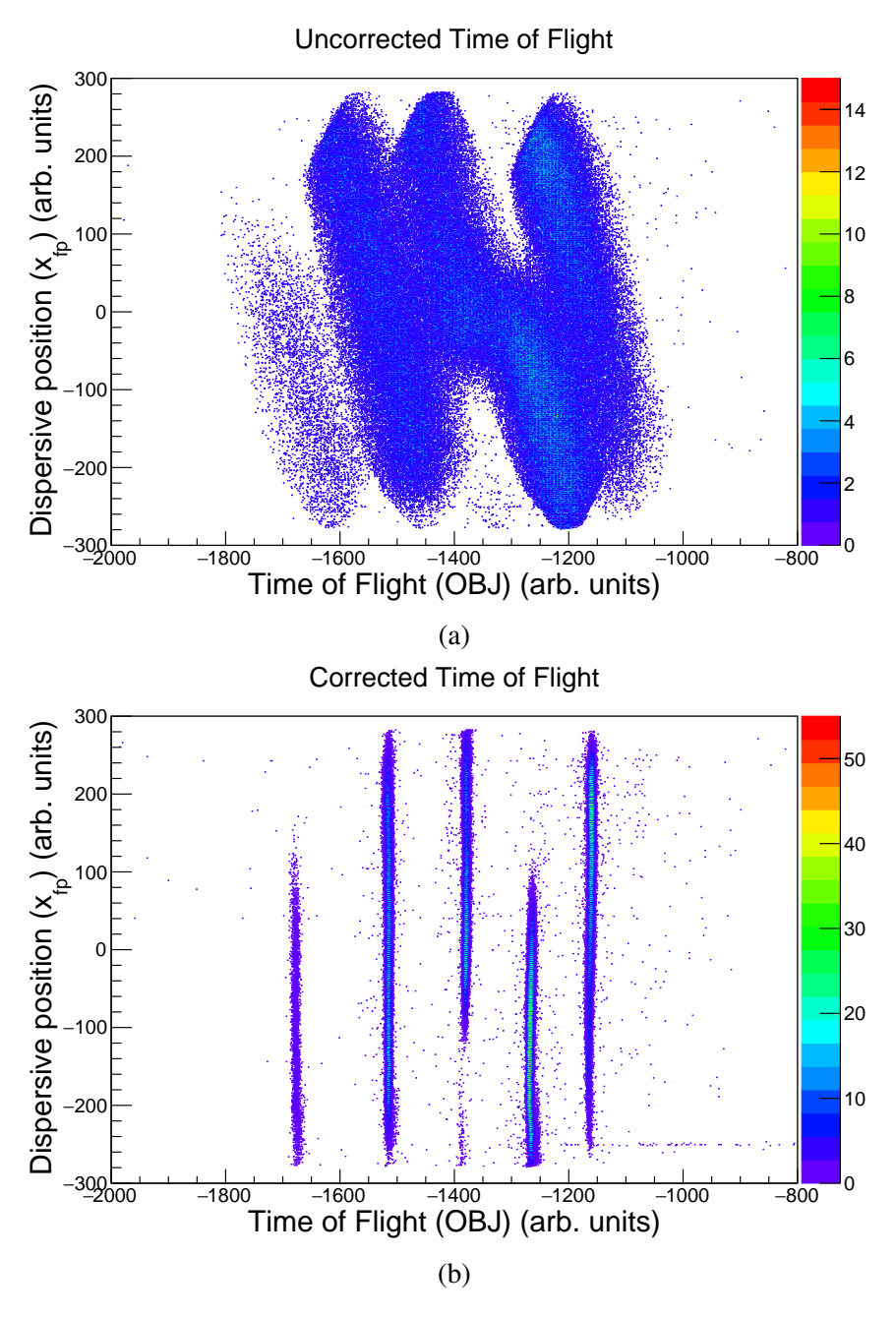


Figure 3.7: Uncorrected (a) and corrected (b) histograms are shown for dispersive position in the focal plane (y axis) vs the time-of-flight (TOF) measurement difference between the S800 Object and E1 scintillators (x axis). The corrected histogram show that the TOF and position are independent of one another, compared to the uncorrected histogram showing a correlation between position and TOF.

3.4.3 Ion Chamber

As shown in Fig. 3.8, the ion chamber in the S800 focal plane is located downstream of the two CRDCs and serves to distinguish between different recoil nuclei based on their atomic number Z. This is accomplished by measuring the energy loss of the ion through a gaseous medium composed of 90% argone and 10% methane, where the energy loss of the ion can be characterized by the Bethe-Bloch formula [96, 97],

$$-\frac{dE}{dx} = \frac{4\pi e^4 Z_p^2}{m_0 v_p^2} NB(v_p)$$
 (3.10)

where Z_p is the atomic number of the projectile (i.e. ion), e is the electron charge, m_0 is the electron mass, v_p is the velocity of the projectile, N is the number density of the absorption material, and $B(v_p)$ is a function of the projectile's velocity and the ionization properties of the absorbing material. From this equation, one can see that the energy loss primarily depends on the atomic number the projectile.

The S800 focal plane ion chamber consists of sixteen individual sections arranged parallel to each other and perpendicular to the beam axis. Averaging across the sixteen chambers minimizes statistical fluctuations that would occur if only a single chamber were used. To properly differentiate between recoil nuclei using the energy loss information collected with the ion chamber, two calibration procedures need to be performed:

- 1. Gain Matching: Assures that the energy-loss signals coming from each of the 16 ion chambers are equally weighted.
- 2. Position Correction: Assures that the energy-loss in the ion chamber is not position dependent.

3.4.3.1 Calibration and Corrections

The gain matching step is performed to equally weigh the 16 voltage signals produced by each sub ionization chamber. Each signal from the 16 different ionization chambers will be adjusted by slope

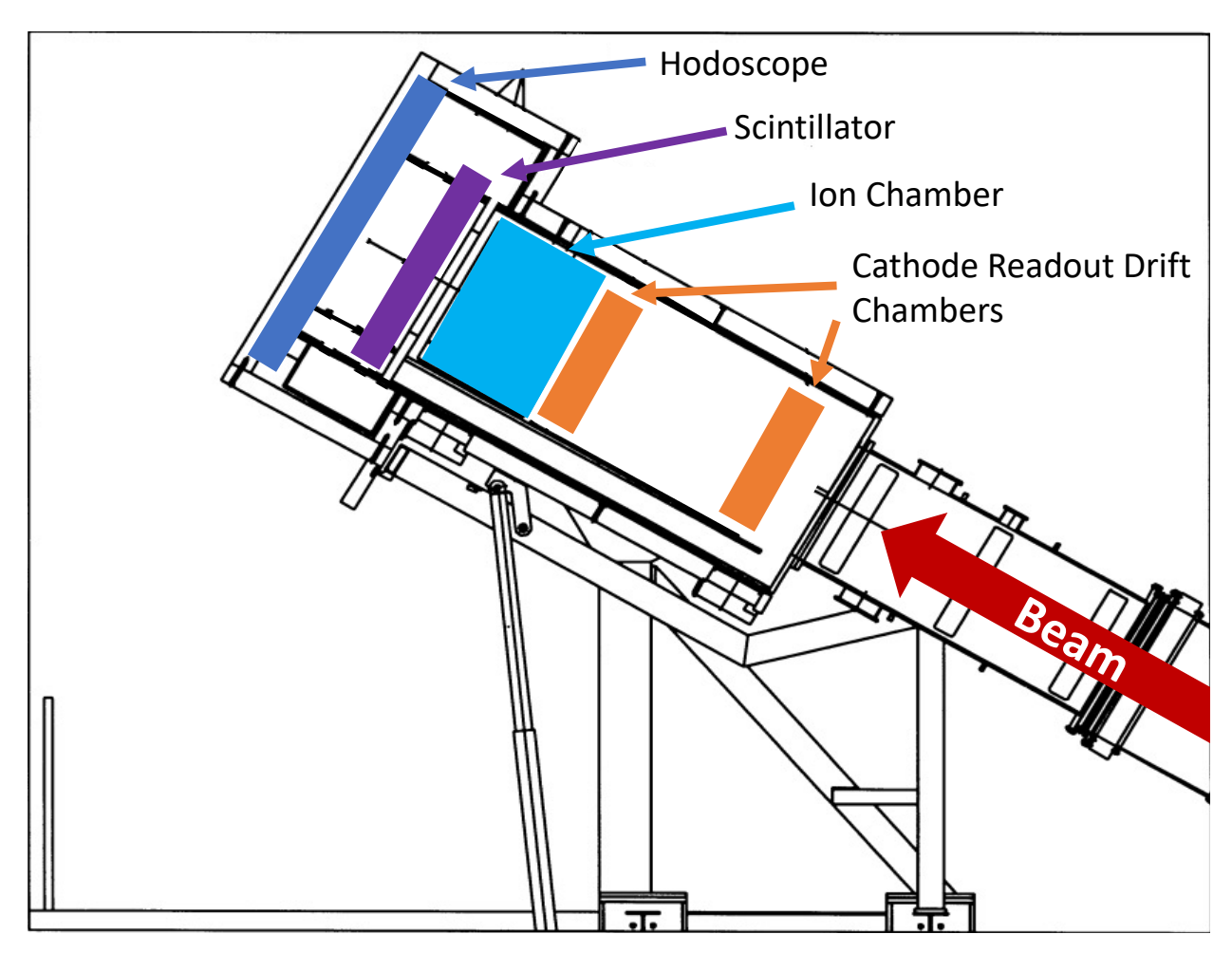


Figure 3.8: Schematic of the S800 spectrograph focal plane showing detectors used in this work. The figure was adapted from Ref. [101].

and offset parameters to reflect the gain of a selected reference signal. Three different reaction products were utilized to perform this calibration, where the mean energy loss is determined for each reaction product across the 16 different ionization chambers. An example of the fit energy loss signal for reaction products for ³¹Na from the fifth ion chamber can be seen in Fig. 3.9. Once this has been done, the mean energy loss for each reaction product is adjusted via slope and offset parameters to match the energy loss of a reference ionization chamber. For this analysis, the first ionization chamber (i.e. 0) was utilized as the reference ion chamber signal.

The next step in the calibration process corrects for any dependencies the energy loss may have on the ion's position in the dispersive plane. This feature is in part due to the ion's momentum

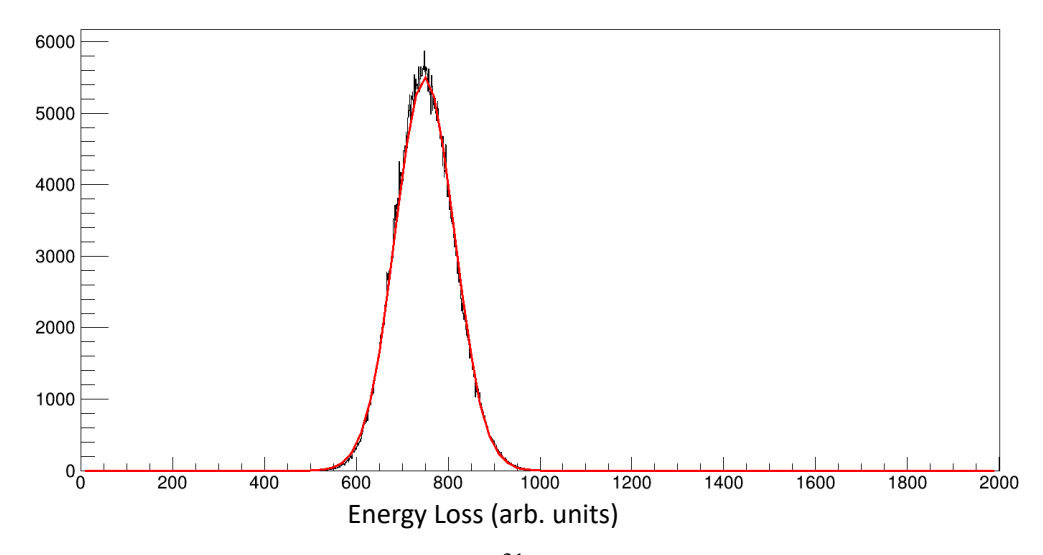


Figure 3.9: Ion chamber energy loss signal for ³¹Na from the fifth ion chamber fit with a Gaussian to determine the mean energy loss.

spread produced in the dispersive plane (x_{fp}) by dipole magnets of the S800. One can relate the momentum of an ion to the position it has in the dispersive plane, and using Eq. 3.10, conclude that the output of the ion chamber must be corrected to assure sensitivity only to the atomic number Z_p of the projectile. The first step is modeling the dependency the energy loss has on position. This is accomplished by fitting the following equation on an event-by-event basis to the average energy loss per x-bin,

$$dE_{\rm UC} = p_0 \cdot e^{-p_1 \cdot (p_2 - x)} \tag{3.11}$$

where $dE_{\rm UC}$ is the uncorrected energy loss, and p_0,p_1 , and p_2 are fitted parameters. An example of this can be seen in Fig. 3.10. Once a good fit is reached, the energy loss is de-trended with the following equation

$$dE_{\rm C} = dE_{\rm UC} \cdot e^{p_1 \cdot (p_2 - x)} \tag{3.12}$$

where $dE_{\rm C}$ is the corrected energy loss (i.e. de-trended), $dE_{\rm UC}$ is the uncorrected energy loss (i.e. position dependent), and p_1 and p_2 being the aforementioned fit parameters to the exponential model. An example of this can be seen in Figs. 3.11a and 3.11b.

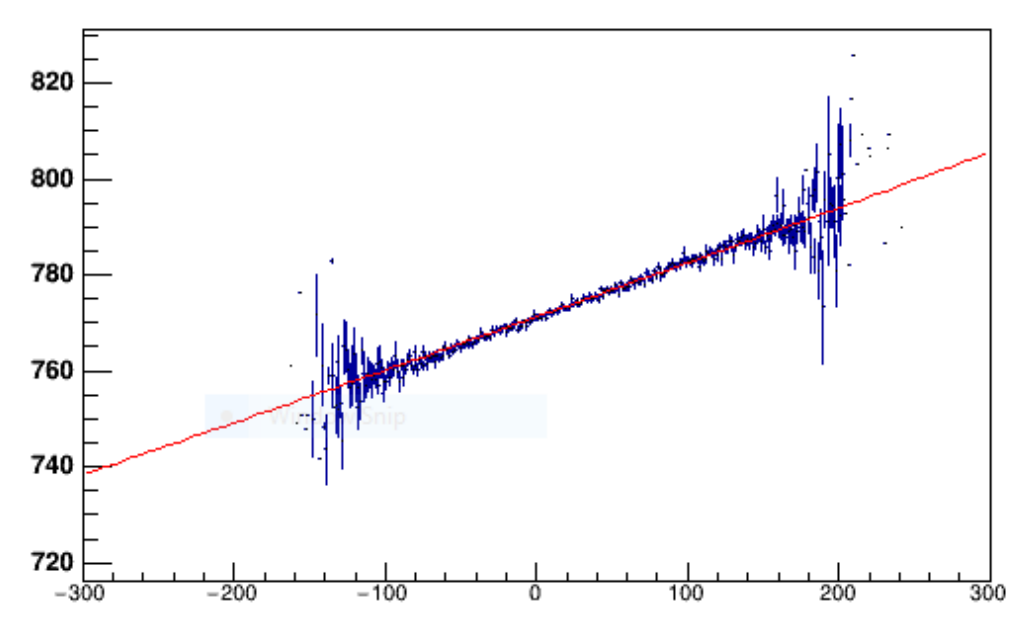


Figure 3.10: Fitted exponential model (red) to average energy loss per x-bin (blue) for 31 Na.

3.4.4 Cathode Readout Drift Chambers

To discuss how positional and angular information is determined for ions traversing through the S800 focal plane, and how this is crucial for the Doppler-reconstruction of gamma rays, we focus on the Cathode Readout Drift Chambers (CRDCs). Precise determination of the ion's trajectory at the reaction target location is critical for accurate Doppler correction of detected gamma-rays. In the laboratory frame, the observed gamma-ray energy is a function of both the emission angle relative to the velocity vector of the recoiling nucleus and the magnitude of the ion's velocity. As such, proper Doppler correction necessitates detailed knowledge of the gamma-ray interaction position within the detector array (i.e. GRETINA), as well as an accurate reconstruction of the recoil nucleus's kinematic vector at the moment of gamma-ray emission.

Within the S800 focal plane, there are two CRDCs as is illustrated in Fig. 3.8. With the detector closest to the ion chamber called CRDC2 and CRDC1 being 1 meter upstream from CRDC2, together they are able to determine the position and angular spread of the ion in the focal plane. The CRDCs are filled with a gas mixture consisting of 80% CF_4 and 20% C_4H_{10} at a typical pressure of 40 torr. As ionizing radiation traverses the volume of the detector, the freed electrons drift

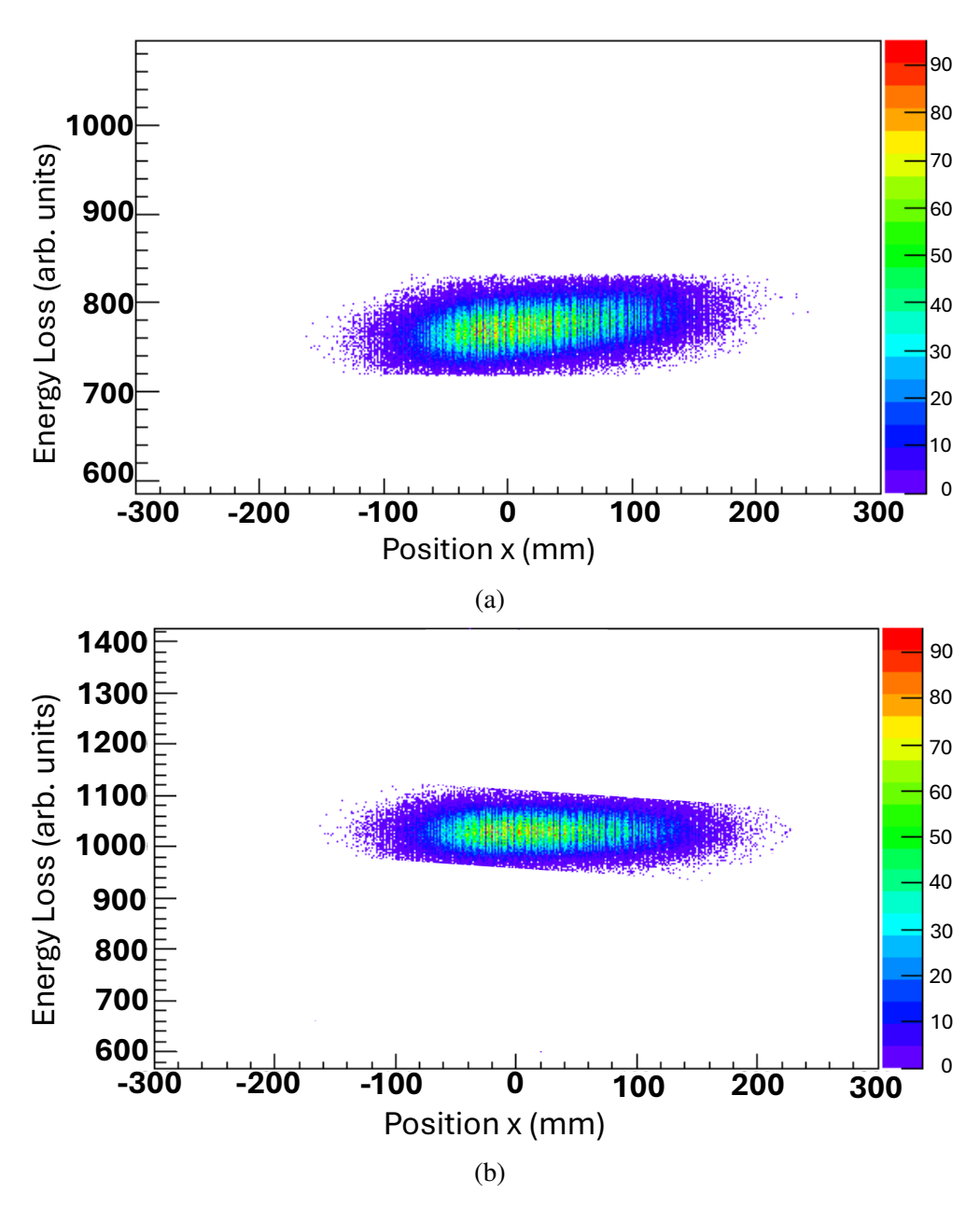


Figure 3.11: Uncorrected (a) and corrected (b) energy loss 2D histograms for ³¹Na. The energy loss is displayed along the y-axis and position along the dispersive plane is shown along the x-axis.

through the applied electric field towards an anode wire arranged along a series of 224 cathode pads. The cathode pads accumulate a positive charge in response to the electrons on the anode wire. The accumulated positive charge produces a distribution amongst the pads which is used to determine the x position of the ion in the focal plane (x_{fp}) . The y position in the focal plane (y_{fp}) is determined from the drift time of the electrons to the anode wire, which is measured relative to the

timing signal of the E1 scintillator. With (x,y) coordinates determined on both CRDCs, the ion's kinematic vector can be constructed providing the dispersive angle a_{fp} and non-dispersive b_{fp} with respect to the z-axis in the xz-plane and yz-plane, respectively. An illustration of a constructed kinematic vector can be seen in Fig. 3.12.

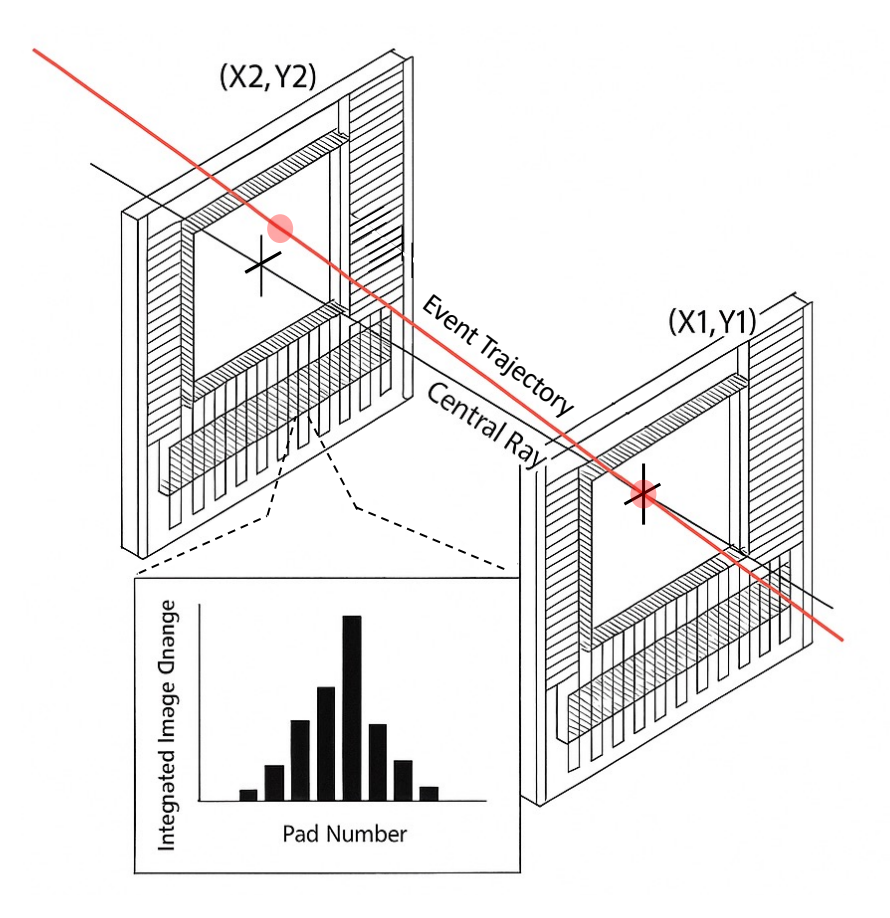


Figure 3.12: Illustration of an event crossing the Cathode Readout Drift Chambers (CRDCs). The two interaction points (X1,Y1) and (X2,Y2) determine the ion trajectory in the focal plane. In this image, the red line corresponds to the vector of an ion reconstructed from (X1,Y1) and (X2,Y2). The integrated image charge is produced by the accumulation of electrons on the anode wire, parallel to the 224 cathode pads. This figure is adapted from Ref. [102].

With the ion's trajectory determined in the focal plane, we can reconstruct the trajectory of the ion of interest at the target position. This is achieved by using the ion optics code COSY INFINITY [99] to produce a transfer matrix S which maps the ion's position at the target location to the position at the focal plane. With this definition of the transfer map, the inverse map S^{-1} transforms the focal plane parameters $(x_{fp}, y_{fp}, a_{fp}, b_{fp})$ to parameters at the target position $(d_{ta}, y_{ta}, a_{ta}, b_{ta})$. Note,

the x_{fp} parameter is used to determine the kinetic energy of the ion (d_{ta}) due to the dipole magnets bending the ions in the *x*-direction.

3.4.4.1 Calibration and Corrections

We now discuss the pad calibration procedure applied to the CRDCs. To make sure that all of the pads were weighted equally, the voltage gain and offset of each pad were be matched to one another. Three different isotope species are used to perform this gain matching process. A reference pad located at the center of the distribution is selected to serve as a reference pad. An example of a CRDC before and after applying this calibration procedure is presented in Fig. 3.13a and Fig. 3.13b for the ³¹Na isotope. Additionally, a mask calibration procedure is done to properly relate the pad position of the two CRDCs to absolute positions. Two metal masks, each having holes with known positions, are placed in front of the beam. This produces a pattern in the CRDCs which are linearly calibrated. In addition to the calibrations, run-by-run corrections must be performed to account for the pressure fluctuations within the two CRDCs. Two corrections are applied:

- 1. CRDC *y*-position correction that centers the beam distribution along the *y* axis to approximately to zero.
- 2. Corrections to the a_{ta} and b_{ta} distributions to center the angular distributions on zero.

The correction to the y-position must be performed first, followed by adjustments to the a_{ta} and b_{ta} distributions. As stated earlier, accurately reconstructing the ion's trajectory at the target location is essential to properly Doppler-correct in-beam gamma rays. Given that the drift time of an electron is inversely proportional to the gas pressure, it is important to account for pressure fluctuations and straggling during the experiment. With improved y-position information, the inverse map S^{-1} reconstructs more accurate target parameters, including a_{ta} and b_{ta} , both of which are expected to centered about zero. While correcting for the fluctuations in the y position improves the angular distributions, it does not guarantee that the a_{ta} and b_{ta} distributions are centered on zero. These secondary corrections are essential for achieving optimal angular resolution, as the

gamma-ray emission angle is reconstructed relative to the particle trajectory consisting of both dispersive and non-dispersive angles.

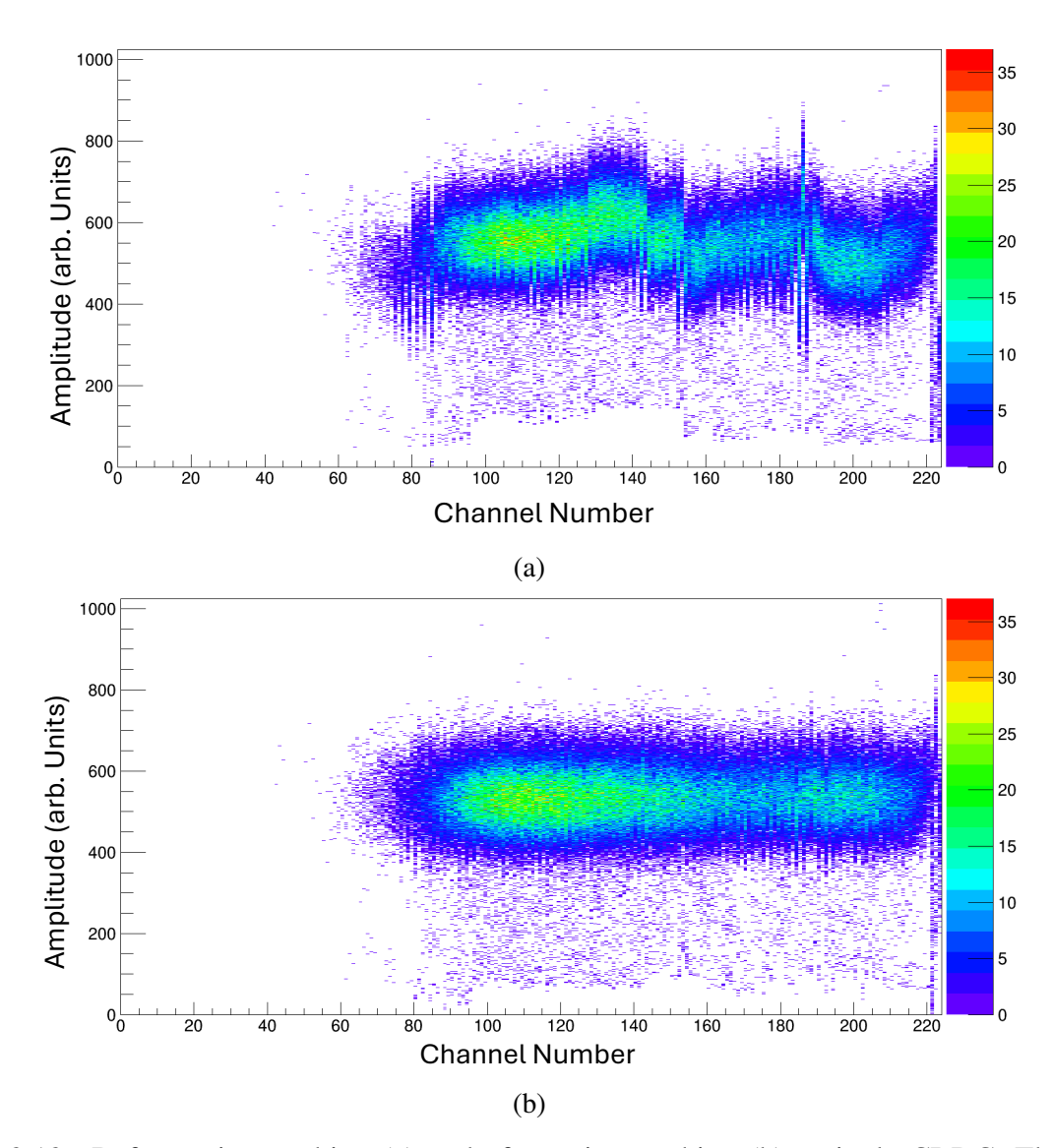


Figure 3.13: Before gain matching (a) and after gain matching (b) a single CRDC. The beam distribution shown corresponds the 31 Na secondary beam. The *x*-axis corresponds to the 224 pads in the CRDC. The gain matching illustrates the importance in assuring that all pads in a single CRDC are weighted equally.

3.5 Gamma-Ray Energy Tracking In-Beam Nuclear Array (GRETINA)

Gamma rays emitted from recoiling nuclei in this experiment were detected using the Gamma-Ray Energy Tracking In-Beam Nuclear Array (GRETINA) [38]. At the time, GRETINA was consid-

ered a state-of-the-art detector for gamma-ray spectroscopy, owing to its capability to precisely reconstruct the path of individual gamma rays within the detector volume. Its highly segmented HPGe crystal design provided not only excellent energy resolution but also enhanced position sensitivity. This capability provided a significant advantage for in-beam experiments, where precise position information is essential for accurate Doppler reconstruction of gamma rays emitted from fast-moving recoiling nuclei. In this work, GRETINA comprised eleven detector modules: four positioned in the 58° ring and seven in the 90° ring. The following sections detail the mechanical design of the GRETINA detector and provide an overview of the signal decomposition algorithm employed.

3.5.1 GRETINA Design

The GRETINA detector frame consists of two solid Aluminum spheres, each providing ten detector module slots. A total of 22 detector module slots are available for use, with the additional two slots being formed once the hemispheres are connected to each other. The 1π solid angle coverage provided by the current geometrical design of GRETINA is motivated by the full 4π coverage to be provided by GRETA. Within each detector module of GRETINA sit four n-type HPGe crystals. Each crystal has a hexagonal face pointed towards the center of GRETINA, known as the front face, with two crystal geometries denoted by A and B as seen in Fig. 3.14b. A photograph of one half of GRETINA, showing the front faces of the detector modules, is presented in Fig. 3.14a. Each crystal comprises 36 electrically separated segments (Fig. 3.14c), with a bore through the center serving as the central contact extending from the back face of the crystal to 15 mm from the front face. The central contact serves to collect all of the energy deposited in all of the segments [37]. The segmentation of the HPGe crystals, along with the signal decomposition algorithm that will be discussed in the next section, provide a position resolution of about 2 mm.

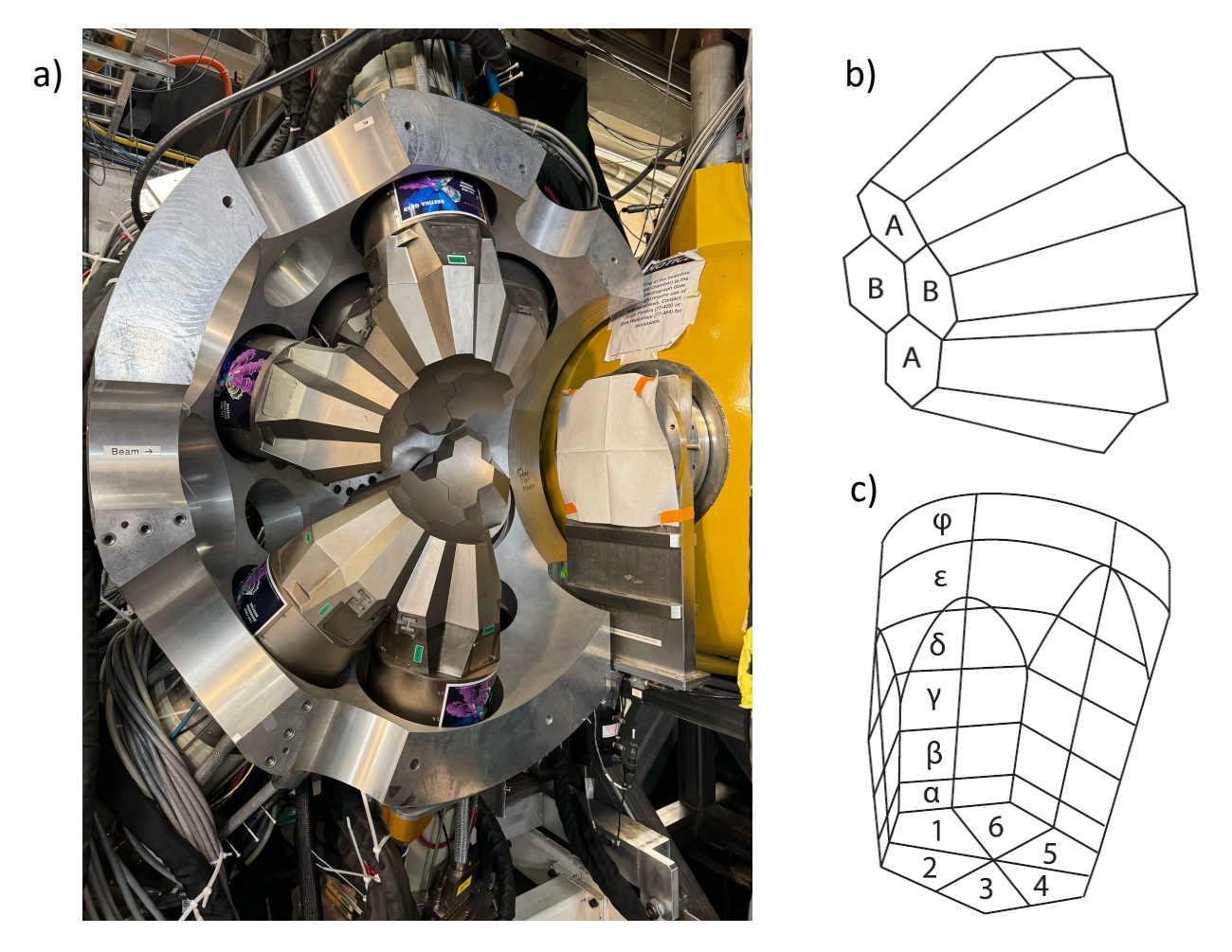


Figure 3.14: The Gamma-Ray Energy Tracking In-Beam Nuclear Array (GRETINA) [38]. Panel a) shows a photo of an open GRETINA from a prior experiment, illustrating the mounting of the detector modules on one of the hemispheres. The front faces of the detector modules are visible in this picture. The four *n*-type HPGe crystals within a detector module are shown in panel b) [38], with the A-type and B-type tapered hexagonal shapes labeled. The 36-fold segmentation of an individual crystal is shown in panel c) [38].

3.5.2 GRETINA Principle of Operation

In this section, we will briefly outline the principle of operation of GRETINA. When an incoming gamma ray interacts with the crystal material in the active detector volume, a signal is produced. This signal is a result of electron-hole pairs produced within the depletion region of the crystal, in which the depletion region is proportional to the square root of the applied reverse bias (i.e. voltage) V and inversely proportional to the square root of the number of impurities N in the crystal [96].

The disassociated electrons drift towards the anode, whereas the positively-charged holes "drift" towards the cathodes. Additionally, an image charge signal is generated in the neighboring segments in which the interaction occurred. A single gamma ray may interact multiple times in a crystal segment through means of Compton scattering, and if the gamma ray is energetic enough, it may undergo pair production, before undergoing the photo-absorption process. Each interaction point in a crystal segment produces a signal, where the signal shape is sensitive to the position of the interaction point. The individual interaction signal is measured by the electrode on the segment, whereas the signal measured by the central contact is a superposition of the various interaction point signals. Both the interaction signal and image-charge signal serve to provide position information of a single interaction point. The rise time of a segment signal, along with that of the central contact signal, provide the radial coordinate of interaction point. The shape and amplitude of the induced image-charge in neighboring segments provide the depth and polar angle of the interaction point.

As mentioned prior, a single gamma ray may interact several times within a single crystal segment. The signal decomposition algorithm used by GRETINA analyzes digitized signals from both the segmented electrodes and the central contact to reconstruct the position of each gamma-ray interaction. This is achieved by comparing the measured waveforms to a library of precomputed simulated signals, each representing the detector's response to a gamma-ray interaction at a specific location within the segment. By identifying the best match between the measured and simulated waveforms, the algorithm determines the most likely interaction point. This process effectively decomposes the observed signal into contributions from discrete, known positions within the detector volume.

3.5.3 Calibration Procedures

In experiments that utilize a gamma-ray spectrometer, there are two main calibration procedures performed for the detector: Energy Calibration and Efficiency Calibration. We will discuss these two calibrations as they pertain to this experiment, beginning with the former. For this experiment, the energy calibration procedure ensured that the digitized signals from the central contacts of

GRETINA are properly associated with the true incident energy of the gamma ray. This typically entails using a radioactive source with well-known energies to generate a linear relationship between the detected peak in GRETINA to the correct energy.

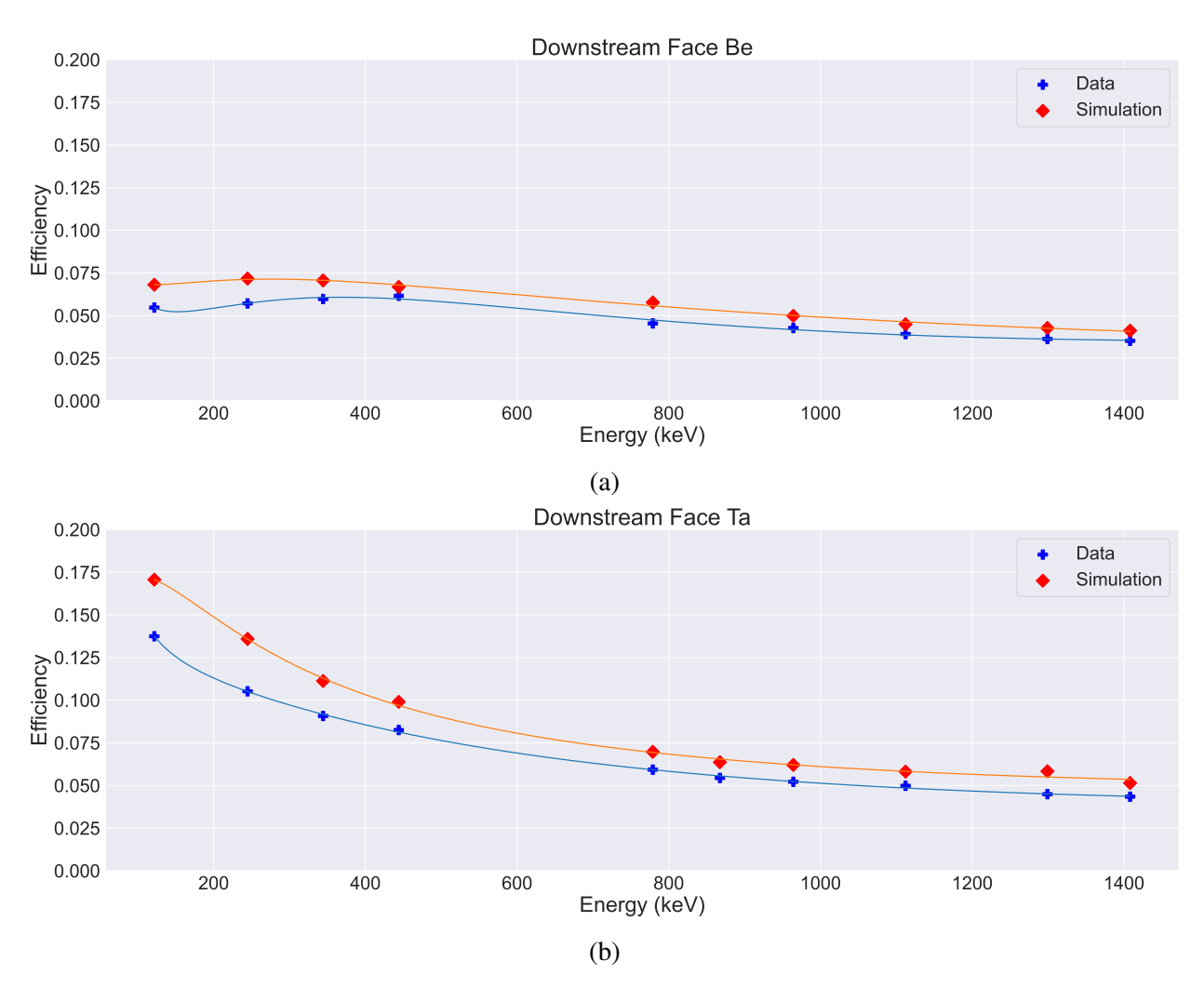


Figure 3.15: The efficiency of GRETINA measured in the laboratory frame placing a ¹⁵²Eu source on the downstream face of the Be foil (a) and on the downstream face of the Ta foil (b). In both curves the experimental data is in blue and the simulated data is in orange.

The efficiency calibration, shown in Figs. 3.15a and 3.15b, serves to properly account for the probability of detecting a full-energy-peak for a gamma ray as a function of energy. The efficiency of an in-beam gamma ray ($\epsilon_{\rm IB}^{\rm exp}$) was deduced by scaling the simulated in-beam efficiency ($\epsilon_{\rm IB}^{\rm sim.}$) at a particular gamma-ray energy by the efficiency ratio between experimental and simulated data ($\epsilon_{\rm Lab}^{\rm exp}/\epsilon_{\rm Lab}^{\rm sim}$) in the laboratory frame. This was achieved by placing a ¹⁵²Eu source on the upstream

and downstream faces of the Be and Ta foils. Two efficiency calculations were performed to study the detection efficiency of gamma rays produced from either the Be or Ta foil. The ¹⁵²Eu source was separately placed on the downstream faces of the Be and Ta foils resulting in the curves presented in Figs. 3.15a and 3.15b.

The efficiency curves obtained from the 152 Eu source were compared to a GEANT4 simulation in Figs. 3.15a and 3.15b. The simulated curves overestimated the experimental curves and had to be scaled down to agree with experimental data. The $\epsilon_{\rm Lab}^{\rm exp}/\epsilon_{\rm Lab}^{\rm sim}$ ratios were found to be approximately 0.84 and 0.82 for the Be and Ta foils, respectively. It is also worth noting the efficiency measured from the Be foil position is lower than that of the Ta foil position even at gamma-ray energies above 1 MeV where effects due to gamma-ray attenuation are marginal. This can be explained by the decrease in detection efficiency the further upstream the target foil is moved. The Ta foil is approximately 130 mm upstream of the center of GRETINA, whereas the Be foil is approximately 155 mm upstream. Notably, the drop in efficiency in the 100-400 keV range in the Be curve is a result of attenuation from the Ta foil positioned between the source and the detectors.

3.6 TRIple PLunger for EXotic beams (TRIPLEX)

The TRIple PLunger for EXotic beams (TRIPLEX) [90] was employed to hold a ⁹Be (target) and ¹⁸¹Ta (degrader) foil. The TRIPLEX device is a modified version of the traditional single-plunger device, able to accommodate up to three metal foils—specifically, a target and two degraders. This capability extends the accessible lifetime range to include excited states within 1 ps to 1 ns [90, 103]. It is important to note that for this experiment this capability was not used. The target was kept at a fixed distance of 25 mm upstream of the degrader foil, which guaranteed the decay of any excited state before reaching the Ta foil. In this section, we will provide general overview of the TRIPLEX device with respect to its use in this experiment.

The TRIPLEX device consists of three main components: the support structure, the bearing unit, and the foil system. The bearing unit is composed of three concentric tubes—inner, middle, and outer—each mechanically decoupled via four low-friction sliding bearings. The central (middle)



Figure 3.16: A picture of the TRIPLEX device. This figure is adapted from Ref. [90].

tube remains stationary and supports all immobile components, including electrical connectors, micrometers, and the external housing. Precision motors, mounted on this central tube, are connected by wires to the inner and outer tubes to drive their motion with minimal stress on the bearings. These movable tubes allow precise adjustment of the distances between the target and degrader foils, which are mounted at the ends of each tube on dedicated conical frames secured by small screws and springs. The target is mounted on the innermost tube, the first degrader on the central tube, and the second degrader on the outermost tube. The dynamic range for foil separation ranges from 0 mm to 25 mm.

In the foil system, each foil is mounted on a conical brass frame connected to its respective tube ring, with spring-loaded screws enabling precise compression and alignment. The target and first-degrader foils face each other directly. The second-degrader cone is uniquely shaped—narrow and extended—so that it can slide into the first-degrader cone, enabling the second-degrader foil to approach and even make contact with the first degrader. This requires the second-degrader foil to be circular in shape, while the target and first-degrader foils are typically square. The inner diameter of the second-degrader cone is about 4.6 cm, which is sufficient to allow the full radioactive beam to pass through without obstruction.

The support structure consists of housing the TRIPLEX device within a custom-designed beam pipe. This beam pipe is wider than the standard GRETINA pipe, allowing the entire TRIPLEX

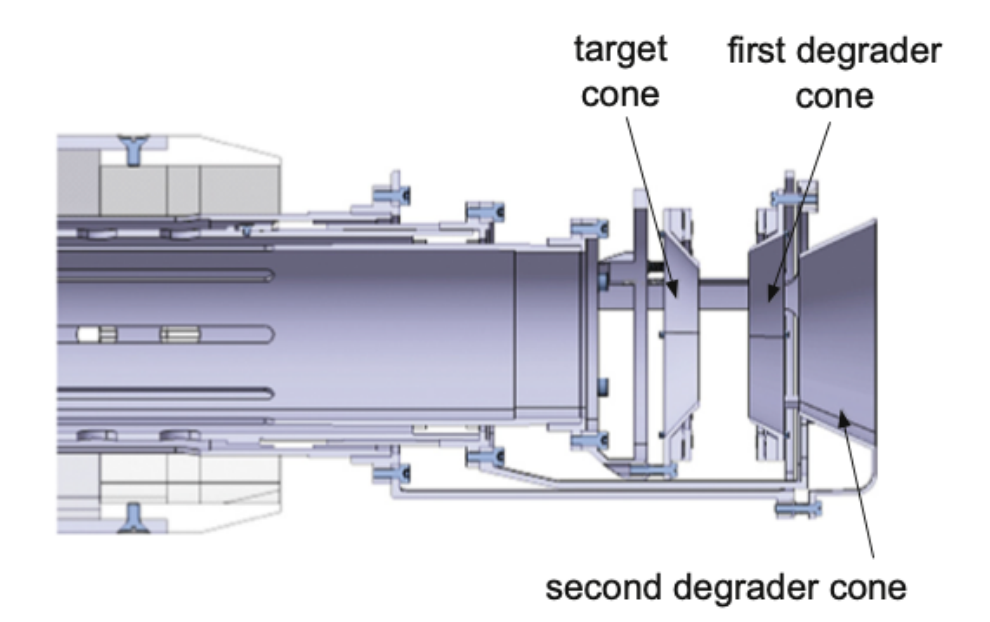


Figure 3.17: Illustration of the TRIple PLunger for EXotic beams (TRIPLEX) [90] device. The device can accommodate up to three foils, with adjustable separation distances ranging from 0 mm to 25 mm between the target and first degrader, as well as between the first and second degraders. In this illustration, the incoming beam enters from the left and interacts with the target material before interacting with the first and second degraders. For this experiment, the TRIPLEX device held a 2-mm-thick ⁹Be foil on the target cone and a 1.3-mm-thick ¹⁸¹Ta foil on the first degrader cone. This figure was adapted from Ref. [90].

assembly to be positioned internally. Rough alignment of the beam pipe is achieved via a flange attached to the downstream end of an S800 spectrograph magnet, while fine alignment is performed using adjusting screws that connect the plunger to the beam pipe itself. Electronic feedthroughs at the upstream end of the pipe link the motors and conductance wires to external control electronics while preserving vacuum integrity. When fully installed, the plunger foils rest approximately 13 cm upstream of GRETINA's geometric center.

3.7 Experimental Setup

To summarize this chapter, this section will provide a distilled description of the experimental set up and pertinent information regarding the inelastic scattering of ^{30,31}Na on a ⁹Be and ¹⁸¹Ta foil. The experiment took place at the Coupled Cyclotron Facility (Sect. 3.2) utilizing the A1900 fragment

separator (Sect. 3.3.1). The setup up was comprised of GRETINA (Sect. 3.5), the TRIPLEX device (Sect. 3.6), and the S800 Spectrograph (Sect. 3.4). A fully stripped ⁴⁸Ca⁺²⁰ primary beam was accelerated to 140 MeV/u and directed onto a ⁹Be production target. The resulting projectile fragments were separated in the A1900 fragment separator by means of their magnetic rigidity. The secondary beam components were identified by means of time-of-flight measurements between two scintillators positioned along the beam line, resulting in purities of ~24% for ³⁰Na and ~18% for ³¹Na. The average incoming beam energies of ³⁰Na and ³¹Na into the plunger device were 113 MeV/u and 106 MeV/u, respectively. Other pertinent beam constituents, such as ³²Mg and ²⁹Ne, each had a beam purity of ~24%, in which investigations of these neutron-rich nuclei were published by Revel *et al.* [76]. All of the reaction products were then delivered to the target location of the S800 spectrograph. To account for the angular acceptance of the S800, the spatial and angular distributions of ³¹Na were analyzed, leading to corrections being applied to both the incoming beam and the reaction products.

At the target position, the TRIPLEX device was employed to facilitate a two-foil inelastic scattering measurement, positioned 13 cm upstream of GRETINA's geometric center to optimize both the detection efficiency of forward-focused gamma rays, and the sensitivity to different recoil velocities. Only one data set was obtained, which consisted of the TRIPLEX device simultaneously holding a 370-mg/cm² ⁹Be foil and a 2158-mg/cm² ¹⁸¹Ta foil separated by 25 mm. This configuration enabled the clear separation in the Doppler-corrected gamma-ray spectrum between reactions originating from each foil. Recoiling nuclei were identified in the S800 Spectrograph using TOF and energy-loss measurements, with those retaining their identity attributed to inelastic scattering. At the center of the Be foil, the average beam energies were 109 MeV/u for ³⁰Na and 102 MeV/u for ³¹Na, while for the Ta foil the corresponding energies were reduced to 88 MeV/u and 81 MeV/u, respectively. The simultaneous use of two foils under identical experimental conditions significantly reduced uncertainties in separating Coulomb and nuclear contributions to the excitation of low-lying states, while also increasing statistics by eliminating the need to change targets.

Gamma rays emitted by the excited nuclei were detected by GRETINA in coincidence with

outgoing particles identified by the S800 Spectrograph. Doppler-shift corrections were then applied on an event-by-event basis using θ_{γ} and the recoil velocity ($\beta = v/c$), resulting in accurately reconstructed in-beam γ -ray spectra. To properly deduce the amount of emitted gamma rays, an in-beam efficiency calibration was performed, which consisted of utilizing a 152 Eu source in conjunction with a GEANT4 simulation. Similarly, the GEANT4 simulation is typically calibrated by data obtained in an unreacted beam setting, which entails not placing any reaction foils at the target location. However, the incoming beam energies of 30,31 Na precluded the use of an unreacted beam setting, as their magnetic rigidities exceeded the 4 Tm limit of the S800 spectrograph. Instead, the inelastic scattering data was used to estimate the incoming beam profile.

CHAPTER 4

EXTRACTION OF B(E2↑) FOR LOW-LYING STATES IN ^{30,31}**Na**

The extraction of the reduced transition strengths to the low-lying excited states in 30,31 Na enabled a richer understanding of the collective phenomenon in the N=20 region. This feat was facilitated by the various software tools at our disposal, in addition to the careful analysis that was performed. To this end, this chapter will describe the software tools utilized (Sect. 4.1), codes used to perform coupled-channel calculations (Sect. 4.2), and the various steps taken in this analysis. The latter entails describing the angular acceptance analysis to properly account for the incoming beam profile (Sect. 4.3), benchmark analysis with the well-characterized 32 Mg (Sect. 4.4), understanding and quantifying background contributions (Sect. 4.5), and ultimately the work undertaken to obtain the $B(E2\uparrow)$ strengths from 30 Na (Sect. 4.6) and 31 Na (Sect. 4.7).

4.1 Data Analysis Tools

4.1.1 GrROOT Analysis Software

The offline analysis performed for data collected from this experiment utilized the GrROOT software package [104]. The GrROOT software package has been developed for the offline analysis of experiments conducted with the S800 spectrograph and GRETINA at FRIB. Data analysis using GrROOT proceeds in three sequential main steps:

- (GrR00T) Conversion of raw data collected by the FRIB data acquisition system to ROOT format.
- 2. (Calculate) Application of calibrations to the data.
- 3. (Cal_histos) Generation of pertinent histograms.

In the first step (GrR00T), the data unpacker extracts raw event data from binary files generated by FRIB's data acquisition system (DAQ) and converts them into a ROOT format. During this process,

the data are sorted into objects of type s800, gretina, and mode3event, without any calibrations or corrections applied. The second step (Calculate) applies calibrations and corrections to the ROOT files produced in the unpacking step by utilizing a user-provided settings file that contains the necessary calibration and correction information. This results in the creation of a calibrated ROOT file. Finally, the third step (Cal_histos) processes the calibrated data to generate user-defined histograms, enabling a meaningful physics analysis to be conducted. The first step is nominally executed once, whereas the second and third steps are often iterated as the experimenter develops a better understanding of the data. The flow chart of the analysis process with GrROOT is displayed in Fig. 4.1.

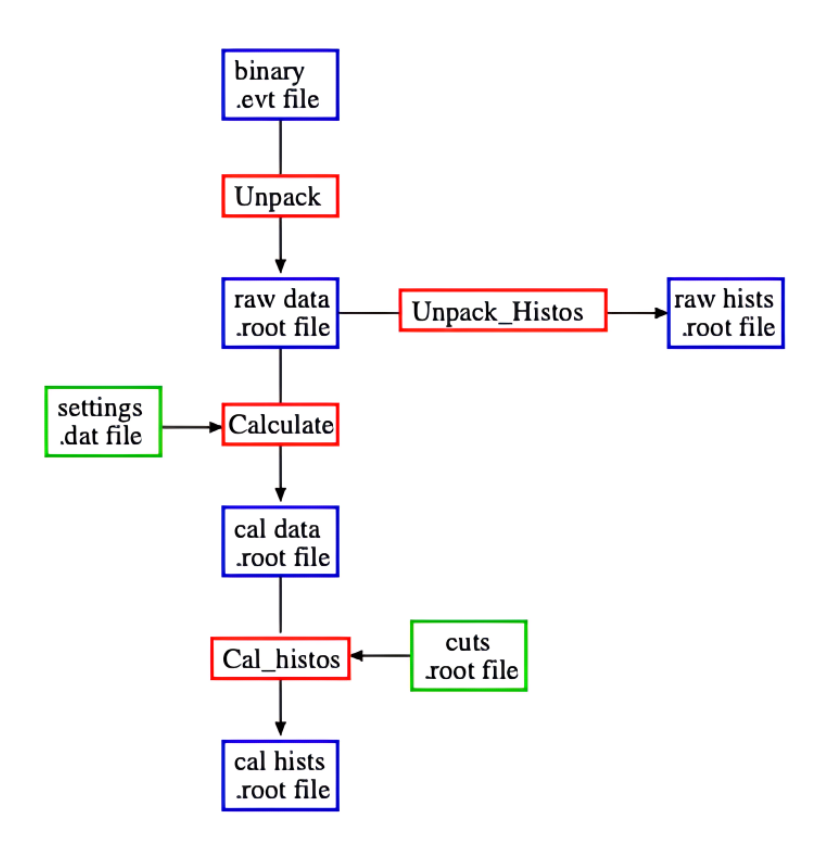


Figure 4.1: A flow chart displaying the analysis process with the GrROOT software package [104]. The red boxes are programs (e.g. Calculate) from GrROOT, blue boxes represent output (input) files generated (required) by the current (subsequent) program, and green boxes are auxiliary information files for the programs. This figure has been adapted from Ref. [105].

4.1.2 G4Lifetime Simulation Software

To understand the underlying physics presented in the unpacked experimental data, the simulation software G4Lifetime [106, 107] was employed. The simulations are based on the GEANT4 toolkit [108], developed for experiments with the TRIPLEX [90] device, which incorporate particle tracking through different mediums and particle interactions with matter. The produced G4Lifetime simulations incorporate the relevant properties of the experiment such as the incoming beam energy, reaction kinematics on different target materials, TRIPLEX device configuration, GRETINA's geometry configuration, and emission of particles and gamma rays. This section will describe the various facets necessitated for a G4Lifetime simulation, and how this software was utilized for this analysis.

4.1.2.1 G4Lifetime Calibration

The initial constraints defined in G4Lifetime pertain to the target materials and the TRIPLEX [90] device located along the beam line. The location of the TRIPLEX device is given by the first-degrader position relative to the center of GRETINA [37, 38]. The TRIPLEX device is able to facilitate the three following configurations:

- 1. Target only: Only target foil in the target position.
- 2. Standard Plunger: Target foil in the target position and degrader foil in the first-degrader position.
- 3. Differential Plunger: Target foil in the target position, degrader foil in the first-degrader position, and second-degrader foil in the second-degrader position.

The element and thickness of each target material is specified, with thicknesses determined from mass measurements of the corresponding foils. Once all target materials are provided, the separation distances between successive foils are defined. Pertaining to this experiment, the

TRIPLEX device utilized the Standard Plunger configuration, holding ⁹Be and ¹⁸¹Ta target foils separated by a distance of 25 mm.

The simulation is designed to model both the incoming secondary beam and the reaction products. Each incoming beam is characterized by specifying the kinetic energy per nucleon (KE/u), mass number (A), and proton number (Z). With the CRDCs located in the S800 focal plane, the measured quantities x_{fp} , y_{fp} , a_{fp} , and b_{fp} are used to reconstruct the corresponding d_{ta} , y_{ta} , a_{ta} , and b_{ta} distributions at the target position. The simulated beam spot, defined by its centroid coordinates (x_0, y_0) and spatial widths (σ_x, σ_y) , along with the angular distribution of the beam, are tuned to match the reconstructed variables y_{ta} , a_{ta} , and b_{ta} . In the absence of a reconstructed x_{ta} , it is assumed that $x_0 = y_0$ and $\sigma_x = \sigma_y$. Additionally, the simulated kinetic energy distribution of the ion (d_{ta}) is also matched to the experimental distribution. Ideally, the incoming beam parameters would be determined from an unreacted beam setting, that is, an experimental configuration without target material in the beam line. In this experiment, however, due to the incoming beam energies of the incoming secondary beam products resulting in a magnetic rigidity exceeding the 4 Tm limit of the S800 spectrograph, no unreacted beam setting was performed. Instead, the incoming beam parameters were deduced from the scattered ions due to the identity of the ion not changing in the reaction. A comparison between the reconstructed and simulated beam properties for ³⁰Na, ³¹Na, and ³²Mg are shown in Figs. 4.2, 4.3, and 4.4, respectively.

To describe the reaction products, the change in the number of protons and neutrons must be provided. Due to this work focusing on inelastically scattered ions, this quantity was set to zero. In order to characterize the beam properties of the reaction products, the simulation's reaction parameters must be adjusted to account for the changes in momentum in the ion from the scattering process. This is achieved by scaling the simulated momentum of each reaction according to the change in mass (zero for this work) and the parameter dp_frac, which specifies the velocity of the reaction product as a fractional amount of the incoming secondary beam velocity. To model the spread of the outgoing momentum, a vector $\Delta \vec{p}$ is sampled randomly from a Gaussian distribution, centered at dp with a width defined by dpFWHM, and added to the simulated momentum.

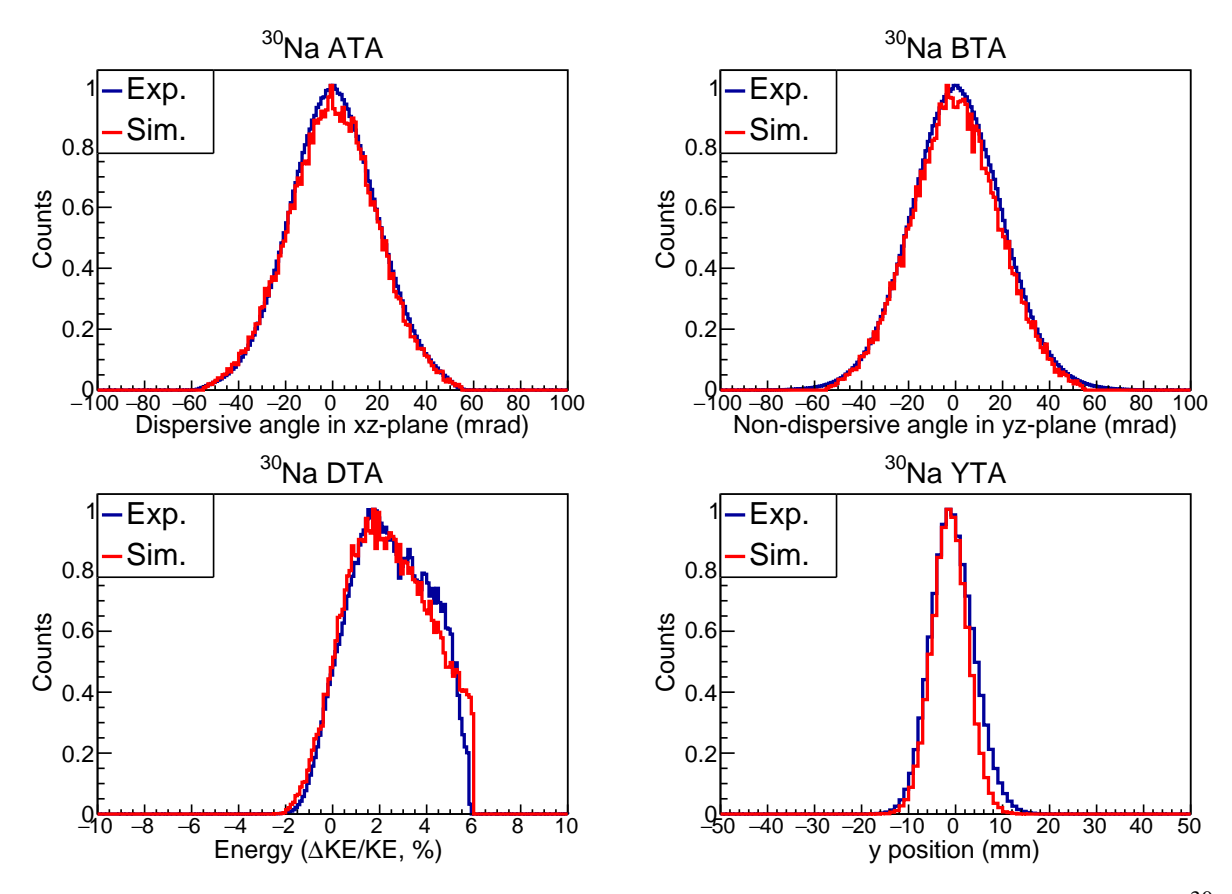


Figure 4.2: Comparison between experimental (blue) and simulated (red) beam properties for 30 Na. The dispersive angle in the xz plane a_{ta} (top left), non-dispersive angle in the yz plane b_{ta} (top right), kinetic energy distribution d_{ta} (bottom left), and position in the non-dispersive plane y_{ta} (bottom right) are shown. The simulated and experimental beam distributions have been scaled to unity.

Pragmatically, the dp parameter represents the magnitude of momentum change felt by the ion in its interaction with the target material. The dp_frac parameter primarily affects the centroid of the kinetic energy distribution (d_{ta}), while the shapes –specifically the width and tails – of the d_{ta} , y_{ta} , a_{ta} , and b_{ta} distributions are governed by dp and dpFWHM. Note, G4Lifetime requires one to define the interaction parameters on the target foil (dp_frac, dp, and dpFWHM) and those for the first-degrader foil (dp_fracR, dpR, and dpFWHMR). In principle, these parameters would be adjusted by independently comparing the measured distributions from each foil to corresponding simulations. In lieu of this procedure, both parameter sets are simultaneously adjusted to match the distributions reconstructed at the target location. This approach partly stems from the assumption

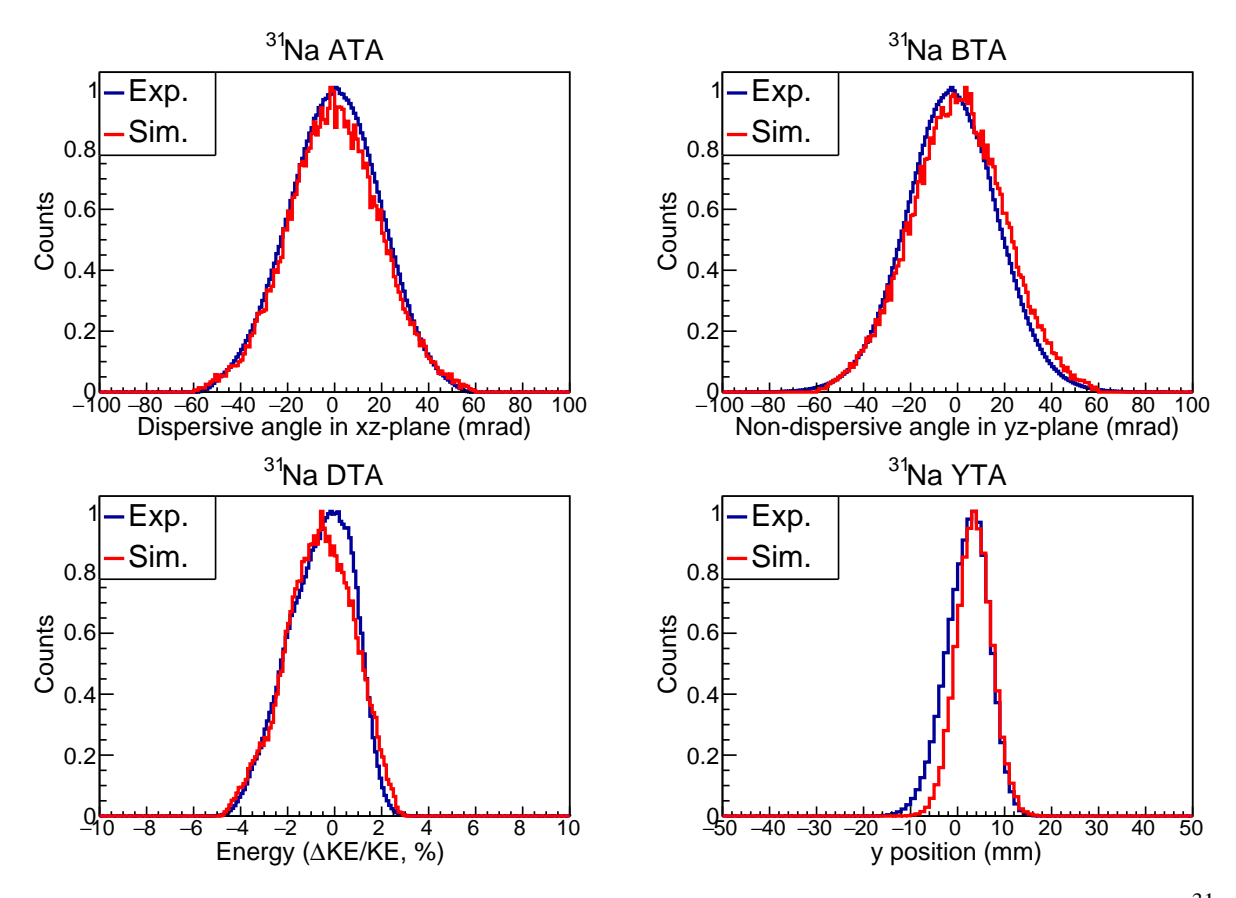


Figure 4.3: Comparison between experimental (blue) and simulated (red) beam properties for 31 Na. The dispersive angle in the xz plane a_{ta} (top left), non-dispersive angle in the yz plane b_{ta} (top right), kinetic energy distribution d_{ta} (bottom left), and position in the non-dispersive plane y_{ta} (bottom right) are shown. The simulated and experimental beam distributions have been scaled to unity.

that the kinematic interactions on both foils are similar. Both sets of parameters are adjusted to align the simulation with experimental data, as seen in Figs. 4.2, 4.3, and 4.4. The G4Lifetime simulation also accounts for the acceptance of the S800 spectrometer by constraining the edges of the simulated distributions. This acceptance effect is evident as a sharp cutoff in the d_{ta} distribution as shown in Fig. 4.2.

The GRETINA detector is also modeled in G4Lifetime, as illustrated in Fig. 4.5. This involves defining the geometry of the individual detector modules relative to the beam axis and the TRIPLEX device. The spatial configuration is given by a set of Euler angles, which for this experiment, correspond to four detector modules positioned in the 58° ring and seven in the 90°

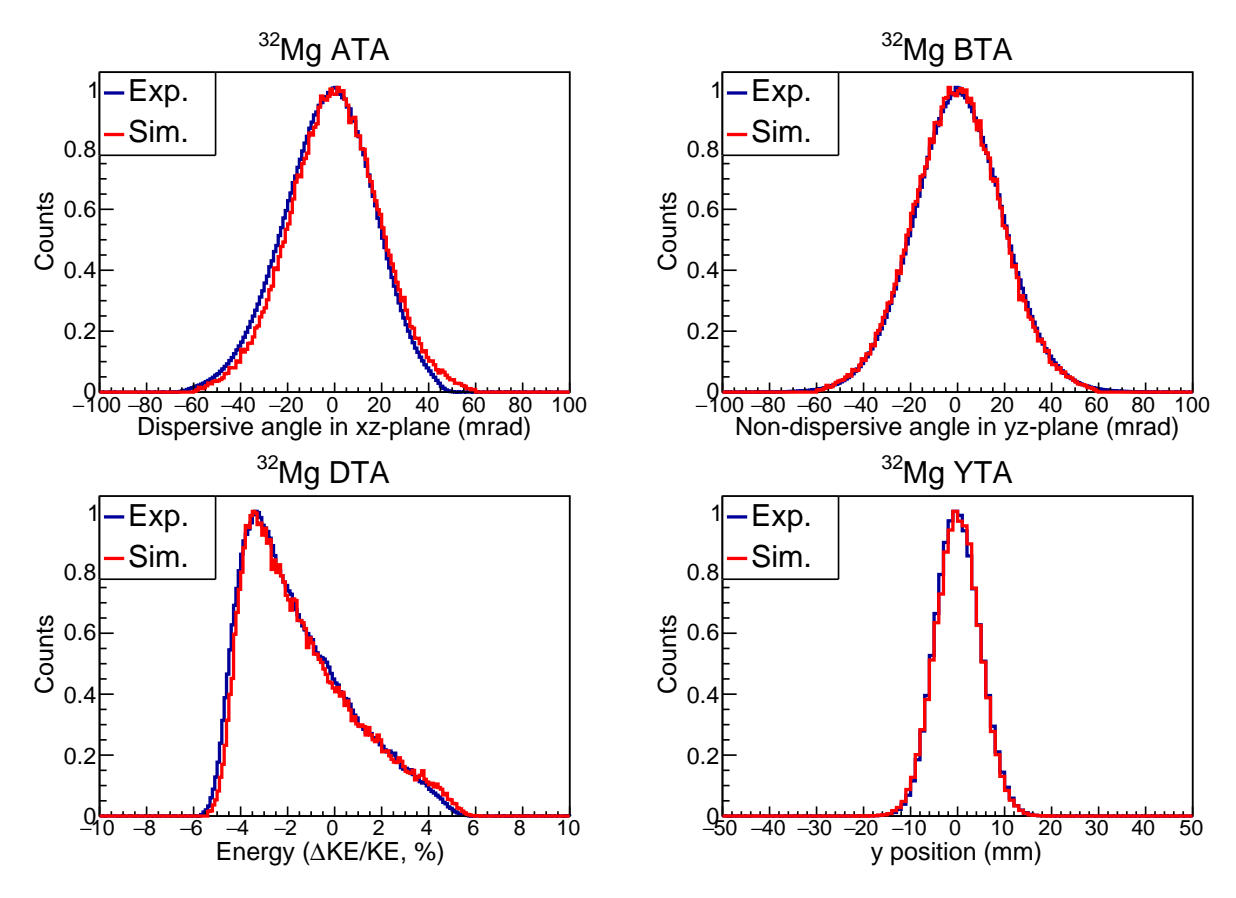


Figure 4.4: Comparison between experimental (blue) and simulated (red) beam properties for 32 Mg. The dispersive angle in the xz plane a_{ta} (top left), non-dispersive angle in the yz plane b_{ta} (top right), kinetic energy distribution d_{ta} (bottom left), and position in the non-dispersive plane y_{ta} (bottom right) are shown. The simulated and experimental beam distributions have been scaled to unity.

ring. The simulation allows for the deactivation of individual crystals, which was necessary for this analysis due to a crystal malfunctioning during the experiment. This can be seen in Fig. 4.6, where the red outlined hexagon displays the location of the disabled crystal. Furthermore, the simulated efficiencies are higher than the experimentally determined values, partly because not all materials between the ion and the GRETINA crystals are included in the simulation (see Figs. 3.15a and 3.15b), in addition to the factors discussed in Sect. 3.5.3. Regarding the Doppler correction, the emission angle of the gamma ray is determined from the ion's trajectory vector and the first interaction point in GRETINA, which is defined as the hit position with the largest energy deposition [37].

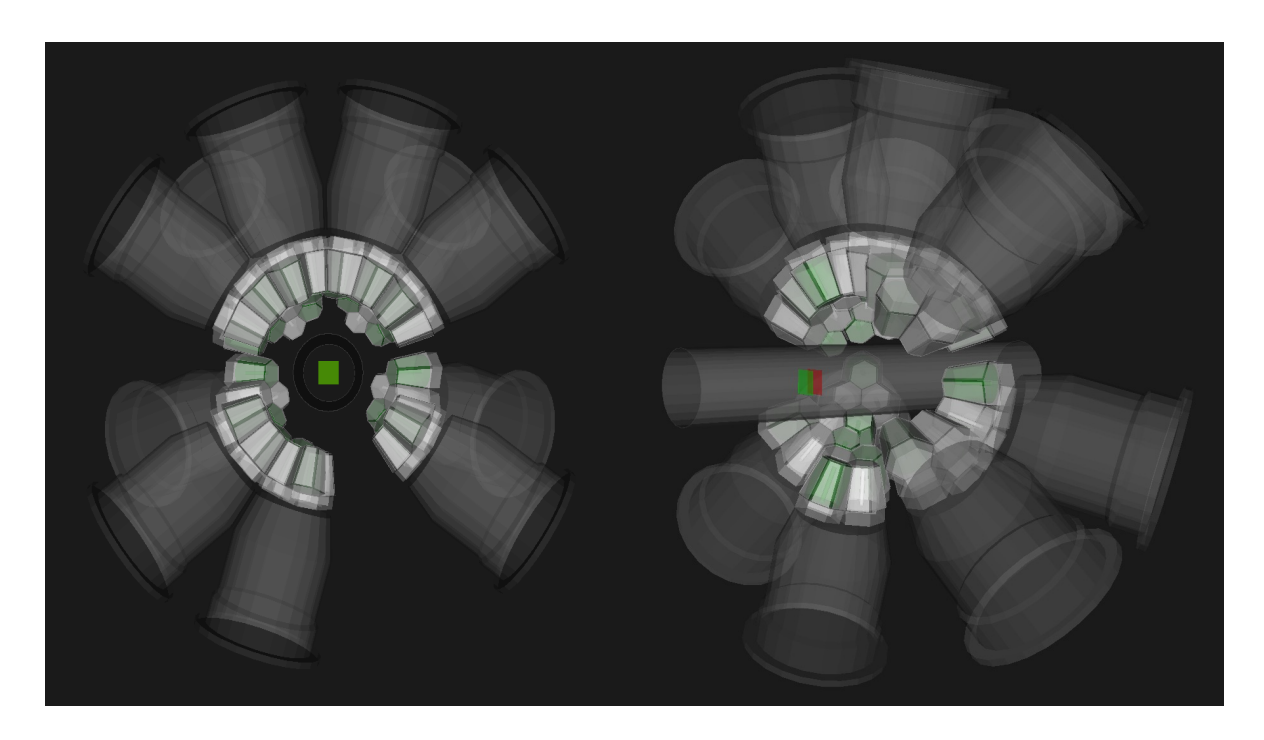


Figure 4.5: GEANT4 rendering of the GRETINA configuration used in this experiment. Liquid cryo-modules are shown in grey, while individual GRETINA crystals are depicted in white and green. The beryllium and tantalum targets are represented by green and red squares, respectively. Two views are provided: a downstream view (left) and an angled downstream view (right). The TRIPLEX device is omitted from the rendering.

The excited states of each nucleus are simulated by listing the state energy, the gamma-ray transition energy, lifetime of the excited state, and the fraction of reactions that populate the particular state. Each simulated event generates a single nucleus directed towards the target and degrader foils within the TRIPLEX device, where it experiences energy loss as it propagates through the foils. The emission of gamma rays from the excited nucleus is dictated by an exponential decay distribution based on the lifetime of the excited state. The photons are assumed to be emitted isotropically in the rest frame of the ion but are Lorentz-boosted (i.e. forward focused) in the laboratory frame due to the relativistic nature of the beam. Note, this assumption of isotropic emission of gamma rays is not necessarily true as there may be an asymmetry in the gamma-ray emission due to the underlying nuclear structure. The simulated gamma rays are then absorbed or scattered by the surrounding materials in the given volume, until they are detected by the emulated GRETINA.

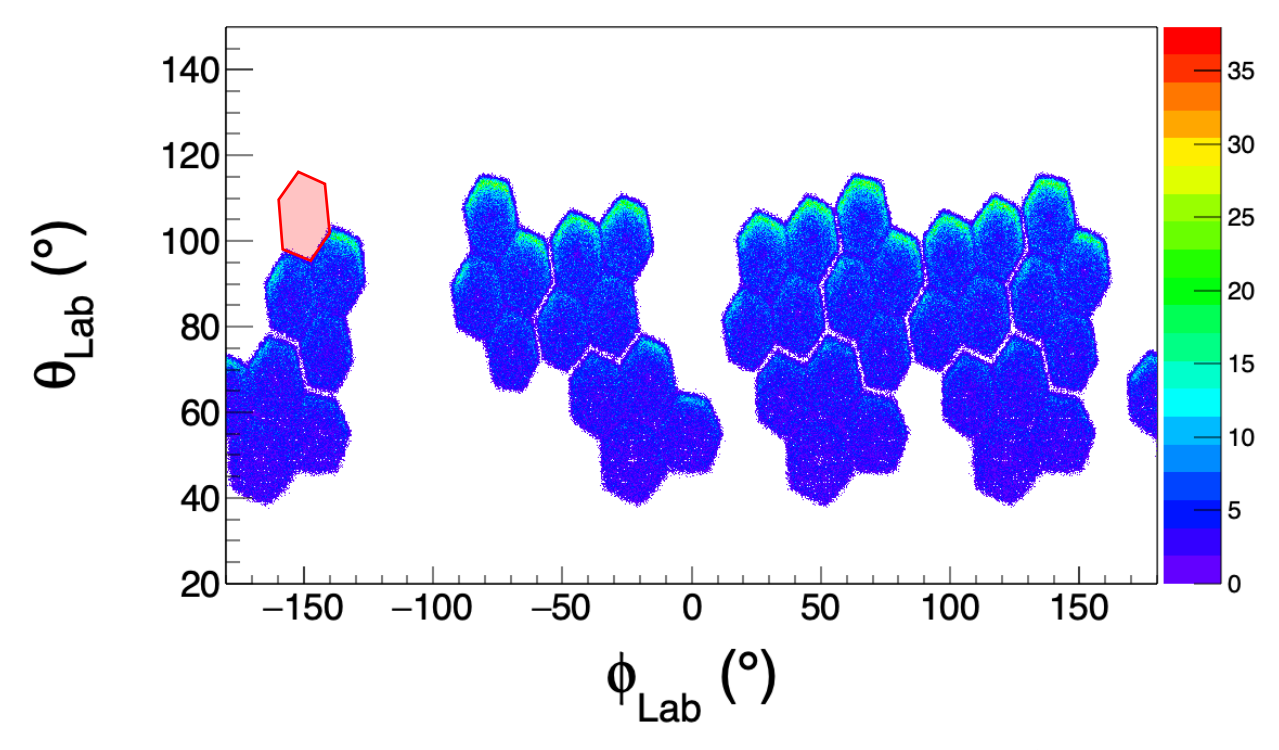


Figure 4.6: G4Lifetime simulation of the GRETINA detector response for a 152 Eu source placed on the downstream face of the tantalum target. Due to the TRIPLEX device being positioned 13 cm upstream from the center of GRETINA, the uppermost edges of the detector modules in the 90° ring exhibit an enhanced response to the incoming radiation. The red hexagon indicates the location of the disabled crystal. The laboratory-frame angles θ_{Lab} and ϕ_{Lab} are the polar and azimuthal angles, respectively.

4.2 Coupled-Channel Calculations

To extract reduced *E*2 transition strengths to the low-lying states in neutron-rich ³⁰Na and ³¹Na, coupled-channel calculations were performed using the general purpose reaction code FRESCO [78]. The reaction code is capable of modeling the Coulomb-nuclear interference that occurs as a result of the intermediate-energy heavy-ion inelastic scattering process. The calculations entail producing differential cross sections for each reaction channel (i.e. particular states of excitation for each of the two nuclei involved in the collision) specified in the input file. This section will describe how FRESCO was used in this analysis, the optical models that were employed to describe the inelastic scattering, and how the angular spread of the reaction products was incorporated into the FRESCO results.

4.2.1 FRESCO

Using FRESCO, it is possible to calculate the differential cross section for elastic and inelastic scattering involving both the Coulomb and nuclear interactions acting between the colliding nuclei. In modeling processes beyond elastic scattering, an effective optical potential containing a real and imaginary part is employed. The real part accounts for elastic scattering, whereas the imaginary part is responsible for the absorption of probability from the elastic channel into different reaction channels. In this framework, the different channels involved in the reaction process are coupled via a truncated sum of differential equations for a two-body system. The truncated sum over the coupled differential equations provides all possible exit channels from the reaction. The individual couplings, informed by theoretical models or experimental data, provide insight into the inner structure of the nucleus. The optical model, further described in Sect. 4.2.1.1, effectively replaces the complex many-body nucleon-nucleon interactions with a phenomenological potential that captures the average interaction between the nuclei.

```
e19005, 30Na on 181Ta with 170 + 208Pb potential params (using 2+ -> 3+ config.).
NAMELIST
&FRESCO hcm=0.001 rmatch=100.0
         jtmin=0.0 jtmax=6000.0 absend=-100 rela='r' rintp=0.1 cutl=0.1
         thmin=0.1 thmax=10.00 thinc=0.01
         iter=0 iblock=2 smats=2 xstabl=1 elab=2651.19672 /
&PARTITION namep='Na30' massp=30.009097931 zp=11
            namet='Ta181' masst=180.947992 zt=73 nex=2 /
&STATES jp=2.0 bandp=+1 kkp=2.0 ep=0.000 cpot=1 et=0.0 jt=0.0 /
&STATES jp=3.0 bandp=+1 kkp=2.0 ep=0.426 cpot=1 copyt=1 /
&partition /
&POT kp=1 ap=30 at=181 rc=1.2 /
&POT kp=1 type=10 p2=18.5 /
&POT kp=1 type=1 p1=50. p2=1.067 p3=0.8 p4=57.9 p5=1.067 p6=0.8 /
&POT kp=1 type=10 p2=1.872 /
&pot /
&overlap /
&coupling /
```

Figure 4.7: FRESCO input file for the 30 Na + 181 Ta reaction. This input file contains an optical potential with the Coulomb term, along with real and imaginary nuclear volume terms. The Coulomb term is associated with an E2 matrix element of $18.5 \ efm^2$. The nuclear volume term is deformed with a nuclear deformation length $\delta_A = 1.872 \ fm$. The real and imaginary values (i.e. type=1, p_1 , ... , p_6) are from the 17 O + 208 Pb reaction [81]. The $^{3+}$ excited state at 426 keV is designated to belong to the K=2 rotational band built upon the $^{2+}_{g.s.}$ via the kkp=2 parameter.

```
e19005, 30Na on 181Ta with 32Mg + 181Ta global potential (2+ -> 3+)
NAMELIST
&FRESCO hcm=0.001 rmatch=100.0
         jtmin=0.0 jtmax=6000.0 absend=-100 rela='r' rintp=0.1 cutl=0.1
         thmin=0.1 thmax=10.00 thinc=0.01
         iter=0 iblock=2 smats=2 xstabl=1 elab=2651.19743 /
&PARTITION namep='Na30' massp=30.009097931 zp=11
            namet='Ta181' masst=180.947992 zt=73 nex=2 /
&STATES jp=2.0 bandp=+1 kkp=2.0 ep=0.000 cpot=1 et=0.0 jt=0.0 /
&STATES jp=3.0 bandp=+1 kkp=2.0 ep=0.426 cpot=1 copyt=1 /
&partition /
&POT kp=1 ap=30 at=181 rc=1.2 /
&POT kp=1 type=10 p2=18.5 /
&POT kp=1 type=1 shape=9 p1=1.0 p2=1.0 /
&POT kp=1 type=10 p2=1.291 /
&pot /
&overlap /
&coupling /
```

Figure 4.8: FRESCO input file for the 30 Na + 181 Ta reaction. This input file contains an optical potential with the Coulomb term, along with theoretically derived real and imaginary nuclear volume terms. The Coulomb term is associated with an E2 matrix element of $18.5 \ e \text{fm}^2$. The nuclear volume term is deformed with a nuclear deformation length $\delta_A = 1.291 \ \text{fm}$. The real and imaginary values for the nuclear volume term (type=1 in the &POT namelist) were determined from theoretically derived optical model potential [109] constructed with a complex G-matrix interaction. The optical potential for the 32 Mg + 181 Ta system was derived and used for the 30 Na + 181 Ta system. The $^{3+}$ excited state at 426 keV is designated to belong to the K=2 rotational band built upon the $^{2+}_{g.s.}$ via the kkp=2 parameter.

The populated 3⁺ and 4⁺ states in ³⁰Na, and 5/2⁺ and 7/2⁺ states in ³¹Na were used in the coupled-channel calculations. The input file to FRESCO required the &FRESCO, &PARTITION, &STATES, and &POT sections to be prepared, with an example presented in Fig. 4.7. A brief description of each section is found in Appendix A.

It is important to ensure that the rmatch and jtmax parameters in the FRESCO namelist are sufficiently large to capture the full extent of the scattering process. Inadequate values can lead to incomplete convergence of the coupled-channel solution, resulting in inaccurate nuclear deformation lengths and transition matrix elements. This sensitivity is illustrated in Fig. 4.9, where the integrated cross section (see Sect. 4.2.2) approaches an asymptotic value as jtmax is increased.

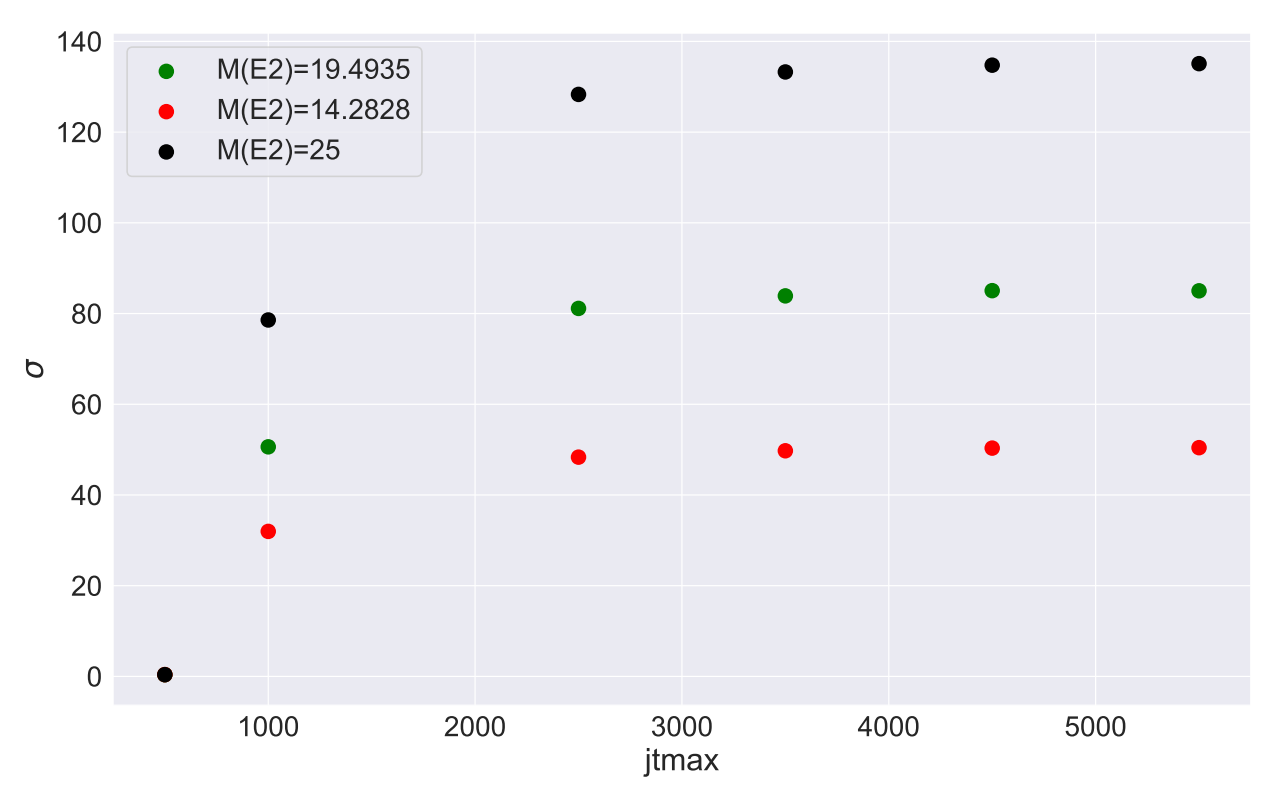


Figure 4.9: Integrated excitation cross section to the $5/2^+$ state in 31 Na as a function of jtmax. Three different E2 matrix elements with M(E2) values of 19.4935, 14.2828, 25 $e fm^2$ were employed, while the nuclear deformation length was fixed to $\delta_A = 1.204$ fm. As jtmax is increased, the integrated cross-section approaches an asymptotic limit.

4.2.1.1 Optical Model Potentials

The optical model simplifies the complex nucleon-nucleon interactions by replacing them with a phenomenological complex potential, whose parameters are constrained by experimental data. The imaginary part of this potential accounts for the loss of flux from the elastic channel to non-elastic processes, analogous to how light is absorbed and scattered in a medium with a complex refractive index.

Inelastic scattering predominantly excites nuclear states associated with collective motion, such as rotational or vibrational modes. In heavier nuclei, the Coulomb interaction becomes increasingly significant, often competing on equal footing or even dominating over that of the nuclear interaction [64, 110]. The role of a model is to define the effective interaction between the

colliding nuclei. This is achieved through a phenomenological potential, containing both nuclear and Coulomb components, that encapsulates the underlying microscopic dynamics. The optical potential takes the form of [111, 112],

$$U_{\rm opt}(r) = \tag{4.1}$$

$$+V_C(r)$$
 A Coulomb term (4.2)

$$-V_V f_V(r)$$
 A real volume term (4.3)

$$+V_s g_V(r)$$
 A real surface term (4.4)

$$-iW_V f_W(r)$$
 An imaginary volume term (4.5)

$$-iW_s g_W(r)$$
 An imaginary surface term (4.6)

$$+V_{so}\vec{l}\cdot\vec{s}$$
 Real spin-orbit term (4.7)

$$+iW_{so}\vec{l}\cdot\vec{s}$$
 Imaginary spin-orbit term (4.8)

which can be succinctly written as

$$U_{\text{opt}}(r) = V_C(r) + V(r) + iW(r)$$
(4.9)

The Coulomb potential is approximated by a uniformly charged sphere with total charge Ze and radius R_C , with the analytical expression given by

$$V_C(r) = \begin{cases} \left(3 - \frac{r^2}{R_C^2}\right) Z_p Z_t e^2 / 2R_C & r \le R_C \\ Z_p Z_t e^2 / r & r > R_C \end{cases}$$

where Z_p , Z_t are the number of protons in the projectile and target nucleus, respectively. The real and imaginary volume terms of the potential are taken to be of the Woods-Saxon form

$$f_i(r) = \frac{1}{1 + \exp[(r - R_i)/a_i]} \qquad i = V, W$$
 (4.10)

with R_i and a_i being the radius and diffuseness, respectively, of the real and imaginary terms. The Woods-Saxon form is plotted in Fig. 4.10 with varying diffuseness parameter values. The strength of the real volume potential term is approximately proportional to the mass of the projectile, and decreases as the incoming energy increases [111, 113, 114]. The imaginary volume component takes into account the loss of projectile particles due to collisions with target nuclei. The imaginary volume term is zero at low energies, as there isn't sufficient energy for a reaction to take place, leaving only the real terms of the optical model potential (i.e. elastic scattering).

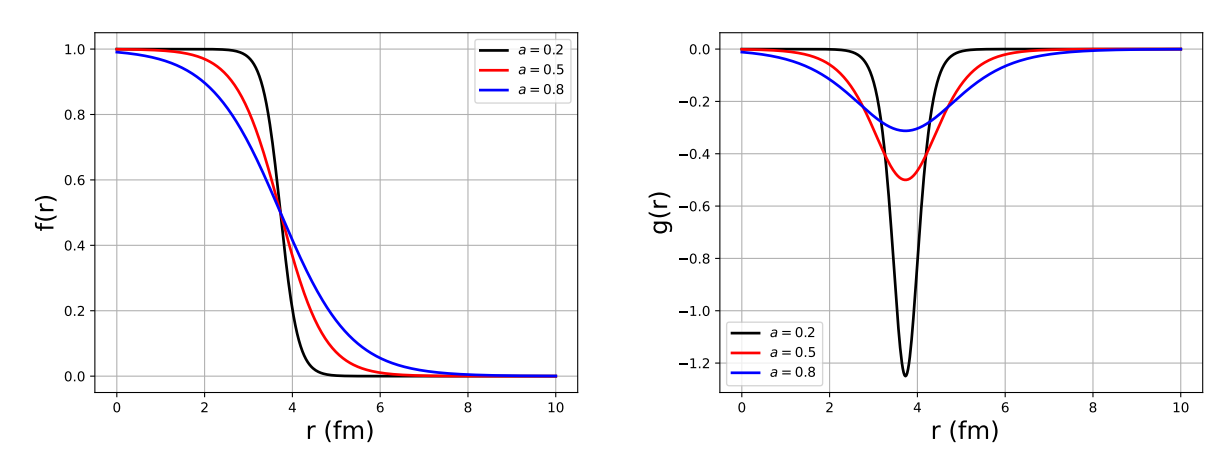


Figure 4.10: Left: Woods-Saxon functions with diffuseness parameters a = 0.3, 0.5, and 0.8 fm. Right: Derivatives of the Wood-Saxon function (surface term). In both, the radius is given by $R = r_0 A^{1/3}$ with $r_0 = 1.2$ fm and A = 30.

The real and imaginary surface terms are the derivatives of a Woods-Saxon function (Eq. 4.10) which are given by,

$$g_i(r) = -\frac{\exp[(r - R_i)/a_i]}{a_i(1 + \exp[(r - R_i)/a_i])^2} \qquad i = V, W$$
(4.11)

and are plotted in Fig. 4.10. The imaginary surface term takes into account the absorption due to the excitation of low-energy collective modes, which have their couplings concentrated on the surface. Additionally, interactions of nuclei with low incoming beam energy are predominantly on the surface region of the nucleus.

In FRESCO, the Coulomb potential is always specified first and defaults to type=0. This entry includes the mass numbers of the projectile (ap) and target (at) nuclei, along with the reduced

Coulomb radius (rc). To apply a deformation, the potential to be deformed must be immediately followed by a line defining the deformation type. As illustrated in Fig. 4.7, the Coulomb potential for the projectile is deformed by specifying type=10, with p2=18.5 specifying the E2 reduced matrix element strength. According to the FRESCO documentation [78], this configuration applies a rotor-model deformation to the projectile's Coulomb field. The nuclear volume potential was defined by using type=1, comprising both real (p1, p2, p3) and imaginary (p4, p5, p6) components, with a default Woods-Saxon shape (shape=0) [79]. The parameters p1, p2, and p3 define the depth (in MeV), reduced radius, and diffuseness of the real part of the potential, while p4, p5, and p6 define the corresponding values for the imaginary part. The real and imaginary parameters for the nuclear volume potential used in this analysis are from the $^{17}O + ^{208}Pb$ reaction [81], following the approaches adopted in Refs. [76, 110]. The projectile's nuclear potential was deformed with a nuclear deformation length p2 = δ_2 = 1.872 fm.

It is also possible to read in the real and imaginary parts of the volume nuclear potential from a theoretically derived optical model, as illustrated in Fig. 4.8. The option of type=1 and shape=9 instructs FRESCO to read in a complex potential. The parameters p1,p2 are scaling parameters for the real and imaginary values, respectively. In order to explore the dependence on the set of optical model parameters being used in this analysis, a theoretically derived optical model potential [109] constructed with a complex G-matrix interaction, CEG07 [115, 116] was utilized. However, due to the optical model potentials derived from Ref. [109] being limited to even-even projectile nuclei within the target mass range of A = 12 - 208, the $^{32}Mg + ^{12}C$ and $^{32}Mg + ^{181}Ta$ potentials were calculated and used for the $^{30,31}Na + ^{9}Be$ and $^{30,31}Na + ^{181}Ta$ reactions.

4.2.2 Determining Angle-Integrated Cross Section

The output from the FRESCO calculations used in this analysis were the differential cross sections per solid angle in the center-of-mass frame, as seen by the red curves in Figs. 4.12 and 4.13. To determine an angle-integrated cross section from the FRESCO output, the center-of-mass differential cross section was first converted to the laboratory-frame cross section. Knowing that the integrated

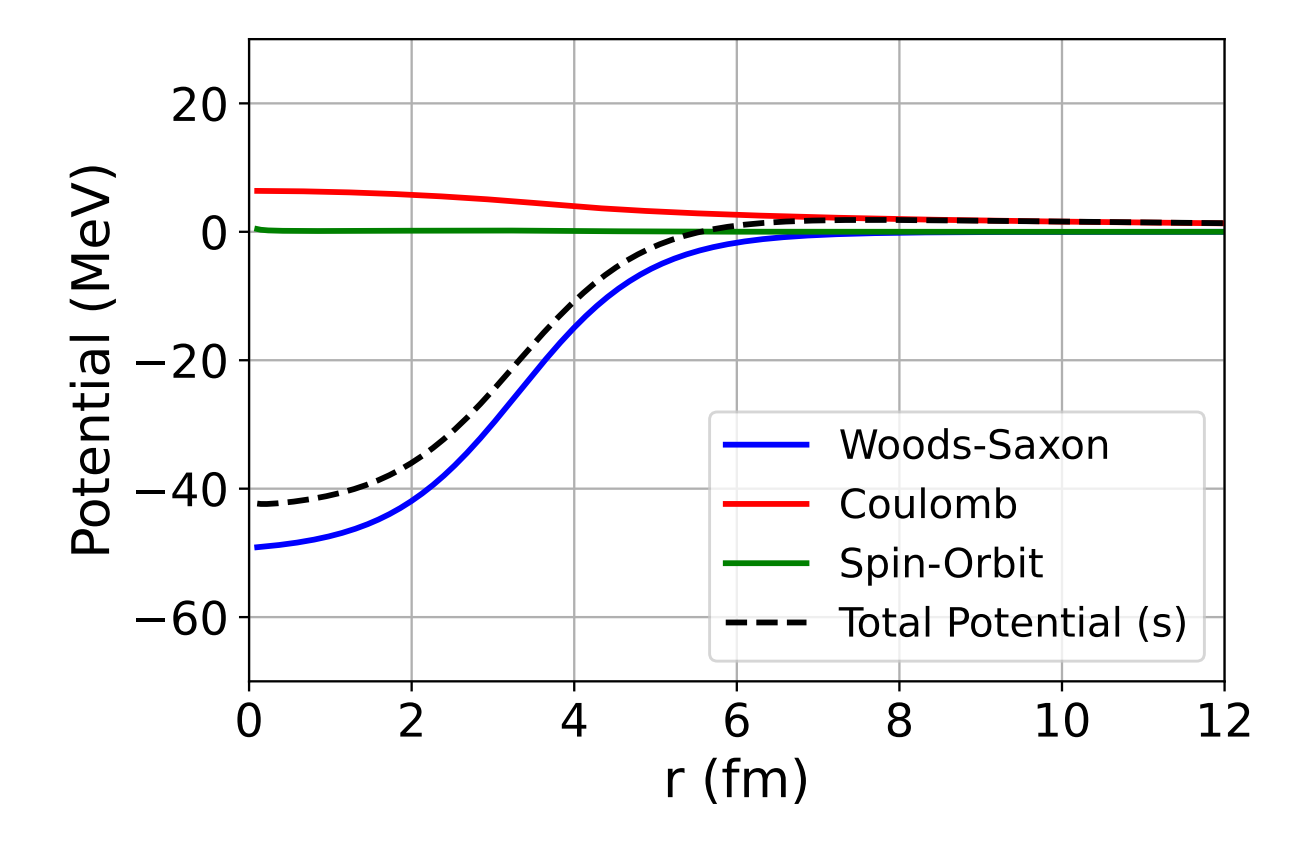


Figure 4.11: Illustrative example of the real components of the optical model potential. The Woods-Saxon potential (blue) is parameterized with $V_0 = 50$ MeV, a = 0.8 fm, and $R = r_0 A^{1/3}$ with $r_0 = 1.067$ fm and A = 30. The Coulomb term (red) assumed Z = 11 and $R_C = 1.2A^{1/3}$, with A = 30. The spin-orbit term (green) is parameterized identically to the Woods-Saxon term.

cross section remains constant in either the laboratory or center-of-mass frame,

$$\frac{d\sigma}{d\Omega_{\text{Lab}}} = \left(\frac{d\sigma}{d\Omega_{\text{CM}}}\right) \cdot \frac{d\theta_{\text{CM}} \sin(\theta_{\text{CM}})}{d\theta_{\text{Lab}} \sin(\theta_{\text{Lab}})}$$
(4.12)

where $d\sigma/d\Omega_{Lab}$ and $d\sigma/d\Omega_{CM}$ are the differential cross sections in the laboratory and center-of-mass frames, respectively. Identical results are achieved when utilizing the form of

$$\frac{d\sigma}{d\Omega_{\text{Lab}}} = \left(\frac{d\sigma}{d\Omega_{\text{CM}}}\right) \cdot \frac{\cos(\theta_{\text{CM}})\Big|_{\theta_f}^{\theta_i}}{\cos(\theta_{\text{Lab}})\Big|_{\theta_f}^{\theta_i}}$$
(4.13)

The angle θ_{Lab} was determined via

$$\tan(\theta_{\text{Lab}}) = \frac{\sin(\theta_{\text{CM}})}{\gamma(v^{\text{CM}}) \cdot (\cos(\theta_{\text{CM}}) + v^{\text{CM}}/v_p^{\text{CM}})}$$
(4.14)

where θ_{Lab} and θ_{CM} are the polar angles in the laboratory and center-of-mass frames, respectively. The center-of-mass frame velocity observed from the laboratory frame is denoted by v^{CM} , and the velocity of the projectile in the center-of-mass frame is indicated by v^{CM}_p . The velocity v^{CM} can be expressed in terms of energy and momentum [117],

$$v^{\rm CM} = \frac{\sum_{i} p_{i} c^{2}}{\sum_{i} E_{i}} \tag{4.15}$$

$$v^{\text{CM}} = \frac{\gamma_p^{\text{Lab}} m_p v_p^{\text{Lab}}}{\gamma_p^{\text{Lab}} m_p + m_t}$$
(4.16)

where p_i and E_i in Eq. 4.15 are the relativistic momentum and energy of each object. Plugging in the appropriate momentum and energy expressions in to Eq. 4.15 results in the center-of-mass velocity being written in terms of projectile (m_p) and target (m_t) masses, projectile velocity in the laboratory frame (v_p^{Lab}) , and associated Lorentz factors (γ) . To validate Eq. 4.16, taking $\gamma_p^{\text{Lab}} \to 1$ is consistent with the non-relativistic expression of $v^{\text{CM}} = (m_p v_p^{\text{Lab}})/(m_p + m_t)$. Eq. 4.16 could also be obtained by utilizing the fact that $p'_p + p'_t = 0$ in the center-of-mass frame, where p'_p, p'_t are the center-of-mass frame momenta (after a Lorentz boost) in the z direction for the projectile and target nucleus, respectively. Similarly, the velocity of the projectile in the center-of-mass frame was determined by a Lorentz boost in the z direction, resulting in

$$v_p^{\text{CM}} = \frac{v_p^{\text{Lab}} - v^{\text{CM}}}{1 - (v^{\text{CM}} v_p^{\text{Lab}} / c^2)}$$
(4.17)

$$= \frac{v_p^{\text{Lab}} m_t}{(m_p / \gamma_p^{\text{Lab}}) + m_t} \tag{4.18}$$

which is consistent with its non-relativistic counterpart $v_p^{\text{CM}} = (v_p^{\text{Lab}} m_t)/(m_p + m_t)$ (i.e. Galilean transformation) when $\gamma_p^{\text{Lab}} \to 1$. Eq. 4.18 was obtained by substituting in the center-of-mass velocity given by Eq. 4.16 into Eq. 4.17.

The differential cross sections for the laboratory (blue histogram) and center-of-mass (red histogram) frames for the ³⁰Na + ⁹Be and ³⁰Na + ¹⁸¹Ta reactions are show in Fig. 4.12 and Fig. 4.13, respectively. In both figures, the leftward compression of the differential cross section as we switch from the center-of-mass to the laboratory reference frame can be understood by the kinematic focusing. The leftward compression of the differential cross section is more extreme in the ³⁰Na + ⁹Be reaction, due in part to the inverse kinematics. The oscillatory patterns observed in Figs. 4.12 and 4.13 arise from the diffraction of the incoming beam wave by the target nucleus, which acts as a diffracting object. Specifically, the pattern in Fig. 4.12 resembles Fraunhofer diffraction [118, 119], which arises in the presence of weak Coulomb barriers. As for the pattern seen in Fig. 4.13, the reactions on the Ta foil are governed by Coulomb excitations [110].

To enable a direct comparison between the experimental cross sections and the FRESCO predictions, a monte carlo simulation was employed to incorporate the effects of the incoming beam profile, finite beam spot size, and angular straggling (see Sect. 4.3.1). The impact of these effects are illustrated by the violet histogram in Fig. 4.14, where the oscillatory features from diffraction are effectively smoothed out. The conversion from differential cross section to yield was done via

$$\Delta\sigma(\theta_i) = \int \left(\frac{d\sigma}{d\Omega}\right)_i \sin(\theta_i) d\theta 2\pi \tag{4.19}$$

where $\Delta \sigma(\theta_i)$ is the yield at angle θ_i , $(d\sigma/d\Omega)_i$ is the differential cross section at θ_i , and $d\theta$ is the step size between θ_i and θ_{i+1} . An alternative and equivalent method to determine the yield is

$$\Delta\sigma(\theta_i) = \left(\frac{d\sigma}{d\Omega}\right)_i \left(\cos\left(\theta_i - \frac{d\theta}{2}\right) - \cos\left(\theta_i + \frac{d\theta}{2}\right)\right) 2\pi \tag{4.20}$$

where both methods were tested and found to give identical results. For each FRESCO calculation performed, the differential cross section was converted to $\Delta\sigma(\theta)$ via Eq. 4.19. This is shown in Fig. 4.15, where the red histogram depicts $\Delta\sigma(\theta)$ versus θ in the center-of-mass frame, and the blue and violet histograms show the corresponding laboratory-frame values with and without the incoming beam's angular spread, respectively. Having these histograms, the angle-integrated cross section was determined by integrating the violet histogram up to the desired angle (θ) .

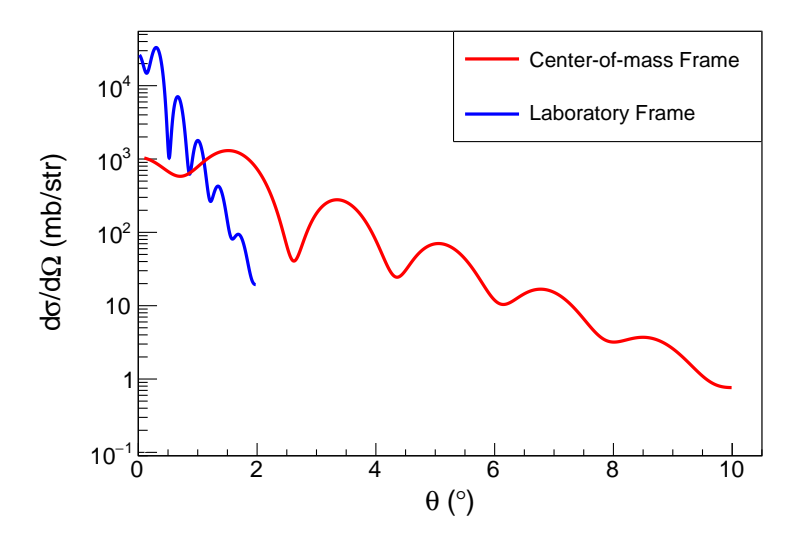


Figure 4.12: Differential cross sections in the laboratory (blue) and center-of-mass (red) frames for the 30 Na + 9 Be FRESCO calculation utilizing the 17 O + 208 Pb optical model potential parameters. The oscillatory pattern seen is due to the incoming wave (i.e. projectile) diffracting from the target nucleus which behaves as a diffracting object.

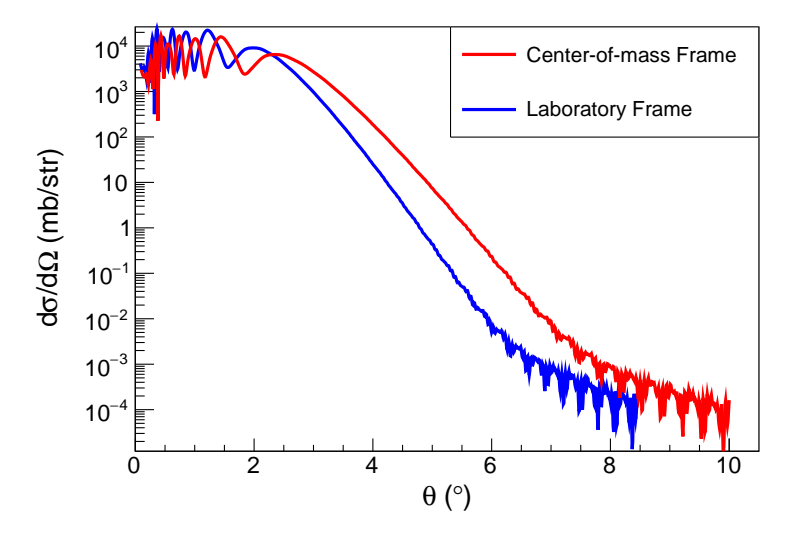


Figure 4.13: Differential cross sections in the laboratory (blue) and center-of-mass (red) frames for the 30 Na + 181 Ta FRESCO calculation utilizing the 17 O + 208 Pb optical model potential parameters. The oscillatory pattern seen is due to the incoming wave (i.e. projectile) diffracting from the target nucleus which behaves as a diffracting object.

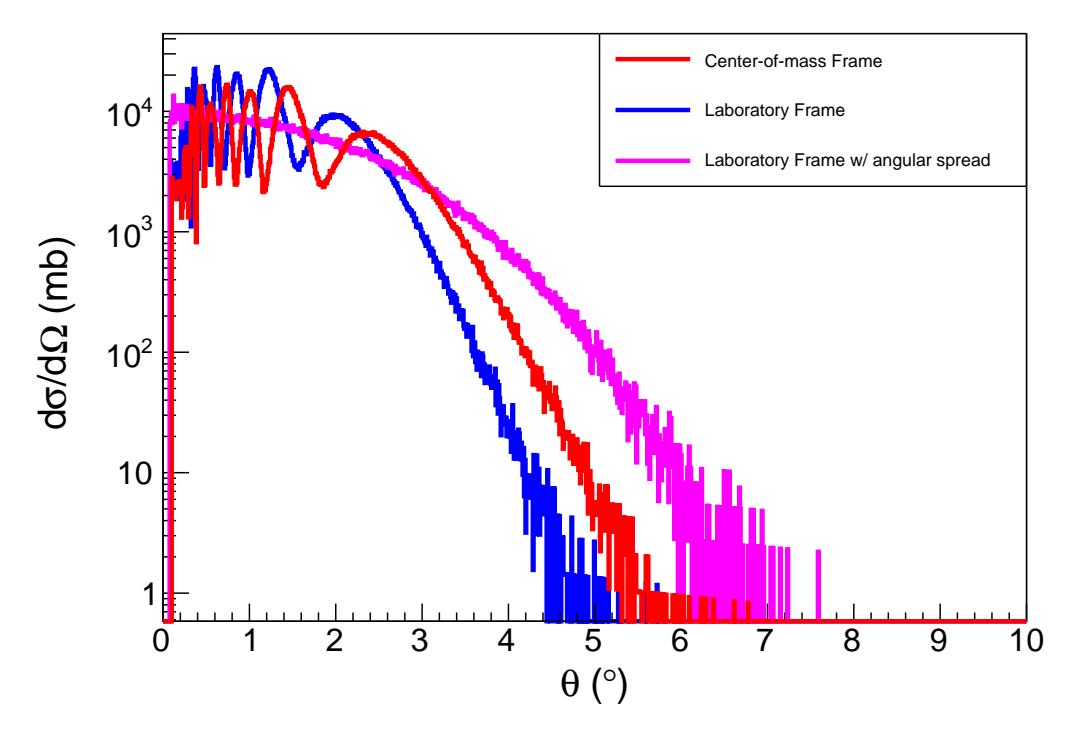


Figure 4.14: Differential cross-section histograms in the laboratory frame with (violet) and without (blue) the angular spread of the incoming beam, along with the corresponding center-of-mass frame distribution (red), all obtained from the monte carlo simulation. These histograms were generated using the FRESCO calculation for the 30 Na + 181 Ta system, utilizing optical model parameters from the 17 O + 208 Pb reaction. The red and blue histograms are identical to the respective curves in Fig. 4.13 up to approximately 5° – 6° , beyond which the low yield is not reproduced by the monte carlo simulation. Incorporating the angular spread into the laboratory-frame via monte carlo greatly diminishes the oscillatory features characteristic of diffraction caused by the interaction of the beam with the target nucleus, and extend the differential cross section to larger θ values.

4.3 Angular Acceptance Analysis

In determining a cross section, confidently estimating the number of incoming beam particles and reaction products entering the S800 is crucial. In particular, the acceptance of the incoming beam and reaction product as a function of θ , where θ is defined as the polar angle (i.e. measured from the laboratory frame *z*-axis), is necessary. In this section, the analysis performed to determine an acceptance curve for the S800 as a function of θ will be discussed. This will be followed by a discussion on the monte carlo simulation that was developed to incorporate the angular spread of

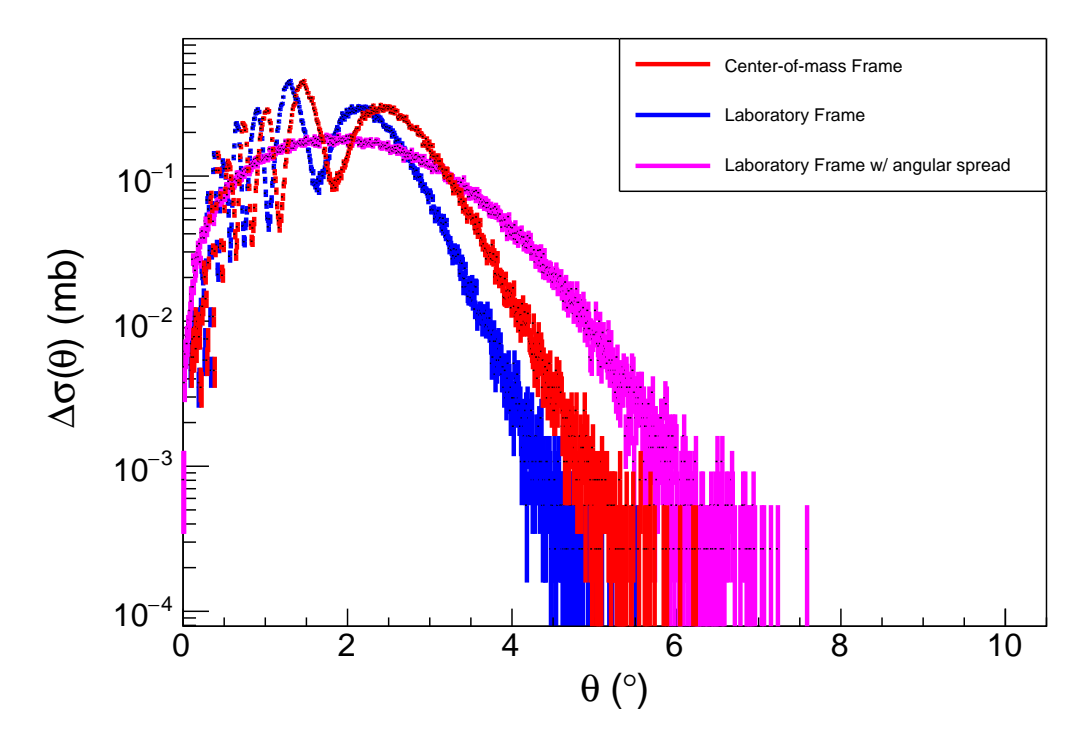


Figure 4.15: Histograms of $\sigma(\theta)$ versus θ produced with Eq. 4.19 in the laboratory frame with (violet) and without (blue) the angular spread of the incoming beam, along with the corresponding center-of-mass frame distribution (red), all obtained from the monte carlo simulation. These histograms were generated using the FRESCO calculation for the 30 Na + 181 Ta system, utilizing optical model parameters from the 17 O + 208 Pb reaction. Due to incorporating the angular spread, the oscillatory pattern caused by diffraction disappears and the yield extends to larger θ values.

the beam to FRESCO results, along with how the acceptance curve was used to correct the number of incoming projectiles and reaction products, both measured at the S800 focal plane.

The acceptance of the S800 as a function of θ was estimated using ³¹Na, whose angular profile is most symmetrically centered around zero, an essential characteristic to accurately determine the acceptance. The 2D b_{ta} vs a_{ta} distribution for ³¹Na was partitioned into different annular regions (i.e. rings), where a selected set of regions are displayed in Fig. 4.16. The coverage of each region spanned 0.5° and ranged from 0° to 3.5° . Minor adjustments were made to the b_{ta} vs a_{ta} distribution of ³¹Na to center it around zero. Each angular region produced a 2D a_{fp} vs x_{fp} distribution, shown in Fig. 4.17, where the distinct two-line feature spanning the x axis (i.e. x_{fp}) is a result of the angular region's ring shape at the target location. The 2D distribution in Fig. 4.17 represents the

ions that reached the focal plane that had an angle θ within $1^{\circ}-1.5^{\circ}$ at the target location. The incoming beam and reaction product are cut off at very large positive $x_{\rm fp}$. For ions with $x_{\rm fp}$ near the center of the S800 focal plane, it is assumed that all $a_{\rm fp}$ angles are accepted. With this feature in mind, a central region spanning 50 mm was selected around $x_{\rm fp}=0$ (i.e. -25 mm to 25 mm) to determine a curve in which a majority of ions were accepted. This central curve is shown in red in the top-left corner of Fig. 4.18 (a), where Eq. 4.21 was the piece-wise function used to fit the selected central region. The parameters σ_L , μ_L , and α_L (σ_R , μ_R , and α_R) represent the standard deviation, centroid, and skewness of the left (right) skewed Gaussians. These values were extracted from the fit to the central region. The left and right boundaries of each component of the fitting function, i.e. x_i^L and x_i^R , were determined separately for each angular region. For a specific angular region (e.g. $1^{\circ}-1.5^{\circ}$), the boundaries were varied until the best possible piece-wise fit was achieved. Given that the skewed Gaussians are normalized to 1, additional scaling parameters, p_0 and p_5 , were included in the fit to set their amplitudes. The regions between the skewed Gaussians were fit with exponentials, where p_1 and p_2 (and similarly p_3 and p_4) are the scaling and decay constants for the left and right regions, respectively, determined from the fitting procedure.

$$f(x) = \begin{cases} \frac{p_0}{\sqrt{2\pi}} e^{-\frac{(x-\mu_L)^2}{2\sigma_L^2}} \cdot \frac{1}{2} \left(1 + \operatorname{erf} \left(\frac{\alpha_L(x-\mu_L)}{\sqrt{2}\sigma_L} \right) \right) & x_1^L \le x < x_1^R \\ e^{p_1} e^{p_2 x} & x_2^L \le x < x_2^R \\ e^{p_3} e^{p_4 x} & x_3^L \le x < x_3^R \\ \frac{p_5}{\sqrt{2\pi}} e^{-\frac{(x-\mu_R)^2}{2\sigma_R^2}} \cdot \frac{1}{2} \left(1 + \operatorname{erf} \left(\frac{\alpha_R(x-\mu_R)}{\sqrt{2}\sigma_R} \right) \right) & x_4^L \le x \le x_4^R \end{cases}$$

$$(4.21)$$

To extract the number of ions in each $x_{\rm fp}$ region, the data were compared to a fit using the piecewise function defined in Eq. 4.21, as shown by the blue curves in Fig. 4.18. Based on the parameters obtained from fitting the central region, a reference curve for each $x_{\rm fp}$ region was generated using a modified version of Eq. 4.21, taking the form of $A \cdot f(x)$. Here, A serves as a scaling factor that adjusts the amplitude of the (red) reference curve for the specific $x_{\rm fp}$ region that is being analyzed, while all other parameters are fixed having been determined from the curve fit

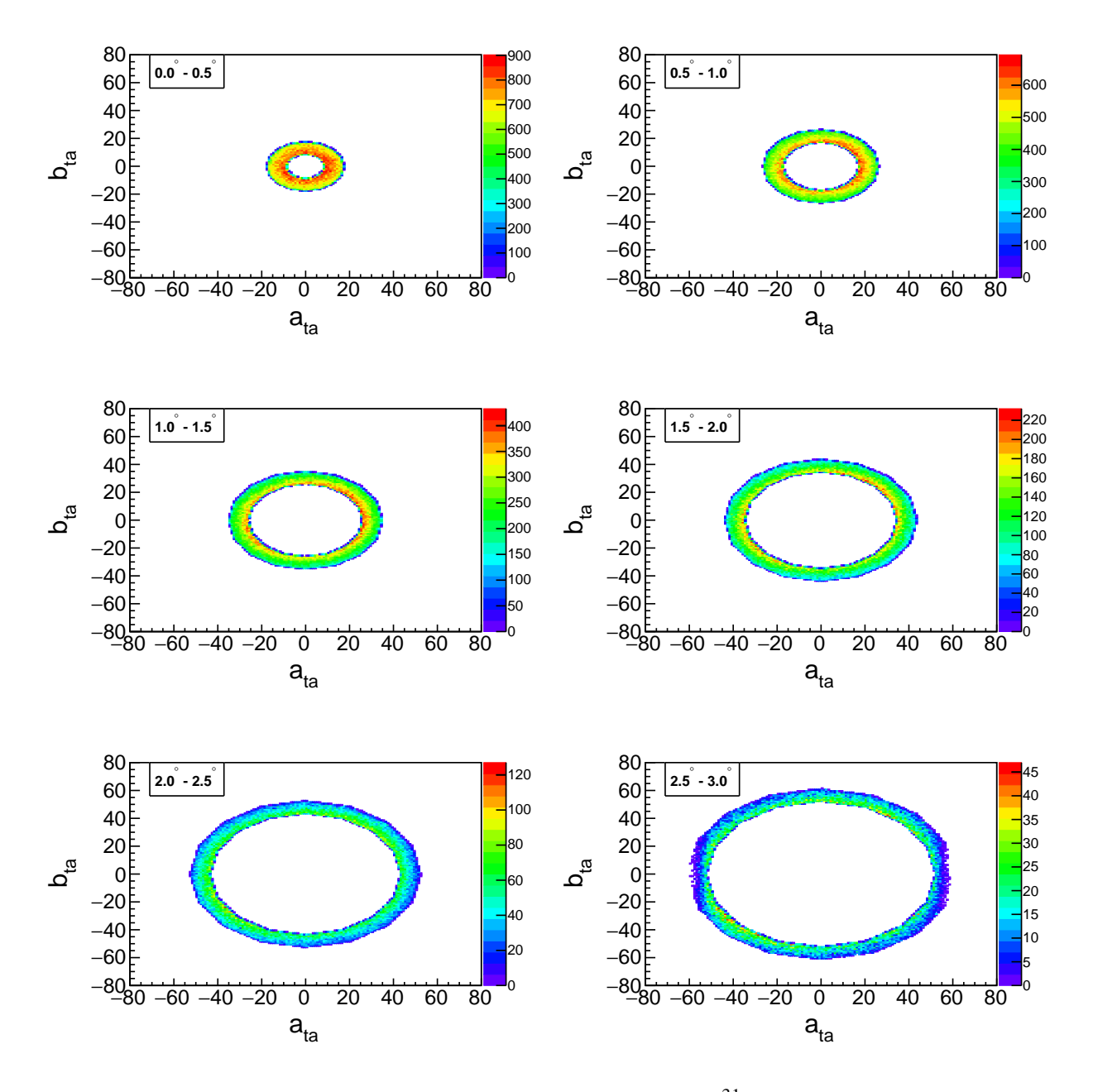


Figure 4.16: Two-dimensional $b_{\rm ta}$ vs $a_{\rm ta}$ annular distributions for ³¹Na. Each region covered 0.5° ranging from 0° to 3.5°. In this figure, only 0° to 3.0° is shown. For each annular region, an averaged acceptance was determined by fitting various $x_{\rm fp}$ slices from the corresponding two-dimensional $a_{\rm fp}$ vs $x_{\rm fp}$ histograms.

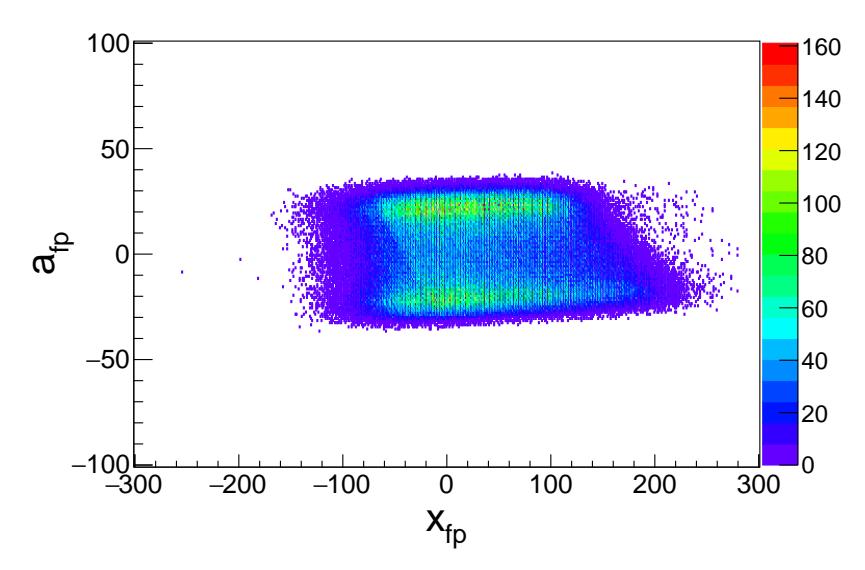


Figure 4.17: Two-dimensional histogram of the dispersive angle $(a_{\rm fp})$ vs the dispersive position $(x_{\rm fp})$ for ³¹Na in the S800 focal plane with an angular coverage of $1.0^{\circ}-1.5^{\circ}$. The two horizontal lines spanning $x_{\rm fp}$ result from the annular shape of the distribution at the target location. A portion of the ³¹Na ions are lost toward positive $x_{\rm fp}$, evidenced by the diagonal cutoff.

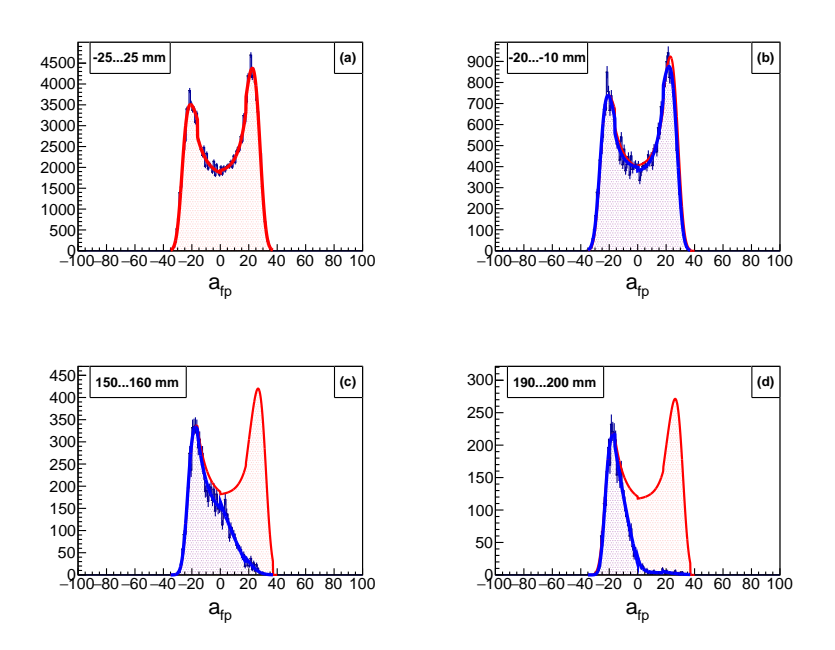


Figure 4.18: One-dimensional histograms of selected $x_{\rm fp}$ slices from the $a_{\rm fp}$ vs $x_{\rm fp}$ distribution for 31 Na in the angular range $1.0^{\circ}-1.5^{\circ}$. The red curve in (a) shows the piecewise function from Eq. 4.21, fit to the central region (-25 mm to 25 mm) in Fig. 4.17. The red and blue curves in (b) – (d) show the reference and region-specific fits, respectively. Increasing $x_{\rm fp}$ (e.g., 150–160 mm to 190–200 mm) reveals the growing loss of 31 Na ions due to the limited $a_{\rm fp}$ acceptance of the S800.

to the central region.

This enabled a comparison to be made between the fitted curve for a given x_{fp} slice (blue) and the corresponding scaled reference curve representing the full a_{fp} acceptance (red). Fig. 4.18 presents selected x_{fp} regions from the $1^{\circ} - 1.5^{\circ}$ angular region. As one moves from 150 - 160 mm to 190 - 200 mm along the positive x_{fp} direction, the impact of the S800 acceptance becomes increasingly evident. Each x_{fp} region spanned 10 mm of the S800 focal plane's dispersive axis, ranging from -140 mm to 300 mm. For every x_{fp} region (i.e. slice) in each annular region, a weighted average for the acceptance was performed, where the weights were the number of events in the particular slice. The results of this procedure are tabulated in Tab. 4.1 and presented in Fig. 4.19, where the weighted average for each angular region is represented by the red dots and a fit is given by the solid red line. This curve, along with the Monte Carlo code, was used to determine the acceptance for the incoming beam and reaction products for all other nuclei. This is based on the assumption of the S800 having an intrinsic acceptance. A detailed discussion on how this was achieved will be given in Sect. 4.3.1.

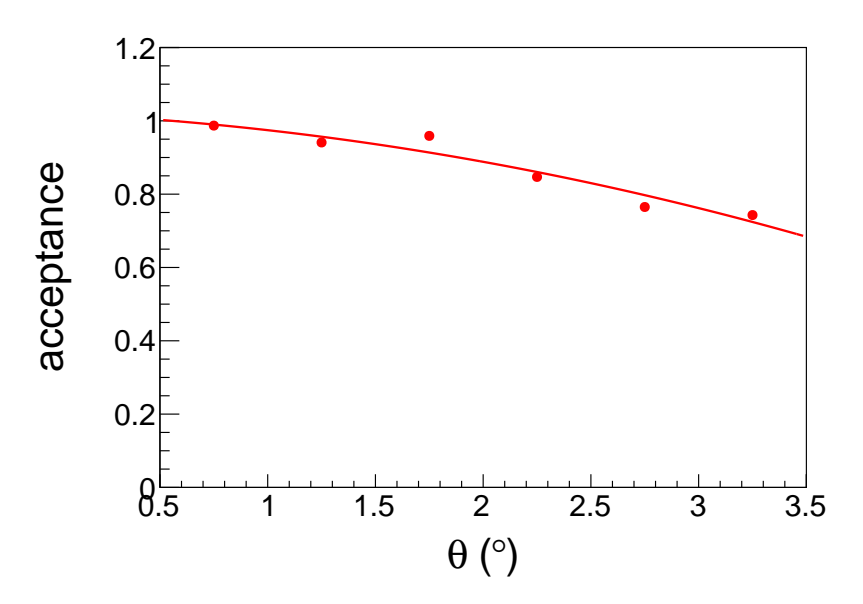


Figure 4.19: Angular acceptance of the S800 as a function of the polar angle θ , measured from the laboratory-frame z-axis. The red dots represent the acceptance obtained for each angular region, where the weighted average was taken for each region using the different x_{fp} slices. The solid red curve shows a fit to these points.

| Angular Range | Acceptance (%) |
|-----------------------------|----------------|
| $0.5^{\circ} - 1.0^{\circ}$ | 0.98 |
| $1.0^{\circ} - 1.5^{\circ}$ | 0.94 |
| $1.5^{\circ} - 2.0^{\circ}$ | 0.95 |
| $2.0^{\circ} - 2.5^{\circ}$ | 0.85 |
| $2.5^{\circ} - 3.0^{\circ}$ | 0.77 |
| $3.0^{\circ} - 3.5^{\circ}$ | 0.74 |
| | |

Table 4.1: Angular acceptances as a function of angular regions spanning 0° –3.5° from the data points in Fig. 4.19.

4.3.1 Incorporating Angular Spread to FRESCO Results

An essential prerequisite to determine a $B(E2\uparrow)$ via a cross-section measurement is the proper comparison between experimental and theoretical results. Particularly, performing a proper comparison between FRESCO and experimental results necessitates a monte carlo simulation to incorporate the experimental angular spread of the incoming beam, along with the finite beam spot size, to the theoretical calculations. This section briefly describes how the monte carlo simulation was used to determine the S800 acceptances for the reaction products and incoming beam. A detailed explanation on how the characteristics of the incoming beam were incorporated into the monte carlo simulation to produce realistic angular distributions of the reaction products can be found in Appendix B.

4.3.1.1 Incoming Beam

The acceptance of the incoming beam was determined using the monte carlo simulation. To prepare for the acceptance calculations of the reaction products (Sect. 4.3.1.2), a FRESCO calculation utilizing the $^{17}\text{O} + ^{208}\text{Pb}$ optical model potential was performed for $^{30}\text{Na},^{31}\text{Na}$, and ^{32}Mg . Differences in acceptances calculated between the $^{17}\text{O} + ^{208}\text{Pb}$ and analytical optical potentials for each foil yielded negligible differences. The monte carlo simulation for the incoming beam did not sample from the FRESCO-calculated yield distributions for each nucleus. Instead, it assumed the sampled scattering angle to be $\theta_{MC} = 0$, meaning the beam did not scatter. This approach incorporated the

beam's angular spread and spatial distribution at the target while ensuring no inelastic scattering reactions took place. The acceptance of the incoming beam, $\epsilon_{\rm IB}^{\rm acc.}$, was determined via

$$\epsilon_{\text{IB}}^{\text{acc.}} = \frac{\text{Yield with } \theta_{MC} = 0 \text{ with acceptance incorporated}}{\text{Yield with } \theta_{MC} = 0 \text{ with acceptance not incorporated}}$$
(4.22)

where the numerator entailed multiplying the calculated yield by the acceptance curve (Fig. 4.19) on a bin-by-bin basis. To minimize possible systematic uncertainties in the acceptance estimate, the yield for both the numerator and denominator were integrated up to 5°, as pertinent beam events were contained within this range. This analysis resulted in incoming beam acceptances of 0.937, 0.938, and 0.939 for ³⁰Na, ³¹Na, and ³²Mg, respectively.

4.3.1.2 Reaction Products

Quantifying the acceptance of the reaction products utilized both FRESCO and the monte carlo simulation. Unlike the incoming beam acceptance analysis, the monte carlo simulation for the reaction products did sample from the FRESCO-calculated yield distributions for each nucleus. The acceptance of the reaction products, ϵ_{RP}^{acc} , was determined via

$$\epsilon_{\text{RP}}^{\text{acc.}} = \frac{\text{Yield with } \theta_{MC} \neq 0 \text{ with acceptance incorporated}}{\text{Yield with } \theta_{MC} \neq 0 \text{ with acceptance not incorporated}}$$
(4.23)

The numerator was calculated by multiplying the corresponding yield (e.g., the violet curve in Fig. 4.15) with the acceptance curve (Fig. 4.19) on a bin-by-bin basis. Both the numerator and denominator were integrated up to 3° for ³⁰Na, ³¹Na and up to 2° for ³²Mg, corresponding to the scattering-angle gate (measured from the laboratory-frame *z*-axis) used in the gamma-ray spectra analyses in Sects. 4.6, 4.7, and 4.4. To ensure the sensitivity to Coulomb excitation components [83, 84, 110], smaller angle cuts of 3° were chosen in the present analysis of ^{30,31}Na, while a different cut of 2° was adopted for ³²Mg to be consistent with the previous work [76]. This procedure yielded reaction product acceptances of 0.905, 0.903, and 0.908 for ³⁰Na, ³¹Na, and ³²Mg, respectively.

4.4 Benchmark of Analysis Procedure with ³²Mg

The primary motivation for this analysis was to determine the electric quadrupole transitions strengths to low-lying excited states $(B(E2\uparrow))$ in 30 Na and 31 Na. Quantifying the $B(E2\uparrow)$ values to these excited states provided insight into the structure of these nuclei, while also supplying information on systematic trends in the N=20 island of inversion. To this end, the amount of gamma rays detected by GRETINA from the de-excitation of excited states had to be determined. To validate the methods utilized in this analysis, 32 Mg was utilized to benchmark the cross-section determination procedures. The cross sections obtained from this benchmark analysis are consistent with those reported by Revel *et. al.* [76], whose results are based on the same experiment performed for 30 Na and 31 Na.

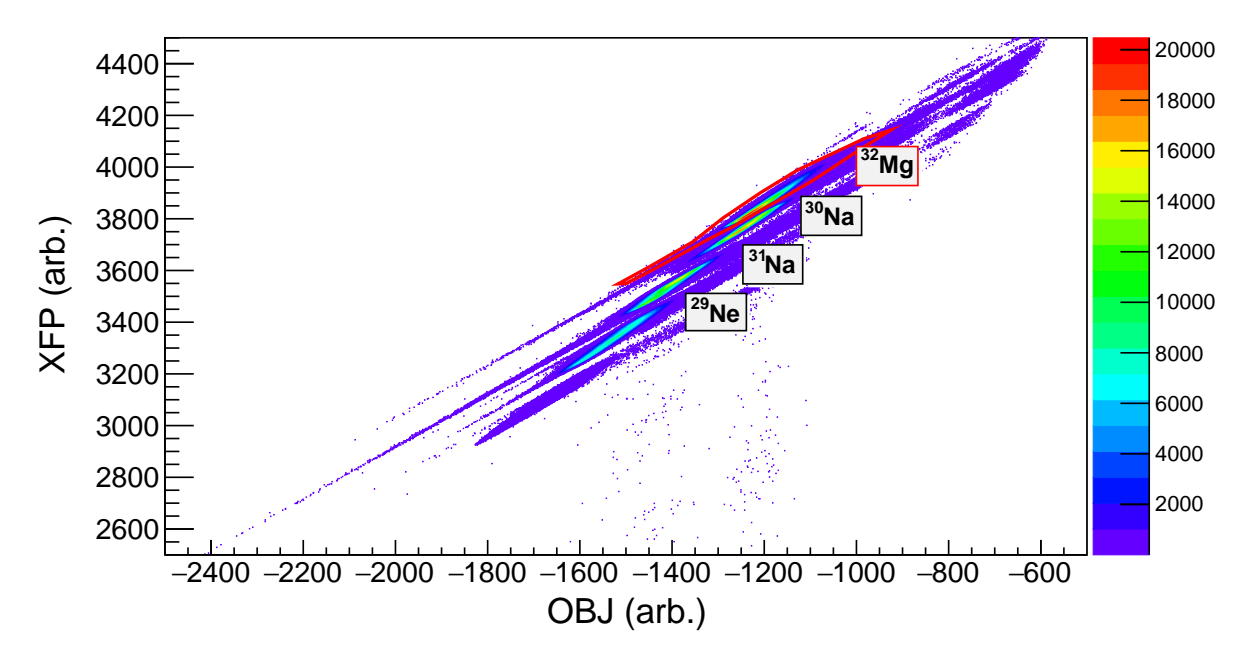


Figure 4.20: Secondary beam components separated by the time-of-flight (TOF) technique. The time-of-flight technique relies on timing differences between a reference timing signal produced from a scintillator located within the S800 focal plane (E1), and two timing signals produced by scintillators located at the A1900 focal plane (XFP) and Object station (OBJ). Both axes are defined relative to the E1 reference signal: the *y*-axis represents the timing difference between E1 and XFP, whereas the *x*-axis shows the difference between E1 and OBJ. The red line represents a software gate applied to select the ³²Mg incoming beam.

The secondary beam of 32 Mg was identified by using the correlation between two time-of-flight (TOF) detectors as shown in Fig. 4.20, where the red line corresponds to a software gate to isolate the desired beam component. The detectors consisted of plastic scintillators located at the focal plane of the A1900 focal plane (XFP), Object station (OBJ), and S800 focal plane (E1) as described in Sects. 3.3.1 and 3.4.2, respectively. In the two-dimensional time-of-flight histogram in Fig. 4.20, the ion's flight duration from the XFP location to S800 focal plane increases downward along the *y*-axis, whereas the flight time increases leftward on the *x*-axis. The four intense blobs seen in Fig. 4.20, starting from the upper right blob and moving diagonally downward (i.e. downward and leftward) correspond to 32 Mg, 30 Na, 31 Na, and 29 Ne.

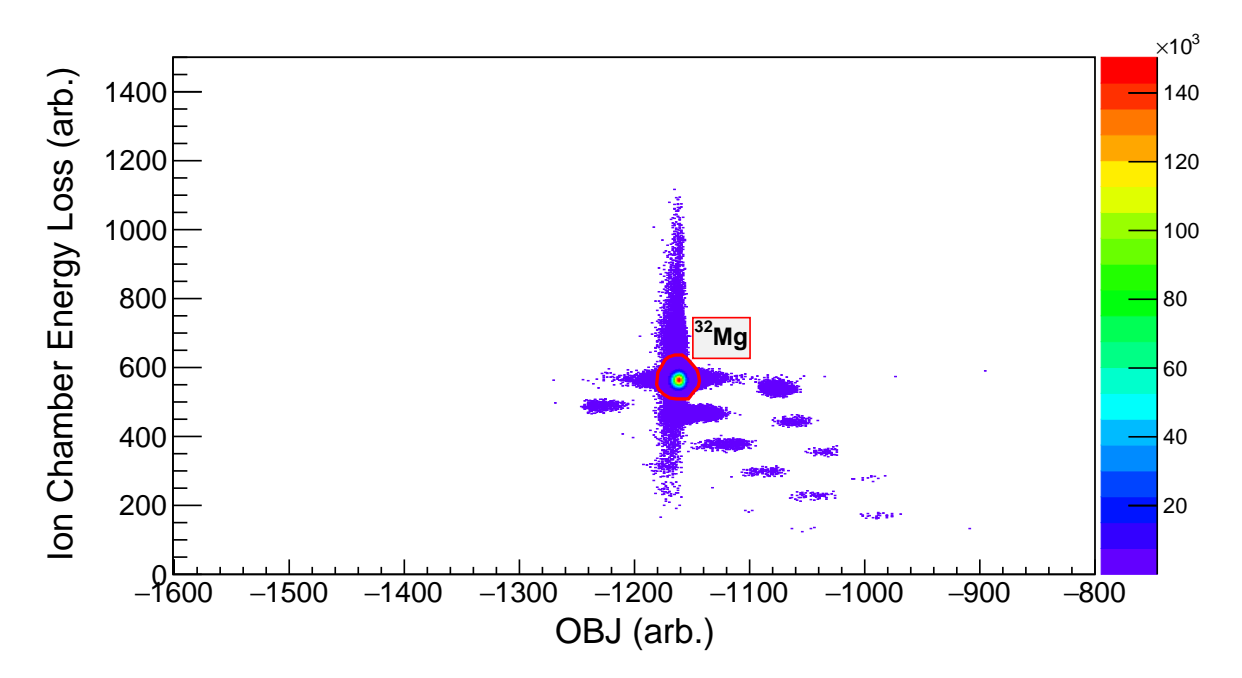


Figure 4.21: Particle identification plot (PID) produced from applying a software gate selecting the 32 Mg secondary beam. The *y*-axis corresponds to energy loss in the S800 focal plane ion chamber with the *x*-axis representing the time-of-flight difference between the E1 and OBJ signals. The most prominent cluster corresponds to 32 Mg ions that reached the S800 focal plane. A software gate, shown as a red circle, was applied to select the scattered 32 Mg ions after passing through the TRIPLEX device holding the Beryllium and Tantalum target foils. This ensured that the resulting gamma-ray spectrum contained inelastically scattered 32 Mg ions.

Once the software gate seen in red in Fig. 4.20 was applied, the outgoing particle identification (PID) plot seen in Fig. 4.21 was generated. The *y*-axis of this histogram represents the energy

lost by the ion as it traversed the 16 different sub-ion chambers (see Sect. 3.4.3), with the x-axis representing the time-of-flight difference between the E1 and the OBJ scintillator. The most intense blob in Fig. 4.21 contains both elastic and inelastically scattered 32 Mg ions, where the red circle around it was the applied software gate to ensure we gated on 32 Mg reaction products. In addition to 32 Mg, there are several other reaction products visible in the plot. These additional reaction products were not of interest due to not being statistically significant and not the main goal of this analysis.

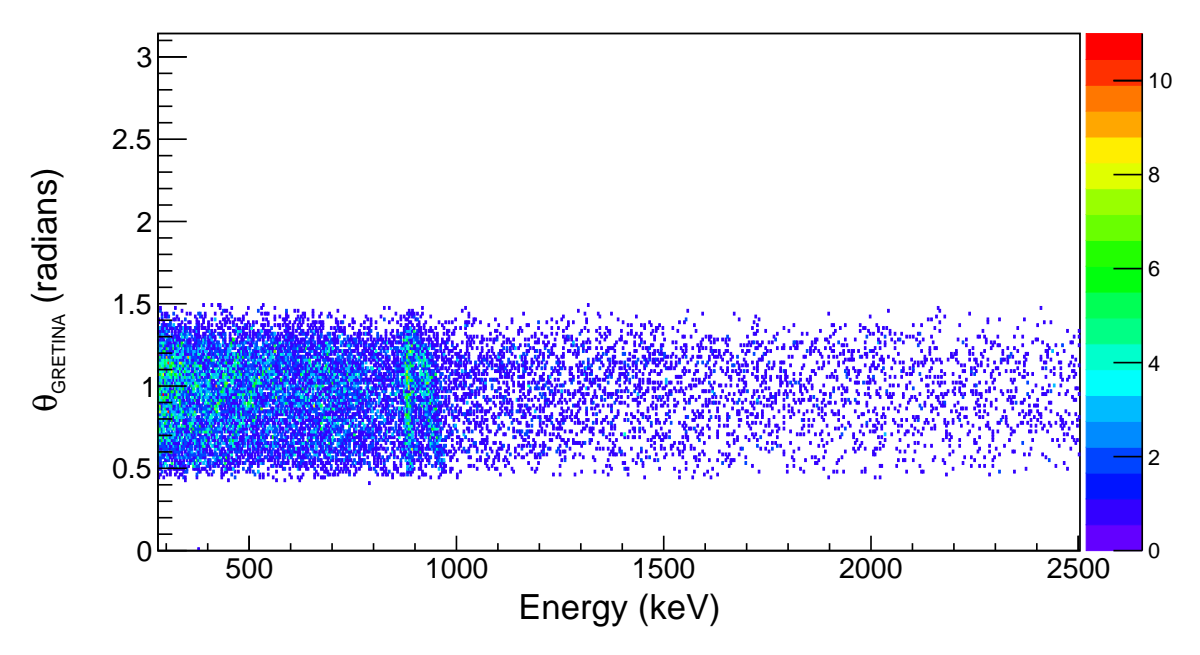


Figure 4.22: Two-dimensional Doppler-corrected gamma-ray spectrum for 32 Mg optimized for reactions originating on the Tantalum foil. The *y*-axis represents the gamma-ray's emission angle defined by the main interaction point in GRETINA. The *x*-axis is the Doppler-corrected energies of the gamma rays detected by GRETINA. Two distinct lines are observed near 900 keV belonging to the $2_1^+ \rightarrow 0_{\rm g.s.}^+$ transition. The lower-energy gamma-ray line is associated with the de-excitation of the 2_1^+ state following reactions on the Tantalum target, whereas the higher-energy line results from reactions involving the Beryllium target foil.

Using the software gates applied to select the incoming beam and reaction products (Figs. 4.20 and 4.21), the two-dimensional spectrum shown in Fig. 4.22 was produced. The spectrum shown in Fig. 4.22 also incorporates a time gate isolating the prompt γ rays (Fig. 4.23), in addition to a scattering-angle condition restricting the reaction products to $\theta_{\text{Lab}}^{\text{scatt.}} \leq 2^{\circ}$ [76]. The y-axis

represents the angle θ_{GRETINA} at which the gamma ray was detected in GRETINA, defined as the gamma-ray's angle of emittance determined by the main interaction point in GRETINA. The *x*-axis is the Doppler-corrected energies of detected gamma rays. The two-dimensional histogram in Fig. 4.22 depicts the relationship between the Doppler-corrected gamma-ray energy, velocity of the ion at the time of emittance, and θ_{GRETINA} as described in Sect. 2.1.1.

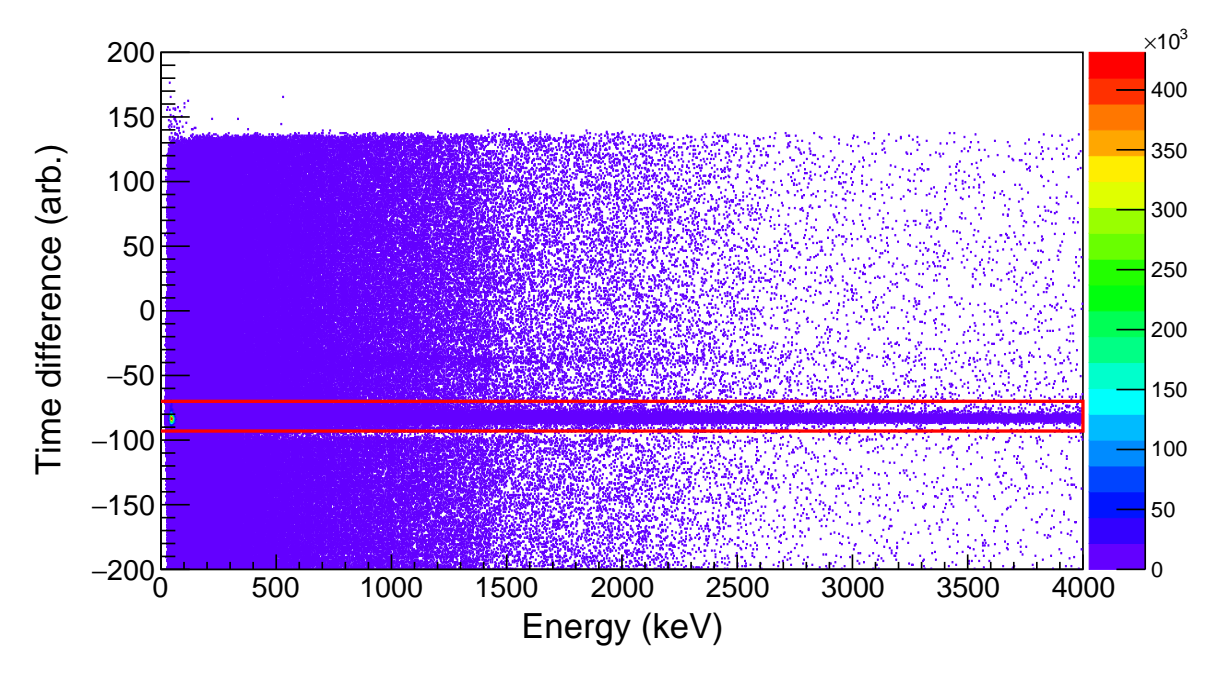


Figure 4.23: Two-dimensional histogram displaying the selection of prompt gamma rays, visualized as a red rectangle, from de-excitations associated with 32 Mg. The *y*-axis corresponds to the timestamp difference between events in GRETINA and correlated 32 Mg event in the E1 scintillator. The *x*-axis is the Doppler-corrected gamma-ray energy.

The prompt gamma-ray gate that was applied entailed selecting a narrow range of events in which the timing difference between the timestamp of an event in GRETINA and a correlated 32 Mg event in the E1 scintillator was small, as seen in Fig. 4.23. The prompt gamma-ray gate greatly suppressed the amount of background contamination in our gamma-ray spectrum. The two-line structure observed around 900 keV in Fig. 4.22 corresponds to de-excitation gamma rays from the $2_1^+ \rightarrow 0_{\rm g.s.}^+$ transition at 885 keV in 32 Mg, where the histogram was Doppler corrected for reactions occurring on the Tantalum foil. The lower- and higher-energy lines originate from reactions on the

Tantalum and Beryllium foils, respectively. As explained in Sect. 2.1.1, the Doppler correction of a gamma ray depends on the angle of emittance and velocity β_{ion} ($\beta_{ion} = v_{ion}/c$). Ions that undergo a reaction on the Beryllium foil will be moving at velocity β_{Be} and similarly β_{Ta} for the Ta foil, where $\beta_{Be} > \beta_{Ta}$ due to the Beryllium foil being upstream of the Tantalum foil. This results in gamma rays originating from reactions on the Beryllium foil being at higher energies due to stronger Doppler shifts.

Projecting the two-dimension histogram illustrated in Fig. 4.22 onto the *x*-axis gives the gamma-ray spectrum for 32 Mg (Fig. 4.24), where no angle cut was introduced for the gamma-ray emission angle. This figure represents the energy spectrum for gamma rays measured by all GRETINA detectors where a Doppler correction was performed utilizing the gamma-ray emission angle and the ion velocity at the downstream face of the Tantalum foil, $\beta_{Ta} = 0.362302$. For this reason, the Beryllium gamma-ray peak is much wider than the Tantalum gamma-ray peak. The peak labeled **Ta** correspond to reactions originating on the Tantalum target (i.e. Tantalum gamma-ray peak) and those originating from the Beryllium target (i.e. Beryllium gamma-ray peak) are labeled with **Be**.

In addition to experimental data, Fig. 4.24 includes a double-exponential background (gray), and the Tantalum (blue) and Beryllium gamma-ray peaks (orange) of the $2_1^+ \rightarrow 0^+$ transition. The sum of the double exponentials and individual Tantalum and Beryllium gamma-ray peaks are shown in red, consistent with experimental data. The double exponentials were parameterized from a fit to the experimental data using the log-likelihood method. The Tantalum and Beryllium peaks were simulated with the G4Lifetime software (Sect. 4.1.2), and once properly calibrated (Sect. 4.1.2.1), the simulation requires four main parameters to reproduce the gamma-ray spectrum: the direct population fraction of the state, the lifetime of the state, the level energy, and the gamma-ray transition energy. Given that there was no cascade for this benchmark analysis, the direct population fraction for the 2_1^+ state was to set 100%. The level energy and transition energy were obtained from the National Nuclear Data Center (NNDC) [120], with the lifetime of 16.4 ps obtained from Elder *et. al.* [23]. Furthermore, the ability to specify the fraction of reactions on the Beryllium target relative to the Tantalum target in the simulation is also available. This feature was utilized to simulate the

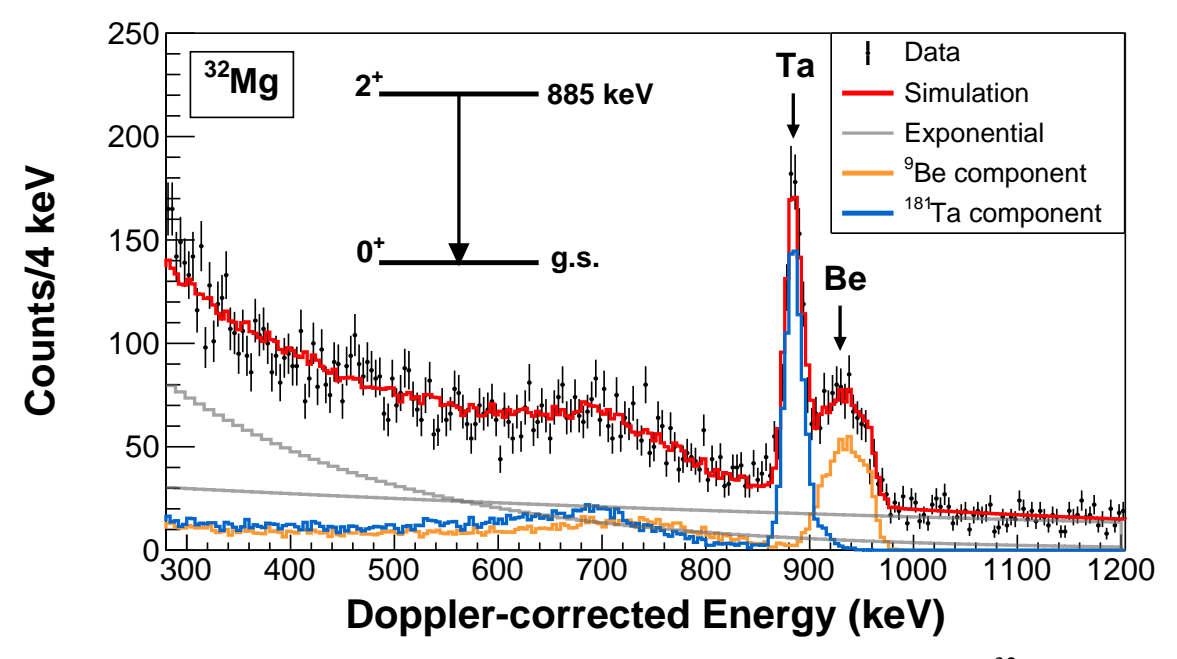


Figure 4.24: One-dimensional Doppler-corrected gamma-ray spectrum for 32 Mg optimized for reactions originating from the Tantalum target foil. The spectrum was produced from applying gates seen in Figs. 4.20, 4.21, 4.23, with an additional 2° scattering angle gate defined from the laboratory's z-axis. The Tantalum (Ta) and Beryllium (Be) peaks for the $2_1^+ \rightarrow 0_{g.s.}^+$ transition are marked accordingly.

Beryllium and Tantalum gamma-ray peaks separately, as it was done for the ³⁰Na (Sect. 4.6) and ³¹Na (Sect. 4.7) analyses. The combined fitting function, consisting of the double exponentials and the Beryllium and Tantalum gamma-ray peaks, were fit to the data utilizing the log-likelihood method. The gamma-ray efficiencies for each peak were determined via the procedure outlined in Sect. 4.1.2.1. Neutron induced background can also impact the Doppler-corrected spectrum due to the laboratory frame gamma-ray peaks creating a spread of energies [121]. These neutron background contributions may contaminate the region in which our peaks of interested are located, further complicating the analysis. For the ³²Mg gamma-ray spectrum, no neutron background contributions were present, thus none were included in the simulation.

The cross-section results from reactions on the Beryllium and Tantalum gamma-ray peaks from this benchmark analysis and those reported by Revel *et al.* [76] are presented in Tab. 4.2. The agreement between the two results indicate that the cross-section determination procedure, the

efficiency calibration procedures, and the G4Lifetime calibration procedure are reliable. This conclusion establishes that the methods utilized in determining the cross sections for 30 Na and 31 Na, which are used in determining the $B(E2,\uparrow)$ to low-lying excited states, are also reliable.

| ${\sigma(J_i^{\pi} \to J_f^{\pi})}$ | This work | Revel et. al [76] |
|---|-----------|-------------------|
| $\sigma_{\text{Be}}(0^+_{\text{g.s.}} \to 2^+_1)$ | 15 (3) | 15 (2) |
| $\sigma_{\text{Ta}}(0^+_{\text{g.s.}} \to 2^+_1)$ | 76 (6) | 75 (8) |

Table 4.2: Comparison of the excitation cross sections to the 2_1^+ state in 32 Mg using a scattering angle gate of $\theta_{Lab}^{scatt.} \le 2^{\circ}$ for each target foil obtained from the present benchmark analysis and those reported in Ref. [76].

4.5 Quantifying Background Contamination

In addition to quantifying the gamma-ray yield for peaks of interest from ³⁰Na and ³¹Na, deducing the amount of contaminant gamma rays is also necessary. The contaminant gamma-ray peaks impact the Doppler-corrected spectrum as they may overlap with regions of interest [121], inflating the gamma-ray yield for transitions observed in ³⁰Na and ³¹Na. To this end, an iterative procedure was established to quantify the amount of contaminant background in the respective gamma-ray spectra. This section will provide a qualitative description of the process undertaken to quantify the amount of neutron-induced background contributions relevant in the gamma-ray spectra of ³⁰Na and ³¹Na.

Both 30 Na and 31 Na contained a prominent 511-keV gamma-ray peak produced from electron-positron annihilation, in addition to neutron-induced gamma rays. The peak near 600 keV, visible in the right panel of Fig. 4.25, originates from the 74 Ge(n, $n'\gamma$) 74 Ge* reaction [96, 121, 122], where its triangular shape is due to the recoiling Germanium nucleus. Only background gamma rays that were pertinent to the analysis of the peaks of interest were included in the G4Lifetime simulation.

Figs. 4.25 and 4.26 display an example of the first and second iterations of this process, respectively. In the first iteration, the Doppler-corrected spectrum was fit first without any simulated

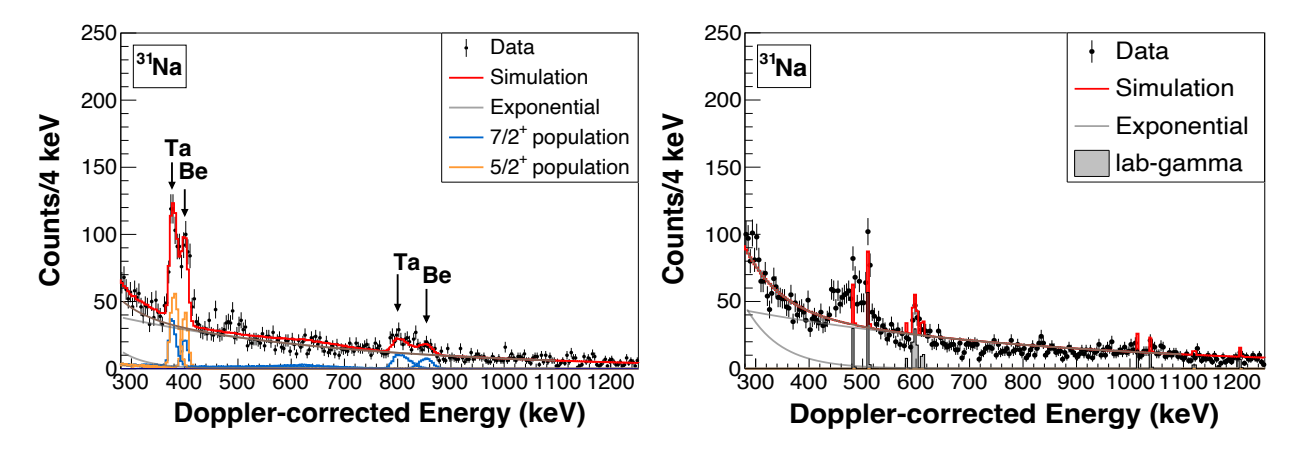


Figure 4.25: First iteration in the process of quantifying background gamma-ray peak contributions for 31 Na. The Doppler-corrected spectrum, shown in the left panel, was fit without any background contributions to determine the initial set of parameters associated with peaks of interest, $P_0 = \{p_1, p_2, ...\}$. A corresponding fit to the laboratory-frame spectrum, shown on the right, was used to extract the initial background scaling parameter $b_{bkg,0}$. Both spectra were fit with simulations from G4Lifetime.

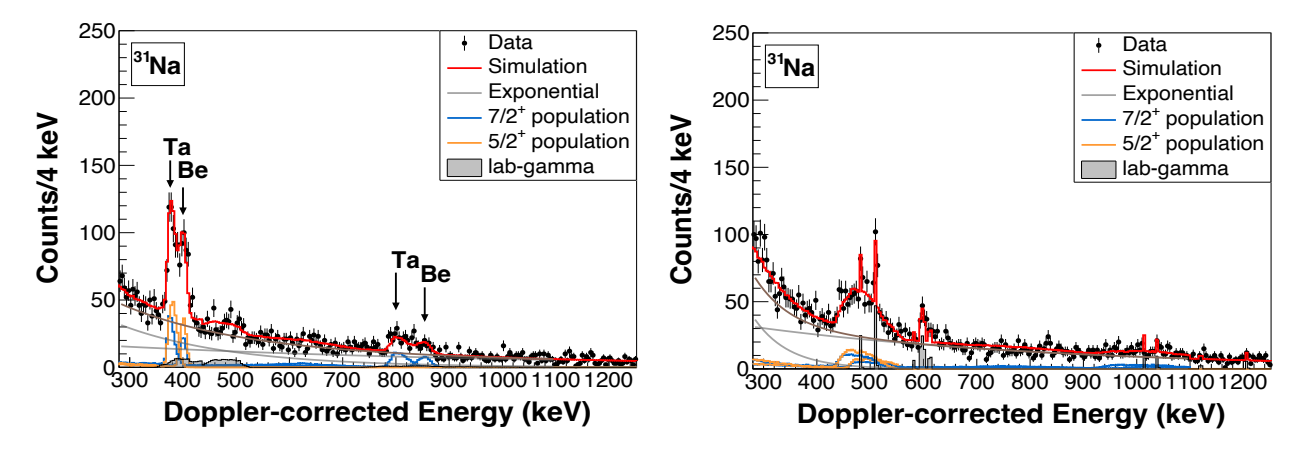


Figure 4.26: Second iteration in the process of quantifying background gamma-ray peak contributions for 31 Na. The Doppler-corrected spectrum, shown in the left panel, was fit with the background contributions determined from the first iteration $(b_{bkg,0})$ resulting in the second set of scaling parameters for the peaks of interest, $P_1 = \{p_1, p_2, ...\}$. Subsequently, the laboratory-frame spectrum was fit with the constraint of P_1 , as shown in the right panel, producing an updated background scaling parameter, $b_{bkg,1}$. Both spectra were fit with simulations from G4Lifetime.

background contributions, as shown in the left panel of Fig. 4.25. This provided the initial set of fitting parameters associated with the peaks of interest, which are denoted by $P_0 = \{p_1, p_2, ...\}$. The parameters p_i , obtained with ROOT, represent the individual scaling factors for each simulated transition response stemming from the population of excited states in each foil. For example, in

 31 Na, p_1 corresponds to the $(7/2^+) \rightarrow (5/2^+) \rightarrow 3/2^+_{g.s.}$ cascade following the population of the $(7/2^+)$ state from reactions on the Be foil. The parameter p_2 corresponds to the $(5/2^+) \rightarrow 3/2^+_{g.s.}$ transition stemming from the direct population of the $(5/2^+)$ state on the Be foil. In the second step of the first iteration, the simulated laboratory-frame gamma rays were fit to the experimental data without including the simulated projectile-frame gamma rays. This procedure, shown in the right panel of Fig. 4.25, yielded the initial background scaling parameter $b_{bkg,0}$.

In the second iteration, the background scaling parameter obtained in the first iteration, $b_{bkg,0}$, was used as a constraint when fitting the experimental Doppler-corrected spectrum, while letting the scaling parameters associated with the peaks of interest vary. The result of this is illustrated in the left panel of Fig. 4.26. This gives rise to an updated set of scaling parameters corresponding to the peaks of interest, denoted by P_1 . The updated set of parameters, P_1 , are then used as constraints when fitting the experimental laboratory-frame spectrum, which is illustrated in the right panel of Fig. 4.26. This iterative cycle was repeated until the fitting parameters for both the peaks of interest and the background converged to satisfactory values. These values were then incorporated into the fitting procedure of 30,31 Na.

4.6 ³⁰Na Analysis

Determining the reduced transition strengths to the low-lying (3⁺) and (4⁺) excited states in 30 Na can be broadly stated to involve quantifying the gamma rays detected by GRETINA, assessing the gamma-ray efficiency of GRETINA (Sect. 3.5.3), accurately modeling the incoming beam and reaction products (Sect. 4.1.2.1), evaluating the acceptances of the S800 spectrograph as a function of scattering angle (Sect. 4.3), and using FRESCO (Sect. 4.2.1). This section discusses the work undertaken to deduce the $B(E2; 2^+_{g.s.} \rightarrow 3^+)$ and $B(E2; 2^+_{g.s.} \rightarrow 4^+)$ transition strengths in 30 Na.

4.6.1 Particle Identification of ³⁰Na

Identification of the secondary ³⁰Na beam was achieved using time-of-flight (TOF) measurements, as shown in Fig. 4.27, utilizing the same scintillator detectors described in Sect. 4.4. A software

gate, shown in red in the same figure, was applied to isolate the 30 Na component of the beam. The flight time of the ions in Fig. 4.27 increases downward along the *y*-axis, whereas it increases leftward along the *x*-axis.

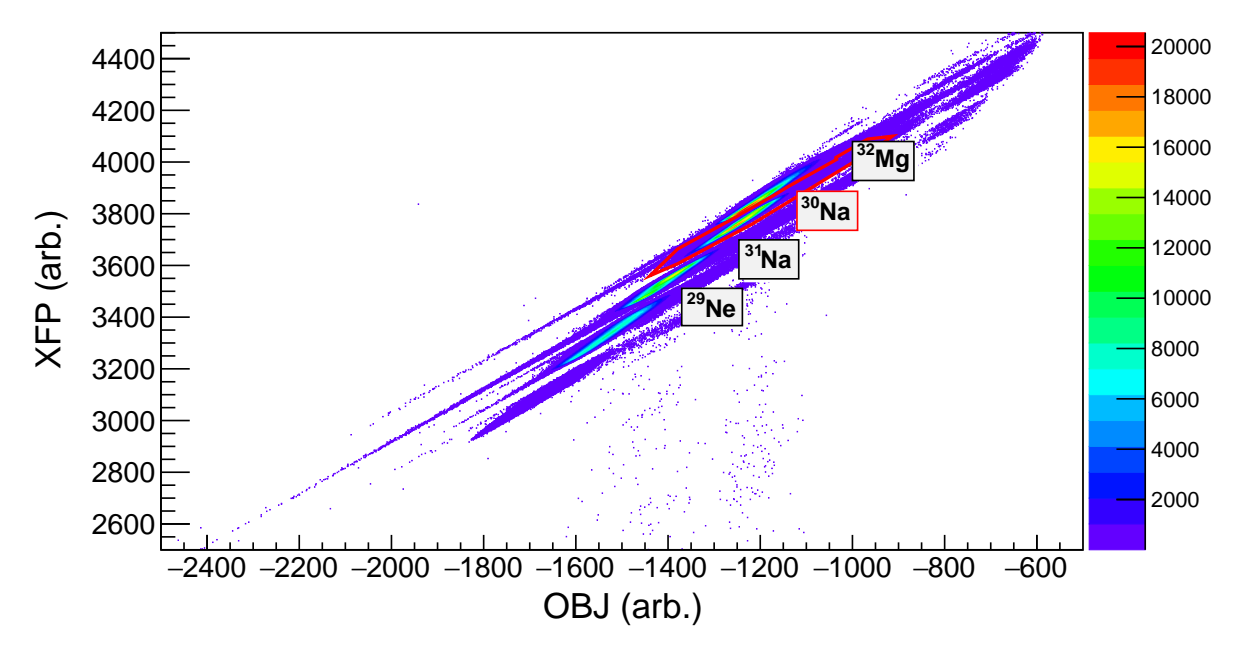


Figure 4.27: Secondary beam components separated by the time-of-flight (TOF) technique. The time-of-flight technique relies on timing differences between a reference timing signal produced from a scintillator located within the S800 focal plane (E1), and two timing signals produced by scintillators located at the A1900 focal plane (XFP) and Object station (OBJ). Both axes are defined relative to the E1 reference signal: the *y*-axis represents the timing difference between E1 and XFP, whereas the *x*-axis shows the difference between E1 and OBJ. The red line represents a software gate applied to select the ³⁰Na incoming beam.

Applying the software gate shown in red in Fig. 4.27 produced the outgoing particle identification (PID) spectrum displayed in Fig. 4.28. In this histogram, the y-axis corresponds to the average energy loss of each ion across the 16 sub-ion chambers (see Sect. 3.4.3), while the x-axis represents the time-of-flight difference between the E1 and OBJ scintillators. The most intense cluster in Fig. 4.28 contains both elastically and inelastically scattered 30 Na ions. A red circle indicates the software gate applied to isolate the 30 Na reaction products. Although several other reaction products are also visible, they were excluded from further analysis due to their limited statistical significance and their irrelevance to the study.

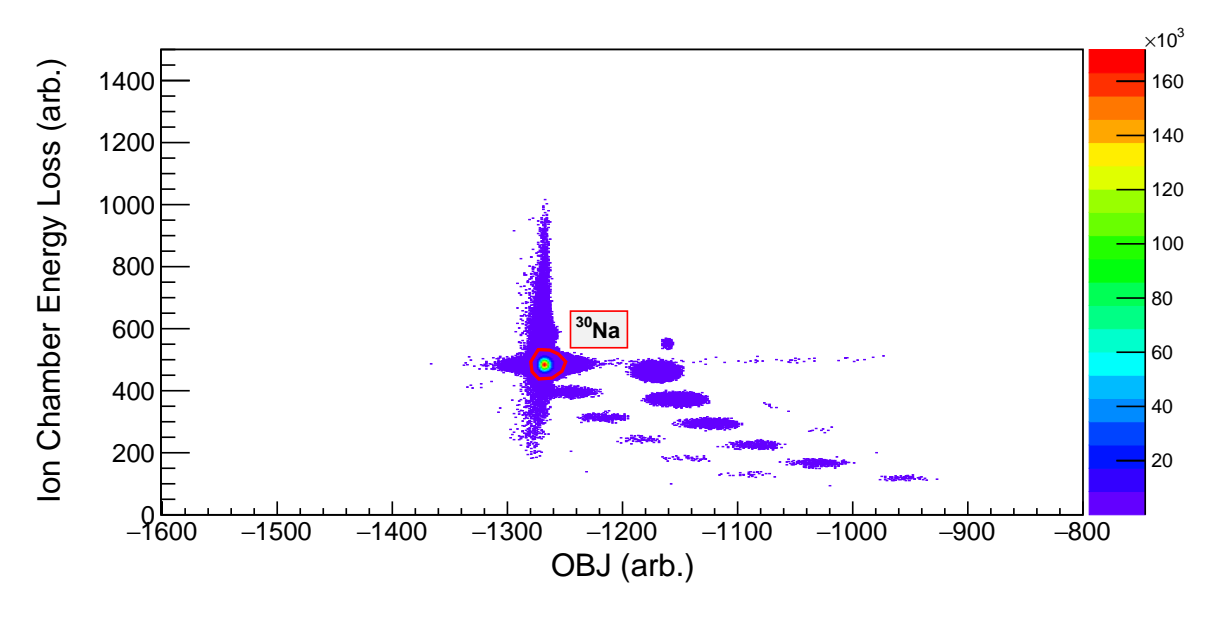


Figure 4.28: Particle identification plot (PID) produced from applying a software gate selecting the 30 Na secondary beam. The y-axis corresponds to energy loss in the S800 focal plane ion chamber with the x-axis representing the time-of-flight difference between the E1 and OBJ signals. The most prominent cluster corresponds to 30 Na ions that reached the S800 focal plane. A software gate, shown as a red circle, was applied to select the scattered 30 Na ions after passing through the TRIPLEX device holding the Beryllium and Tantalum target foils. This ensured that the resulting gamma-ray spectrum contained inelastically scattered 30 Na ions.

4.6.2 Gamma-Ray Spectrum

A time gate (similar to Fig. 4.23) was applied to isolate the prompt gamma rays from most background contributions. To best distinguish between the Ta and Be peaks, gamma rays detected at angles up to 55° from the laboratory-frame z-axis were selected. Furthermore, a scattering angle of 3°, taken from the laboratory-frame z-axis, was imposed on the 30 Na reaction products. Due to the scattered 30 Na ions not being fully covered by the S800 spectrograph in this experiment (see d_{ta} histogram in Fig. 4.2), a careful inspection was performed to investigate a possible bias in the gamma-ray spectra. Thus, to obtain a gamma-ray spectrum that is representative of reactions on both the Be and Ta foils, the data were analyzed as a function of x_{fp} , with spectra corresponding to each 50 mm interval spanning the S800 spectrograph's x_{fp} shown in Fig. 4.29. It was observed that the peaks corresponding to excitations from the Ta and Be foils did not follow the expected trend

of both transition components uniformly changing. Rather, the Ta component of a given transition was generally more prominent in negative x_{fp} regions, while the Be component became dominant towards more positive x_{fp} regions.

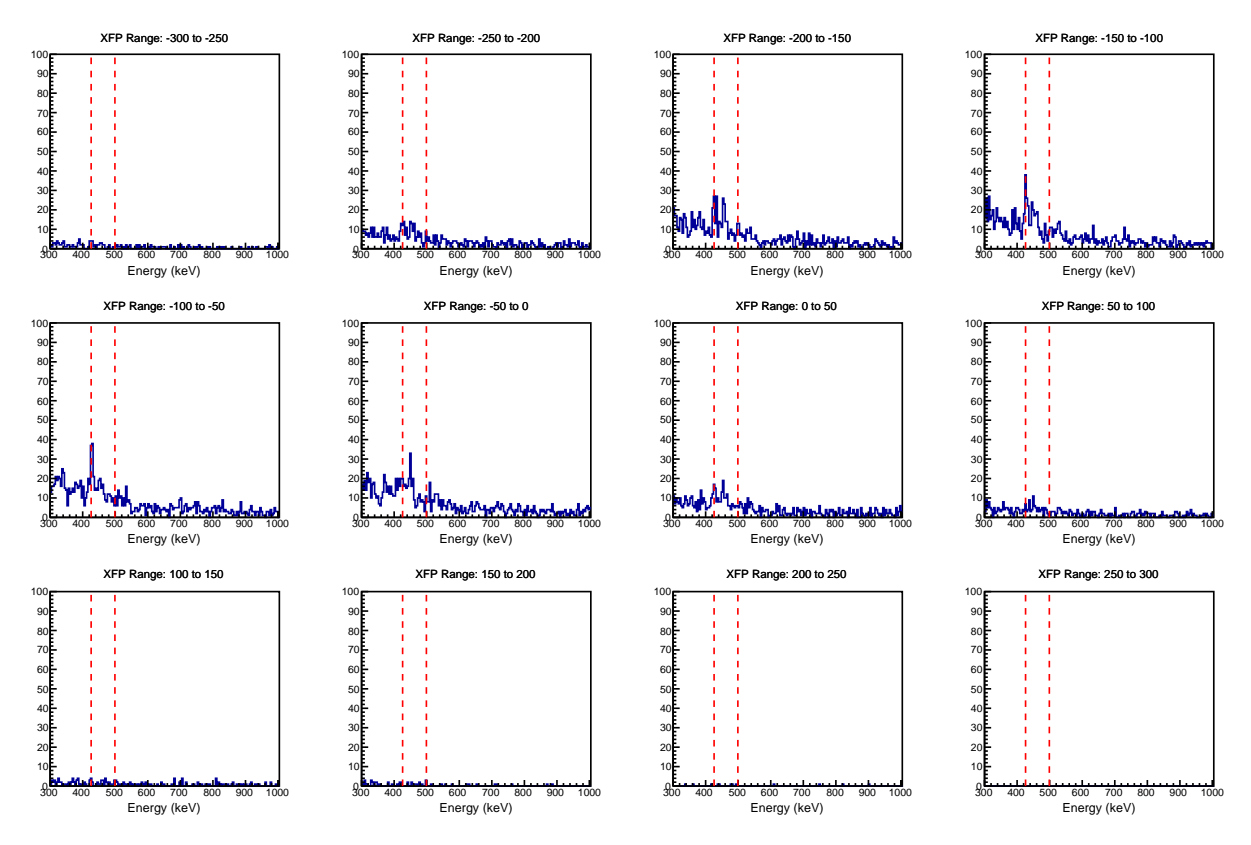


Figure 4.29: One-dimensional Doppler-corrected gamma-ray spectra per 50 mm of the S800 spectrograph's $x_{\rm fp}$ for $^{30}{\rm Na}$. The spectra have been optimized for reactions originating from the Ta foil. The dashed vertical red lines in each spectrum display the locations of the Ta components of the 426-keV and 499-keV transitions corresponding to the $(3^+) \rightarrow 2^+_{\rm g.s.}$ and $(4^+) \rightarrow (3^+)$ decays, respectively. The Ta component generally appears more prominent for negative $x_{\rm fp}$ values whereas the Be component becomes further pronounced towards positive values.

This characteristic of the gamma-ray spectrum was attributed to the kinematic behavior of the 30 Na as it traversed through the Be and the Ta foils, combined with the acceptance of the S800 spectrograph, depicted by the sharp cut off towards the negative $x_{\rm fp}$ region in Fig. 4.30. From the kinematic curves seen in Fig. 4.31, the 30 Na reaction product loses more energy as a function of laboratory-frame scattering angle from reaction on the Be foil. Thus, ions that have inelastically scattered from the Be foil have lost more energy and tend towards positive $x_{\rm fp}$ whereas those from

the Ta foil tend towards the more negative $x_{\rm fp}$ region.

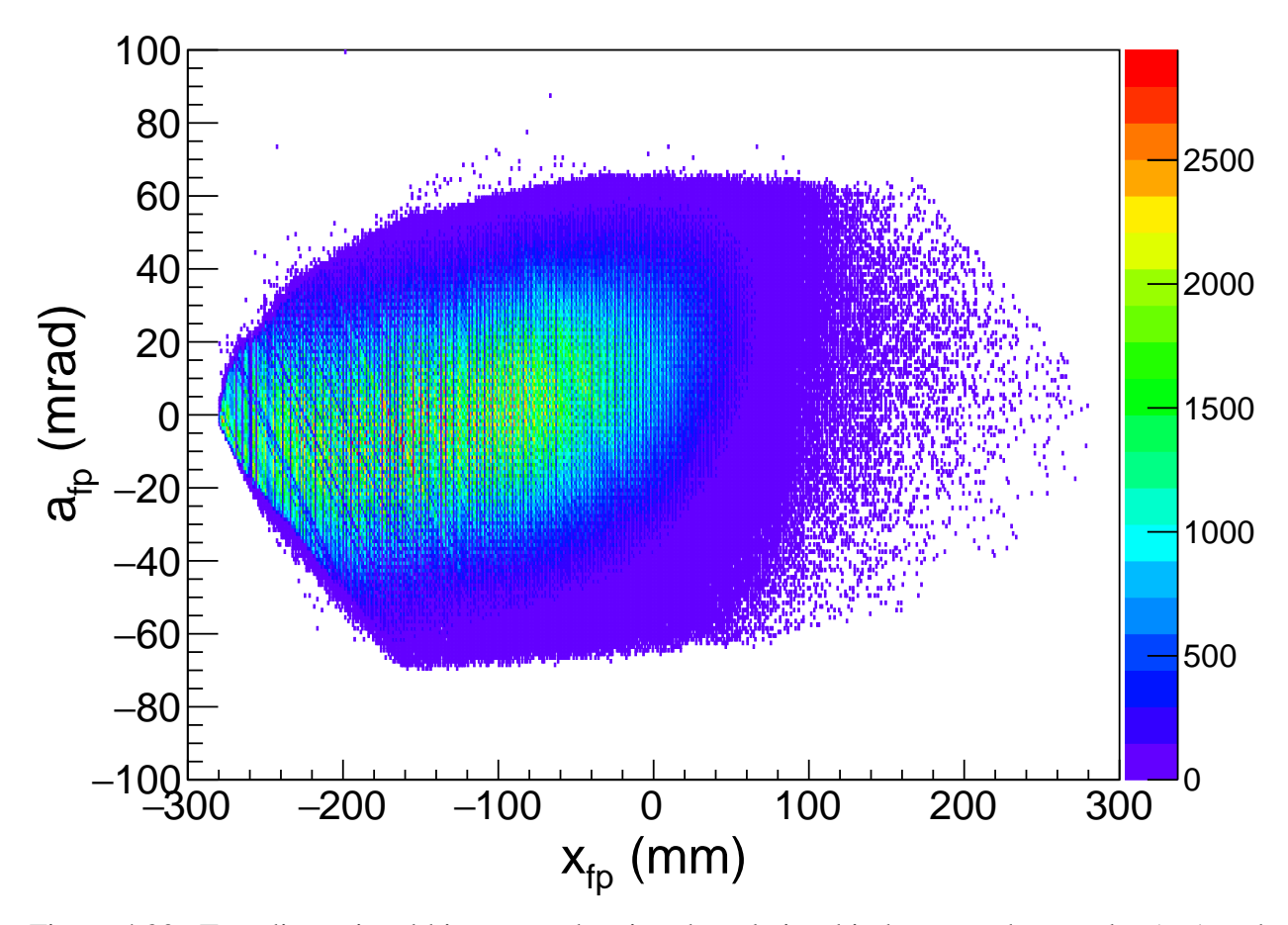


Figure 4.30: Two-dimensional histogram showing the relationship between the angular $(a_{\rm fp})$ and spatial $(x_{\rm fp})$ distributions of 30 Na ions at the focal plane of the S800 spectrograph. The spectrograph's acceptance is evidenced by the diagonal boundaries extending into both the positive and negative $x_{\rm fp}$ regions. The incoming 30 Na beam exhibits a non-uniform profile across $x_{\rm fp}$, skewing toward more negative $a_{\rm fp}$ values in the negative spatial region. A sharp cutoff in the beam is observed at large negative $x_{\rm fp}$ values, reflecting the acceptance limits of the S800 spectrograph.

From this assessment, it was deduced that the S800 spectrograph acceptance reduced the amount of gamma rays associated with excitations on the Ta foil, biasing the gamma-ray spectrum towards excitations on the Be foil. To address this, spectra were generated with $x_{\rm fp}$ between -300 and x_R , where x_R denotes to the right bound of an applied $x_{\rm fp}$ gate. Each spectrum was then fit to determine the ratio of gamma-ray efficiency corrected counts between the Ta and Be components, R_{γ} (Ta/Be). The selection criterion for x_R was guided by the requirement that the resulting R_{γ} (Ta/Be) value for 30 Na be consistent with those of 32 Mg (~ 1.5) and 31 Na (~ 1.38). This approach assumed

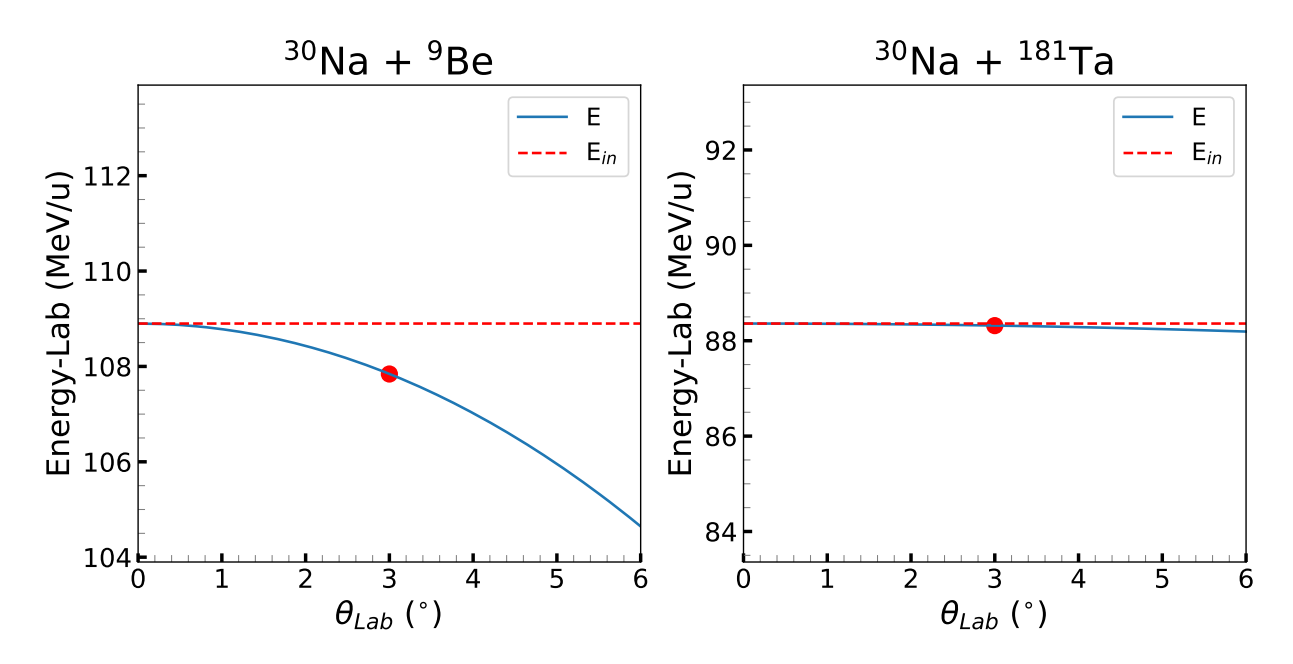


Figure 4.31: Kinematic curves for 30 Na + 9 Be (left) and 30 Na + 181 Ta (right) scattering calculated with LISE++ [123–125]. The dashed horizontal red line corresponds to the energy the ion had before any reaction took place.

that $R_{\gamma}(\text{Ta/Be})$ values should be comparable between $^{32}\text{Mg},^{31}\text{Na}$, and ^{30}Na , given that all three undergo similar reaction process (i.e. inelastic scattering). Due to the smaller atomic number for Na isotopes, slightly smaller values in $R_{\gamma}(\text{Ta/Be})$ are expected compared to ^{32}Mg , as seen in the ^{29}Ne case in Ref. [76]. From this analysis, the right bound was selected to be $x_R = -50$ resulting in a $R_{\gamma}(\text{Ta/Be}) \sim 1.0$ for ^{30}Na consistent with ^{32}Mg and ^{31}Na . The resulting two-dimensional gamma-ray histogram is shown in Fig. 4.32, where the *y*-axis indicates the angle at which the gamma ray was detected in GRETINA and the *x*-axis corresponds to the Doppler-corrected energy. The associated one-dimensional spectrum for ^{30}Na with gamma rays detected up to 55° from the laboratory-frame *z* axis is shown in Fig. 4.33 with $R_{\gamma}(\text{Ta/Be}) \sim 1.0$.

The two-peak structure in Fig. 4.33 can be explained with the illustration in Fig. 4.34. The 25 mm separation between the Be and Ta foils ensured that all excitations originating in the Be foil decayed before reaching the Ta foil. This is illustrated in Fig. 4.34 (a) by the blue (Be component) and red (Ta component) arrows, along with the corresponding two-dimensional histogram in Fig. 4.34 (b) highlighting the associated components. Figure 4.34 (b) shows a two-dimensional

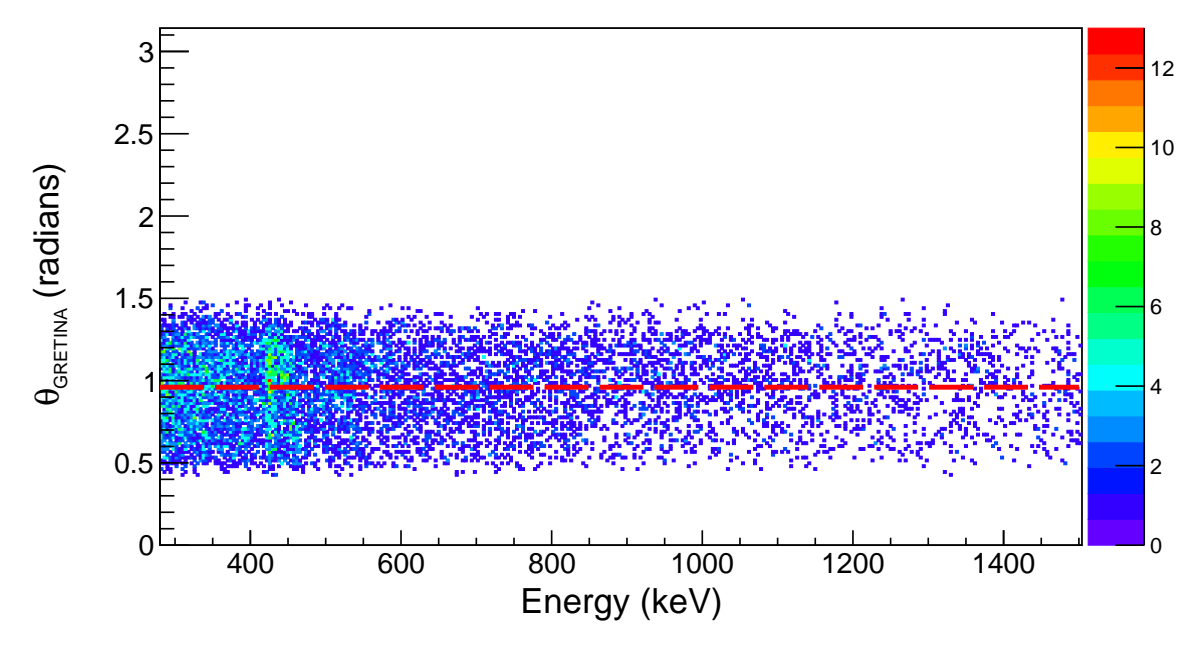


Figure 4.32: Two-dimensional Doppler-corrected gamma-ray spectrum for 30 Na, optimized for reactions on the Tantalum (Ta) foil. The *y*-axis shows the gamma-ray emission angle, defined by the main interaction point in GRETINA, while the *x*-axis corresponds to the Doppler-corrected gamma-ray energy. Due to limited statistics, only the $(3^+) \rightarrow 2^+_{g.s.}$ transition components originating from reactions on the Be and Ta foils are distinctly visible. The lower-energy line is associated with the de-excitation of the (3^+) state following reactions on the Ta foil, while the higher-energy line corresponds reactions on the Be foil. The horizontal dashed red line corresponds to the angle cut $\theta_{GRETINA} \leq 55^{\circ}$ that was imposed.

histogram Doppler-corrected for excitations on the Ta foil, resulting in a straight red band (Ta component) and a diagonally spread blue band (Be component).

4.6.3 $2_{g,s}^+ \to (4^+)$ Excitation

The excitation cross section to the (4^+) state in 30 Na was extracted by quantifying the gamma-ray efficiency-corrected counts from the $(4^+) \rightarrow (3^+)$ and $(4^+) \rightarrow 2^+_{g.s.}$ transitions having 925- and 499-keV de-excitation energies, respectively [55, 126]. This state was simulated at an excitation energy of 925 keV [54–56, 126, 127], assuming a mean lifetime of $\tau = 5$ ps. The lifetime was estimated by fitting the simulated line shape to the experimental spectrum. A more detailed lifetime analysis was not possible due to the lack of multiple target distance settings in this experiment [24,

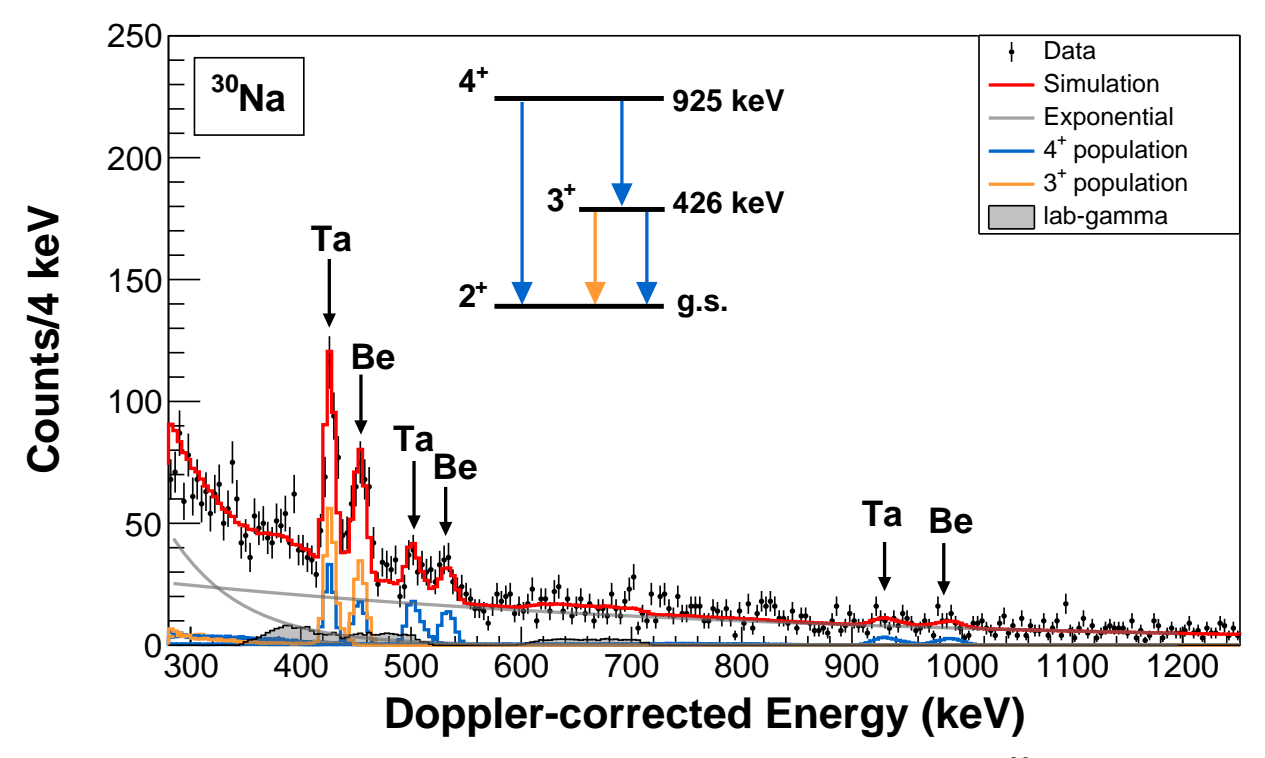


Figure 4.33: One-dimensional Doppler-corrected gamma-ray spectrum for ³⁰Na, optimized for reactions originating on the Tantalum (Ta) foil, gated for the laboratory-frame gamma-ray GRETI-INA detection angle up to 55°. A separate gate was applied to restrict the laboratory scattering angle up to 3°. The data are represented with black dots and error bars, with laboratory-frame background contributions shown in gray. Simulated decay of the (3⁺) state populated directly in the reaction is shown by the orange histograms, while gamma-ray decays associated with the (4⁺) direct population are represented by the blue histograms. The sum of all components is shown by the red histogram. The Tantalum (Ta) and Beryllium (Be) peaks for each transition are marked accordingly.

58, 90, 121, 128, 129]. Both transitions were simulated independently, with separate simulations also performed for the Be and Ta components. Yields associated with the direct population of the (4^+) state are indicated by the blue arrows and histograms in Fig. 4.33. The peaks labeled **Ta** correspond to reactions originating on the Tantalum foil (i.e. Tantalum gamma-ray peak) and those originating from the Beryllium foil (i.e. Beryllium gamma-ray peak) are labeled with **Be**. The excitation cross section to the (4^+) state (σ_{4^+}) was determined via the equation

$$Y_{\gamma} = \left(\frac{\Phi_{\rm IB}}{\epsilon_{\rm IB}^{\rm acc.}}\right) N \sigma_{4^{+}} \epsilon_{\gamma} \epsilon_{\rm RP}^{\rm acc.}$$
(4.24)

where the incoming beam ($\epsilon_{\rm IB}^{\rm acc.}$) and reaction products ($\epsilon_{\rm RP}^{\rm acc.}$) S800 acceptances are those quoted

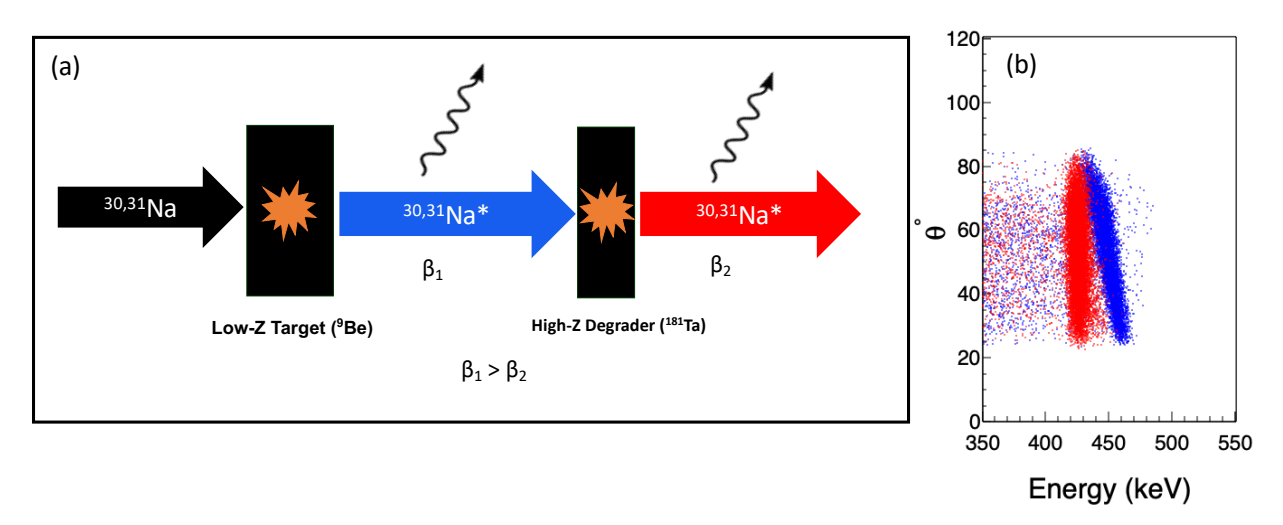


Figure 4.34: Effect of the 25 mm target separation on emitted gamma rays. Panel (a) illustrates gamma-ray emission following reactions on the Be (blue) and Ta (red) foils. Panel (b) shows the corresponding two-dimensional histogram, with GRETINA detector angle on the *y*-axis and Doppler-corrected energy on the *x*-axis. The energy correction in panel (b) has been optimized for gamma rays originating from the Ta foil.

in Sects. 4.3.1.1 and 4.3.1.2. As shown in Eq. 4.24, the cross section depends on the ratio of $\epsilon_{\rm IB}^{\rm acc.}/\epsilon_{\rm RP}^{\rm acc.}$, not on the absolute value of each individual acceptance. Furthermore, part of the systematic error associated with determining the cross section depends on the accuracy of the ratio. Due to the dependence on the ratio and not the absolute values themselves, this ensured that the systematic errors in the acceptance calculations described in Sects. 4.3.1.1 and 4.3.1.2 are well under control. The gamma-ray efficiencies for each transition were determined by following the procedure described in Sect. 3.5.3. The target number density N is given by

$$N = t \frac{N_A}{m_A} \tag{4.25}$$

where N_A is Avogadro's number, m_A is the atomic mass (A) of the material, and t is the thickness of the material. The areal density of the foil was determined from a weight measurement and known dimensions of the foil, allowing the foil thickness to be determined if the material density (ρ) is well known. For this experiment, the 9 Be and 181 Ta foils were measured to have a thickness of 0.370 g/cm² and 2.158 g/cm², respectively. The incoming beam was determined from the S800 spectra that were produced from the software gate selecting the 30 Na beam (seen in red in Fig. 4.27).

The gamma-ray yield Y_{γ} was determined from the gamma-ray counts from the $(4^+) \rightarrow (3^+)$ and $(4^+) \rightarrow 2^+_{g.s.}$ transitions.

No dead-time corrections were applied to the detected gamma rays or the number of incoming projectiles. The S800 data acquisition system is triggered by the E1 scintillator located at the focal plane, which experiences periods of dead time during signal processing. Broadly stated, GRETINA can be coupled to auxiliary systems (such as the S800 spectrograph) to receive external trigger signals to readout data stored locally on digitizers. The coupled S800-GRETINA data acquisition system ensures that GRETINA events are properly correlated with the corresponding E1 scintillator events. Since both the gamma-ray readout in GRETINA and the time-of-flight method used to determine the number of incoming beam projectiles rely on the E1 scintillator, any associated dead-time effects effectively negate in Eq. 4.24.

To account for an unknown amount of beam loss caused by the S800 spectrograph – evident from the sharp diagonal cutoff at negative $x_{\rm fp}$ values in Fig. 4.30 – an additional incoming beam gate was applied, while all other gates remained unchanged. This additional gate excluded a region of the $x_{\rm fp}$ in which beam particles were lost due to the spectrograph's acceptance. The difference between the cross section extracted using this modified gate and the original cross section from Fig. 4.33 was added in quadrature to the total uncertainty. The angle-integrated inelastic scattering cross sections for the direct population of the low-lying (4⁺) state in 30 Na for the Be and Ta foils are shown in Table 4.3.

| | $J_i^\pi 	o J_f^\pi$ | Е | $\sigma(3^{\circ})^{\text{Be}}_{\text{exp.}}$ | $\sigma(3^{\circ})_{\text{exp.}}^{\text{Ta}}$ |
|------------------|------------------------------------|-------|---|---|
| | J | (keV) | (mb) | (mb) |
| ³⁰ Na | $2_{\rm g.s.}^+ \rightarrow (4^+)$ | 925 | 5(1) | 18(4) |

Table 4.3: Inelastic scattering cross sections for the $2^+_{g.s.} \to (4^+)$ excitation in 30 Na from the present work. Cross sections for each foil were obtained from the $(4^+) \to (3^+)$ and $(4^+) \to 2^+_{g.s.}$ decays. Results for both Be and Ta targets are shown.

The reduced transition strength $B(E2, 2_{g.s.}^+ \to (4^+))$ was extracted by comparing the experimentally determined cross sections in Table 4.3 to angle-integrated cross sections from coupled-channel

calculations performed with FRESCO [80, 130], following the procedures described in Refs. [76, 83]. This process is outlined in Fig. 4.35. To meaningfully compare the experimental cross sections with the coupled-channel calculation, the beam characteristics – namely, the incoming beam profile, finite beam spot size, and angular distribution – were incorporated into the monte carlo simulation together with differential cross section calculations obtained from FRESCO, as discussed in Sects. 4.2.1 and 4.3.1. Due to the lack of elastic scattering data for the present reaction, the set of optical model parameters from the $^{17}\text{O} + ^{208}\text{Pb}$ reaction [81] were adopted into this analysis. To assess the sensitivity of the results to the choice of optical model parameters, an alternative theoretically-derived potential was employed [109], constructed from a complex G-matrix interaction, CEG07 [115, 116]. Due to the restriction of the derived optical model potentials from Ref. [109] being limited to even-even projectile nuclei with a target mass range of A = 12 - 208, the $^{32}\text{Mg} + ^{12}\text{C}$ and $^{32}\text{Mg} + ^{181}\text{Ta}$ potentials were calculated for the $^{30,31}\text{Na} + ^{9}\text{Be}$ and $^{30,31}\text{Na} + ^{181}\text{Ta}$ reactions.

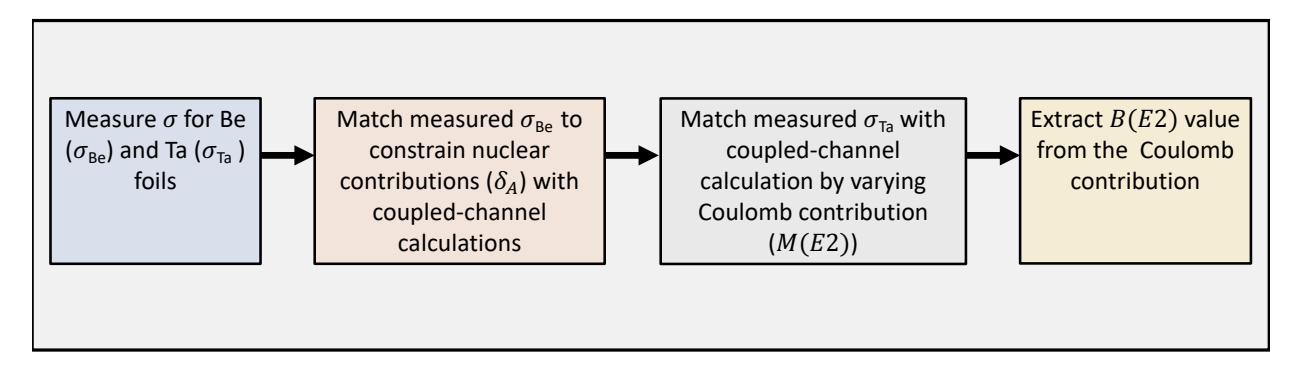


Figure 4.35: Diagram outlining the general procedure used in obtaining the nuclear deformation length δ_A and the reduced transition strength $B(E2 \uparrow)$.

The two main parameters varied in the FRESCO analysis were the nuclear deformation length, δ_A , and the reduced electromagnetic E2 matrix element, M(E2). In FRESCO, the evaluation of the reduced matrix element is model dependent [131, 132], and in the simple axially symmetric deformed rotor model, it is defined as [131]

$$M(E2) = \frac{\langle J_f || O(E2) || J_i \rangle}{\sqrt{2J_i + 1} \langle J_i K20 | J_f K \rangle}$$

$$\tag{4.26}$$

where $\langle J_f || O(E2) || J_i \rangle$ is the reduced E2 matrix element, K is the rotational band head, $\langle J_i K20 | J_f K \rangle$ is the Clebsh-Gordan coefficient, and M(E2) is the intrinsic E2 matrix element. The E2 reduced transition strength is then given by [7, 31]

$$B(E2; J_i \to J_f) = \frac{|\langle J_f || O(E2) || J_i \rangle|^2}{(2J_i + 1)}$$
(4.27)

We first investigated the nuclear deformation lengths, where results using the measured cross sections to the (4^+) from excitations occurring on the 9 Be foil are summarized in Table 4.4.

$$\frac{\delta_A (fm)}{J_i^{\pi} \to J_f^{\pi}} \quad \frac{\delta_A (fm)}{^{17}\text{O} + ^{208}\text{Pb}} \quad ^{32}\text{Mg} + ^{12}\text{C}$$

$$\frac{^{30}\text{Na} \quad 2_{\text{g.s.}}^{+} \to (4^{+}) \quad 1.51(^{+0.17}_{-0.20}) \quad 1.38(^{+0.16}_{-0.18})}{^{12}\text{Ng}}$$

Table 4.4: Extracted nuclear matter deformation lengths (δ_A) from inelastic scattering on the 9 Be target for the $2^+_{g.s.} \rightarrow (4^+)$ excitation. Results from the 17 O + 208 Pb [81] and 32 Mg + 181 Ta [109] optical model potentials are listed.

The $B(E2\uparrow)$ strengths were extracted by determining the E2 matrix elements from the measured 181 Ta foil cross sections, which assumed equal amounts of nuclear contributions between the Ta and Be foils. Similarly, using the deformation lengths obtained from each optical model potential, the corresponding $B(E2\uparrow)$ strengths are shown in Table 4.5. Although the results are in good agreement, the dependence on optical potential is not negligible. Therefore, an average was determined from the two obtained $B(E2\uparrow)$ values, where error includes both statistical and systematic contributions, including those arising from the choice of potential.

$$\frac{B(E2\uparrow) (e^2 fm^4)}{J_i^{\pi} \to J_f^{\pi}} \frac{B(E2\uparrow) (e^2 fm^4)}{^{17}\text{O} + ^{208}\text{Pb}} \frac{^{32}\text{Mg} + ^{181}\text{Ta}}{^{32}\text{Mg} + ^{181}\text{Ta}} \text{Avg.}$$

$$\frac{^{30}\text{Na} \quad 2_{\text{g.s.}}^{+} \to (4^+)}{^{32}\text{Mg} + ^{22}\text{Ng}} \frac{64(_{-33}^{+26})}{^{42}} \frac{64(_{-33}^{+26})}{^{42}}$$

Table 4.5: Extracted reduced transition probabilities to the (4⁺) state, $B(E2, 2_{g.s.}^+ \rightarrow (4^+))$, from inelastic scattering on the ¹⁸¹Ta target and δ_A from Table 4.4. Results from the ¹⁷O + ²⁰⁸Pb [81] and ³²Mg + ¹⁸¹Ta [109] optical model potentials are listed. Averages are also shown.

4.6.4 $2_{g,s}^+ \to (3^+)$ Excitation

The excitation cross section to the (3^+) state in 30 Na was determined by analyzing gamma-ray efficiency-corrected counts from the 426-keV $(3^+) \rightarrow 2^+_{g.s.}$ transition, while accounting for feeding from the $(4^+) \rightarrow (3^+)$ decay. This state was simulated at an excitation energy of 426 keV [54–56, 126, 127], assuming a mean lifetime of $\tau = 18$ ps. The lifetime was estimated by fitting the simulated line shape to the experimental spectrum. A more detailed lifetime analysis was not possible due to the lack of multiple target distance settings in this experiment [24, 58, 90, 121, 128, 129]. Separate simulations were generated for the Be and Ta foil components, where yields associated with the direct population of the (3^+) state are indicated by the orange arrow and histograms in Fig. 4.33. The peaks labeled **Ta** correspond to reactions originating on the Tantalum foil (i.e. Tantalum gamma-ray peak) and those originating from the Beryllium foil (i.e. Beryllium gamma-ray peak) are labeled with **Be**. The excitation cross section to the (3^+) state (σ_{3^+}) was determined via Eq. 4.24. A process identical to what was described for the $2^+_{g.s.} \rightarrow (4^+)$ excitation (Sect. 4.6.3) was performed for the $2^+_{g.s.} \rightarrow (3^+)$ case.

4.6.4.1 Gamma-Ray Yield Feeding Corrections

To accurately determine the (3^+) excitation cross section, it was necessary to account for feeding contributions from the higher-lying (4^+) state reactions arising from the Ta and Be foils. This was achieved by simulating – for each foil – the cascade resulting from the direct population of the (4^+) state, namely, the $(4^+) \rightarrow (3^+)$ and $(3^+) \rightarrow 2^+_{g.s.}$ sequence. This sequence was simulated independently from the $(4^+) \rightarrow 2^+_{g.s.}$ decay. In this manner, the Be and Ta components associated with each transition were determined. Having obtained all the components, the observed $(3^+) \rightarrow 2^+_{g.s.}$ transition was distinctly composed of contributions from the direct population of both the (4^+) and (3^+) states, along with background components. Thus, the angle-integrated inelastic scattering cross sections for the direct population of the low-lying (3^+) state in 30 Na for the Be and Ta foils – summarized in Table 4.6 – were calculated from decays stemming only from the direct population of the (3^+) state.

| | $J_i^\pi 	o J_f^\pi$ | E | $\sigma(3^{\circ})^{\text{Be}}_{\text{exp.}}$ | $\sigma(3^{\circ})_{\rm exp.}^{\rm Ta}$ |
|------------------|------------------------------------|-------|---|---|
| | J | (keV) | (mb) | (mb) |
| ³⁰ Na | $2_{\rm g.s.}^+ \rightarrow (3^+)$ | 426 | 9(2) | 32(5) |

Table 4.6: Inelastic scattering cross sections for the $2_{g.s.}^+ \rightarrow (3^+)$ transition in 30 Na from the present work. Results for both Be and Ta targets are shown.

From the deduced cross sections listed in 4.6, the nuclear deformation lengths (δ_A) and E2 reduced transition strengths $B(E2, 2^+_{g.s.} \to (3^+))$ were determined. The process to determine each value followed the diagram in Fig. 4.35, where the process taken is identical to what is described in Sect. 4.6.3. The extracted δ_A values are listed in Table 4.7, with the associated $B(E2, 2^+_{g.s.} \to (3^+))$ presented in Table 4.8. While the results show good agreement, the dependence on the choice of optical model potential is not negligible. Consequently, the adopted $B(E2 \uparrow)$ value was taken as the average of the two, with the uncertainty containing both statistical and systematic contributions, including those associated with the optical potential.

$$\frac{\delta_A (fm)}{J_i^{\pi} \to J_f^{\pi}} \quad \frac{\delta_A (fm)}{^{17}\text{O} + ^{208}\text{Pb}} \quad ^{32}\text{Mg} + ^{12}\text{C}$$

$$\frac{^{30}\text{Na}}{^{2}\text{g.s.}} \to (3^+) \quad 1.37(^{+0.12}_{-0.13}) \quad 1.26(^{+0.11}_{-0.12})$$

Table 4.7: Extracted nuclear matter deformation lengths (δ_A) from inelastic scattering on the 9 Be target for the $2^+_{\rm g.s.} \to (3^+)$ excitation. Results from the $^{17}{\rm O}$ + $^{208}{\rm Pb}$ [81] and $^{32}{\rm Mg}$ + $^{181}{\rm Ta}$ [109] optical model potentials are listed.

$$\frac{B(E2\uparrow) (e^2 f m^4)}{J_i^{\pi} \to J_f^{\pi}} \frac{B(E2\uparrow) (e^2 f m^4)}{^{17}\text{O} + ^{208}\text{Pb}} \frac{^{32}\text{Mg} + ^{181}\text{Ta}}{^{32}\text{Mg} + ^{181}\text{Ta}} \frac{\text{Avg.}}{^{30}\text{Na}}$$

$$\frac{^{30}\text{Na} \quad 2_{\text{g.s.}}^{+} \to (3^+) \quad 129(^{+28}_{-32}) \quad 113(^{+32}_{-40}) \quad 122(^{+34}_{-39})}{^{32}\text{Ng} + ^{181}\text{Ta}} \frac{^{32}\text{Ng}}{^{32}\text{Ng} + ^{181}\text{Ta}} \frac{^{32}\text{Ng}}{^{32}\text{Ng}}$$

Table 4.8: Extracted reduced transition probabilities to the (3⁺) state, $B(E2, 2_{\rm g.s.}^+ \to (3^+))$, from inelastic scattering on the ¹⁸¹Ta target and δ_A from Table 4.7. Results from the ¹⁷O + ²⁰⁸Pb [81] and ³²Mg + ¹⁸¹Ta [109] optical model potentials are listed. Averages are also shown.

The branching ratios for the $(4^+) \rightarrow (3^+)$ and $(4^+) \rightarrow 2^+_{g.s.}$ transitions were determined from the gamma-ray spectrum over the full S800 x_{fp} range. Owing to the experimental setup, these

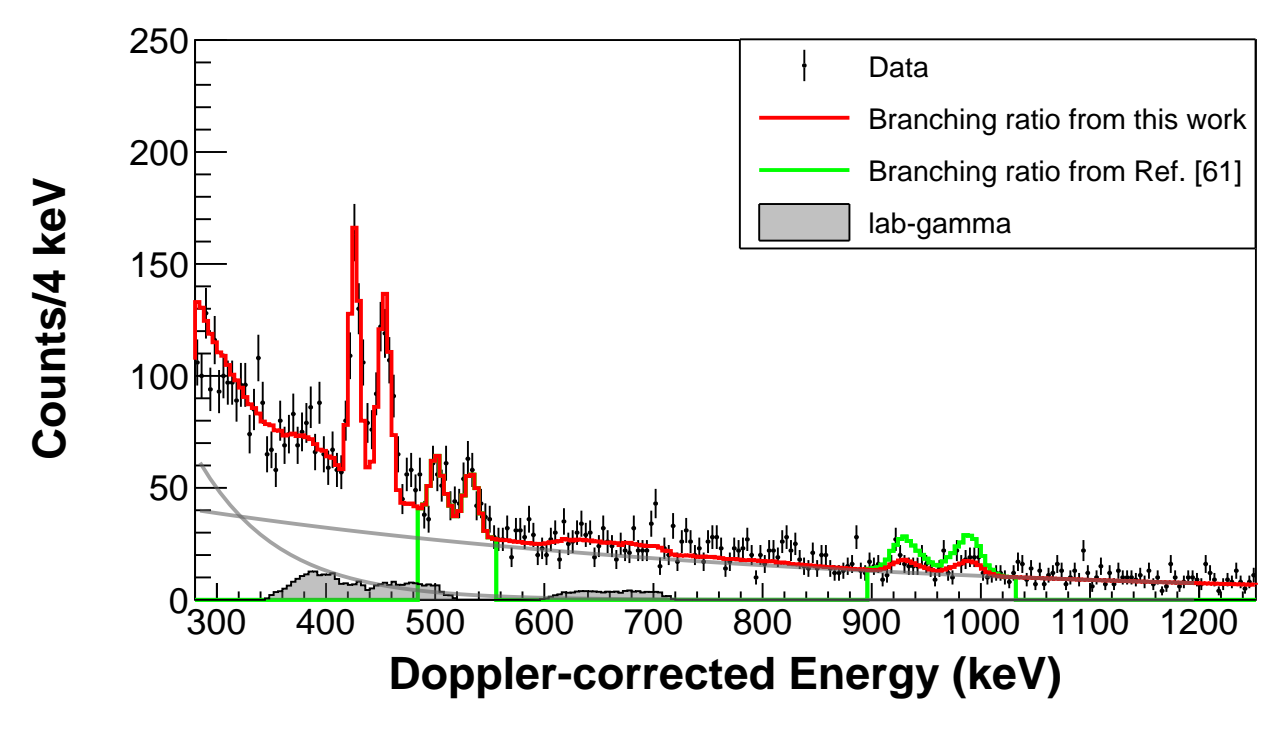


Figure 4.36: Comparison of branching ratios obtained in the present work with those reported in Refs. [55, 126]. The gamma-ray spectrum was generated using the full $x_{\rm fp}$ range (-300 to 300) to determine the branching ratios. The red histogram represents a simulation based on the branching ratios obtained from this work, while the green histogram corresponds to the literature values. The individual components de-exciting the (3⁺) and (4⁺) states were constrained in the same manner as in Fig. 4.33, but are not shown here. For reference, the red histogram based on the branching ratios determined in this work is overlaid with the prediction using the values reported in Ref. [126] for the (4⁺) \rightarrow (3⁺) transition near 500 keV. The disagreement between the green histogram and the experimental data highlights the inconsistency of the literature values.

ratios were independently extracted from decay components associated with the Ta and Be foils. The results obtained from the two foils were consistent within 1%, with their average producing branching ratios of 77(16)% for the $(4^+) \rightarrow (3^+)$ transition and 23(11)% for the $(4^+) \rightarrow 2^+_{g.s.}$ transition. Conversely, previous measurements reported in Refs. [55, 126] found significantly different values for these transitions. Namely, Petri *et al.* [126] report 40(5)% and 60(8)% while Seidlitz *et al.* [55] report 33(10)% and 67(10)% for the $(4^+) \rightarrow (3^+)$ and $(4^+) \rightarrow 2^+_{g.s.}$ transitions, respectively. To examine the discrepancy in branching ratios, a simulation incorporating the values reported in Refs. [55, 126] was compared with the experimental gamma-ray spectrum from this work. As shown by the green histograms in Fig. 4.36, the simulation predicts a $(4^+) \rightarrow 2^+_{g.s.}$ yield

nearly twice that of the red histogram, which is incompatible with the present data. Notably, the present dataset provides significantly improved statistics and energy resolution for the 499-keV $(4^+) \rightarrow (3^+)$ transition compared to earlier measurements.

4.7 ³¹Na Analysis

The determination of reduced transition strengths to the low-lying $(5/2^+)$ and $(7/2^+)$ excited states in 31 Na broadly involves quantifying the gamma rays detected by GRETINA, evaluating GRETINA's gamma-ray efficiency (Sect. 3.5.3), accurately modeling the incoming beam and reaction products (Sect. 4.1.2.1), assessing the acceptance of the S800 spectrograph as a function of scattering angle (Sect. 4.3), and performing coupled-channel calculations with FRESCO (Sect. 4.2.1). This section details the procedures undertaken to extract the $B(E2; 3/2^+_{g.s.} \to 5/2^+)$ and $B(E2; 3/2^+_{g.s.} \to 7/2^+)$ transition strengths in 31 Na.

4.7.1 Particle Identification of ³¹Na

The secondary 31 Na beam was identified through time-of-flight (TOF) measurements, as illustrated in Fig. 4.37, using the scintillator detectors described in Sect. 4.4. A software gate – highlighted in red in the figure – was applied to selectively isolate the 31 Na component. Worth noting is the software gate selecting the 31 Na ions excluding a portion of beam. This was done due to the 31 Na cluster displaying two distinct components with different intensities. This distinction was made evident when analyzing the reconstructed energy distributions of the ions. The more intense and central component was selected for this work. In Fig. 4.37, the ion flight time increases downward along the *y*-axis and leftward along the *x*-axis.

The software gate highlighted in red in Fig. 4.37 was applied to generate the outgoing particle identification (PID) spectrum shown in Fig. 4.38. In this histogram, the *y*-axis represents the average energy loss of each ion across the 16 sub-ion chambers (see Sect. 3.4.3), while the *x*-axis corresponds to the time-of-flight difference between the E1 and OBJ scintillators. The most prominent cluster in Fig. 4.38 comprises both elastically and inelastically scattered ³¹Na ions. A

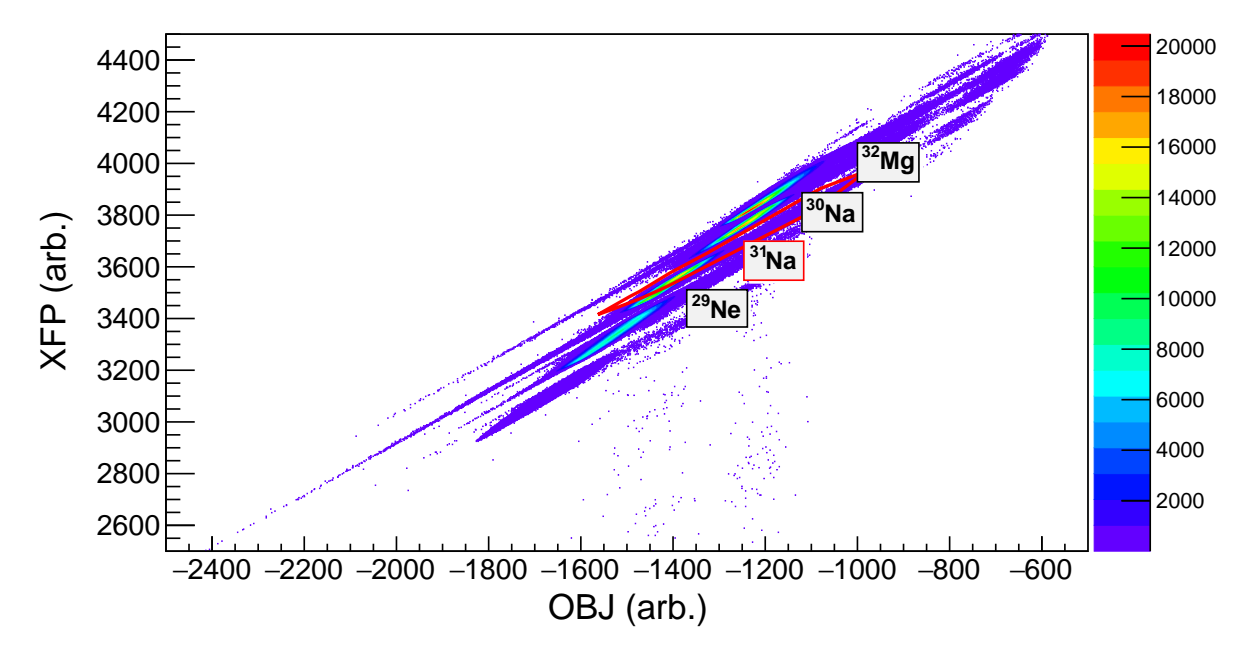


Figure 4.37: Secondary beam components separated by the time-of-flight (TOF) technique. The time-of-flight technique relies on timing differences between a reference timing signal produced from a scintillator located within the S800 focal plane (E1), and two timing signals produced by scintillators located at the A1900 focal plane (XFP) and Object station (OBJ). Both axes are defined relative to the E1 reference signal: the y-axis represents the timing difference between E1 and XFP, whereas the x-axis shows the difference between E1 and OBJ. The red line represents a software gate applied to select the 31 Na incoming beam.

red circular line marks the software gate used to isolate the ³¹Na reaction products. Although other reaction products are visible, they were excluded from further analysis due to their limited statistical significance and lack of relevance to this study.

4.7.2 Gamma-Ray Spectrum

A time gate (similar to Fig. 4.23) was applied to isolate the prompt gamma rays from most background contributions. To best distinguish between the Ta and Be peaks, gamma rays detected at angles up to 55° from the laboratory-frame z-axis were selected, as indicated by the red line in Fig. 4.39. Furthermore, a scattering angle of 3° , taken from the laboratory-frame z-axis, was imposed on the 31 Na reaction products.

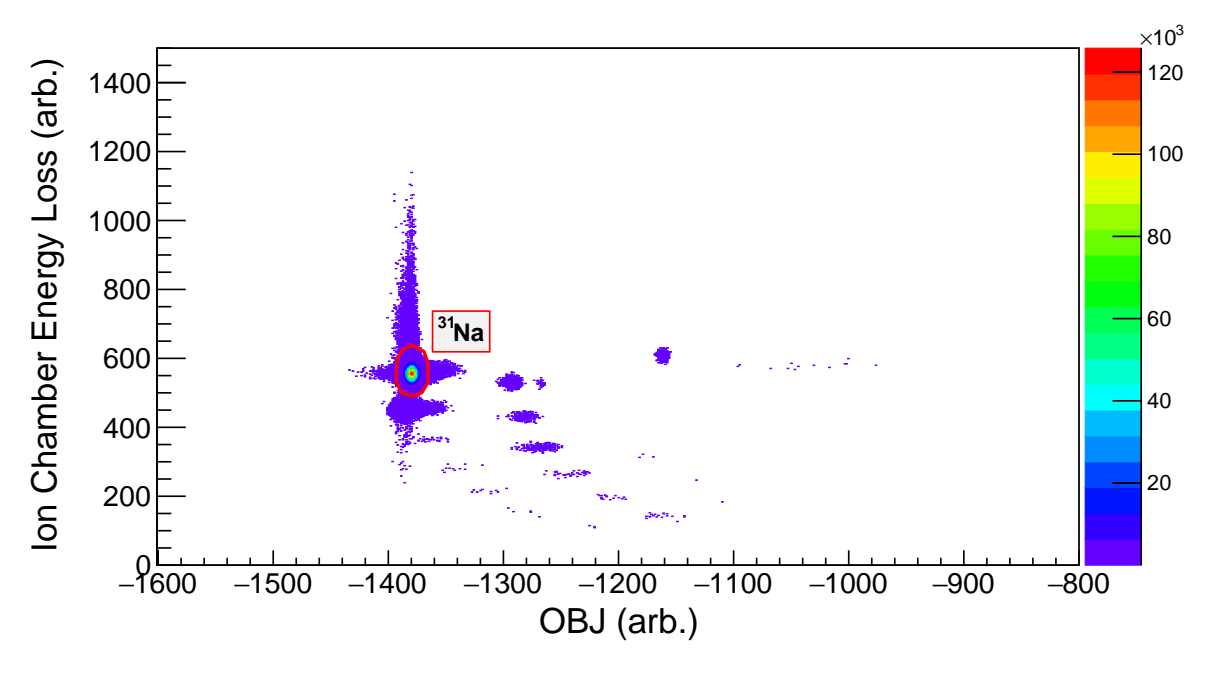


Figure 4.38: Particle identification plot (PID) produced from applying a software gate selecting the ³¹Na secondary beam. The *y*-axis corresponds to energy loss in the S800 focal plane ion chamber with the *x*-axis representing the time-of-flight difference between the E1 and OBJ signals. The most prominent cluster corresponds to ³¹Na ions that reached the S800 focal plane. A software gate, shown as a red circle, was applied to select the scattered ³¹Na ions after passing through the TRIPLEX device holding the Beryllium and Tantalum target foils. This ensured that the resulting gamma-ray spectrum contained inelastically scattered ³¹Na ions.

The two-peak structure in Fig. 4.40 can be best understood via the illustration in Fig. 4.34. Due to the large separation distance (25 mm) between the two foils, all excitations stemming from the Be foil decay before reaching the subsequent Ta foil. The excitations from each foil are illustrated in Fig. 4.34 (a) by the blue (Be component) and red (Ta component) arrows. The corresponding decays are shown in Fig. 4.34 (b) as a two-dimensional histogram of GRETINA detection angle versus Doppler-corrected energy, where the de-excitations have been optimized for reactions occurring on the Ta foil.

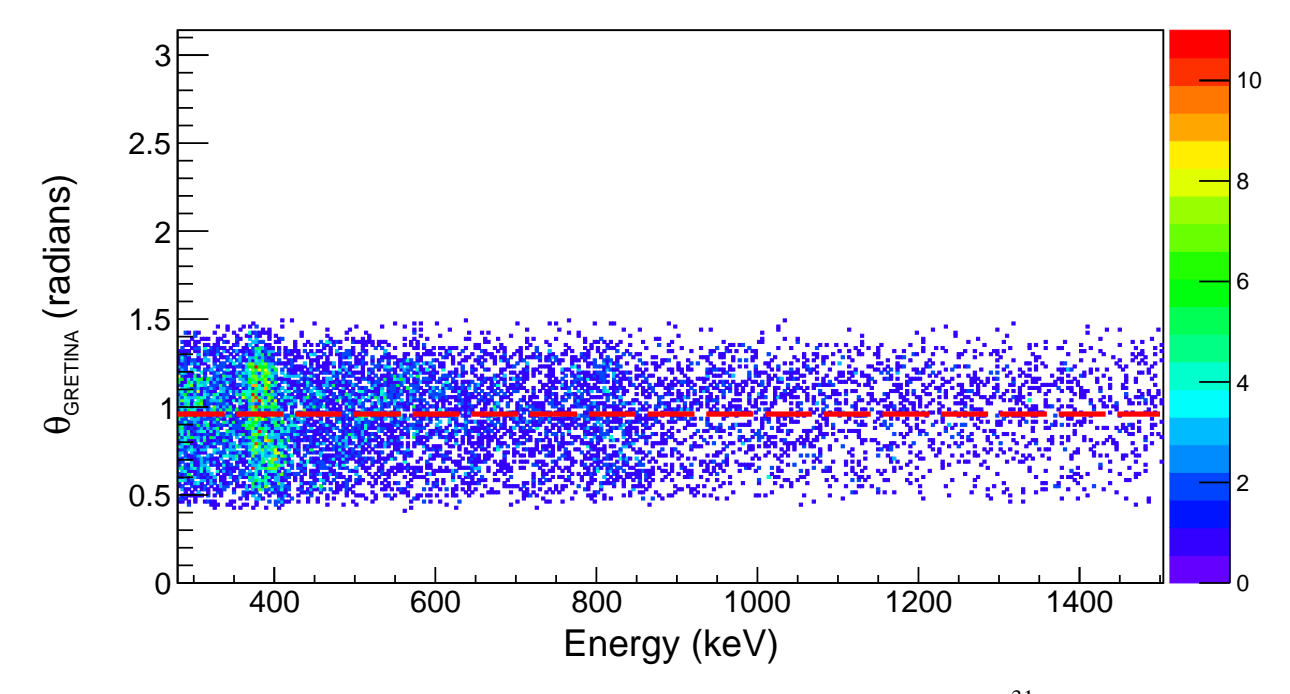


Figure 4.39: Two-dimensional Doppler-corrected gamma-ray spectrum for 31 Na, optimized for reactions on the Tantalum (Ta) foil. The *y*-axis shows the gamma-ray emission angle, defined by the main interaction point in GRETINA, while the *x*-axis corresponds to the Doppler-corrected gamma-ray energy. Due to limited statistics, only the $(5/2^+) \rightarrow 3/2^+_{\rm g.s.}$ transition components originating from reactions on the Be and Ta foils are distinctly visible, whereas only a hint of the two-peak structure for the $(7/2^+) \rightarrow (5/2^+)$ decay is apparent at 800 keV. The lower-energy line is associated with the de-excitation of the $(5/2^+)$ state following reactions on the Ta foil, while the higher-energy line corresponds reactions on the Be foil. The horizontal dashed red line corresponds to the angle cut $\theta_{\rm GRETINA} \leq 55^{\circ}$ that was imposed.

4.7.3 $3/2_{g,s}^+ \rightarrow (7/2^+)$ Excitation

The excitation cross section to the $(7/2^+)$ state in 31 Na was extracted by quantifying the gamma-ray efficiency-corrected counts from the $(7/2^+) \rightarrow (5/2^+)$ transition with a 797 keV de-excitation energy [36, 66, 127, 133]. This state was simulated at an excitation energy of 1171 keV [134], assuming a mean lifetime of $\tau = 3$ ps. The determination of the $\tau = 3$ ps is described in greater detail in Sect. 4.7.5. The transitions originating from reactions on the Ta and Be foils were simulated independently. The decays associated with the direct population of the $(7/2^+)$ state are indicated by the blue arrows and histograms in Fig. 4.40. The peaks labeled **Ta** correspond to reactions originating on the Tantalum foil (i.e. Tantalum gamma-ray peak) and those originating from the

Beryllium foil (i.e. Beryllium gamma-ray peak) are labeled with **Be**. The excitation cross section to the $(7/2^+)$ state $(\sigma_{7/2^+})$ was determined via the equation

$$Y_{\gamma} = \left(\frac{\Phi_{\rm IB}}{\epsilon_{\rm IB}^{\rm acc.}}\right) N \sigma_{7/2^{+}} \epsilon_{\gamma} \epsilon_{\rm RP}^{\rm acc.}$$
(4.28)

where the incoming beam ($\epsilon_{\rm IB}^{\rm acc.}$) and reaction products ($\epsilon_{\rm RP}^{\rm acc.}$) S800 acceptances are those quoted in Sects. 4.3.1.1 and 4.3.1.2. The gamma-ray efficiencies for each transition were determined by following the procedure outlined in Sect. 3.5.3. The areal density of scattering centers N is given by Eq. 4.25, and determined in the same manner as described in Sect. 4.6.3. The incoming beam was determined from the S800 spectra that were produced from the software gate selecting the 31 Na ions (seen in red in Fig. 4.37). The gamma-ray yield Y_{γ} was determined from the gamma-ray counts from the $(7/2^+) \rightarrow (5/2^+)$ transition. Similar to what was done in Sect. 4.6.3, no dead-time corrections were applied to the detected gamma rays or the number of incoming projectiles.

| | $J_i^\pi 	o J_f^\pi$ | E | $\sigma(3^{\circ})^{\text{Be}}_{\text{exp.}}$ | |
|------------------|--------------------------------|-------|---|-------|
| | | (keV) | (mb) | (mb) |
| ³¹ Na | $3/2_{\rm g.s.}^+ \to (7/2^+)$ | 1171 | 6(1) | 28(5) |

Table 4.9: Inelastic scattering cross sections for the $2^+_{g.s.} \to (7/2^+)$ excitation in 31 Na from the present work. Results for both Be and Ta targets are shown.

The reduced transition strength $B(E2,3/2_{\rm g.s.}^+ \to (7/2^+))$ was extracted by comparing the experimentally determined cross sections in Table 4.9 to angle-integrated cross sections from coupled-channel calculations performed using FRESCO [80, 130], as described in Sect. 4.6.3. A diagram broadly describing the process is shown in Fig. 4.35. To facilitate an accurate comparison between experimental and theoretically-derived cross sections, the incoming beam profile, finite beam spot size, and angular spread were incorporated into the monte carlo simulation along with the differential cross sections obtained from FRESCO. This process is described in Sects. 4.2.1 and 4.3.1. Due to the absence of elastic scattering data for the present reaction, the optical model parameters from the $^{17}\text{O} + ^{208}\text{Pb}$ reaction [81] were adopted. To evaluate the sensitivity of the results to the choice of optical model parameters, an alternative theoretically-derived potential was employed

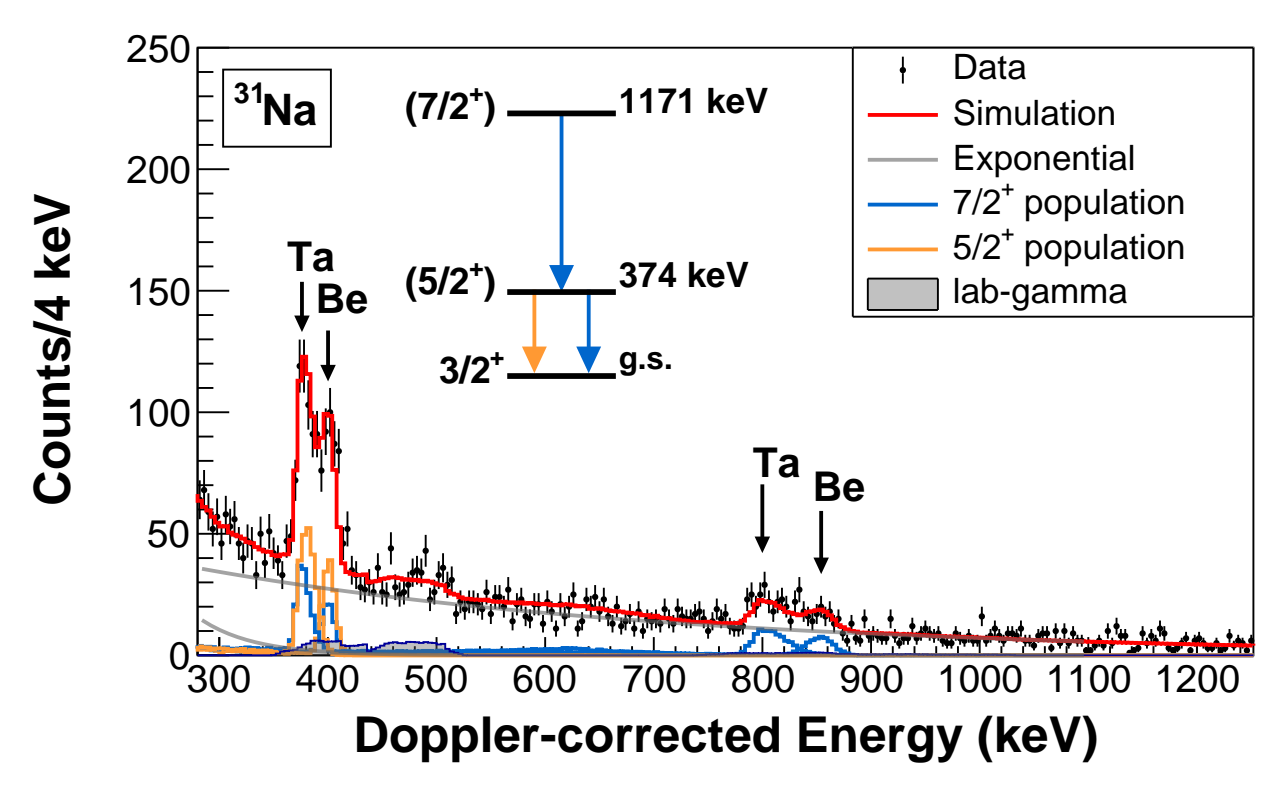


Figure 4.40: One-dimensional Doppler-corrected gamma-ray spectrum for 31 Na, optimized for reactions originating on the Tantalum (Ta) foil, gated for the laboratory-frame gamma-ray GRETI-INA detection angle up to 55° . A separate gate was applied to restrict the laboratory scattering angle up to 3° . The data are represented with black dots and error bars, with laboratory-frame background contributions shown in gray. Simulated decay of the $(5/2^{+})$ state populated directly in the reaction is shown by the orange histograms, while gamma-ray decays associated with the $(7/2^{+})$ direct population are represented by the blue histograms. The sum of all components is shown by the red histogram. The Tantalum (Ta) and Beryllium (Be) peaks for each transition are marked accordingly.

[109], constructed from a complex G-matrix interaction, CEG07 [115, 116]. Because the optical model potentials from Ref. [109] are limited to even-even projectile nuclei with target masses in the range A = 12 - 208, the $^{32}\text{Mg} + ^{12}\text{C}$ and $^{32}\text{Mg} + ^{181}\text{Ta}$ optical model potentials were derived for the $^{30,31}\text{Na} + ^{181}\text{Ta}$ reactions.

The two main parameters varied in the FRESCO analysis were the nuclear deformation length, δ_A , and the reduced electromagnetic E2 matrix element, $\langle J_f || O(E2) || J_i \rangle$. In FRESCO, the evaluation of the reduced matrix element is model dependent [131, 132]. The definition used for this analysis is given by that of the axially symmetric deformed rotor model, presented in Eq. 4.26. From the

reduced matrix element, one can determined the reduced transition strength given by Eq. 4.27.

The nuclear deformation lengths were first determined from the two different optical model parameters. The results for δ_A pertaining to the $(7/2^+)$ excited state are presented in Table 4.10.

Table 4.10: Extracted nuclear matter deformation lengths (δ_A) from inelastic scattering on the 9 Be target for the $3/2^+_{\rm g.s.} \to (7/2^+)$ excitation. Results from the $^{17}{\rm O}$ + $^{208}{\rm Pb}$ [81] and $^{32}{\rm Mg}$ + $^{181}{\rm Ta}$ [109] optical model potentials are listed.

The reduced transition strengths to the $(7/2^+)$ state were obtained from the determined E2 matrix elements from the experimentally measured 181 Ta foil cross sections. This assumed an equal amount of nuclear contributions between the Ta and Be foils. Using the deformation lengths obtained from each optical model potential, the corresponding $B(E2\uparrow)$ strengths were determined and are shown in Table 4.11. Although the results are in good agreement, a possible dependence on optical potential cannot be ignored. Therefore, an average was determined from the two obtained $B(E2\uparrow)$ values, where error includes both statistical and systematic contributions, including those arising from the choice of potential.

$$\frac{B(E2\uparrow) (e^2 f m^4)}{J_i^{\pi} \to J_f^{\pi}} \frac{B(E2\uparrow) (e^2 f m^4)}{^{17}\text{O} + ^{208}\text{Pb}} \frac{32}{^{32}\text{Mg} + ^{181}\text{Ta}} \text{Avg.}$$

$$\frac{^{31}\text{Na} \quad 3/2_{\text{g.s.}}^{+} \to (7/2^{+})}{115(^{+25}_{-29})} \frac{109(^{+27}_{-33})}{109(^{+27}_{-32})} \frac{112(^{+27}_{-32})}{^{11}}$$

Table 4.11: Extracted reduced transition probabilities to the $(7/2^+)$ state, $B(E2, 3/2^+_{\rm g.s.} \to (7/2^+))$, from inelastic scattering on the 181 Ta target and δ_A from Table 4.10. Results from the 17 O + 208 Pb [81] and 32 Mg + 181 Ta [109] optical model potentials are listed. Averages are also shown.

4.7.4 $3/2_{g,s}^+ \rightarrow (5/2^+)$ Excitation

The excitation cross section to the $(5/2^+)$ state in 31 Na was determined by analyzing gamma-ray efficiency-corrected counts from the 374 keV gamma-rays stemming from the $(5/2^+) \rightarrow 3/2^+_{\rm g.s.}$

transition, while accounting for feeding contributions from the $(7/2^+) \rightarrow (5/2^+)$ decay. This state was simulated at an excitation energy of 374 keV [36, 66, 127, 133], assuming a mean lifetime of $\tau=1$ ps [134]. The lifetime was estimated by fitting the simulated line shape to the experimental spectrum. A more detailed lifetime analysis was not possible due to the lack of multiple target distance settings in this experiment [24, 58, 90, 121, 128, 129]. Separate simulations were generated for the Be and Ta foil components, where yields associated with the direct population of the $(5/2^+)$ state are indicated by the orange arrow and histograms in Fig. 4.40. The peaks labeled **Ta** correspond to reactions originating on the Tantalum foil (i.e. Tantalum gamma-ray peak) and those originating from the Beryllium foil (i.e. Beryllium gamma-ray peak) are labeled with **Be**. The excitation cross section to the $(5/2^+)$ state $(\sigma_{5/2^+})$ was determined via Eq. 4.28. A process identical to what was described for the $3/2^+_{\rm g.s.} \rightarrow (7/2^+)$ excitation (Sect. 4.7.3) was performed for the $3/2^+_{\rm g.s.} \rightarrow (5/2^+)$ case.

4.7.4.1 Gamma-ray Yield Feeding Corrections

To accurately determine the $(5/2^+)$ excitation cross section, it was necessary to account for feeding contributions from the higher-lying $(7/2^+)$ state resulting from reactions on the Ta and Be foils. This was done by simulating, for each foil, the cascade following the direct population of the $(7/2^+)$ state, specifically, the $(7/2^+) \rightarrow (5/2^+)$ and $(5/2^+) \rightarrow 3/2^+_{g.s.}$ sequence. This approach allowed the Be and Ta contributions for each transition to be determined. Having obtained all the individual components, the observed $(5/2^+) \rightarrow 3/2^+_{g.s.}$ transition was distinctly composed of contributions from the direct population of both the $(7/2^+)$ and $(5/2^+)$ states, along with background components. To this end, the angle-integrated inelastic scattering cross sections for the direct population of the low-lying $(5/2^+)$ state in 31 Na for the Be and Ta foils – summarized in Table 4.12 – were calculated from decays stemming only from the direct population of the $(5/2^+)$ state.

From the deduced cross sections listed in Tab. 4.12, the nuclear deformation lengths (δ_A) and E2 reduced transition strengths $B(E2, 3/2_{\rm g.s.}^+ \to (5/2^+))$ were determined. The diagram Fig. 4.35 broadly shows the steps taken to determine each value, where the details of the process are identical

| | $J_i^\pi 	o J_f^\pi$ | E (keV) | $\sigma(3^{\circ})^{\text{Be}}_{\text{exp.}}$ (mb) | $\sigma(3^{\circ})_{\text{exp.}}^{\text{Ta}}$ (mb) |
|------------------|--------------------------------|---------|--|--|
| ³¹ Na | $3/2_{\rm g.s.}^+ \to (5/2^+)$ | 374 | 11(2) | 51(8) |

Table 4.12: Inelastic scattering cross sections for the $3/2^+_{g.s.} \to (5/2^+)$ transition in 31 Na from the present work. Results for both Be and Ta targets are shown.

to what is described in Sect. 4.6.3. The extracted δ_A are listed in Tab. 4.13, with the associated $B(E2, 3/2_{\rm g.s.}^+ \to (5/2^+))$ presented in Tab. 4.14. While the results show good agreement, the sensitivity to optical model potential should not be ignored. Consequently, the adopted $B(E2\uparrow)$ value was taken as the average of the two, with the uncertainty containing both statistical and systematic contributions, including those associated with the optical potential.

$$\frac{J_i^{\pi} \to J_f^{\pi}}{J_i^{\pi} \to J_f^{\pi}} \frac{\delta_A (fm)}{{}^{17}\text{O} + {}^{208}\text{Pb}} {}^{32}\text{Mg} + {}^{12}\text{C}}$$

$$^{31}\text{Na} \quad 3/2_{\text{g.s.}}^+ \to (5/2^+) \quad 1.48({}^{+0.12}_{-0.13}) \quad 1.33({}^{+0.11}_{-0.12})$$

Table 4.13: Extracted nuclear matter deformation lengths (δ_A) from inelastic scattering on the 9 Be target for the $3/2^+_{\rm g.s.} \rightarrow (5/2^+)$ excitation. Results from the $^{17}{\rm O}$ + $^{208}{\rm Pb}$ [81] and $^{32}{\rm Mg}$ + $^{181}{\rm Ta}$ [109] optical model potentials are listed.

$$\frac{B(E2\uparrow) (e^2fm^4)}{J_i^{\pi} \to J_f^{\pi}} \frac{B(E2\uparrow) (e^2fm^4)}{^{17}O + ^{208}Pb} \frac{^{32}Mg + ^{181}Ta}{^{32}Mg + ^{181}Ta} \frac{Avg.}{210\binom{+41}{-46}}$$

Table 4.14: Extracted reduced transition probabilities to the $(5/2^+)$ state, $B(E2, 3/2^+_{\rm g.s.} \to (5/2^+))$, from inelastic scattering on the 181 Ta target and δ_A from Table 4.13. Results from the 17 O + 208 Pb [81] and 32 Mg + 181 Ta [109] optical model potentials are listed. Averages are also shown.

4.7.5 Lifetime Determination via Lineshape Analysis for the (7/2⁺) State

The lifetime of the excited state for $(7/2^+)$ had to be further investigated due to the excess of counts that appeared to be statistically significant near 830 keV in Fig. 4.40. To gain a clearer

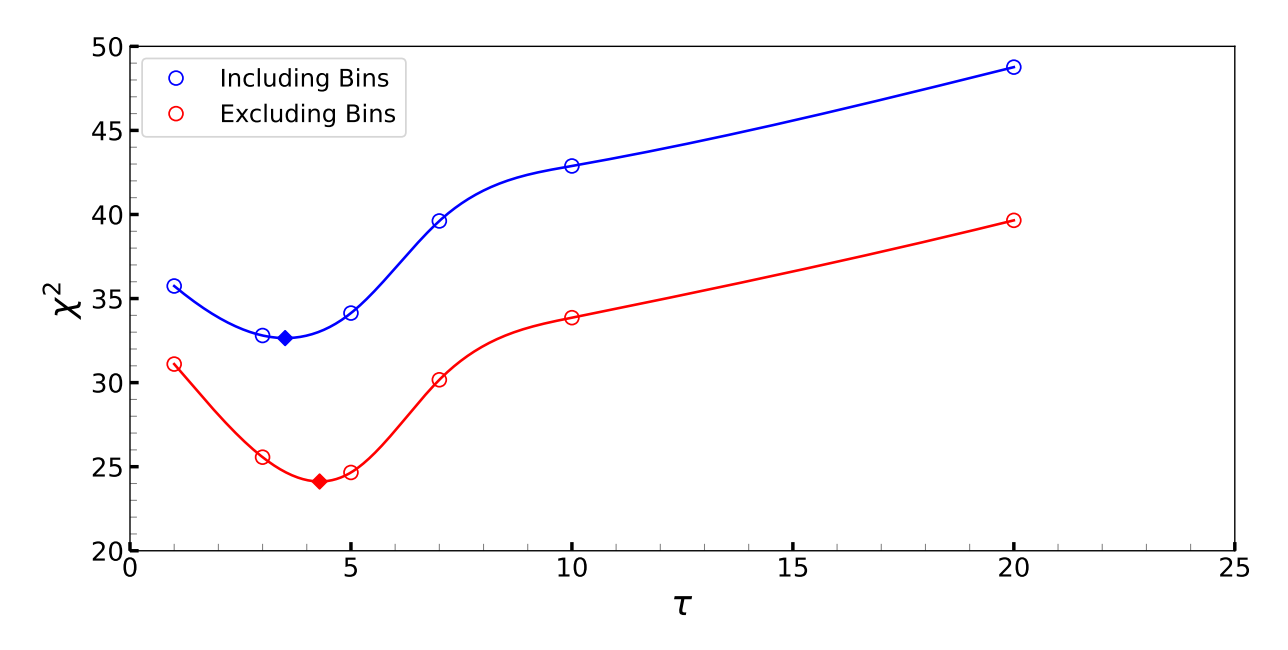


Figure 4.41: χ^2 curves as a function of the mean lifetime (τ) for the (7/2⁺) state in ³¹Na. The blue curve shows the χ^2 values obtained from fits that include the bins corresponding to the excess counts observed near 830 keV in Fig. 4.40. The red curve represents fits performed while excluding those bins. Open circles denote the χ^2 values obtained from fitting simulated spectra to the gamma-ray data shown in Fig. 4.40 within the 750–900 keV energy range while varying τ . The red and blue diamonds are where the minimum χ^2 is found for each curve.

understanding of this excess, a χ^2 analysis was conducted within the region of interest (750–900 keV), comparing results both including and excluding the bins associated with the excess counts, while systematically varying the lifetime of the $(7/2^+)$ state at 1171 keV. The fit including the excess bins had 25 degrees of freedom, as opposed to 23 degrees of freedom when excluding these bins. The χ^2 values obtained from this analysis are presented in Fig. 4.41, where open circles represent fits performed on the 750–900 keV region both including and excluding the bins associated with the excess counts. The lifetime extracted from the analysis including these bins is $\tau = 3.5(^{+1.2}_{-1.4})$ ps. Likewise, the analysis excluding the excess bins yields a lifetime of $\tau = 4.3(10)$ ps. Comparable results were obtained for lifetimes between 1 and 5 ps. The spectral shape of the $(7/2^+) \rightarrow (5/2^+)$ transition shown in Fig. 4.40 clearly rules out lifetimes exceeding 10 ps, as such values would produce a distinct two-peak structure that is not observed. As a result from this spectral shape analysis, the excess counts were attributed to statistical fluctuations in the data. Worth mentioning

that a more detailed lifetime analysis was not possible due to the lack of multiple target distance settings in this experiment [24, 58, 90, 121, 128, 129].

CHAPTER 5

DISCUSSION OF RESULTS

The reduced transition strengths determined for for low-lying excited states in neutron-rich 30,31 Na offer an improved understanding of the collective properties within the N=20 island of inversion. Particularly, the excitation strengths to the first and second excited states provide a means to assess the presumed common deformation amongst the low-lying states. To this end, two shell-model calculations utilizing the FSU [135, 136] and SDPF-M [47, 137, 138] effective interactions were used to interpret the microscopic origin of collectivity. We also compared our results with calculations based on the USDB [139, 140] interaction, serving as a reference for sd-shell calculations. Furthermore, the results are interpreted within the frame of an axially-symmetric deformed rotor, in addition to its asymmetric counterpart – the triaxial particle-rotor model. This chapter will provide a brief discussion on results previously reported, along with interpretations made based on available theoretical shell-model predictions and rotor models. The latter entails interpretations with an axially-symmetric rotor, along with a comparison to an axially asymmetric particle-rotor model to evaluate the sensitivity of the present measurements to triaxiality – a form of non-axial deformation of the nucleus.

We first compare the results obtained in this work with those reported in the literature [54–56, 126, 127]. Table 5.1 summarizes the reduced E2 transition strengths, Coulomb deformation parameters (β_C), and intrinsic quadrupole moments (Q_0) obtained in the present study, alongside previously reported values for 30,31 Na. The Coulomb deformation parameter depicts the proton density deformation within the nucleus [54, 141, 142] and was extracted under the assumption of an axially-symmetric rotor [31],

$$|\beta_C| = \frac{4\pi\sqrt{B(E2, I_i \to I_f)}}{3ZR_C^2 \langle I_i K20 | I_f K \rangle}$$
(5.1)

where $R_C = r_C A^{1/3}$, $r_C = 1.2$ fm, and $|\langle I_i K 20 | I_f K \rangle|$ is the corresponding Clebsch-Gordan coeffi-

cient. Under the same assumption, the intrinsic quadrupole moment was determined via

$$Q_0 = \sqrt{\frac{16\pi}{5}} \frac{3}{4\pi} Z R_0^2 \beta_C \tag{5.2}$$

with $R_0 = r_0 A^{1/3}$ and $r_0 = 1.2$ fm [54]. The β_C and Q_0 values listed in Table 5.1 represent the averages of results obtained from each optical potential.

| | $J_i^\pi \to J_f^\pi$ | $B(E2\uparrow) (e^2 \text{fm}^4)$ | | | eta_C | | Q_0 ($e \mathrm{fm}^2$) | | |
|------------------|-----------------------|-----------------------------------|-----------|---------|----------|--------------------------|------------------------------|--------------------|--------|
| | | This work | [54] | [56] | [55] | This work | [54] | This work | [54] |
| ³⁰ Na | $2^+ \to (3^+)$ | 122(+34) | 130(+90) | 147(21) | 320(100) | $0.43(^{+0.06}_{-0.08})$ | 0.41(10) | 49(+7) | 51(15) |
| 1144 | $2^+ \to (4^+)$ | $64(^{+26}_{-33})$ | _ | _ | 96(50) | $0.47(^{+0.12}_{-0.16})$ | _ | $54(^{+14}_{-18})$ | - |
| ³¹ Na | $3/2^+ \to (5/2^+)$ | 210(+41) | 311(+170) | _ | _ | 0.54(4) | 0.66(16) | 64(5) | 78(19) |
| | $3/2^+ \to (7/2^+)$ | $112(^{+27}_{-32})$ | _ | _ | _ | 0.53(5) | _ | 63 (6) | _ |

Table 5.1: Adopted $B(E2\uparrow)$, β_C , and Q_0 values for 30 Na and 31 Na are compared to previous experimental results [54–56]. β_C and Q_0 values are averaged from the different optical model potential results from the 17 O + 208 Pb [81] and 32 Mg + 181 Ta [109].

The present $B(E2, 2^+_{g.s.} \to (3^+))$ result for 30 Na – presented in Table 5.1 – showcases better agreement with values reported in Refs. [54, 56], as displayed in the top panel of Fig. 5.1. Likewise, the reduced transition strength obtained for the $2^+_{g.s.} \to (4^+)$ excitation indicates a degree of collectivity consistent with the value reported in Ref. [55]. A comparison is also made with the assumption of an axially-symmetric rotor in the lower panel of Fig. 5.1. In this framework, the axially-symmetric rotor assumes the same intrinsic quadrupole moment for all members of the rotational band. That is, all of the rotational excited states share a common deformation. Thus, a ratio of reduced E2 strengths to the (4^+) and (3^+) states (utilizing Eqs. 5.1 and 5.2) can be expressed in terms of the modulus squared Clebsch-Gordan coefficients,

$$\frac{B(E2, 2_{g.s.}^+ \to 4^+)}{B(E2, 2_{g.s.}^+ \to 3^+)} = \frac{|\langle 2220|42\rangle|^2}{|\langle 2220|32\rangle|^2} = 0.43$$
 (5.3)

The present results, and those reported by Seidlitz [55], suggest ³⁰Na possessing features of an axially-symmetric rotor.

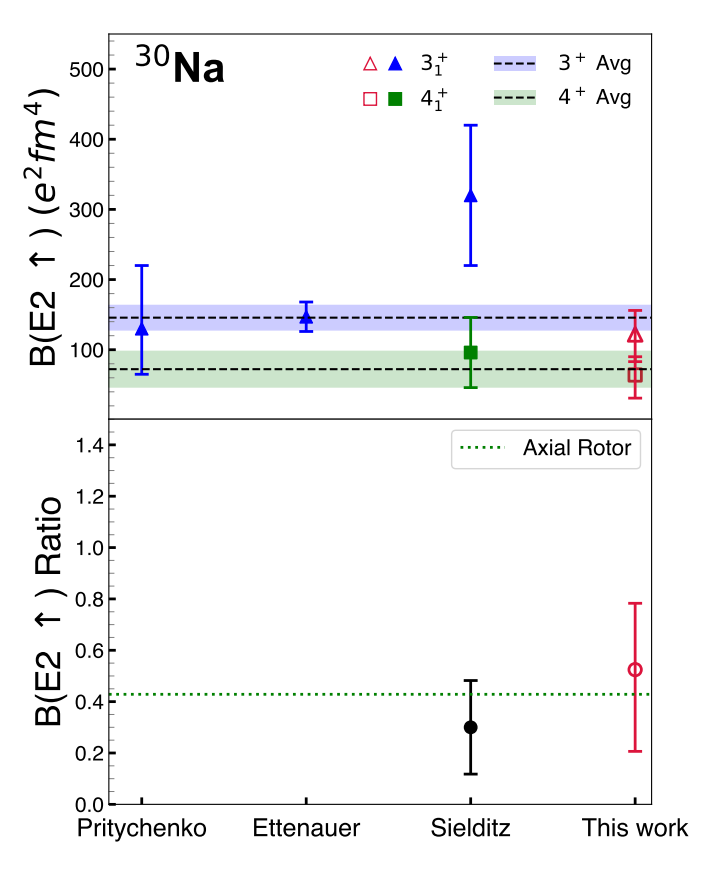


Figure 5.1: Comparison of $B(E2\uparrow)$ strengths for 30 Na from this work and those previously reported [54–56] (top) along with available $B(E2, 2^+_{g.s.} \to (4^+))/B(E2, 2^+_{g.s.} \to (3^+))$ ratios (bottom). In the top panel, triangles denote $B(E2, 2^+_{g.s.} \to (3^+))$ values and squares correspond to $B(E2, 2^+_{g.s.} \to (4^+))$. Weighted averages of all available measurements, including those from this work, are shown as shaded bands in blue and green for the (3^+) and (4^+) states, respectively.

The 30 Na results reported here provide improved precision, enabling a more stringent assessment of collective structure in this region by inferring whether the ground state and low-lying excited states exhibit a common deformation. A comparison with the Weisskopf estimate (Eq. 1.24) highlights the collective nature of the transition. For instance, the reduced transition rate for the $2^+_{g.s.} \rightarrow (3^+)$ excitation in Weisskopf units is $B(E2, 2^+_{g.s.} \rightarrow (3^+)) = 22 \binom{+6}{-7}$ W.u., indicating a strength twenty-two times greater than expected from the assumption of a single-nucleon being responsible for the transition.

As for ³¹Na, only a comparison for the $B(E2, 3/2_{g.s.}^+ \to (5/2^+))$ can be made due to the limited electromagnetic transition data available [54], as shown in the top panel of Fig. 5.2. The result

for the $(5/2^+)$ state significantly improves upon the uncertainty of the reduced transition strength. Markedly, the $B(E2, 3/2^+_{\rm g.s.} \to (7/2^+))$ reported here enables a comparison to be made between the experimental values and those obtained through the axially-symmetric rotor model assumption. The resulting ratio of reduced E2 matrix elements is

$$\frac{B(E2, 3/2_{g.s.}^{+} \to 7/2^{+})}{B(E2, 3/2_{g.s.}^{+} \to 5/2^{+})} = \frac{\left| \langle \frac{3}{2} \frac{3}{2} 20 | \frac{7}{2} \frac{3}{2} \rangle \right|^{2}}{\left| \langle \frac{3}{2} \frac{3}{2} 20 | \frac{5}{2} \frac{3}{2} \rangle \right|^{2}} = 0.56$$
 (5.4)

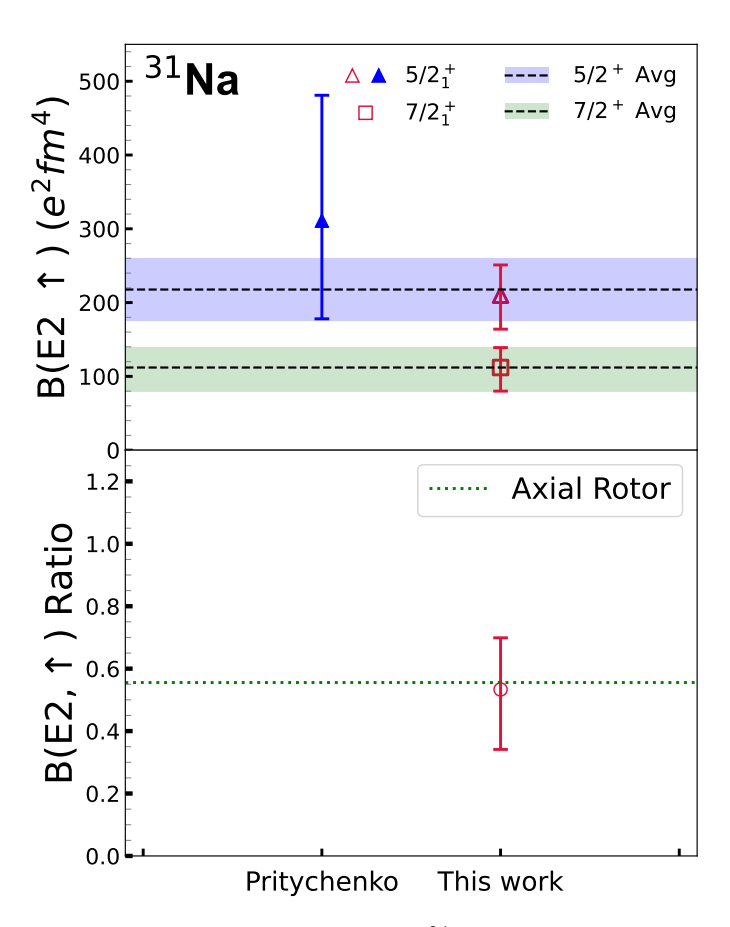


Figure 5.2: Comparison of $B(E2\uparrow)$ strengths for 31 Na from this work and those previously reported [54] (top) along with available $B(E2,3/2^+_{g.s.} \to (7/2^+))/B(E2,3/2^+_{g.s.} \to (5/2^+))$ ratios (bottom). In the top panel, triangles denote $B(E2,3/2^+_{g.s.} \to (5/2^+))$ values and squares correspond to $B(E2,3/2^+_{g.s.} \to (7/2^+))$. Weighted averages of all available measurements, including those from this work, are shown as shaded bands in blue and green for the $(5/2^+)$ and $(7/2^+)$ states, respectively.

The comparison of the B(E2) ratios obtained experimentally and through the framework of an axially-symmetric rotor are presented in the lower panel of Fig. 5.2. The ratio obtained from

this work suggests ³¹Na demonstrating a congruency with the assumption of a static ground-state deformation.

The recently obtained $B(E2, 3/2^+_{g.s.} \to (7/2^+))$ value, shown in the top panel of Fig. 5.2 and in Table 5.1, provides deeper insight into the collective properties of this region. With respect to the Weisskopf estimate (Eq. 1.24), the experimental reduced transition strength for the $3/2^+_{g.s.} \to 5/2^+$ excitation corresponds to $B(E2) = 36 \binom{+7}{-8}$ W.u., further supporting the presence of significant collectivity in 31 Na.

In regard to the Q_0 moments extracted from the experimental $B(E2 \uparrow)$ values, the Q_0 results are found to align well with the measured spectroscopic moments $Q_0 = 51.5(6)$ efm² and $Q_0 = 52.5(13)$ efm² reported for the ground states of ³⁰Na and ³¹Na from Refs. [44, 45]. It is important to distinguish that the Q_0 moments obtained from experimental $B(E2 \uparrow)$ strengths are transitional quadrupole moments $Q_{0,t}$, which are assumed to be the same as the intrinsic quadrupole moments based on the presence of static deformation. For ^{30,31}Na, the intrinsic frame quadrupole moments inferred from the transition strengths are consistent with the spectroscopic moments measured for the ground states, suggesting a static in-band deformation.

5.1 Comparison of B(E2 ↑) to Shell-Model Calculations

Effective interactions in shell-model calculations provide a more computationally feasible means in reproducing experimental observables by simplifying the complex forces experienced by individual nucleons. Particularly, effective interactions are adapted to a specific model space in which the description of nuclei are governed by an average potential along with residual interactions between nucleons. These interactions are often parameterized from fits to experimental observables such as excitation energies and nuclear masses, for example.

The FSU interaction [135, 136] is a microscopic effective interaction obtained by fitting shell-model cross-shell matrix elements over a broad range of particle-hole states spanning the sd and fp shells. It was originally constructed from a modified version of the WBP interaction [143], within a model space comprising the spsdpf major oscillator shells. The interaction assumes

isospin invariance but incorporates Coulomb corrections to the binding energies. For the more inert orbitals, the single-particle energies (SPEs) and two-body matrix elements (TBMEs) of the sp shells were retained from the WBP interaction, while the sd-shell TBMEs were adopted from the USDB interaction [140]. Only selected monopole terms of the sd - fp cross-shell matrix elements were refitted to experimental data. For the fp shell, the TBMEs were taken from the GXPF1A [144] interaction, with modifications limited to the $0f_{7/2}$ and $1p_{3/2}$ orbitals. The dataset used to constrain the FSU interaction was partitioned into four categories, each targeting different aspects of the effective interaction [136]. Overall, the FSU interaction – assuming pure n-particle-n-hole configurations between the sd and fp shells – has successfully reproduced key properties of neutron-rich nuclei in the N=20 island of inversion. The present FSU calculations, applied for 30,31 Na, assume a pure 2p-2h configuration between the sd and fp shells.

The SDPF-M interaction [47, 137] was formulated by combining the USD interaction [145] for the sd shell, the Kuo-Brown interaction [146] for the fp shell, and the Millener-Kurath interaction [147] for the cross-shell TBMEs. Two further modifications were introduced in Refs. [47, 137]: one to the monopole component of the interaction and the other to the pairing interaction in the sd shell. The adjustment to the monopole term was done due to it serving an important role in determining the binding energy and shell gap as a function of proton and neutron numbers. The pairing interaction in the sd shell was modified to explicitly account for contributions from the fp shell. Accordingly, the development of the SDPF-M interaction was aimed at examining the robustness and impact of the shell gap at N=20, having provided accurate energy-level predictions for odd-Z, even- and odd-N nuclei [47, 133]. The SDPF-M interaction was defined relative to an inert ^{16}O core, with a valence space encompassing the full sd shell together with the $0f_{7/2}$ and $1p_{3/2}$ orbitals. For the present calculation, the SDPF-M interaction allowed for configuration mixing between different particle-hole excitations across the N=20 shell gap and were performed with the KSHELL computer code [148].

Finally, the well-established USDB interaction [139, 140] was employed to perform shell-model calculations within the *sd*-shell. The USDB Hamiltonian represents the culmination of systematic

refinements to earlier versions (USD and USDA), aiming to improve the global description of nuclei in this mass region. In constructing the USDB Hamiltonian with an updated and comprehensive dataset, Brown and Richter [140] incorporated 608 experimentally known states from 77 nuclei spanning mass numbers A = 16 - 40. This broad fitting set allowed the interaction to reliably reproduce binding energies, excitation spectra, and electromagnetic transition strengths across the sd-shell. Owing to its predictive power and extensive benchmarking, the USDB interaction has since become a standard tool for shell-model studies of light and medium-mass nuclei, particularly for probing structural evolution near the limits of stability. For the purpose of this dissertation, the USDB interaction – utilizing a 0p-0h configuration – functions as a reference to gauge the enhanced collectivity in both 30,31 Na.

5.1.1 ³⁰Na Comparison

In order to assess the experimental results, the reduced transition strengths were compared to shell-model calculations utilizing the FSU and SDPF-M interactions in Table 5.2. The $B(E2\uparrow)$ values for 30 Na calculated with the FSU interaction employ the effective charges of $e_p=1.36e$ and $e_n=0.45e$ [139], which are well established for describing observables in the sd shell. The calculated excitation energies place the 3^+ and 4^+ states at 476 keV and 1003 keV, respectively, with corresponding reduced transition strengths of $B(E2, 2^+_{g.s.} \rightarrow 3^+) = 206 \ e^2 \text{fm}^4$ and $B(E2, 2^+_{g.s.} \rightarrow 4^+) = 96 \ e^2 \text{fm}^4$. The FSU interaction tends to overestimate the excitation strengths of both low-lying states, though it shows better agreement for the $B(E2, 2^+_{g.s.} \rightarrow 4^+)$ transition. It is important to note, however, that the choice of effective charges plays a critical role in determining E2 observables. This is demonstrated in Fig. 5.3, where the B(E2) strengths were obtained using the proton matrix element,

$$M_p = e_p A_p + e_n A_n \tag{5.5}$$

with the relation of

$$B(E2, J_i \to J_f) = \frac{|M_p|^2}{2J_i + 1}$$
 (5.6)

Figure 5.3 compares the reduced transition strengths of the (3^+) and (4^+) states obtained using different sets of effective charges [137, 139, 149–152]. Among them, the values $(e_p, e_n) = (1.25e, 0.25e)$ [151] show the closest agreement with the present experimental results. In contrast, the recently proposed empirical effective charges for the sd and fp shells [152] yield results that overestimate the experimental E2 transition strengths deduced in this work. Due to the effective charges for the FSU interaction having not yet been established on account of the limited data for states exemplifying dominant 2p-2h configurations, we adopted the original values of $e_p = 1.36e$ and $e_n = 0.45e$ in the present discussion. These values have been established in the sd shell and are in line with the theoretical assessment of $e_p = 1.31e$ and $e_n = 0.46e$ [150].

| | $J_i^{\pi} 	o J_f^{\pi}$ | $B(E2\uparrow) (e^2 \text{fm}^4)$ | | | |
|------------------|---|-----------------------------------|------------------|---------------------|----------|
| | | This work | FSU ^a | SDPF-M ^b | $USDB^a$ |
| ³⁰ Na | $2^+ \to (3^+)$ | $122\binom{+34}{-39}$ | 206 | 153 | 2.5 |
| | $2^+ \rightarrow (3^+)$ $2^+ \rightarrow (4^+)$ | $64(^{+26}_{-33})$ | 96 | 90 | 34 |

^a $(e_p, e_n = 1.36e, 0.45e)$ ^b $(e_p, e_n = 1.3e, 0.5e)$

Table 5.2: Present $B(E2 \uparrow)$ for ³⁰Na results comparing the adopted values from this work with FSU,SDPF-M, and USDB calculations.

As for the SDPF-M interaction, the (3^+) and (4^+) excited states were predicted at 408 keV and 731 keV, respectively, with effective charges of $e_p = 1.3$ and $e_n = 0.5$. The associated reduced E2 strengths are $B(E2, 2^+_{g.s.} \rightarrow 3^+) = 153 \ e^2 \text{fm}^4$ and $B(E2, 2^+_{g.s.} \rightarrow 4^+) = 90 \ e^2 \text{fm}^4$. The B(E2) results obtained with the SPDF-M interaction agree with the present results, supporting claims [47] of a dominant 2p-2h intruder configuration, giving rise to the K=2 deformed band structure at low excitation energies.

Lastly, a comparison with the USDB interaction further underscores the collective phenomena in the ground-states of ³⁰Na, predicting the (3+) and (4⁺) states at 213 keV and 680 keV, respectively.

Utilizing effective charges of $e_p = 1.36$ and $e_n = 0.45$, and assuming a nearly spherical 0p-0h configuration, the reduced transition strengths were predicted to be $B(E2, 2_{g.s.}^+ \rightarrow 3^+) = 2.5 e^2 \text{fm}^4$ and $B(E2, 2_{g.s.}^+ \rightarrow 4^+) = 34 e^2 \text{fm}^4$. This large deviation from the measured reduced E2 strengths conclusively confirm the presence of enhanced collectivity in 30 Na.

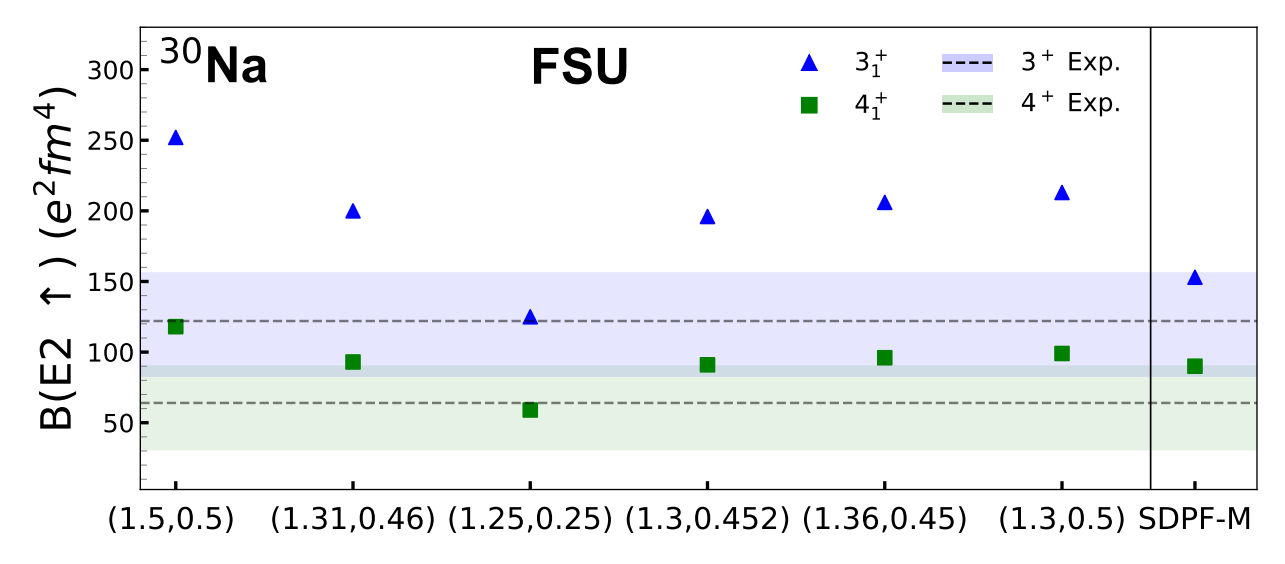


Figure 5.3: Comparison of $B(E2, 2^+_{g.s.} \to (3^+))$ and $B(E2, 2^+_{g.s.} \to (4^+))$ strengths calculated with the FSU and SDPF-M interactions. The sensitivity of calculated B(E2) strengths results to the choice of effective charges [137, 139, 149–152] is highlighted using the FSU interaction.

5.1.2 ³¹Na Comparison

The comparison between the adopted B(E2) strengths for the low-lying $(5/2^+)$ and $(7/2^+)$ states in 31 Na with the FSU and SDPF-M interaction are presented in Table 5.3. We begin by discussing the calculations utilizing the FSU interaction with effective charge values of $e_p = 1.36e$ and $e_n = 0.45e$ [139]. The $5/2^+$ and $7/2^+$ states were predicted at 418 keV and 1339 keV, respectively. The associated $B(E2 \uparrow)$ values are $B(E2, 3/2^+_{g.s.} \rightarrow 5/2^+) = 228 \ e^2 \text{fm}^4$ and $B(E2, 3/2^+_{g.s.} \rightarrow 7/2^+) = 118 \ e^2 \text{fm}^4$. These predictions are consistent with the adopted $B(E2 \uparrow)$ values for the $3/2^+_{g.s.} \rightarrow (5/2^+)$ and $3/2^+_{g.s.} \rightarrow (7/2^+)$ transitions, lending support to interpretations [135] that assign these excited states to the K = 3/2 band. To investigate the impact of effective charges on the theoretical predictions, Fig. 5.4 displays $B(E2 \uparrow)$ values determined from several effective

charges [137, 139, 149–152]. Fig. 5.4 illustrates a general agreement between the experimentally obtained reduced transition strengths with those obtained using the FSU interaction with different effective charges. In the present comparison, values of $e_p = 1.36e$ and $e_n = 0.45e$ were adopted as a result of already being established in the sd shell and in agreement with prior theoretical discussions [150].

| | $J_i^\pi 	o J_f^\pi$ | B(B) | $E2\uparrow) (e^2$ | | |
|------------------|----------------------|-----------------------|--------------------|---------------------|----------|
| | | This work | FSU ^a | SDPF-M ^b | $USDB^a$ |
| ³¹ Na | $3/2^+ \to (5/2^+)$ | 210(+41) | 228 | 201 | 94 |
| | $3/2^+ \to (7/2^+)$ | $112\binom{+27}{-32}$ | 118 | 98 | 34 |

^a $(e_p, e_n = 1.36e, 0.45e)$ ^b $(e_p, e_n = 1.3e, 0.5e)$

Table 5.3: Present $B(E2 \uparrow)$ for ³¹Na results comparing the adopted values from this work with FSU, SDPF-M, and USDB calculations.

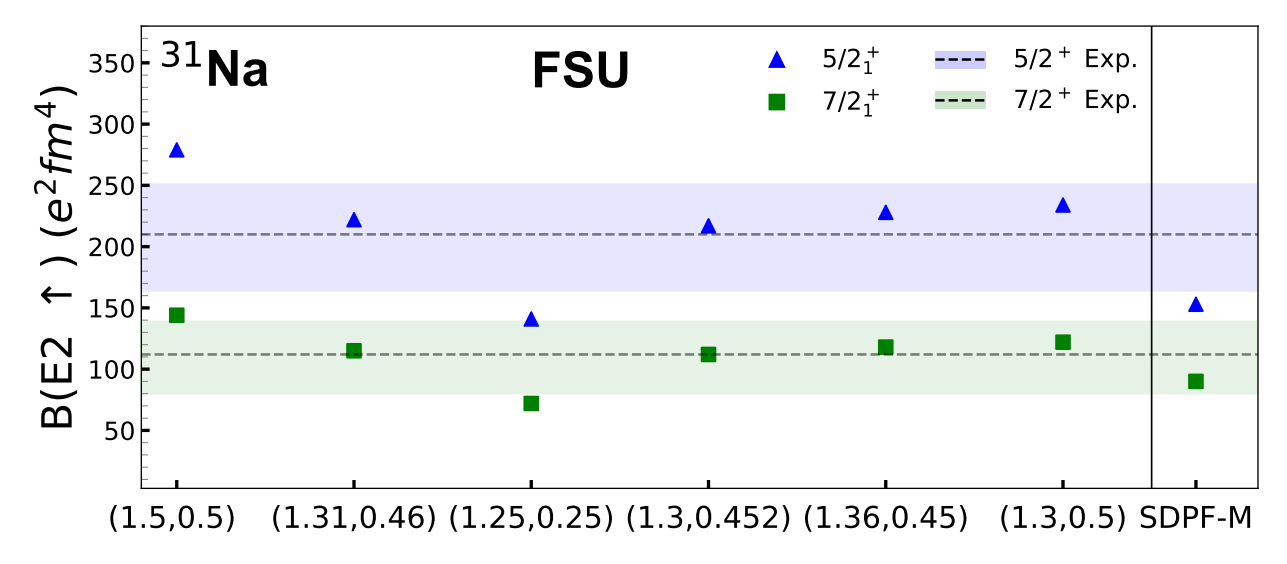


Figure 5.4: Comparison of $B(E2, 3/2_{g.s.}^+ \rightarrow (5/2^+))$ and $B(E2, 3/2_{g.s.}^+ \rightarrow (7/2^+))$ strengths calculated with the FSU and SDPF-M interactions. The sensitivity of calculated B(E2) strengths results to the choice of effective charges [137, 139, 149–152] is highlighted using the FSU interaction.

In regard to the SDPF-M shell-model calculations, the $5/2^+$ and $7/2^+$ excited states are predicted at 245 keV 1407 keV, respectively. The $B(E2 \uparrow)$ values listed in Table 5.3 are consistent with those

adopted in this work and further support a predominant 2p-2h intruder configuration for the ground state and its associated K = 3/2 band members [47].

A comparison with the USBD interaction – predicting a $J^{\pi}=5/2^+$ ground state – enhances the argument of enhanced collectivity in 31 Na. With the USDB interaction, the $3/2^+$ and $7/2^+$ states were predicted to have state-level energies of 372 keV and 4947 keV with respect to the $5/2^+$ ground state. Supplementary, transition strengths of $B(E2, 3/2^+_{g.s.} \rightarrow 5/2^+) = 94 \ e^2 \text{fm}^4$ and $B(E2, 3/2^+_{g.s.} \rightarrow 7/2^+) = 34 \ e^2 \text{fm}^4$ strongly suggest calculations within the sd shell do not suffice to describe the experimental data, further corroborating the occurrence of collectivity in 31 Na.

5.1.3 Trends of B(E2) and Excitation Energies Along the Na Isotopic Chain

To gain a comprehensive view of the structural behavior in the $N \sim 20$ region, Fig. 5.5 displays the systematic trends of $B(E2\uparrow)$ strengths and excitation energies in selected odd-A Na isotopes with $J^{\pi}=3/2^+$ ground states. SDPF-M calculations suggest that the B(E2) trends for the $5/2^+$ and $7/2^+$ excitations are expected to continue into the neutron-rich A=31-35 region. The presence of the K=3/2 band structure can be evaluated using the B(E2) values and energy ratios of the low-lying $5/2^+$ and $7/2^+$ states, as illustrated in Fig. 5.5 (b) and (c), respectively. As reported in Ref. [36], the energy ratios for 31,33,35 Na are consistent with the strong-coupling limit of 2.4 (See Sect. 1.3.2), indicating an ideal region of axial deformation. The newly determined $B(E2, 3/2^+_{g.s.} \to 7/2^+)$ result enables the firm confirmation of this interpretation (Fig. 5.5 (b)), consistent with the 0.55 ratio expected for a rigid rotor built on the K=3/2 band. This region is expected to extend to the N=22 and N=24 Na isotopes, while theoretical studies of 39,41 Na [49, 50] predict a transition to stronger triaxial deformation towards the neutron drip line. The scarcity of experimental data on structural behavior near the neutron drip line highlights the need for future B(E2) measurements in neutron-rich Na nuclei.

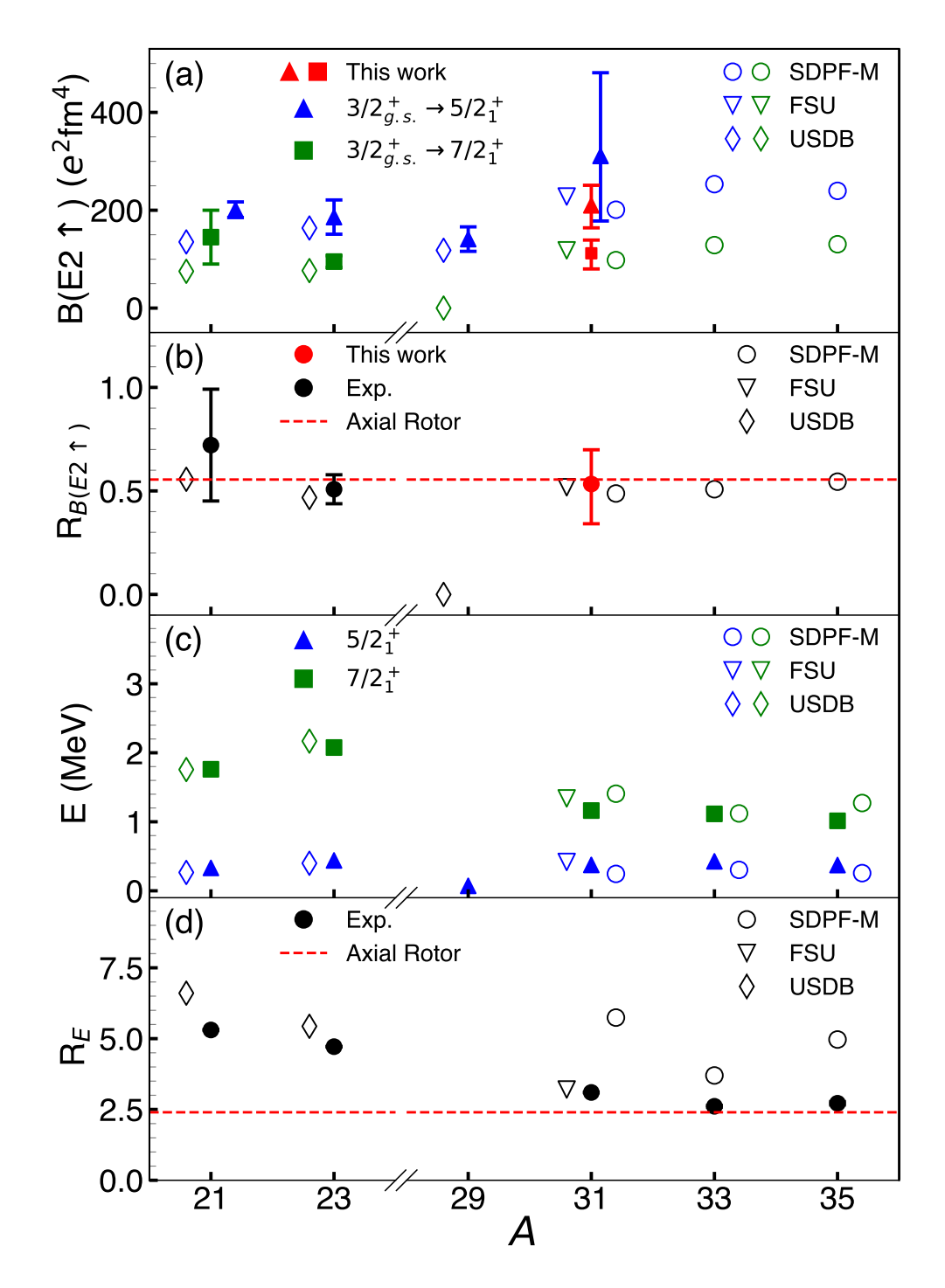


Figure 5.5: Systematic trends for selected odd-A Na isotopes are presented for (a) reduced transition strengths, (b) $B(E2, 3/2^+ \text{g.s.} \rightarrow 7/2^+)/B(E2, 3/2^+ \text{g.s.} \rightarrow 5/2^+)$ ratios, (c) excitation energies, and (d) excitation-energy ratios of the yrast $7/2^+$ and $5/2^+$ states. The present results are shown in red, while prior data are taken from evaluated data sets [134, 153]. Shell-model predictions using the FSU and SDPF-M interactions are included, with SDPF-M values for 33,35 Na taken from Ref. [36]. USDB energy results for 29,31 Na are omitted from the figure since the ground states are predicted as $5/2^+$, with the $3/2^+$ and $7/2^+$ states at 71 and 2742 keV for 29 Na, and 372 and 4947 keV for 31 Na, respectively. In panel (a), blue symbols denote $5/2^+$ states and green symbols denote $7/2^+$ states.

5.2 Comparison of B(E2) to Triaxial Particle-Rotor Model Calculations

The possible occurrence of asymmetric deformation, as suggested for drip-line Na isotopes [49, 50], casts a new interest in the presently studied 30,31 Na isotopes. To explore this possibility, we employed the triaxial particle-rotor model to determine B(E2) strengths and state-level energies, as shown in Figs. 5.6 and 5.7. A comparison of the experimentally deduced $B(E2\uparrow)$ values with those predicted by the triaxial particle-rotor model for 31 Na is presented in Fig. 5.6. The particle-rotor model computer codes utilized to perform these calculations are those described by Refs. [154–157]. The computer codes utilized a modified oscillator (Nilsson) potential allowing for asymmetries to be included when calculating the nuclear potential energy surface [155]. The parameterizations of the deformed single-particle energies in this calculation were taken from Refs. [154, 158], while the $E(2_1^+) \approx 800$ keV energy was adopted from the assumed even-even 30 Ne core.

The comparison of excited-state energies and reduced transition strengths in Figs. 5.6 and 5.7 encompassed varying the deformation parameter ϵ_2 ($\epsilon_2 \approx 0.95\beta_2$) [34], which informs on how pronounced the deformation of the nucleus is in the Nilsson model. Subsequently, for each ϵ_2 value, the degree of axial asymmetry γ was varied. The two limits of the axial asymmetry parameter are $\epsilon_2 > 0, \gamma = 0^{\circ}$, corresponding to a prolate nucleus, and $\epsilon_2 > 0, \gamma = 60^{\circ}$, corresponding to an oblate nucleus. A value of $\gamma = 30^{\circ}$ defines the maximum amount of triaxiality a nucleus may possess, residing between both prolate and oblate shape configurations. Calculations shown in panels (a) and (b) of Figs. 5.6 and 5.7 indicate that predictions with $\epsilon_2 \sim 0.4$ and γ between 0° and 10° are consistent with both the experimental excited-state energies and $B(E2 \uparrow)$ values. Even though the ratios of reduced transition strengths calculated with the triaxial particle-rotor model in Fig. 5.6 (c) are consistent with the experimental ratio, it proves to be indistinguishable from the axially-symmetric case in the range of $0 \le \gamma \le 20$. Similarly, the calculated ratio of excited-state energies with varying ϵ_2 and γ in Fig. 5.7 (c) showcase better agreement with smaller values of γ . Moreover, theoretical studies of neutron-rich nuclei near the drip line predict little to no triaxiality [49, 159]. Otsuka et al. [49] suggests a minor degree of triaxiality for ³¹Na with $\gamma \approx 15^{\circ} - 20^{\circ}$,

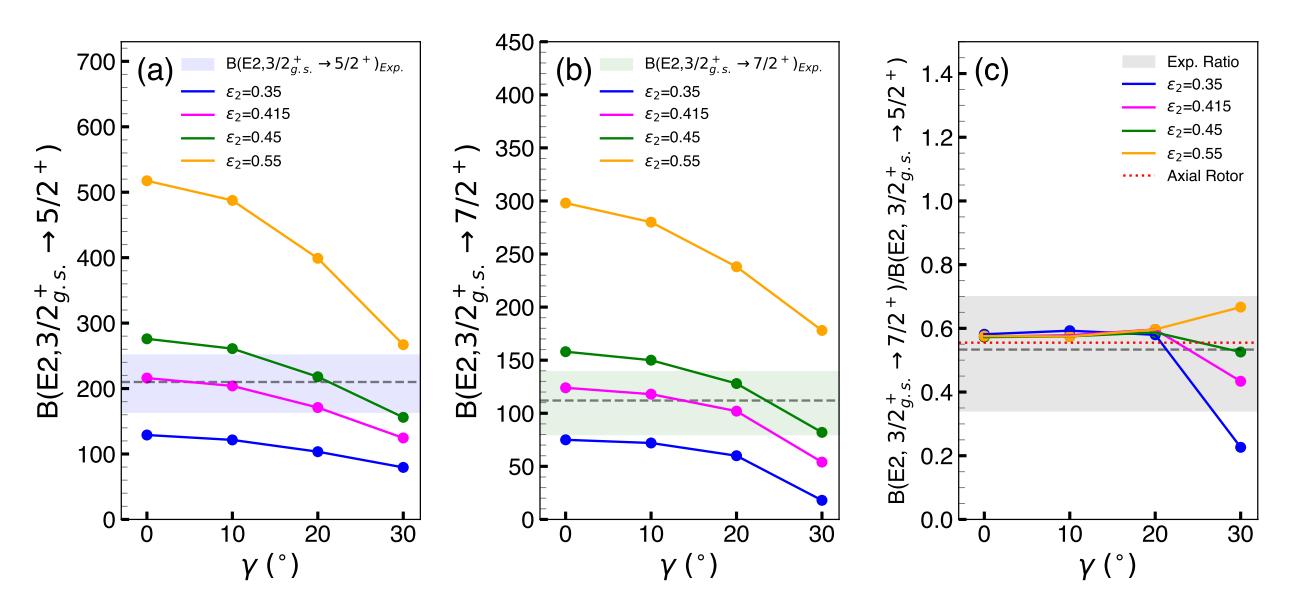


Figure 5.6: Comparison of reduced transition strengths between experimental and the triaxial particle-rotor model calculations for 31 Na. Panels (a) and (b) compare the reduced transition strengths for $B(E2, 3/2^+\text{g.s.} \rightarrow 5/2^+)$ and $B(E2, 3/2^+\text{g.s.} \rightarrow 7/2^+)$ with varying ϵ_2 and γ values, respectively, while panel (c) shows the ratio between these values.

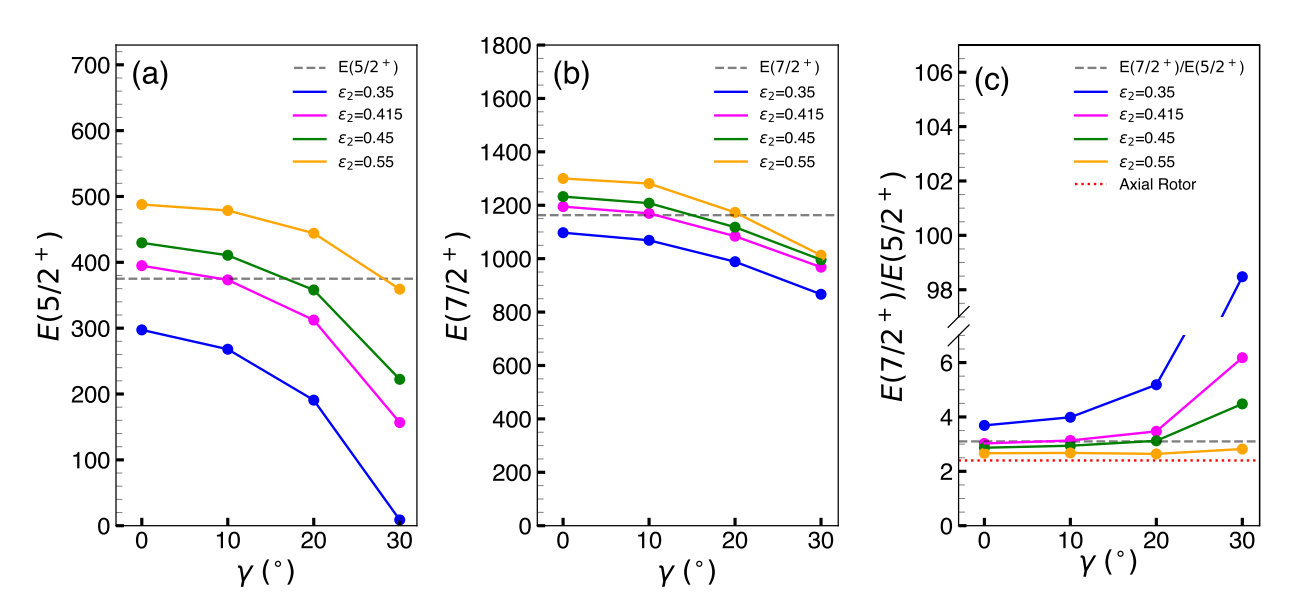


Figure 5.7: Comparison of state-level energies between experimental and the triaxial particle-rotor model calculations for ³¹Na. Panels (a) and (b) compare the state-level energies of $E(5/2^+)$ and $E(7/2^+)$ with varying ϵ_2 and γ values, respectively, while panel (c) shows the ratio between these values.

while Dong *et al.* [159] predict $\gamma \approx 0^\circ$. Nonetheless, this exercise – employing the modified oscillator (Nilsson) potential to evaluate $B(E2\uparrow)$ strengths and excited-state energies – indicates that any triaxiality in 31 Na, if present, would be minor, and that an axially-symmetric prolate rotor provides an adequate description.

CHAPTER 6

CONCLUSION

The observation of deformation-driven structures in the N=20 island of inversion, particularly in the neutron-rich 30,31 Na nuclei, prompts the question of whether such features persist within the ground-state bands beyond the first excited state. Obtaining the reduced E2 transition strengths to the first and second excited states of 30 Na and 31 Na allowed for a more stringent evaluation to be made of the large collectivity in this region. The sustained in-band deformation revealed in this work establishes the basis for understanding the structural evolution of well-deformed ground-state bands towards the neutron drip line along the Z=11 isotopic chain.

This work presents the reduced E2 transition rates to the (3^+) and (4^+) , and $(5/2^+)$ and $(7/2^+)$ excited states in 30 Na and 31 Na, respectively. These values were extracted using the recently developed technique for intermediate-energy heavy-ion inelastic scattering [76]. This technique exploits the ability to separate the nuclear and Coulomb contributions to the excitation cross sections by performing a simultaneous two-foil measurement with low- and high-Z target materials. Furthermore, inelastic scattering in this energy range allows for the direct population of higher-lying spin states in collective excitations. For 30 Na, prior measurements of the $B(E2, 2^+_{g.s.} \rightarrow (3^+)) = 96(50) \ e^2 \text{fm}^4$ [55] strengths had associated uncertainties of $\sim 50\%$, hindering the ability to distinctly infer the presence of well-deformed ground-state bands. In the case for 31 Na, the E2 transition data were particularly more limited. The only reported value, $B(E2, 3/2^+_{g.s.} \rightarrow (5/2^+)) = 311(^{+170}_{-133}) \ e^2 \text{fm}^4$ [54], possessed an average uncertainty of $\sim 50\%$, with no measurement of the $B(E2, 3/2^+_{g.s.} \rightarrow (7/2^+))$) strength.

The $B(E2 \uparrow)$ values obtained from this study enabled an improved ability to make sound interpretations based on experimental data. With regard to 30 Na, $B(E2 \uparrow)$ values from this work provided an overall improved measurement, having lower associated uncertainties. Concerning 31 Na, the E2 transition strength obtained in this work boasts a significant improvement in its uncertainty, having been determined to be $B(E2, 3/2_{\rm g.s.}^+ \to (5/2^+)) = 210(^{+41}_{-46})~e^2{\rm fm}^4$. Markedly,

we have obtained the first $B(E2,3/2_{\rm g.s.}^+ \to (7/2^+))$ strength, determined to be $112(^{+27}_{-32})$ $e^2 {\rm fm}^4$, enabling the $B(E2,3/2_{\rm g.s.}^+ \to (7/2^+))/B(E2,3/2_{\rm g.s.}^+ \to (5/2^+))$ ratio to be calculated. This provided evidence of the occurrence of a static in-band deformation, going beyond energy ratios alone.

Comparisons of shell-model calculations employing the FSU and SDPF-M interactions gave a more comprehensive understanding of the microscopic collective properties in these nuclei. Predictions with the FSU interaction employed a pure 2p-2h configuration, whereas an admixtures of np-nh configurations were allowed in the SDPF-M calculations. The B(E2) strengths determined with the FSU interaction for 30 Na showed a propensity to overestimate the experimental values. However, it should be noted that the choice of effective charges (e_p, e_n) plays a critical role in determining E2 observables, and that the values of (e_p, e_n) for the FSU interaction have not yet been established. As for 31 Na, a good agreement was found between the FSU predicted B(E2) values and experimental strengths. Pertaining to predictions made SDPF-M interaction, values calculated for 30 Na were found to be consistent with the $B(E2 \uparrow)$ values extracted in this work. Similarly, SDPF-M predictions for 31 Na were in line with the experimentally determined B(E2) strengths.

In addition to the shell-model calculations, the triaxial particle-rotor model was employed to compute the reduced E2 transition strengths for 31 Na. This was done by varying the parameters that govern the magnitude of deformation, ϵ_2 ($\epsilon_2 \approx 0.95\beta_2$), and the degree of axial asymmetry, γ . From these calculations, it was then concluded that triaxiality is not prominent in 31 Na, and an axially-symmetric rotor would suffice in interpreting these results. From the work presented here, a static ground-state band deformation was indeed present, governed by a dominant 2p-2h configuration cross the N=20 shell gap, firmly establishing a region characterized by an axially-symmetric rotor.

In summary, this dissertation provided improved measurements for the E2 transition strengths to the low-lying excited states in 30,31 Na using the newly established technique for intermediate-energy heavy-ion inelastic scattering. This included the first determination of the $B(E2, 3/2_{\rm g.s.}^+ \to (7/2^+))$ strength, allowing a definitive precedent of axial deformation to be established for the odd-A Na

nuclei. Furthermore, this measurement showcased the utility of this technique, being able to discern between the nuclear and Coulomb contributions to the excitation cross section by simultaneously performing two measurements. As an outlook for future studies, this work further underscores the limited experimental information on the structural evolution towards the neutron drip line, placing an emphasis on B(E2) measurements. With the technique used here, features of triaxiality could be evidenced by ascertaining the E2 strengths to the low-lying excited states of the odd-A neutron-rich Na isotopes near the neutron drip line.

BIBLIOGRAPHY

- [1] International Atomic Energy Agency, Atomic mass data center (amdc) (2025), accessed: 2025-09-04.
- [2] F. G. Kondev, M. Wang, W. J. Huang, S. Naimi, and G. Audi, Chinese Physics C **45**, 030001 (2021).
- [3] M. G. Mayer, Phys. Rev. **74**, 235 (1948).
- [4] M. G. Mayer, Phys. Rev. **75**, 1969 (1949).
- [5] O. Haxel, J. H. D. Jensen, and H. E. Suess, Phys. Rev. **75**, 1766 (1949).
- [6] T. Otsuka, A. Gade, O. Sorlin, T. Suzuki, and Y. Utsuno, Rev. Mod. Phys. **92**, 015002 (2020).
- [7] A. Obertelli and H. Sagawa, *Modern Nuclear Physics: From Fundamentals to Frontiers*, UNITEXT for Physics (Springer Nature Singapore Pte Ltd., Singapore, 2021).
- [8] B. A. Brown, Lecture notes on nuclear physics, University lecture notes, Michigan State University (2025), available at https://people.frib.msu.edu/~brown/2025/brown-lecture-notes-2025.pdf.
- [9] O. Sorlin and M.-G. Porquet, Progress in Particle and Nuclear Physics **61**, 602 (2008).
- [10] I. Talmi and I. Unna, Phys. Rev. Lett. 4, 469 (1960).
- [11] C. Thibault, R. Klapisch, C. Rigaud, A. M. Poskanzer, R. Prieels, L. Lessard, and W. Reisdorf, Phys. Rev. C 12, 644 (1975).
- [12] G. Huber, F. Touchard, S. Büttgenbach, C. Thibault, R. Klapisch, H. T. Duong, S. Liberman, J. Pinard, J. L. Vialle, P. Juncar, and P. Jacquinot, Phys. Rev. C **18**, 2342 (1978).
- [13] C. Détraz, D. Guillemaud, G. Huber, R. Klapisch, M. Langevin, F. Naulin, C. Thibault, L. C. Carraz, and F. Touchard, Phys. Rev. C **19**, 164 (1979).
- [14] D. Guillemaud-Mueller, C. Detraz, M. Langevin, F. Naulin, M. de Saint-Simon, C. Thibault, F. Touchard, and M. Epherre, Nuclear Physics A **426**, 37 (1984).
- [15] E. K. Warburton, J. A. Becker, and B. A. Brown, Phys. Rev. C 41, 1147 (1990).
- [16] X. Campi, H. Flocard, A. Kerman, and S. Koonin, Nuclear Physics A 251, 193 (1975).

- [17] A. Poves and J. Retamosa, Physics Letters B **184**, 311 (1987).
- [18] T. Otsuka, T. Suzuki, R. Fujimoto, H. Grawe, and Y. Akaishi, Phys. Rev. Lett. **95**, 232502 (2005).
- [19] T. Otsuka, Physica Scripta **T152**, 014007 (2013).
- [20] I. Tanihata, Physica Scripta **T152**, 014021 (2013).
- [21] H. Iwasaki, T. Motobayashi, H. Akiyoshi, Y. Ando, N. Fukuda, H. Fujiwara, Z. Fülöp, K. Hahn, Y. Higurashi, M. Hirai, I. Hisanaga, N. Iwasa, T. Kijima, A. Mengoni, T. Minemura, T. Nakamura, M. Notani, S. Ozawa, H. Sagawa, H. Sakurai, S. Shimoura, S. Takeuchi, T. Teranishi, Y. Yanagisawa, and M. Ishihara, Physics Letters B 491, 8 (2000).
- [22] A. Navin, D. W. Anthony, T. Aumann, T. Baumann, D. Bazin, Y. Blumenfeld, B. A. Brown, T. Glasmacher, P. G. Hansen, R. W. Ibbotson, P. A. Lofy, V. Maddalena, K. Miller, T. Nakamura, B. V. Pritychenko, B. M. Sherrill, E. Spears, M. Steiner, J. A. Tostevin, J. Yurkon, and A. Wagner, Phys. Rev. Lett. 85, 266 (2000).
- [23] R. Elder, H. Iwasaki, J. Ash, D. Bazin, P. C. Bender, T. Braunroth, B. A. Brown, C. M. Campbell, H. L. Crawford, B. Elman, A. Gade, M. Grinder, N. Kobayashi, B. Longfellow, A. O. Macchiavelli, T. Mijatović, J. Pereira, A. Revel, D. Rhodes, J. A. Tostevin, and D. Weisshaar, Phys. Rev. C **100**, 041301 (2019).
- [24] R. Elder, H. Iwasaki, J. Ash, D. Bazin, P. C. Bender, T. Braunroth, C. M. Campbell, H. L. Crawford, B. Elman, A. Gade, M. Grinder, N. Kobayashi, B. Longfellow, T. Mijatović, J. Pereira, A. Revel, D. Rhodes, and D. Weisshaar, Phys. Rev. C **104**, 024307 (2021).
- [25] V. Tripathi, S. L. Tabor, P. Bender, C. R. Hoffman, S. Lee, K. Pepper, M. Perry, P. F. Mantica, J. M. Cook, J. Pereira, J. S. Pinter, J. B. Stoker, D. Weisshaar, Y. Utsuno, and T. Otsuka, Phys. Rev. C 77, 034310 (2008).
- [26] A. Ozawa, T. Kobayashi, T. Suzuki, K. Yoshida, and I. Tanihata, Phys. Rev. Lett. **84**, 5493 (2000).
- [27] R. Kanungo, C. Nociforo, A. Prochazka, T. Aumann, D. Boutin, D. Cortina-Gil, B. Davids, M. Diakaki, F. Farinon, H. Geissel, R. Gernhäuser, J. Gerl, R. Janik, B. Jonson, B. Kindler, R. Knöbel, R. Krücken, M. Lantz, H. Lenske, Y. Litvinov, B. Lommel, K. Mahata, P. Maierbeck, A. Musumarra, T. Nilsson, T. Otsuka, C. Perro, C. Scheidenberger, B. Sitar, P. Strmen, B. Sun, I. Szarka, I. Tanihata, Y. Utsuno, H. Weick, and M. Winkler, Phys. Rev. Lett. 102, 152501 (2009).
- [28] A. Bohr and B. R. Mottelson, *Nuclear Structure, Volume II: Nuclear Deformations*, 1st ed. (World Scientific, Singapore, 1998).

- [29] K. S. Krane, *Introductory Nuclear Physics*, 1st ed. (Wiley, New York, NY, 1987).
- [30] P. E. Garrett, M. Zielińska, and E. Clément, Progress in Particle and Nuclear Physics **124**, 103931 (2022).
- [31] P. Ring and P. Schuck, *The Nuclear Many-Body Problem*, Texts and Monographs in Physics (Springer, New York, 1980).
- [32] E. M. Henley and J. P. Schiffer, Rev. Mod. Phys. **71**, S205 (1999).
- [33] P. J. Twin, B. M. Nyakó, A. H. Nelson, J. Simpson, M. A. Bentley, H. W. Cranmer-Gordon, P. D. Forsyth, D. Howe, A. R. Mokhtar, J. D. Morrison, J. F. Sharpey-Schafer, and G. Sletten, Phys. Rev. Lett. **57**, 811 (1986).
- [34] R. Casten, *Nuclear Structure from a Simple Perspective*, Oxford Studies in Nuclear Physics, Vol. 23 (Oxford University Press, New York, 1990) p. 256.
- [35] A. L. Richard, H. L. Crawford, P. Fallon, A. O. Macchiavelli, V. M. Bader, D. Bazin, M. Bowry, C. M. Campbell, M. P. Carpenter, R. M. Clark, M. Cromaz, A. Gade, E. Ideguchi, H. Iwasaki, M. D. Jones, C. Langer, I. Y. Lee, C. Loelius, E. Lunderberg, C. Morse, J. Rissanen, M. Salathe, D. Smalley, S. R. Stroberg, D. Weisshaar, K. Whitmore, A. Wiens, S. J. Williams, K. Wimmer, and T. Yamamato, Phys. Rev. C 96, 011303 (2017).
- [36] P. Doornenbal, H. Scheit, S. Takeuchi, Y. Utsuno, N. Aoi, K. Li, M. Matsushita, D. Steppenbeck, H. Wang, H. Baba, E. Ideguchi, N. Kobayashi, Y. Kondo, J. Lee, S. Michimasa, T. Motobayashi, T. Otsuka, H. Sakurai, M. Takechi, Y. Togano, and K. Yoneda, Progress of Theoretical and Experimental Physics 2014, 053D01 (2014), https://academic.oup.com/ptep/article-pdf/2014/5/053D01/4451406/ptu057.pdf.
- [37] D. Weisshaar, D. Bazin, P. Bender, C. Campbell, F. Recchia, V. Bader, T. Baugher, J. Belarge, M. Carpenter, H. Crawford, M. Cromaz, B. Elman, P. Fallon, A. Forney, A. Gade, J. Harker, N. Kobayashi, C. Langer, T. Lauritsen, I. Lee, A. Lemasson, B. Longfellow, E. Lunderberg, A. Macchiavelli, K. Miki, S. Momiyama, S. Noji, D. Radford, M. Scott, J. Sethi, S. Stroberg, C. Sullivan, R. Titus, A. Wiens, S. Williams, K. Wimmer, and S. Zhu, Nuclear Instruments and Methods in Physics Research Section A: Accelerators, Spectrometers, Detectors and Associated Equipment 847, 187 (2017).
- [38] S. Paschalis, I. Lee, A. Macchiavelli, C. Campbell, M. Cromaz, S. Gros, J. Pavan, J. Qian, R. Clark, H. Crawford, D. Doering, P. Fallon, C. Lionberger, T. Loew, M. Petri, T. Stezelberger, S. Zimmermann, D. Radford, K. Lagergren, D. Weisshaar, R. Winkler, T. Glasmacher, J. Anderson, and C. Beausang, Nuclear Instruments and Methods in Physics Research Section A: Accelerators, Spectrometers, Detectors and Associated Equipment 709, 44 (2013).
- [39] G. Collaboration, Annual Review of Nuclear and Particle Science 66, 1 (2016).

- [40] L. B. N. Laboratory, Greta documents (2025), accessed: 2025-09-10.
- [41] C. Détraz, M. Langevin, D. Guillemaud, M. Epherre, G. Audi, C. Thibault, and F. Touchard, Nuclear Physics A **394**, 378 (1983).
- [42] G. Lalazissis, A. Farhan, and M. Sharma, Nuclear Physics A **628**, 221 (1998).
- [43] P.-G. Reinhard, D. J. Dean, W. Nazarewicz, J. Dobaczewski, J. A. Maruhn, and M. R. Strayer, Phys. Rev. C **60**, 014316 (1999).
- [44] G. Neyens, P. Himpe, D. L. Balabanski, P. Morel, L. Perrot, M. D. Rydt, I. Stefan, C. Stodel, J. C. Thomas, N. Vermeulen, and D. T. Yordanov, The European Physical Journal Special Topics **150**, 149 (2007).
- [45] M. Keim, in *Exotic Nuclear and Atomic Masses AIP Conference Proceedings*, 50, Vol. 455 (1998).
- [46] A. Revel, O. Sorlin, F. M. Marqués, Y. Kondo, J. Kahlbow, T. Nakamura, N. A. Orr, F. Nowacki, J. A. Tostevin, C. X. Yuan, N. L. Achouri, H. Al Falou, L. Atar, T. Aumann, H. Baba, K. Boretzky, C. Caesar, D. Calvet, H. Chae, N. Chiga, A. Corsi, H. L. Crawford, F. Delaunay, A. Delbart, Q. Deshayes, Z. Dombrádi, C. A. Douma, Z. Elekes, P. Fallon, I. Gašparić, J.-M. Gheller, J. Gibelin, A. Gillibert, M. N. Harakeh, W. He, A. Hirayama, C. R. Hoffman, M. Holl, A. Horvat, A. Horváth, J. W. Hwang, T. Isobe, N. Kalantar-Nayestanaki, S. Kawase, S. Kim, K. Kisamori, T. Kobayashi, D. Körper, S. Koyama, I. Kuti, V. Lapoux, S. Lindberg, S. Masuoka, J. Mayer, K. Miki, T. Murakami, M. Najafi, K. Nakano, N. Nakatsuka, T. Nilsson, A. Obertelli, F. de Oliveira Santos, H. Otsu, T. Ozaki, V. Panin, S. Paschalis, D. Rossi, A. T. Saito, T. Saito, M. Sasano, H. Sato, Y. Satou, H. Scheit, F. Schindler, P. Schrock, M. Shikata, Y. Shimizu, H. Simon, D. Sohler, L. Stuhl, S. Takeuchi, M. Tanaka, M. Thoennessen, H. Törnqvist, Y. Togano, T. Tomai, J. Tscheuschner, J. Tsubota, T. Uesaka, Z. Yang, M. Yasuda, and K. Yoneda (SAMURAI21 collaboration), Phys. Rev. Lett. 124, 152502 (2020).
- [47] Y. Utsuno, T. Otsuka, T. Glasmacher, T. Mizusaki, and M. Honma, Phys. Rev. C **70**, 044307 (2004).
- [48] T. J. Gray, J. M. Allmond, Z. Xu, T. T. King, R. S. Lubna, H. L. Crawford, V. Tripathi, B. P. Crider, R. Grzywacz, S. N. Liddick, A. O. Macchiavelli, T. Miyagi, A. Poves, A. Andalib, E. Argo, C. Benetti, S. Bhattacharya, C. M. Campbell, M. P. Carpenter, J. Chan, A. Chester, J. Christie, B. R. Clark, I. Cox, A. A. Doetsch, J. Dopfer, J. G. Duarte, P. Fallon, A. Frotscher, T. Gaballah, J. T. Harke, J. Heideman, H. Huegen, J. D. Holt, R. Jain, N. Kitamura, K. Kolos, F. G. Kondev, A. Laminack, B. Longfellow, S. Luitel, M. Madurga, R. Mahajan, M. J. Mogannam, C. Morse, S. Neupane, A. Nowicki, T. H. Ogunbeku, W.-J. Ong, C. Porzio, C. J. Prokop, B. C. Rasco, E. K. Ronning, E. Rubino, T. J. Ruland, K. P. Rykaczewski, L. Schaedig, D. Seweryniak, K. Siegl, M. Singh, A. E. Stuchbery, S. L. Tabor, T. L. Tang, T. Wheeler, J. A. Winger, and J. L. Wood, Phys. Rev. Lett. 130, 242501 (2023).

- [49] T. Otsuka, N. Shimizu, and Y. Tsunoda, Phys. Rev. C **105**, 014319 (2022).
- [50] N. Tsunoda, T. Otsuka, K. Takayanagi, N. Shimizu, T. Suzuki, Y. Utsuno, S. Yoshida, and H. Ueno, Nature **587**, 66 (2020).
- [51] E. M. Lykiardopoulou, C. Walls, J. Bergmann, M. Brodeur, C. Brown, J. Cardona, A. Czihaly, T. Dickel, T. Duguet, J.-P. Ebran, M. Frosini, Z. Hockenbery, J. D. Holt, A. Jacobs, S. Kakkar, B. Kootte, T. Miyagi, A. Mollaebrahimi, T. Murboeck, P. Navratil, T. Otsuka, W. R. Plaß, S. Paul, W. S. Porter, M. P. Reiter, A. Scalesi, C. Scheidenberger, V. Somà, N. Shimizu, Y. Wang, D. Lunney, J. Dilling, and A. A. Kwiatkowski, Phys. Rev. Lett. 134, 052503 (2025).
- [52] P. Doornenbal, H. Scheit, S. Takeuchi, Y. Utsuno, N. Aoi, K. Li, M. Matsushita, D. Steppenbeck, H. Wang, H. Baba, E. Ideguchi, N. Kobayashi, Y. Kondo, J. Lee, S. Michimasa, T. Motobayashi, T. Otsuka, H. Sakurai, M. Takechi, Y. Togano, and K. Yoneda, Phys. Rev. C **95**, 041301 (2017).
- [53] Y. Kondo, N. L. Achouri, H. Alfalou, L. Atar, T. Aumann, H. Baba, K. Boretzky, C. Caesar, D. Calvet, and H. Chae, Nature **620**, 965 (2023).
- [54] B. V. Pritychenko, T. Glasmacher, P. D. Cottle, R. W. Ibbotson, K. W. Kemper, K. L. Miller, L. A. Riley, and H. Scheit, Phys. Rev. C 66, 024325 (2002).
- [55] M. Seidlitz, P. Reiter, R. Altenkirch, B. Bastin, C. Bauer, A. Blazhev, N. Bree, B. Bruyneel, P. A. Butler, J. Cederkäll, T. Davinson, H. De Witte, D. D. DiJulio, J. Diriken, L. P. Gaffney, K. Geibel, G. Georgiev, R. Gernhäuser, M. Huyse, N. Kesteloot, T. Kröll, R. Krücken, R. Lutter, J. Pakarinen, F. Radeck, M. Scheck, D. Schneiders, B. Siebeck, C. Sotty, T. Steinbach, J. Taprogge, P. Van Duppen, J. Van de Walle, D. Voulot, N. Warr, F. Wenander, K. Wimmer, P. J. Woods, and K. Wrzosek-Lipska, Phys. Rev. C 89, 024309 (2014).
- [56] S. Ettenauer, H. Zwahlen, P. Adrich, D. Bazin, C. M. Campbell, J. M. Cook, A. D. Davies, D.-C. Dinca, A. Gade, T. Glasmacher, J.-L. Lecouey, W. F. Mueller, T. Otsuka, R. R. Reynolds, L. A. Riley, J. R. Terry, Y. Utsuno, and K. Yoneda, Phys. Rev. C 78, 017302 (2008).
- [57] H. Iwasaki, A. Lemasson, C. Morse, A. Dewald, T. Braunroth, V. M. Bader, T. Baugher, D. Bazin, J. S. Berryman, C. M. Campbell, A. Gade, C. Langer, I. Y. Lee, C. Loelius, E. Lunderberg, F. Recchia, D. Smalley, S. R. Stroberg, R. Wadsworth, C. Walz, D. Weisshaar, A. Westerberg, K. Whitmore, and K. Wimmer, Phys. Rev. Lett. 112, 142502 (2014).
- [58] D. Smalley, H. Iwasaki, P. Navrátil, R. Roth, J. Langhammer, V. M. Bader, D. Bazin, J. S. Berryman, C. M. Campbell, J. Dohet-Eraly, P. Fallon, A. Gade, C. Langer, A. Lemasson, C. Loelius, A. O. Macchiavelli, C. Morse, J. Parker, S. Quaglioni, F. Recchia, S. R. Stroberg, D. Weisshaar, K. Whitmore, and K. Wimmer, Phys. Rev. C 92, 064314 (2015).
- [59] T. Glasmacher, Annual Review of Nuclear and Particle Science 48, 1 (1998).

- [60] I. Tanihata, H. Toki, and T. Kajino, eds., *Handbook of Nuclear Physics* (Springer Singapore, 2023).
- [61] P. Doornenbal, Progress of Theoretical and Experimental Physics **2012**, 03C004 (2012), https://academic.oup.com/ptep/article-pdf/2012/1/03C004/11597694/pts076.pdf.
- [62] S. Takeuchi, T. Motobayashi, Y. Togano, M. Matsushita, N. Aoi, K. Demichi, H. Hasegawa, and H. Murakami, Nuclear Instruments and Methods in Physics Research Section A: Accelerators, Spectrometers, Detectors and Associated Equipment **763**, 596 (2014).
- [63] W. Mueller, J. Church, T. Glasmacher, D. Gutknecht, G. Hackman, P. Hansen, Z. Hu, K. Miller, and P. Quirin, Nuclear Instruments and Methods in Physics Research Section A: Accelerators, Spectrometers, Detectors and Associated Equipment **466**, 492 (2001).
- [64] R. Bass, *Nuclear Reactions with Heavy Ions* (Springer-Verlag, Berlin, Heidelberg, 1980).
- [65] G. R. Satchler, *Introduction to Nuclear Reactions*, 2nd ed. (Macmillan Education, London, 1990).
- [66] B. V. Pritychenko, T. Glasmacher, B. A. Brown, P. D. Cottle, R. W. Ibbotson, K. W. Kemper, L. A. Riley, and H. Scheit, Phys. Rev. C 63, 011305 (2000).
- [67] K. Alder and A. Winther, Phys. Rev. **96**, 237 (1954).
- [68] A. Gade and T. Glasmacher, Progress in Particle and Nuclear Physics **60**, 161 (2008).
- [69] M. Rocchini and M. Zielińska, Physics **3**, 1237 (2021).
- [70] D. Cline, Annual Review of Nuclear and Particle Science **36**, 683 (1986).
- [71] A. Winther and K. Alder, Nuclear Physics A **319**, 518 (1979).
- [72] K. Alder, A. Bohr, T. Huus, B. Mottelson, and A. Winther, Reviews of Modern Physics **28**, 432 (1956).
- [73] P. Danielewicz and C. A. Bertulani, *Introduction to Nuclear Reactions* (CRC Press, 2004) iSBN: 9780750309325.
- [74] C. A. Bertulani, A. E. Stuchbery, T. J. Mertzimekis, and A. D. Davies, Phys. Rev. C **68**, 044609 (2003).
- [75] A. Gade, D. Bazin, C. M. Campbell, J. A. Church, D. C. Dinca, J. Enders, T. Glasmacher, Z. Hu, K. W. Kemper, W. F. Mueller, H. Olliver, B. C. Perry, L. A. Riley, B. T. Roeder, B. M. Sherrill, and J. R. Terry, Phys. Rev. C 68, 014302 (2003).

- [76] A. Revel, J. Wu, H. Iwasaki, J. Ash, D. Bazin, B. Brown, J. Chen, R. Elder, P. Farris, A. Gade, M. Grinder, N. Kobayashi, J. Li, B. Longfellow, T. Mijatović, J. Pereira, A. Poves, A. Sanchez, N. Shimizu, M. Spieker, Y. Utsuno, and D. Weisshaar, Physics Letters B 838, 137704 (2023).
- [77] J. Gibelin, D. Beaumel, T. Motobayashi, N. Aoi, H. Baba, Y. Blumenfeld, Z. Dombrádi, Z. Elekes, S. Fortier, N. Frascaria, N. Fukuda, T. Gomi, K. Ishikawa, Y. Kondo, T. Kubo, V. Lima, T. Nakamura, A. Saito, Y. Satou, E. Takeshita, S. Takeuchi, T. Teranishi, Y. Togano, A. M. Vinodkumar, Y. Yanagisawa, and K. Yoshida, Phys. Rev. C 75, 057306 (2007).
- [78] I. J. Thompson, FRESCO: Coupled Reaction Channels Calculations, Comput. Phys. Rep. 7, 167 (1988), http://www.fresco.org.uk.
- [79] I. J. Thompson and F. M. Nunes, *Nuclear Reactions for Astrophysics: Principles, Calculation and Applications of Low-Energy Reactions* (Cambridge University Press, Cambridge, 2009) see Appendix B.
- [80] I. J. Thompson, FRESCO: Coupled reaction channels calculations, https://www.fresco.org.uk (1988), computer code, version maintained by I. J. Thompson.
- [81] J. Barrette, N. Alamanos, F. Auger, B. Fernandez, A. Gillibert, D. Horen, J. Beene, F. Bertrand, R. Auble, B. Burks, J. Gomez Del Campo, M. Halbert, R. Sayer, W. Mittig, Y. Schutz, B. Haas, and J. Vivien, Physics Letters B 209, 182 (1988).
- [82] K. Yoshida, T. Fukui, K. Minomo, and K. Ogata, Progress of Theoretical and Experimental Physics **2014**, 053D03 (2014), https://academic.oup.com/ptep/article-pdf/2014/5/053D03/4452869/ptu063.pdf.
- [83] K. Wimmer, T. Arici, W. Korten, P. Doornenbal, J.-P. Delaroche, M. Girod, J. Libert, T. R. Rodríguez, P. Aguilera, A. Algora, T. Ando, H. Baba, B. Blank, A. Boso, S. Chen, A. Corsi, P. Davies, G. de Angelis, G. de Grance, D. T. Doherty, J. Gerl, R. Gernhäuser, T. Goigoux, D. Jenkins, G. Kiss, S. Joyama, T. Motobayashi, S. Nagamine, M. Niikura, S. Nishimura, A. Obertelli, D. Lubos, V. H. Phong, B. Rubio, E. Sahin, T. Saito, H. Sakurai, L. S. D. Steppenbeck, R. Taniuchi, V. Vaquero, R. Wadsworth, J. Wu, and M. Zielinska, The European Physical Journal A 56, https://doi.org/10.1140/epja/s10050-020-00171-3 (2020).
- [84] V. Vaquero, A. Jungclaus, P. Doornenbal, K. Wimmer, A. M. Moro, K. Ogata, T. Furumoto, S. Chen, E. Nácher, E. Sahin, Y. Shiga, D. Steppenbeck, R. Taniuchi, Z. Y. Xu, T. Ando, H. Baba, F. L. Bello Garrote, S. Franchoo, K. Hadynska-Klek, A. Kusoglu, J. Liu, T. Lokotko, S. Momiyama, T. Motobayashi, S. Nagamine, N. Nakatsuka, M. Niikura, R. Orlandi, T. Y. Saito, H. Sakurai, P. A. Söderström, G. M. Tveten, Z. Vajta, and M. Yalcinkaya, Phys. Rev. C 99, 034306 (2019).
- [85] P. Zavodszky, B. Arend, D. Cole, J. DeKamp, G. Machicoane, F. Marti, P. Miller, J. Moskalik, J. Ottarson, J. Vincent, and A. Zeller, Nuclear Instruments and Methods in Physics Research

- Section B: Beam Interactions with Materials and Atoms **241**, 959 (2005), the Application of Accelerators in Research and Industry.
- [86] R. C. York, H. G. Blosser, T. L. Grimm, F. Marti, J. Vincent, X. Y. Wu, and A. Zeller, in *15th International Conference on Cyclotrons and Their Applications* (1999) p. K01.
- [87] D. Morrissey, Nuclear Physics A **616**, 45 (1997), radioactive Nuclear Beams.
- [88] B.-M. Sherrill, Progress of Theoretical Physics Supplement **146**, 60 (2002), https://academic.oup.com/ptps/article-pdf/doi/10.1143/PTPS.146.60/5274782/146-60.pdf.
- [89] D. Morrissey, B. Sherrill, M. Steiner, A. Stolz, and I. Wiedenhoever, Nuclear Instruments and Methods in Physics Research Section B: Beam Interactions with Materials and Atoms **204**, 90 (2003), 14th International Conference on Electromagnetic Isotope Separators and Techniques Related to their Applications.
- [90] H. Iwasaki, A. Dewald, T. Braunroth, C. Fransen, D. Smalley, A. Lemasson, C. Morse, K. Whitmore, and C. Loelius, Nuclear Instruments and Methods in Physics Research Section A: Accelerators, Spectrometers, Detectors and Associated Equipment 806, 123 (2016).
- [91] D. Bazin, J. Caggiano, B. Sherrill, J. Yurkon, and A. Zeller, Nuclear Instruments and Methods in Physics Research Section B: Beam Interactions with Materials and Atoms 204, 629 (2003), 14th International Conference on Electromagnetic Isotope Separators and Techniques Related to their Applications.
- [92] M. Famiano, International Journal of Modern Physics E **28** (2019).
- [93] D. Leitner and C. Lyneis, Ecr ion sources, in *The Physics and Technology of Ion Sources* (John Wiley Sons, Ltd, 2004) Chap. 11, pp. 203–231, https://onlinelibrary.wiley.com/doi/pdf/10.1002/3527603956.ch11.
- [94] L. T. Sun, High intensity operation for heavy ion cyclotron of highly charged ecr ion sources (2014).
- [95] J.-J. Gaimard and K.-H. Schmidt, Nuclear Physics A **531**, 709 (1991).
- [96] G. Knoll, Radiation Detection and Measurement (4th ed.) (John Wiley, Hoboken, NJ, 2010).
- [97] W. R. Leo, *Techniques for nuclear and particle physics experiments:a how-to approach; 2nd ed.* (Springer, Berlin, 1994).
- [98] J. Dufour, R. Del Moral, H. Emmermann, F. Hubert, D. Jean, C. Poinot, M. Pravikoff, A. Fleury, H. Delagrange, and K.-H. Schmidt, Nuclear Instruments and Methods in Physics Research Section A: Accelerators, Spectrometers, Detectors and Associated Equipment 248, 267 (1986).

- [99] M. Berz, K. Joh, J. A. Nolen, B. M. Sherrill, and A. F. Zeller, Phys. Rev. C 47, 537 (1993).
- [100] J. Pereira-Conca, S800 Documentation (2023).
- [101] J. Yurkon, D. Bazin, W. Benenson, D. Morrissey, B. Sherrill, D. Swan, and R. Swanson, Nuclear Instruments and Methods in Physics Research Section A: Accelerators, Spectrometers, Detectors and Associated Equipment **422**, 291 (1999).
- [102] S800 spectrograph documentation, https://wikihost.frib.msu.edu/S800Doc/doku.php?id=detectors, accessed: 05-30-2025.
- [103] C. Morse, H. Iwasaki, A. Lemasson, T. Baugher, D. Bazin, J. S. Berryman, A. Dewald, C. Fransen, A. Gade, S. McDaniel, A. J. Nichols, A. Ratkiewicz, S. R. Stroberg, P. Voss, R. Wadsworth, D. Weisshaar, K. Wimmer, and R. Winkler, Phys. Rev. C 90, 034310 (2014).
- [104] K. Wimmer and E. Lunderberg, GrROOT: ROOT based analysis software for GRETINA + S800 spectrograph., https://github.com/wimmer-k/GrROOT.
- [105] K. Wimmer and E. Lunderberg, Internal documentation (2012).
- [106] A. Lemasson, H. Iwasaki, C. Morse, D. Bazin, T. Baugher, J. S. Berryman, A. Dewald, C. Fransen, A. Gade, S. McDaniel, A. Nichols, A. Ratkiewicz, S. Stroberg, P. Voss, R. Wadsworth, D. Weisshaar, K. Wimmer, and R. Winkler, Phys. Rev. C 85, 041303 (2012).
- [107] P. Adrich, D. Enderich, D. Miller, V. Moeller, R. Norris, K. Starosta, C. Vaman, P. Voss, and A. Dewald, Nuclear Instruments and Methods in Physics Research Section A: Accelerators, Spectrometers, Detectors and Associated Equipment **598**, 454 (2009).
- [108] S. Agostinelli, J. Allison, K. Amako, J. Apostolakis, H. Araujo, P. Arce, M. Asai, D. Axen, S. Banerjee, G. Barrand, F. Behner, L. Bellagamba, J. Boudreau, L. Broglia, A. Brunengo, H. Burkhardt, S. Chauvie, J. Chuma, R. Chytracek, G. Cooperman, G. Cosmo, P. Degtyarenko, A. Dell'Acqua, G. Depaola, D. Dietrich, R. Enami, A. Feliciello, C. Ferguson, H. Fesefeldt, G. Folger, F. Foppiano, A. Forti, S. Garelli, S. Giani, R. Giannitrapani, D. Gibin, J. Gómez Cadenas, I. González, G. Gracia Abril, G. Greeniaus, W. Greiner, V. Grichine, A. Grossheim, S. Guatelli, P. Gumplinger, R. Hamatsu, K. Hashimoto, H. Hasui, A. Heikkinen, A. Howard, V. Ivanchenko, A. Johnson, F. Jones, J. Kallenbach, N. Kanaya, M. Kawabata, Y. Kawabata, M. Kawaguti, S. Kelner, P. Kent, A. Kimura, T. Kodama, R. Kokoulin, M. Kossov, H. Kurashige, E. Lamanna, T. Lampén, V. Lara, V. Lefebure, F. Lei, M. Liendl, W. Lockman, F. Longo, S. Magni, M. Maire, E. Medernach, K. Minamimoto, P. Mora de Freitas, Y. Morita, K. Murakami, M. Nagamatu, R. Nartallo, P. Nieminen, T. Nishimura, K. Ohtsubo, M. Okamura, S. O'Neale, Y. Oohata, K. Paech, J. Perl, A. Pfeiffer, M. Pia, F. Ranjard, A. Rybin, S. Sadilov, E. Di Salvo, G. Santin, T. Sasaki, N. Savvas, Y. Sawada, S. Scherer, S. Sei, V. Sirotenko, D. Smith, N. Starkov, H. Stoecker, J. Sulkimo, M. Takahata, S. Tanaka, E. Tcherniaev, E. Safai Tehrani, M. Tropeano, P. Truscott, H. Uno, L. Urban, P. Urban, M. Verderi, A. Walkden, W. Wander, H. Weber, J. Wellisch, T. Wenaus, D. Williams,

- D. Wright, T. Yamada, H. Yoshida, and D. Zschiesche, Nuclear Instruments and Methods in Physics Research Section A: Accelerators, Spectrometers, Detectors and Associated Equipment **506**, 250 (2003).
- [109] T. Furumoto, W. Horiuchi, M. Takashina, Y. Yamamoto, and Y. Sakuragi, Phys. Rev. C 85, 044607 (2012).
- [110] T. Motobayashi, Y. Ikeda, K. Ieki, M. Inoue, N. Iwasa, T. Kikuchi, M. Kurokawa, S. Moriya, S. Ogawa, H. Murakami, S. Shimoura, Y. Yanagisawa, T. Nakamura, Y. Watanabe, M. Ishihara, T. Teranishi, H. Okuno, and R. Casten, Physics Letters B **346**, 9 (1995).
- [111] B. Carlson, Joint ICTP-IAEA Workshop on Nuclear Reaction Data for Advanced Reactor Technologies:the optical model, Presented at ICTP Workshop Session 34 (2010), pDF available at https://indico.ictp.it/event/a09144/session/34/contribution/19/material/0/1.pdf.
- [112] F. D. Becchetti and G. W. Greenlees, Phys. Rev. **182**, 1190 (1969).
- [113] W. Van Oers and H. Haw, Physics Letters B **45**, 227 (1973).
- [114] P. E. Hodgson, *The nuclear optical model introductory overview*, Tech. Rep. (Oxford Univ. Nucl. Phys., Oxford, 1996).
- [115] T. Furumoto, Y. Sakuragi, and Y. Yamamoto, Phys. Rev. C 80, 044614 (2009).
- [116] T. Furumoto, Y. Sakuragi, and Y. Yamamoto, Phys. Rev. C 78, 044610 (2008).
- [117] L. D. Landau and E. M. Lifshitz, *The Classical Theory of Fields*, 4th ed., Course of Theoretical Physics, Vol. 2 (Pergamon Press, Oxford; New York, 1975) p. 44.
- [118] W. Frahn, Nuclear Physics **75**, 577 (1966).
- [119] W. E. Frahn, Phys. Rev. Lett. **26**, 568 (1971).
- [120] National Nuclear Data Center, National nuclear data center (2025), accessed: 2025-07-18.
- [121] C. Loelius, H. Iwasaki, B. A. Brown, M. Honma, V. M. Bader, T. Baugher, D. Bazin, J. S. Berryman, T. Braunroth, C. M. Campbell, A. Dewald, A. Gade, N. Kobayashi, C. Langer, I. Y. Lee, A. Lemasson, E. Lunderberg, C. Morse, F. Recchia, D. Smalley, S. R. Stroberg, R. Wadsworth, C. Walz, D. Weisshaar, A. Westerberg, K. Whitmore, and K. Wimmer, Phys. Rev. C 94, 024340 (2016).
- [122] M. Baginova, P. Vojtyla, and P. Povinec, Applied Radiation and Isotopes 166, 109422 (2020).
- [123] O. Tarasov, D. Bazin, M. Lewitowicz, and O. Sorlin, Nuclear Physics A 701, 661 (2002), 5th

- International Conference on Radioactive Nuclear Beams.
- [124] D. Bazin, O. Tarasov, M. Lewitowicz, and O. Sorlin, Nuclear Instruments and Methods in Physics Research Section A: Accelerators, Spectrometers, Detectors and Associated Equipment **482**, 307 (2002).
- [125] O. Tarasov, D. Bazin, M. Hausmann, M. Kuchera, P. Ostroumov, M. Portillo, B. Sherrill, K. Tarasova, and T. Zhang, Nuclear Instruments and Methods in Physics Research Section B: Beam Interactions with Materials and Atoms 541, 4 (2023).
- [126] M. Petri, P. Fallon, A. Macchiavelli, S. Heil, E. Rodriguez-Vieitez, D. Bazin, C. Campbell, R. Clark, M. Cromaz, A. Gade, T. Glasmacher, I. Lee, S. Malbrunot-Ettenauer, S. Paschalis, A. Ratkiewicz, J. Terry, D. Weisshaar, and M. Wiedeking, Physics Letters B 748, 173 (2015).
- [127] Z. Elekes, Z. Dombrádi, A. Saito, N. Aoi, H. Baba, K. Demichi, Z. Fülöp, J. Gibelin, T. Gomi, H. Hasegawa, N. Imai, M. Ishihara, H. Iwasaki, S. Kanno, S. Kawai, T. Kishida, T. Kubo, K. Kurita, Y. Matsuyama, S. Michimasa, T. Minemura, T. Motobayashi, M. Notani, T. Ohnishi, H. J. Ong, S. Ota, A. Ozawa, H. K. Sakai, H. Sakurai, S. Shimoura, E. Takeshita, S. Takeuchi, M. Tamaki, Y. Togano, K. Yamada, Y. Yanagisawa, and K. Yoneda, Phys. Rev. C 73, 044314 (2006).
- [128] A. Sanchez, H. Iwasaki, A. Revel, B. A. Brown, J. Ash, D. Bazin, J. Chen, R. Elder, A. Gade, A. Goldkuhle, M. Grinder, D. Lempke, J. Li, B. Longfellow, C. Müller-Gatermann, J. Pereira, D. Rhodes, R. Salinas, and D. Weisshaar, Phys. Rev. C 110, 024322 (2024).
- [129] A. Dewald, O. Möller, and P. Petkov, Progress in Particle and Nuclear Physics 67, 786 (2012).
- [130] I. J. Thompson, Computer Physics Reports 7, 167 (1988).
- [131] I. J. Thompson, FRESCO: Input description, http://www.fresco.org.uk/input3. 4/fresco-namelist-manual.pdf (2020), computer code, version maintained by I. J. Thompson.
- [132] A. M. Moro, 3.2.0.2 coulomb deformation, http://www.fresco.org.uk/moro/frnotes/node12.html (2004), fRESCO notes, accessed August 2025.
- [133] P. Doornenbal, H. Scheit, N. Kobayashi, N. Aoi, S. Takeuchi, K. Li, E. Takeshita, Y. Togano, H. Wang, S. Deguchi, Y. Kawada, Y. Kondo, T. Motobayashi, T. Nakamura, Y. Satou, K. N. Tanaka, and H. Sakurai, Phys. Rev. C **81**, 041305 (2010).
- [134] J. Chen and B. Singh, Nucl.Data Sheets **184**, 29 (2022).
- [135] R. S. Lubna, K. Kravvaris, S. L. Tabor, V. Tripathi, A. Volya, E. Rubino, J. M. Allmond, B. Abromeit, L. T. Baby, and T. C. Hensley, Phys. Rev. C 100, 034308 (2019).

- [136] R. S. Lubna, K. Kravvaris, S. L. Tabor, V. Tripathi, E. Rubino, and A. Volya, Phys. Rev. Res. **2**, 043342 (2020).
- [137] Y. Utsuno, T. Otsuka, T. Mizusaki, and M. Honma, Phys. Rev. C 60, 054315 (1999).
- [138] Y. Utsuno, T. Otsuka, T. Mizusaki, and M. Honma, Nuclear Physics A 704, 50 (2002).
- [139] W. A. Richter, S. Mkhize, and B. A. Brown, Phys. Rev. C 78, 064302 (2008).
- [140] B. A. Brown and W. A. Richter, Phys. Rev. C 74, 034315 (2006).
- [141] A. M. Bernstein, V. R. Brown, and V. A. Madsen, Comments Nucl. Part. Phys. 11, 203 (1983).
- [142] A. Bernstein, V. Brown, and V. Madsen, Physics Letters B 103, 255 (1981).
- [143] E. K. Warburton and B. A. Brown, Phys. Rev. C 46, 923 (1992).
- [144] M. Honma, T. Otsuka, B. A. Brown, and T. Mizusaki, The European Physical Journal A 25, 499 (2005).
- [145] B. Brown and B. Wildenthal, Annual Review of Nuclear and Particle Science 38, 29 (1988).
- [146] T. Kuo and G. Brown, Nuclear Physics A **114**, 241 (1968).
- [147] D. Millener and D. Kurath, Nuclear Physics A **255**, 315 (1975).
- [148] N. Shimizu, T. Mizusaki, Y. Utsuno, and Y. Tsunoda, Computer Physics Communications **244**, 372 (2019).
- [149] M. Honma, T. Otsuka, B. A. Brown, and T. Mizusaki, Phys. Rev. C 69, 034335 (2004).
- [150] M. Dufour and A. P. Zuker, Phys. Rev. C **54**, 1641 (1996).
- [151] N. Tsunoda, T. Otsuka, N. Shimizu, M. Hjorth-Jensen, K. Takayanagi, and T. Suzuki, Phys. Rev. C **95**, 021304 (2017).
- [152] T. H. Ogunbeku, J. M. Allmond, T. J. Gray, W.-J. Ong, B. A. Brown, A. Gargano, R. Grzywacz, J. D. Holt, A. O. Macchiavelli, T. Miyagi, S. Neupane, B. C. Rasco, H. Schatz, B. M. Sherrill, O. B. Tarasov, H. Arora, A. D. Ayangeakaa, H. C. Berg, J. M. Berkman, D. L. Bleuel, K. Bosmpotinis, M. P. Carpenter, G. Cerizza, A. Chester, J. M. Christie, I. Cox, H. L. Crawford, B. P. Crider, J. Davis, A. A. Doetsch, J. G. Duarte, A. Estrade, A. Fijałkowska, C. Frantzis, T. Gaballah, E. C. Good, K. Haak, S. Hanai, J. T. Harke, A. C. Hartley, K. Hermansen, D. E. M. Hoff, D. Hoskins, J. Huffman, P. Van Isacker, R. Jain, M. Karny, T. T. King, N. Kitamura, K. Kolos, A. Laminack, S. N. Liddick, B. Longfellow, R. S. Lubna, S. Lyons,

- M. Madurga, M. J. Mogannam, G. Owens-Fryar, J. R. Palomino, M. M. Rajabali, A. L. Richard, I. J. Richardson, E. K. Ronning, G. E. Rose, T. J. Ruland, K. P. Rykaczewski, N. D. Scielzo, D. P. Scriven, D. Seweryniak, K. Siegl, M. Singh, A. Spyrou, M. Stepaniuk, A. E. Stuchbery, A. Sweet, V. Tripathi, A. Tsantiri, S. Uthayakumaar, W. B. Walters, S. Watters, Z. Xu, and R. Yokoyama, Phys. Rev. Lett. **135**, 072501 (2025).
- [153] M. Basunia and A. Chakraborty, Nucl.Data Sheets 197, 1 (2024).
- [154] S. Larsson, G. Leander, and I. Ragnarsson, Nuclear Physics A 307, 189 (1978).
- [155] S. E. Larsson, Physica Scripta 8, 17 (1973).
- [156] G. Leander and R. Sheline, Nuclear Physics A **413**, 375 (1984).
- [157] H. Toki and A. Faessler, Nuclear Physics A 253, 231 (1975).
- [158] T. Bengtsson and I. Ragnarsson, Nuclear Physics A 436, 14 (1985).
- [159] G. Dong, X. Wang, and S. Yu, Science China Physics, Mechanics & Astronomy **58**, 112004 (2015).
- [160] G. Cowan, *Statistical Data Analysis* (Clarendon Press, Oxford University Press, Oxford, 1998).

APPENDIX

A FRESCO Input

A brief description of each section is found below [78]:

- &FRESCO General numerical parameters that control the calculation. Namely,
 - hcm the integration step taken over the coupled-channel equations
 - rmatch the radius at which the wave function is matched to its asymptotic form containing a plane wave term, elastic channel term, and sum over all possible exit channels term
 - jtmin, jtmax initial and final total angular momentum J, respectively, defining the
 total number of partial waves used in the calculation
 - thmin, thmin minimum and maximum center-of-mass scattering angles to be considered in the calculation.
 - elab laboratory frame energy of the projectile
- &PARTITION Intrinsic properties of the incoming and target nuclei,
 - namep, namet name of the projectile and target nucleus
 - bandp, bandt parity of the state defined for the projectile and target nucleus
 - ep, et energy of the defined state for the projectile and target nucleus
 - nex number of projectile-target excited-state pairs in the current partition
- &STATES Defines the pairs of projectile and target states associated with nex within the &PARTITION namelist.
 - jp, jt angular momentum of the projectile and target nucleus
 - massp, masst mass of the projectile and target nucleus
 - zp, zt atomic numbers of the projectile and target nucleus
 - kkp rotational band containing the projectile state

- cpot index of effective potential to be used for the excitation and relative motion between the projectile and target for each reaction channel. Index is given by the kp parameter in the &POT namelist.
- copyt used after defining the first &STATES namelist, copies the properties of previous target state to the current &STATES namelist
- &POT Defines the Coulomb and nuclear potentials to be used. Each &POT namelist with the same kp index constitute an effective potential. Information about the specific potentials used in this analysis are found in Sect. 4.2.1.1.
 - kp index associated with the cpot variable in the &STATES namelist. Each potential
 is characterized by a type and shape.
 - ap, at mass number of projectile and target nucleus
 - rc reduced Coulomb radius
 - type defines the type of potential to be used (e.g. central volume potential for type=1)
 - shape defines the shape of the potential (e.g. shape=0 (Woods-Saxon) is default value)

B Monte Carlo Description

This section discusses the Monte Carlo simulation that was developed to relate the FRESCO calculations to experimental results, along with how the acceptances for the reaction products and incoming beam were determined.

To begin, we define two coordinate systems: a global coordinate system G, which corresponds to the laboratory frame, and the projectile coordinate system P, which is associated with the projectile's reference frame. As illustrated in Fig. B.1 (a), coordinate system P is overlaid on coordinate system G, with P's z-axis aligned along the ion's velocity vector. This assumes that the

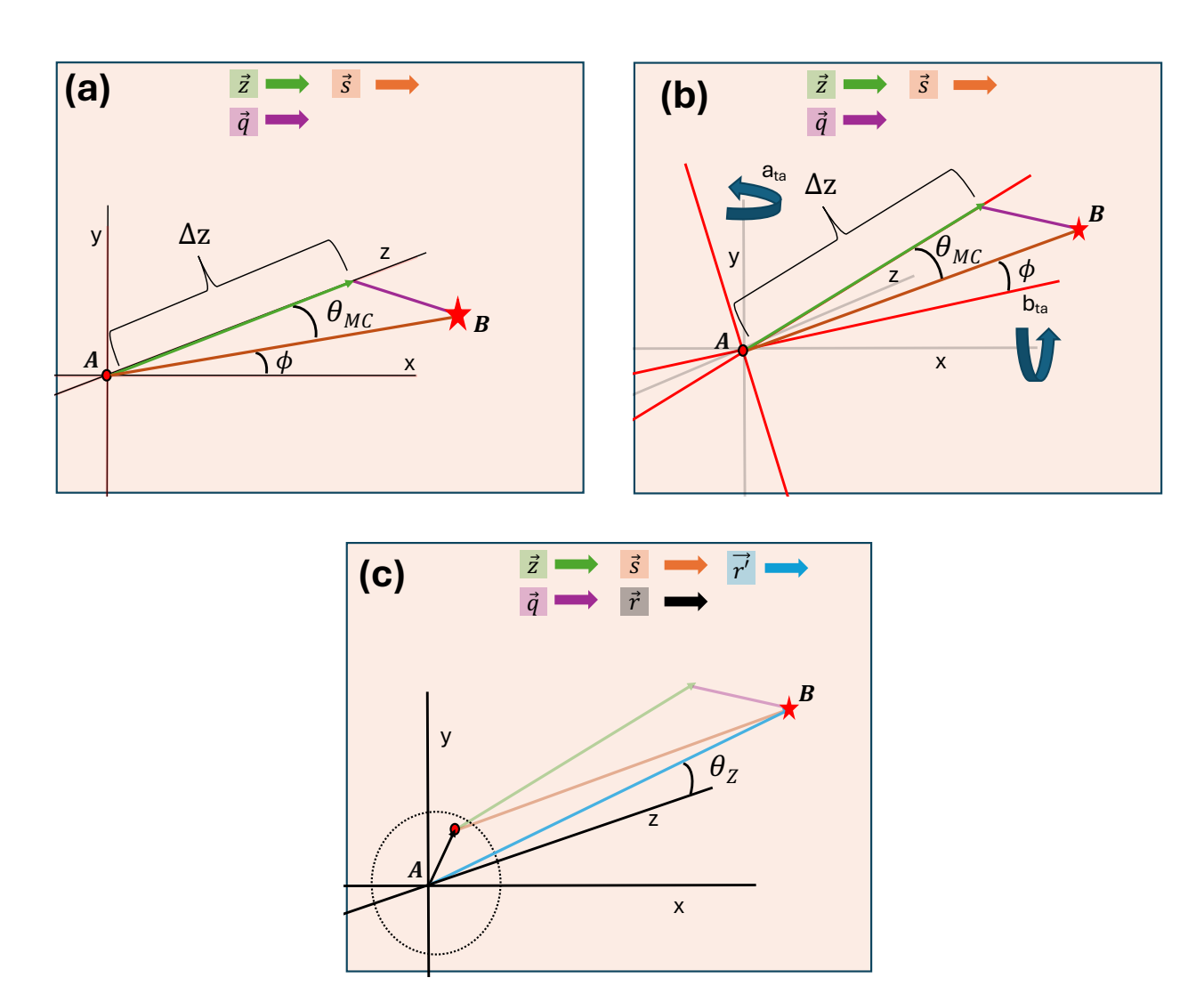


Figure B.1: Coordinate systems in the projectile frame (P) and laboratory frame (G) shown at different stages of incorporating the finite beam spot size and angular spread. Panel (a) overlays coordinate systems P and G, and introduces vectors \vec{z} , \vec{q} , and \vec{s} , which describe the scattering process. The vector \vec{z} corresponds to the ion's initial direction along its trajectory. \vec{q} represents the transverse displacement of the ion at a downstream focal plane located a distance Δz from the origin point A. \vec{s} denotes the scattered trajectory at an angle θ_{MC} relative to the projectile's z-axis. The angle θ_{MC} is sampled from a yield distribution, while the azimuthal angle ϕ is measured from the projectile's y-axis and sampled uniformly from 0 to 2π . Panel (b) illustrates the effect of the ion's angular spread on vectors \vec{z} , \vec{q} , and \vec{s} by rotating coordinate system P. Panel (c) shows the translation of coordinate system P due to the beam spot size, relative to G.

incoming projectile passes through the origin of coordinate system G, with the projectile's velocity vector aligned with the laboratory frame's z-axis. With the coordinate system defined and overlaid, vectors \vec{q} , \vec{s} , and \vec{z} are introduced within P's reference frame, as shown in Fig B.1 (a). These vectors are responsible for describing the scattering process in the ion's reference frame. Vector \vec{z}

corresponds to the z component of the ion's trajectory with magnitude $|\vec{z}| = \Delta z$ and $\vec{z} = \Delta z \hat{z}$.

The distance traveled by the ion along a focal plane at distance Δz from origin point A is given by \vec{q} , and calculated such as

$$|\vec{q}| = \tan(\theta_{MC})\Delta z \tag{1}$$

$$\vec{q} = \begin{pmatrix} \sin(\phi)|\vec{q}|\\ \cos(\phi)|\vec{q}|\\ 0 \end{pmatrix} \tag{2}$$

where θ_{MC} is sampled according to the acceptance-rejection method [160] from the yield distribution and ϕ is randomly selected between 0 and 2π . The scattering vector \vec{s} in the P coordinate system is given by

$$|\vec{s}| = \Delta z^2 + |\vec{q}|^2 = \Delta z^2 + (\tan(\theta_{MC})\Delta z)^2$$
 (3)

$$=\Delta z^2 (1 + \tan(\theta_{MC})^2) \tag{4}$$

$$\vec{s} = \vec{z} + \vec{q} = \begin{pmatrix} \sin(\phi)|\vec{q}| \\ \cos(\phi)|\vec{q}| \\ \Delta z \end{pmatrix}$$
 (5)

which corresponds to the trajectory of the ion at some angle θ_{MC} from the laboratory frame's z-axis and angle ϕ from the y-axis. At this point, having not incorporated the angular spread of the incoming beam, we set the final scattering angle $\theta_Z = \theta_{MC}$. Coordinate system P is then rotated by the angles a_{ta} and b_{ta} , as depicted in Fig. B.1 (b), where the former corresponds to the dispersive angle in the xz-plane and the latter to the yz-plane. The distributions of a_{ta} and b_{ta} are determined from the ion's reconstructed trajectory using the S800 inverse map. Rotating coordinate system P also rotates vectors \vec{q} , \vec{s} , and \vec{z} , reorienting them according to the ion's angular spread at the target position while preserving the scattering kinematics. To describe the rotation, a set of basis vectors in the laboratory frame G are defined,

$$\hat{G}_{1} = \begin{pmatrix} 1 \\ 0 \\ 0 \end{pmatrix} \qquad \hat{G}_{2} = \begin{pmatrix} 0 \\ 1 \\ 0 \end{pmatrix} \qquad \hat{G}_{3} = \begin{pmatrix} 0 \\ 0 \\ 1 \end{pmatrix} \tag{6}$$

along with basis vectors in the ion's reference frame P as

$$\hat{P}_1 = \begin{pmatrix} 1 \\ 0 \\ 0 \end{pmatrix} \qquad \hat{P}_2 = \begin{pmatrix} 0 \\ 1 \\ 0 \end{pmatrix} \qquad \hat{P}_3 = \begin{pmatrix} 0 \\ 0 \\ 1 \end{pmatrix} \tag{7}$$

To express coordinates defined in P's reference frame in G's reference frame, a change of basis is required such that

$$\left[\vec{k}\right]_G = T_{P \to G} \left[\vec{k}\right]_P \tag{8}$$

where \vec{k} is an arbitrary vector being transformed. The $T_{R\to G}$ is the transformation matrix in the form of a 3D rotation matrix,

$$R(\alpha = 0, \beta, \gamma) = R_z(\alpha = 0)R_y(\beta)R_x(\gamma)$$
(9)

$$= \begin{pmatrix} \cos(\beta) & \sin(\beta)\sin(\gamma) & \sin(\beta)\cos(\gamma) \\ 0 & \cos(\gamma) & -\sin(\gamma) \\ -\sin(\beta) & \cos(\beta)\sin(\gamma) & \cos(\beta)\cos(\gamma) \end{pmatrix}$$
(10)

We set $\alpha = 0$ to indicate that we are not performing any rotations about the *z*-axis. The change of basis matrix $T_{P \to G}$ is the rotation matrix and is defined as

$$T_{P \to G} = \left[[P_1]_G [P_2]_G [P_3]_G \right] \tag{11}$$

$$[P_1]_G = \begin{bmatrix} \cos(\beta) \\ 0 \\ -\sin(\beta) \end{bmatrix}$$
 (12)

$$[P_2]_G = \begin{bmatrix} \sin(\beta)\sin(\gamma) \\ \cos(\gamma) \\ \cos(\beta)\sin(\gamma) \end{bmatrix}$$
(13)

$$[P_3]_G = \begin{bmatrix} \sin(\beta)\cos(\gamma) \\ -\sin(\gamma) \\ \cos(\beta)\cos(\gamma) \end{bmatrix}$$
(14)

where $[P_i]_G$ with i=1,2,3 expressing the vectors in the rotated projectile coordinate system P in the laboratory-frame basis vectors. The transformation matrix is defined as $T_{P\to G} \equiv R(\alpha=0,\beta,\gamma)$. To account for the finite beam spot size, the P coordinate system is displaced by a vector \vec{r} relative to the G coordinate system. The displacement vector \vec{r} is randomly generated in each iteration of the Monte Carlo simulation, being defined as

$$\vec{r} = \begin{pmatrix} \delta_x \\ \delta_y \end{pmatrix} \tag{15}$$

where δ_x and δ_y are randomly selected from independent Gaussian distributions. The Gaussian distribution describing the position of the ion along the y-axis is parameterized by the y_{ta} distribution described in Sect. 4.1.2.1. Due to not having any spatial information of the ion along the x-axis at the target location, position of the ion along the x-axis is described by a Gaussian parameterized by the y_{ta} distribution. Incorporating the angular spread of the incoming beam at the target position into the FRESCO results yields the violet histograms in Figs. 4.14 and 4.15.

To determine the scattering angle θ_Z in the laboratory frame with the angular spread and the beam-spot size incorporated, the vector \vec{r}' is defined from the laboratory-frame origin (i.e. G coordinate system), as shown in Fig. B.1 (c),

$$\vec{r'} = \vec{r} + \vec{s} \tag{16}$$

The scattering angle θ_Z in the laboratory frame is then defined as

$$\theta_Z = \cos^-\left(\Delta z/|\vec{r'}|\right) \tag{17}$$

The overall process can be described as follows:

- 1. Read in FRESCO results (i.e. differential cross section in center-of-mass frame)
- 2. Convert differential cross section from center-of-mass to laboratory frame
- 3. Calculate center-of-mass and laboratory frame yield from respective differential cross sections
- 4. Perform Monte Carlo simulation to incorporate the beam's angular spread and beam spot
 - The B(E2) strengths and deformation lengths were determined in this step by comparing the experimental yields with FRESCO calculations integrated up to the chosen scattering angle.
- 5. Convert yield back to differential cross section
 - This step was done to ensure all conversions were performed correctly.